An Investigation Of The Operation Of Electrolyte Gated Organic Field Effect Transistors And The Potential Applications In Biosensors

A thesis submitted to the University of Manchester for the degree of Doctor of Philosophy in the Faculty of Biology, Medicine and Health

Glenn Sunley Saez

School of Biological Sciences

University of Manchester

2020

Table of Contents

Table of Contents 1

List of Figures 5

List of Tables 21

Abstract 23

Declaration 25

Copyright Statement 26

Acknowledgements 27

1 Introduction 28

1.1 Preface 28

1.2 Biosensors 30

1.2.1 Labelled assays 32

1.2.1.1 Amperometric glucometers 33

1.2.1.2 Potentiometric biosensors 34

1.2.1.3 Immunosensors 35

1.2.2 Label-free assays 35

1.2.3 Biosensor figures of merit 36

1.2.3.1 Calibration curve 36

1.2.3.2 Sensitivity 38

1.2.3.3 Limit of detection 38

1.2.3.4 Dynamic range 40

1.2.3.5 Selectivity 40

1.2.3.6 Reproducibility 41

1.2.3.7 Response and recovery time 42

1.2.3.8 Stability 42

1.3 Organic field-effect transistors (OFETs) 44

1.3.1 Organic electronics 44

1.3.2 Origin of charge transport in OFETs/OSCs 45
1.3.3 OFET device architectures 50
1.3.4 Organic semiconductor for use in OFETs 52
1.3.5 OFET Device operation 54
1.3.5.1 Band bending and the field effect 54
1.3.5.2 Role of charge injecting electrodes 56
1.3.6 Device characteristics and key parameters 58
1.3.7 EGOFET Operation the role of the EDL 65
1.3.8 Applications 67
1.4 OFETs as Biosensors in aqueous environments 68
1.4.1.1 Sensing in OFETs 68
1.4.1.2 Analysing sensing response in OFET biosensors 68
1.4.3 EGOFETs as biosensors 75
1.4.4 Improvements to device operation 84
1.5 Cancer 91
1.5.1 Breast Cancer 93
1.5.2 Breast Cancer Biomarkers 95
1.5.3 Additional biomarkers 97
1.5.4 Current Breast Cancer biomarker detection techniques 100
1.5.4.1 Immunohistochemistry (IHC) test 101
1.5.4.2 Fluorescent *in situ* Hybridisation (FISH) test 102
2 Aims and Objectives 104
3 Materials and Methods 106
3.1 Thin film deposition 108
3.1.1 DPPTTT 113
3.1.2 PBTTT 115
4 Experimental 117
4.1 Materials 117

4.2 Equipment and measurements 117
4.3 Device Fabrication 118
PBTTT-based device fabrication 119
DPPTTT-based device fabrication 119
P3HT-based device fabrication 119
Bilayer device fabrication 120
Evaporated gold substrates for AFM 120
4.4 Fluorescent binding assay 120
4.5 Gate functionalised EGOFET biosensors 121
4.6 Procedure for flow cell functionalization and measurements 123
4.7 PMMA – COOH synthesis 124
5 Immobilisation strategies 128
5.1 Bilayer functionalisation 129
5.1.1 PMMA co-polymer synthesis 131
5.1.2 Thin film surface functionalisation and characterisation 135
5.1.2.1 AFM and Contact angle measurements 136
5.1.2.2 Fluorescent Binding Assay 139
5.2 Gate functionalisation strategy 145
5.2.1 Lipoic acid-based SAM for THC sensing 145
5.2.2 3MPA/11MUA-based BioSAM for HER2 ECD sensing 147
5.3 Summary 150
6 Droplet-based EGOFET devices 151
6.1 PBTTT Tungsten-gated water droplet devices 152
6.1.1 EGOFETs using PBTTT – PMMA blends 159
6.2 DPPTTT Tungsten-gated water droplet devices 162
6.3 EGOFET devices using different gate metals 165
6.4 Interdigitated electrodes with Au gated EGOFETs 170
6.5 Summary 175

7 Gate functionalised EGOFET biosensors 176
7.1 HER2 ECD sensing with 3MPA/11MUA-based BioSAM 178
7.2 THC sensing using OBPs and Lipoic acid-based SAM 185
7.3 Summary 193
8 Flow cell-based EGOFET devices 195
8.1 Design of flow cell and measuring platform 196
8.2 PBTTT-based devices 201
8.2.1 PBTTT-based devices with shadow mask design 201
8.2.2 PBTTT-based devices with IDE design 210
8.3 DPPTTT-based devices 214
8.3.1 DPPTTT -based devices with shadow mask design 214
8.3.2 DPPTTT -based devices with IDE design 216
8.3.3 Functionalisation of DPPTTT/PMMA COOH devices 219
8.3.4 Calibration curve and baseline stability assays 222
8.3.5 Stabilising bias stress drift 228
9 Conclusions and future work 234
9.1 Conclusions 234
9.2 Future work 236
10 Appendix 237
10.1 Tables 237
10.2 Figures 239
10.3 Achievements 245
11 References 246

Word Count 79423

List of Figures

Figure 1 Schematic representation of signal transduction in Label-free (left) and Labelled assays (right). In a Label-free assay (left) a signal is generated directly through interaction with the analyte, and a molecular capturing element (blue) that is immobilised onto a transducer surface. In labelled "sandwich" assays (right) the analyte is sandwiched between a detector and a capture agent (e.g. antibodies), one of which is immobilised on a solid surface (capture element). The signalling moiety attached to the immobilised detector element (green) transduces the formation of the complex into a detectable output signal. 32

Figure 2 An example calibration curve showing the relative figures of merit that can be extracted. 37

Figure 3 Figure showing normal distribution of a set of blank values and how this effect the separation of the LOD and LOQ. The area under the curves at α signifies the values corresponding to false positives and β signifies the false negatives. 39

Figure 4 Distribution of available electronic states or energy levels. The y axis represents energy whilst the x-axis represents the density of available states of a certain energy for each material. The shading represents the distribution of filled states (black = all states filled and white = no states filled). 46

Figure 5 The Gaussian distribution of localised states that form the energy levels of the highest occupied molecular orbital (HOMO) and the lowest unoccupied molecular orbital (LUMO) for an organic semiconductor. 48

Figure 6 OFET (a and b) and electrolyte gated transistors (EGTs) architectures reported in the literature as possible biosensors: c) ISOFET; d) EGOFET; e) OECT. The red circle indicates the different interfaces involved in the detection of biomolecules.[50] 51

Figure 7 Molecular structures of selected high mobility p-type OSCs. 53

Figure 8, Band structures showing the distribution of holes and the energy level alignment across the metal–insulator–(p-type) semiconductor structure at different gate voltages. (a) zero gate bias (V_{GS} = 0), (b) accumulation (V_{GS} < 0) and (c) depletion (V_{GS} >0) modes.[51] The arrow points towards the region of the accumulated charges at the interfacial channel region where 2D charge transport is confined. 55

Figure 9 A diagram showing the work function of several metals and the HOMO/LUMO levels of several p-type organic semiconductors relative to the vacuum level in eV.[68] 57

Figure 10 Schematic structure of a classic BGBC OFET showing the shape of the conductive channel in blue, together with the evolution of a current-voltage characteristic for the device with fixed V_G in different operating regimes: a) in the linear regime; b) at pinch-off; d) in the saturation regime. 60

Figure 11 Current-voltage (I_{DS}-V_{DS}) curves of DPPTTT p-channel OFET at different V_{GS} gate voltages. The linear region ($V_{DS}<V_{GS}-V_T$), saturation region ($V_{DS}>V_{GS}-V_T$) and pinch-off at $V_{DS}=V_{GS}-V_T$ are labelled.[51] 61

Figure 12 Transfer characteristic of a typical p-type EGOFET device showing the extractable parameters in the saturation regime. I_{SD} (black – solid lines) is plotted in a semi-log scale (left) highlighted are I_{On} and I_{Off} used in calculating the I_{On}/I_{Off} ratio. A linear fit to I_{SD} plotted in a square root scale (blue – right) gives the gradient (A) and intercept (B) from which the mobility (μ) and threshold voltage (V_T) are calculated through Equation 9-5. 62

Figure 13 Electrochemical reactions of water. Standard potentials *vs.* Standardised Hydrogen Electrode (SHE). The difference of these two voltages provides the electrochemical window of water as 1.23 V 65

Figure 14 Illustration of the ion distribution in the Stern model. Showing the Helmholtz layer (HL), the Gouy-Chapman diffuse layer and the bulk electrolyte (above), and spatial distribution of the potential between the gate and the semiconductor in an electrolyte-gated transistor (below)[50] 66

Figure 15 Representation of the change in transfer characteristic and parameters caused by sensing for different FET biosensors. The devices are operating in the saturation regime and the IDS vs VG curves represent measurement taken before (blue) and after (red) a binding event. The architecture of each device is shown below. A) An EGOFET device modulated by the change in capacitance of the biolayer and VT, but μsat is constant; B) An FBI transistor, the effective gating capacitance remains constant and μsat and VT change; C) An ISFET, only VT varies as μsat and Ci remain constant. 69

Figure 16 Scheme of the most commonly used immobilisation strategies for bio-recognition elements in biosensors.[103] 77

Figure 17 Chemical structure of the regioregular poly(3-hexylthiophene) (P3HT) (a) and the carboxylated poly[3-(5-carboxypentyl)thiophene-2,5-diyl] (P3PT-COOH) derivative (b). 80

Figure 18 Polymers used for the deposition of ultra-thin-films onto the surface of the OSC containing the reactive functional groups required for in-situ covalent attachment of the recognition elements. 82

Figure 19 Scheme showing procedure for EGOFET biosensor device fabrication developed by Mulla and co-others.[114] The device uses an Au source and drain contacts and PBTTT deposited as the device organic Semiconductor (OSC). (a) Initial device structure on the substrate. (b) PAA is spin-coated onto the OSC and crosslinked by UV radiation. (c) Biotinalyted phospholipids are covalently attached to the surface using EDC/NHS amine coupling. (d) Aqueous sample containing analyte in PBS is applied and the electrolyte used to gate the EGOFET device using a gold gate electrode. Image reproduced from Ref.[114] with permission from The Royal Society of Chemistry. 83

Figure 20 Schematic representations of gate (top) and OSC functionalised (bottom) EGOFET sensors demonstrated by B. Piro and co-workers used in displacement immunoassays.[121,122] 84
Figure 21 (a) Cartoon representation of antibodies (blue) immobilised on a sensing interface and bound to an analyte (orange) in Schenk model.[165] Approximate Debye length shown by dashed line. (b) A more realistic representation of antibody alignment, depicting a more random orientation relative to the surface. 89
Figure 22 The cellular domain structure of HER2, composed of an extracellular domain (ECD), transmembrane domain (TD) and a tyrosine kinase domain which is the target for the drug Lapatinib.[27] The ECD is itself composed of four individual domains and the two cysteine-rich domains CR1 and CR2 are the targets for monoclonal antibody therapies Pertuzumab and Trastuzumab. HER2 can be cleaved by proteases at specific sites to produce the soluble ECD and a truncated receptor. 96
Figure 23 Fluorescence image of a typical pattern of immobilisation. Picture taken from conventional interphase FISH protocol completed on a patient sample with a microscope slide after 14 hours of hybridisation. The probe used was LSI D13S319 for detecting 13q14.3 deletions, present in malignant cells.[38] 102
Figure 24 Schematic representation of the developed gate functionalised EGOFET biosensor devices. The gold gate electrode was functionalised using carboxylic acid terminated thiol-based self-assembled monolayers (SAMs) followed by EDC/NHS coupling of the relevant biorecognition element. The resulting biorecognition layer is shown in red and schematic structures of the two different SAM layers used are shown in Figure 45 and Figure 46. Au source and drain electrodes are patterned onto a glass substrate followed by spin-coating of the OSC. 106
Figure 25 Schematic representation of the developed bilayer EGOFET device. Au source and drain electrodes are patterned onto a glass substrate followed by spin-coating of the OSC and PMMA-based co-polymer containing carboxylic acid groups (shown in red). 107
Figure 26 Chemical structures for p-type OSC used in devices. a) PBTTT-C14 b) DPPTTT. 108
Figure 27 Film thicknesses determined by Dektak of PMMA COOH 10 % in anisole deposited on glass substrates at 2000 rpm. 112
Figure 28 Film thicknesses determined by Dektak of Commercial high molecular weight PMMA and PMMA COOH 10 % in n- butyl acetate and toluene. The samples were prepared by spinning PMMA solutions on DPPTTT films on glass substrates. 113
Figure 29 Optical microscope images at x100 magnification of a pristine DPPTTT (left) and a DPPTTT / PMMA COOH 10 % film (right). 114

Figure 30 AFM tapping mode 2 µm scans of spin-coated thin films on glass substrates of a) Pristine DPPTTT (RMS roughness = 1.2 nm); b) DPPTTT / PMMA COOH 10 % film (RMS roughness = 0.6 nm). 114

Figure 31 AFM tapping mode 1 µm scans of spin-coated thin films on glass substrates of a) Pristine PBTTT (RMS roughness = 2.7 nm); b) PBTTT / PMMA COOH 10 % film (RMS roughness = 0.6 nm). 115

Figure 32 SEM images of spin-coated PBTTT films deposited on glass substrates (a) Pristine PBTTT film; (b) PBTTT film covered by a PMMA COOH layer (b). The samples were prepared by spinning PMMA COOH 10% in n-butyl acetate on PBTTT. The images were obtained by tilting the sample by 55°. 116

Figure 33 FT-IR spectra of PMMA/PMMA-COOH. (**6A, 6B, 6C**). 127

Figure 34 OFET biosensor architecture (a & b). The red circle indicates interfaces available for functionalisation and detection of biomolecules. Picture of water gated field effect transistor as fabricated in OMIC (c). 128

Figure 35 ^{1}H NMR spectra of PMMA COOH copolymers 6A-C. 133

Figure 36 ^{1}H NMR spectra for PMMA 10% mol. (6A), showing the showing the resonances compared to calculate the experimental loading in the polymer. 134

Figure 37 Formation of amide bonds can be achieved by EDC/NHS coupling reaction through the formation of highly reactive intermediates *1* and *2*. 136

Figure 38 AFM tapping mode 2 µm scans of the DPPTTT / PMMA COOH 10 % films; a) Pristine; b) after incubation in PBS for 2 hours; c) after antibody functionalisation by EDC/NHS. White lines on the images signify the areas displayed below in line scans. Root mean squared (RMS) roughness of the films is shown in Table 8. 137

Figure 39 AFM tapping mode 500 nm scans of the DPPTTT / PMMA COOH 10 % films; a) after incubation in PBS for 2 hours (RMS roughness = 0.4 nm); b) after antibody functionalisation by EDC/NHS (RMS roughness = 1.7 nm). White lines on the images signify the areas displayed below in line scans. 138

Figure 40 Scheme showing the procedure for fluorescence binding assay. (a) Cleaned SiO_2 substrate. (b) COOH functionalised Co-polymer spin-coated onto the substrate surface. (c) Primary HER2 antibody covalently attached to the surface. (d) Fluorescently labelled secondary antibody immobilised. (e) Substrates are probed by fluorescent microscopy. (f) Relative intensity of the fluorescence is extracted from images in imageJ. 140

Figure 41 Fluorescent microscope images and corresponding 3D plots of intensity: left, FITC-labelled secondary antibody (no primary antibody) on PMMA COOH 10% (control); right, FITC-labelled secondary antibody after primary antibody immobilisation on PMMA COOH 10% surface. Z axis

represents the fluorescence emission intensity; X and Y axes are the 2D substrate surface in units of pixel from the original image. 140

Figure 42 Results from fluorescent binding assay to determine the concentration of primary antibody used in immobilisation procedure. 141

Figure 43 Results from controls in the fluorescent binding assay for PMMA co-polymer. Negative controls are shown as unfilled bars and hash filled bars indicate assay where strong fluorescence signal is expected. The assay used a 270 nM solution of HER2 antibody as the primary antibody and a 75 nM solution of fluorescently labelled secondary antibody. 142

Figure 44 Results from fluorescent binding assay for PMMA co-polymer, comparing fluorescence between COOH loadings in PMMA co-polymer and use of complementary and non-complementary pairs of antibodies. The assay used 270 nM solutions of primary antibodies and 75 nM solutions of fluorescently labelled secondary antibodies. 144

Figure 45 Scheme showing the procedure for the immobilisation of the THC sensing OBP onto the gold gate electrode used in the EGOFET sensor. A self-assembled monolayer (SAM) is prepared on the surface of the bare gold gate electrode. The OBPs are then covalently attached to the carboxylic acid bearing SAM by EDC/NHS coupling with a free amine group on the protein. 146

Figure 46 Scheme for the formation of the BioSAM from the chemSAM. 147

Figure 47 2D schematic representation of the BioSAM on gold gate electrode and the formation of hydrogen bonds between the amide groups of neighbouring chains (red arrows), leading to a dipole moment. 148

Figure 48 AFM tapping mode 2 µm scans of the thermally evaporated gold substrates; left) as prepared gold substrate (RMS roughness = 2.13 nm); middle) after ChemSAM formation (RMS roughness = 2.39 nm); right) after antibody functionalisation by EDC/NHS (RMS roughness = 2.7 nm). White lines on the images signify the areas displayed below in line scans. 149

Figure 49 AFM tapping mode 2 µm and 1 µm scans of the template-stripped ultra-flat gold films; a) after ChemSAM formation, 2 µm scan (RMS roughness = 0.49 nm); b) after ChemSAM formation, 1 µm scan (RMS roughness = 0.46 nm); c) after antibody functionalisation by EDC/NHS, 2 µm scan (RMS roughness = 1.62 nm); d) after antibody functionalisation by EDC/NHS, 1 µm scan (RMS roughness = 1.81 nm). White lines on the images signify the areas displayed below in line scans. 149

Figure 50 Transfer characteristic of a representative PBTTT EGOFET device using water droplet and W pin as the gate electrode. Source and drain electrode where patterned using a shadow mask. I_{SD} (black – solid lines) and I_G (black – dotted lines) plotted in a semi-log scale (left). I_{SD} plotted in a square root scale (blue – right) from which characteristic parameters are extracted from the saturation regime. 153

Figure 51 Transfer characteristics showing the variation of performance of four PBTTT EGOFET devices fabricated on the same substrate with I_{SD} and plotted in a semi-log scale. The devices were operated using water droplet and W pin as the gate electrode and source and drain electrode were patterned using a shadow mask. 154

Figure 52 Variation in device parameters extracted from transfer characteristics of fabricated from concentrations of PBTTT varying from 3 -7 mg/ml. The EGOFET water droplet gated devices were measured using a W tip as the gate electrode. The averages and errors are taken from 12 devices fabricated on 3 different substrates for each concentration. 155

Figure 53 Intra-substrate variation in device parameters extracted from transfer characteristics of fabricated from concentrations of PBTTT varying from 3 -7 mg/ml. The EGOFET water droplet gated devices were measured using a W tip as the gate electrode. The averages and errors are taken from 4 devices fabricated on 3 separate substrates for each concentration. 156

Figure 54 Output characteristic for PBTTT bilayer device in DI water V_{DS} 0.05 to -0.5V and V_{GS} 0 to -0.7V in 0.1V steps. The migration in x axis intercept at higher gate voltages is highlighted in the inset. 157

Figure 55 Transfer hysteresis performance of single layer device analysed using the 3-point probe station and a 4µl droplet as the gating electrolyte. (Left)-Averaged transfer hysteresis and standard deviation of 4 devices on the same substrate. (Right)- Averaged transfer hysteresis of 4 devices over 10 repeat cycles. The extracted parameters are shown in Table 12. 158

Figure 56 Charts showing mean device performance as a function of PBTTT ratio. The devices have different blends of PBTTT and PMMA, with standard deviation shown across the 4 devices on each substrates a) I_{on}/I_{off} ratio; b) V_T ; c) I_{on} d) mobility expressed as $\mu*C$. 160

Figure 57 Optical microscope images of phase separation in devices. A) 100% PBTTT; B) 70% PBTTT/ 30% PMMA Blend; C) 50% PBTTT/ 50% PMMA Blend. 161

Figure 58 Transfer Characteristic DPPTTT EGOFET device using water droplet and W pin as the gate electrode. Source and drain electrode where patterned using a shadow mask. I_{SD} (black – solid lines) and I_G (black – dotted lines) plotted in a semi-log scale (left). I_{SD} plotted in a square root scale (blue – right) from which characteristic parameters are extracted from the saturation regime. 162

Figure 59 Transfer characteristic displaying the effect on electrical performance of spin-coating n-butyl acetate onto a DPPTTT device. The device was operated using 4 ul water droplet and W tip gate electrode. 163

Figure 60 Transfer characteristics of water droplet gated DPPTTT devices operated with a tungsten gate electrode. Displayed are pristine OSC device and bilayer devices: DPPTTT (black), DPPTTT / PMMA COOH bilayer (red) and DPPTTT / PMMA bilayer (blue). a) I_{SD} plotted in a semi-log scale. b) I_{SD}

plotted in a square root scale from which characteristic parameters for V_T and $\mu*C$ are extracted from the saturation regime. 164

Figure 61 Transfer characteristics of water droplet gated DPPTTT devices with three different gate electrodes: Pt (blue), Au (red), W (black). a) I_{SD} (left – solid lines) and I_G (right – dotted lines) plotted in a semi-log scale. b) I_{SD} plotted in a square root scale from which characteristic parameters for V_T and $\mu*C$ are extracted from the saturation regime. The extracted parameters are displayed in Table 13. 166

Figure 62 Transfer characteristics of water droplet gated PBTTT devices with three different gate electrodes: Pt (blue), Au (red), W (black). a) I_{SD} (left – solid lines) and I_G (right – dotted lines) plotted in a semi-log scale. b) I_{SD} plotted in a square root scale from which characteristic parameters for V_T and $\mu*C$ are extracted from the saturation regime. The extracted parameters are displayed in Table 13. 167

Figure 63 Transfer characteristics of water droplet gated DPPTTT/PMMA COOH devices with three different gate electrodes: Pt (blue), Au (red), W (black). a) I_{SD} (left – solid lines) and I_G (right – dotted lines) plotted in a semi-log scale. b) I_{SD} plotted in a square root scale from which characteristic parameters for V_T and $\mu*C$ are extracted from the saturation regime. The extracted parameters are displayed in Table 13. 167

Figure 64 Threshold voltage as a function of the theoretical work function of the gate material used in water droplet gated EGOFET devices with three different gate electrodes: Pt (5.65 eV), Au (5.4 eV), W (4.65 eV). a) DPPTTT based devices. b) PBTTT based devices. A linear fit is plotted for both OSCs. Pristine OSC devices are plotted in red and OCS/ PMMA COOH 10% bilayer devices are plotted in black. Errors are displayed as the standard deviation across 4 devices. 168

Figure 65 Transfer characteristics comparing typical DPPTTT (left) and PBTTT (right) EGOFET devices using source and drain electrodes patterned by evaporation using a shadow mask (red) and photolithography defined IDE design (black), with 60 µm channel length. Devices operated with water droplet and Au wire as the gate electrode. I_{SD} (solid lines) and I_G (dotted lines) plotted in a semi-log scale (left). I_{SD} plotted in a square root scale (blue – right) from which characteristic parameters are extracted from the saturation regime. 170

Figure 66 Transfer characteristics and output characteristics of typical DPPTTT EGOFET devices using an 8 µl water droplet and Au wire as gate electrode with varying channel lengths: a) 10 µm IDE; b) 20 µm IDE; c) 40 µm IDE; d) 60 µm IDE; e) 60 µm shadow mask design. 172

Figure 67 Transfer characteristic comparing typical DPPTTT EGOFET devices of varying channel lengths using source and drain electrodes patterned by photolithography defined IDE design (L= 60,

40, 20, 10 µm, W = 16.9 mm)and evaporation using a shadow mask (L= 60 µm, W = 1 mm). Devices operated with DI water droplet and Au wire as the gate electrode. 173

Figure 68 Variation in key transfer characteristics parameters DPPTTT EGOFET devices of varying channel lengths: a) Variation of maximum I_{DS} as a function of device geometry factor; b) Variation of V_T against device channel length; c) Variation of $\mu*C$ against device channel length. Errors are displayed as the standard deviation across 4 devices. 174

Figure 69 Schematic showing a patterned glass substrate with four separate wells of 30 µl for holding the aqueous gating medium in the EGOFET device (left). Inset the photolithographically defined interdigitated source and drain electrodes with a channel lengths of L= 20 µm and channel width of W= 16.9 mm used in these devices. 176

Figure 70 Three-dimensional structure of the constructed Electrolyte-gated OFET device. 177

Figure 71 Exploded view of all the components – left PTFE block with gate electrodes, lower right the sensing chamber that contains 4 compartments that form 4 EGOFET devices, top – block containing spring loaded contacts that make the electrical connections to the devices. Inset- PTFE block holding 4 gate electrodes. 178

Figure 72 Transfer I-V curves (I_{DS} vs. V_G at V_D=-0.4V) displaying the change in the device performance before and after the completion of the HER2 calibration curve for one device. The black (before) and red (after) curves show the measurement recorded with a bare Au gate, and the blue curve was recorded using the functionalised Biosam gate before the calibration curve measurements are taken. 179

F**igure 73** EGOFET HER2 BioSAM sensing transfer characteristics (I_{DS} vs. V_G at V_D=-0.4V). Displayed are the measurements collected for the calibration curve for one of the devices in response to increasing concentrations of analyte covering the range 1 x 10^{-18} M to 1 x 10^{-8} M for HER2 ECD (a) and negative control VEGF (b). The measurements are displayed with I_{DS} in the linear scale on the left and as √I_{DS} on the right which is used to extract V_T and µ*C. 181

F**igure 74** EGOFET HER2 antibody BioSAM calibration curves of device response vs ligand concentration covering the range 1 x 10^{-18} M to 1 x 10^{-8} M. a) The relative change of the I_{DS} current ($\Delta I/I0$); b) the relative change of the V_T ($\Delta VT/VT0$); c) the relative change of the µ*C ($\Delta\mu C/\mu C0$). The blue squares are the responses for HER2 ECD as the ligand. The red circles are the responses to VEGF protein used as a negative control. The green triangles are the responses to a blank assay performed under the same conditions with PBS solutions but no analyte. A trend line has been fitted for the HER2 ECD responses (blue) using the Hill equation. From this the LoD is calculated as ~1 x 10^{-18} M from the concentration equating to a signal response of -5.8%. 182

F**igure 75** The chemical structures of the cannabinoids of interest THC, CBD and CBN. 186

Figure 76 The effect of solvent and solubilising agent on EGOFET OBP-Lipoic acid SAM device response measured as $\Delta I/I0$ from 0.1 µM concentration of THC. The recovery to the baseline I_0 value is investigated to the reversible nature of the response. The solvent used are DI water, 2% solution of isopropanol (IPA) in DI water and 0.0035% w/v TweeN-20 detergent in water. Each solvent system was used for all measurements (I_0, I and recovery) in that group. 187

Figure 77 EGOFET biosensor with OBP-Lipoic acid SAM sensing transfer characteristics (I_{DS} vs. V_G at V_D=-0.4V). Displayed are the measurements collected for the calibration curve for one of the device each in response to increasing concentrations of analyte covering the range 1 x 10^{-14} M to 1 x 10^{-8} M for: (a) THC; and the negative controls (b) CBD and (c) CBD. The measurements are displayed with I_{DS} in the linear scale on the left and as $\sqrt{I_{DS}}$ on the right which is used to extract V_T and µ*C. 189

Figure 78 EGOFET biosensor with OBP-Lipoic acid SAM calibration curves of device response vs ligand concentration covering the range 1 x 10^{-14} M to 1 x 10^{-7} M. Top) The relative change of the I_{DS} current ($\Delta I/I0$); Middle) the relative change of the V_T current ($\Delta VT/VT0$); Bottom) the relative change of the µ*C ($\Delta \mu C/\mu C0$). The blue squares are the responses for THC as the ligand. The red circles are the responses to CBN used as a negative control. CBD is investigated as a second control analyte shown by orange diamonds. The green triangles are the responses to a blank assay performed under the same conditions with PBS solutions but no analyte. 191

Figure 79 EGOFET biosensor with OBP-Lipoic acid SAM calibration curve of device response $\Delta I/I0$ vs ligand concentration covering the range 1 x 10^{-14} M to 1 x 10^{-7} M. A trend line has been fitted for the THC responses (blue) using the Hill equation. From this the THC LoD is calculated as 1.6 x 10^{-14} M from the concentration equating to a signal response of -5.6%. 192

Figure 80 Flow cell design V1. Clockwise A) 3D rendered image showing acrylic top cover (pink), laser cut tape (blue) and gold plated gate electrode pins. B) Exploded CAD image of the flow cell components in isometric view. C) Picture showing constructed flow cell. Gold plated pins are used as gate electrodes and their position fixed within the CNC milled acrylic top cover. Holes are placed through the acrylic and tape to allow access to the source and drain contact pads. The bottom surface of the pin serves as the gate electrode surface, which is fitted flush with the acrylic top cover and mounted onto the substrate with the double sided adhesive to give a controlled gate height of 280 µm. The double sided tape has a laser cut design to produce a sealed flow cell of 51.8 mm^2 in area and controlled chamber volume of 14.5 µl. The flow cell is accessed by inlet and outlet holes to which stainless steel tubing is inserted for connection to a syringe or micro-pump station. 197

Figure 81 Images comparing liquid filling different designs of microfluidic flow cell with the water stained blue for visualisation purposes. Left: Original single chamber design as depicted in Figure 80,

showing example of bubble formation. Right: Flow cell design V2 with two separate chambers as depicted in Figure 82, showing a typically filled chamber. 198
Figure 82 Flow cell design V2. The modified flow cell design features a two chamber design to improve fluid flow and reduce bubble formation. Each chamber has a width of 2.5 mm and a volume of 7 µl. 199
Figure 83 Design for characterisation platform. a) 3D rendered image of top plate housing spring loaded micro-pins that are positioned to contact the S/D contact pads. b) 3D rendered image of bottom plate with flow cell fitted with gate electrodes and inlet/outlet tubing. c) Picture of characterisation platform and interface box for connection to Agilent. d) Top down picture of characterisation platform including and gate electrode receptacles. Wiring from the connections on the characterisation platform is neatly minimised by the mounted printed circuit board (PCB), that is connected to a coaxial cable by a 12 pin Molex connector. The coaxial cabling provides screening from external interference when connecting the connecting the platform with a cable interfacing box which allows for simple cable connection to the Agilent for device characterisation. 200
Figure 84 Transfer hysteresis of single layer device with DI water comparing the reproducibility of the characterisation platforms over a short period of time. Left – As analysed using the 3 point probe station and a 4µl droplet of DI water as the gating electrolyte. The device was analysed at regular timed intervals and after 10 mins the initial droplet was removed and replaced with a second droplet; Right – As analysed with the characterisation platform using a flow cell device. Source and drain electrode where patterned using a shadow mask (W = 1 mm, L = 60 µm). V_{DS} = -0.5V was used for device operation. 201
Figure 85 Comparing performance of PBTTT devices analysed by water droplet (left) and in a flow cell (right). Displayed are the averaged transfer hysteresis and standard deviation of 4 devices on the same substrate. Droplet-based devices were analysed using the 3 point probe station, W gate electrode and a 4µl droplet as the gating electrolyte. The flow cell devices were analysed with the characterisation platform. Source and drain electrode where patterned using a shadow mask (W = 1 mm, L = 60 µm). V_{DS} = -0.5V was used for device operation. 202
Figure 86 Comparing performance of PBTTT devices analysed by water droplet (black) and in a flow cell (red I_{SD} (solid lines) and I_G (dotted lines) are displayed on a linear scale (left graph) and plotted in a semi-log scale (right graph). Droplet devices are analysed using the 3 point probe station, W gate electrode and a 4µl droplet as the gating electrolyte. The flow cell devices were analysed with the characterisation platform. Source and drain electrode where patterned using a shadow mask (W = 1 mm, L = 60 µm). V_{DS} = -0.5V was used for device operation. 203

Figure 87 Change in transfer characteristic of PBTTT EGOFET device in a flow cell over 24 hours. The devices where tested initially in the flow cell (red) and after 24 hours incubation in water (blue). Source and drain electrode where patterned using a shadow mask (W = 1 mm, L = 60 µm). I_{SD} (solid lines) and I_G (dotted lines) are plotted in a semi-log scale. Plotted are the averaged transfer forwards sweep of transfer curve and standard deviation of 4 devices on the same substrate. V_{DS} = -0.5V was used for device operation. 204

Figure 88 Variation in characteristic parameters extracted from the transfer hysteresis for a single layer device in DI water over 10 repeated cycles in a 10 minute period, analysed in characterisation platform using a flow cell device. Displayed are values for each of the four devices on the same substrate. 204

Figure 89 Transfer characteristic performance of single layer (top) and bilayer type devices (bottom), analysed in characterisation platform using a flow cell device. Left - Performance of a single device over 10 mins. Centre - Averaged transfer hysteresis and standard deviation of 4 devices on the same substrate on cycle 1. Right- Averaged transfer hysteresis during 10 repeat cycle tests. The source and drain electrode where patterned using a shadow mask. (W = 1 mm, L = 60 µm). V_{DS} = -0.5V was used for device operation. 205

Figure 90 Transfer hysteresis of PBTTT device tested in a flow cell in DI water (left) and PBS (right) over 2 hours, analysed in the characterisation platform using a flow cell device. The source and drain electrode where patterned using a shadow mask. (W = 1 mm, L = 60 µm). V_{DS} = -0.5V was used for device operation. 207

Figure 91 Transfer hysteresis of PBTTT/PMMA COOH layer device in DI water (left) and PBS (right) over 2 hours, analysed in the characterisation platform using a flow cell device. The source and drain electrode where patterned using a shadow mask. (W = 1 mm, L = 60 µm). V_{DS} = -0.5V was used for device operation. 207

Figure 92 Variation in characteristic parameters extracted from the transfer hysteresis from the various PBTTT-based devices described in Figure 90-Figure 91 over 2 hours, analysed in the characterisation platform using a flow cell device. The mean average of the four devices on the same substrate and their standard deviation is displayed in each chart. Red - Single Layer devices in DI water. Orange - Single layer devices in PBS. Blue - Bilayer devices in DI water. Green - Bilayer devices in PBS. The Source and drain electrode where patterned using a shadow mask. (W = 1 mm, L = 60 µm). V_{DS} = -0.5V was used for device operation. 208

Figure 93. 'On current' monitored over time; this was performed by holding the V_{DS} at -0.5V and V_{GS} at -0.4V, using a flow cell device in DI water, analysed in the characterisation platform. 209

Figure 94 PBTTT / PMMA COOH IDE design in flow cell with water. Left) Transfer characteristic, V_{DS} = -0.7V was used for device operation.; Right) Output characteristic. The Source and drain electrode where patterned by photolithography with a IDE design. (W = 16.9 mm, L = 60 µm). 211

Figure 95 Transfer hysteresis of PBTTT / PMMA COOH IDE design device in PBS over 2 hours operated under constant bias stress of repeated transfer hysteresis cycles. The device was analysed in the characterisation platform using a flow cell device and the extracted parameters are displayed in Figure 96. 212

Figure 96 Variation in characteristic parameters extracted from the transfer hysteresis PBTTT / PMMA COOH IDE design device in PBS over 2 hours operated under bias stress of repeated transfer hysteresis cycles as described in Figure 95 over 2 hours. The devices were analysed in the characterisation platform using a flow cell device. Top; I_{SD} (black) and I_G (red) at maximum V_G extracted from transfer hysteresis cycles; Middle V_T extracted from transfer hysteresis cycles; Bottom $\mu*C$ extracted from transfer hysteresis cycles. 213

Figure 97 Typical performance of a single layer DPPTTT device with the shadow mask design (W = 1 mm, L = 60 µm) operated in flow cell with water as electrolyte. Left) Transfer characteristic, V_{DS} = -0.8V was used for device operation; Right) Output characteristic. The transfer characteristic was measured with V_{DS} = -0.8V. 214

Figure 98 Comparing the electrical performance of typical DPPTTT devices analysed by water droplet (black) and in a flow cell (red). I_{SD} (solid lines) and I_G (dotted lines) are displayed on a linear scale (left graph) and plotted in a semi-log scale (right graph). Droplet devices are analysed using the 3 point probe station, Au gate electrode and a 4µl droplet as the gating electrolyte. The flow cell devices were analysed with the characterisation platform and V_{DS} = -0.8V was used for device operation. The Source and drain electrode where patterned using a shadow mask (W = 1 mm, L = 60 µm). 215

Figure 99 Typical transfer characteristic (left) and output characteristic (right) of DPPTTT/ PMMA COOH devices with the shadow mask design (W = 1 mm, L = 60 µm) operated in a flow cell with water (top) and PBS (bottom) as the electrolyte. The transfer characteristic was measured with V_{DS} = -0.8V. 216

Figure 100 Typical transfer characteristic (left) and output characteristic (right) of DPPTTT devices with the IDE design operated in a flow cell with water (top) and PBS (bottom) as the electrolyte. The Source and drain electrode where patterned by photolithography with an IDE design (W = 16.9 mm, L = 20 µm). The transfer characteristic was measured with V_{DS} = -0.7V. 217

Figure 101 Averaged transfer characteristics of DPPTTT devices with IDE operated in a flow cell with water as the electrolyte. I_{SD} (solid lines) and I_G (dotted lines) are plotted in a semi-log scale. Plotted are the averaged forwards sweeps of the transfer curves and standard deviations of the 4 devices on

the same substrate. The source and drain electrode where patterned by photolithography with an IDE design (W = 16.9 mm, L = 20 µm). The transfer characteristic was measured with V_{DS} = -0.7V. 218
Figure 102 Typical transfer characteristic (left) and output characteristic (right) of a DPPTTT/ PMMA COOH device with the IDE design operated in a flow cell with PBS as the electrolyte. The source and drain electrode where patterned by photolithography with an IDE design (W = 16.9 mm, L = 20 µm). The transfer characteristic was measured with V_{DS} = -0.7V. 219
Figure 103 Averaged transfer characteristics of DPPTTT/ PMMA COOH devices with IDE operated in a flow cell with PBS as the electrolyte. I_{SD} (solid lines) and I_G (dotted lines) are plotted in a semi-log scale. Plotted are the averaged forwards sweeps of the transfer curves and standard deviations of the 4 devices on the same substrate. The source and drain electrode where patterned by photolithography with an IDE design (W = 16.9 mm, L = 20 µm). The transfer characteristic was measured with V_{DS} = -0.7V. 219
Figure 104 Monitoring the typical device performance during the functionalisation procedure for DPPTTT/ PMMA COOH devices. A schematic representation of the tested EGOFET devices is shown for before functionalisation (left), following immobilisation of the antibodies by EDC/NHS (middle) and after blocking with BSA (right). The transfer (top) and output characteristics (bottom) of typical devices are shown. The devices were fabricated with the IDE design and operated in a flow cell with PBS as the electrolyte. The source and drain electrode where patterned by photolithography with an IDE design (W = 16.9 mm, L = 20 µm). The transfer characteristic was measured with V_{DS} = -0.7V. 220
Figure 105 Averaged transfer characteristics of DPPTTT/ PMMA COOH devices during the functionalisation procedure. Plotted are the averaged transfer curves and standard deviations of 4 devices on the same substrate before functionalisation, following immobilisation of the antibodies and after blocking with BSA. The devices were fabricated with the IDE design and operated in a flow cell with PBS as the electrolyte. I_{SD} (solid lines) and I_G before functionalisation (dotted lines) are plotted in a semi-log scale. The source and drain electrode where patterned by photolithography with an IDE design (W = 16.9 mm, L = 20 µm). The transfer characteristic was measured with V_{DS} = -0.7V. 221
F**igure 106** Transfer characteristics of functionalised DPPTTT/ PMMA COOH devices in the flow cell across the range of concentrations investigated in the calibration curve. Plotted are the measurements recorded using PBS as the gating medium following incubation at each concentration level. The measurements displayed here correspond to the extracted parameters for D3 in **Figure 107**. The source and drain electrode where patterned by photolithography with an IDE design (W = 16.9 mm, L = 20 µm). The transfer characteristic was measured with V_{DS} = -0.7V. 223

Figure 107 Calibration curves for the antibody functionalised flow cell devices for the detection of HER2 ECD in PBS. The normalised response calculated from the extracted I_{DS}, V_T and µ*C is shown across the 0.1 to 1000 ng/ml concentration range which was investigated. 224

Figure 108 Device transfer characteristic parameter variation during baseline assay experiment in PBS. Tests were conducted in groups of 20 cycled transfer curve measurements with 20 mins incubation period and 2 mins rinsing of the flow cell in between each test group. Displayed is the average of the last 5 transfer curves of each of the 7 sequentially tested groups. The source and drain electrode where patterned by photolithography with an IDE design (W = 16.9 mm, L = 20 µm). The transfer characteristic was measured with V_{DS} = -0.7V and V_{GS} swept in both directions from + 0.2.V to -0.8V. 227

Figure 109 Typical transfer characteristic of DPPTTT-based devices with the IDE design operated in a flow cell with PBS as the electrolyte. Compared are devices fabricated with pristine DPPTTT, DPPTTT/PMMA devices annealed at 80 °C and 110 °C for 1 hour to give PMMA thickness of 20 nm and DPPTTT/PMMA device fabricated to give a PMMA thickness of 110 nm and annealed at 80 °C. The source and drain electrode where patterned by photolithography with an IDE design (W = 16.9 mm, L = 20 µm). 229

Figure 110 Typical transfer curves of DPPTTT-based devices during bias stress measurements of 50 repeated cycles. Compared is a single device fabricated with pristine DPPTTT (left) and DPPTTT/PMMA devices annealed at 80 °C (middle) and 110 °C (right) fabricated with the IDE design and operated in a flow cell with PBS as the electrolyte. The source and drain electrode where patterned by photolithography with an IDE design (W = 16.9 mm, L = 20 µm). The transfer characteristic was measured with V_{DS} = -0.7V. 230

Figure 111 Bias stress averaged transfer curves over repeated cycles. Compared are devices with pristine DPPTTT (left) and DPPTTT/PMMA devices annealed at 80 °C (middle) and 110 °C (right) fabricated with the IDE design and operated in a flow cell with PBS as the electrolyte. I_{SD} (solid lines) and I_G (dotted lines) are plotted in a semi-log scale. Plotted are the averaged forwards sweeps of the transfer curves and standard deviations of the 4 devices on the same substrate. The source and drain electrode where patterned by photolithography with an IDE design (W = 16.9 mm, L = 20 µm). The transfer characteristic was measured with V_{DS} = -0.7V. 230

Figure 112 The device transfer characteristic parameter variation of DPPTTT-based devices under bias stress. Displayed are the absolute parameters values (left) and relative change as a percentage (right) for I_{on}, $\mu*C$ and V_T. The percentage change is calculated relative to the 10th cycle. The averages and standard deviations are taken across 4 devices. Compared are devices with pristine DPPTTT (red) and DPPTTT/PMMA devices annealed at 80 °C (green) and 110 °C (blue) fabricated with the IDE

design and operated in a flow cell with PBS as the electrolyte. The source and drain electrode where patterned by photolithography with an IDE design (W = 16.9 mm, L = 20 µm). The transfer characteristic was measured with V_{DS} = -0.7V and V_{GS} swept in both directions from + 0.2.V to -0.8V. 231

Figure 113 GPC showing variation in reaction solvent and duration on Mw distribution 239

Figure 114 GPC showing effect in reaction concentration on Mw distribution from polymerisation reaction in toluene 239

Figure 115 GPC showing effect of initiator concentration and reaction duration on Mw distribution from polymerisation reaction in toluene 240

Figure 116 GPC showing effect of initiator concentration on Mw distribution from polymerisation reaction in dioxane 240

Figure 117 GPC showing repeatability of Mw distribution from polymerisation reaction in dioxane 241

Figure 118 GPC showing Mw distribution from polymerisation reaction in dioxane with different loadings of COOH containing monomer 241

Figure 119. Cross section image of 3M™ Double Coated Membrane Switch Spacer (3M 7961MP). Features 0.05 mm adhesive layers, 0.18 mm PET carrier and 0.11 mm Polycoated Kraft Paper (Liner). This gives an applied thickness of ~280 µm. 241

Figure 120 The set up used for flow cell measurements. A three-way stopcock tap is connected to two syringes containing the prepared fluids needed for the experiment. The syringes are mounted on to separate syringe pumps allowing the flow rate to be controlled. Only one syringe pump is used at a time. The fluid is introduced into the cell through by PTFE tubing connected to the stainless-steel inlet tube. The system dead volume (including the three-way stopcock and tubing) was ~150 µl. 242

Figure 121 Assembled measurement system inside a probe station and the contacts are connected to the electrical measurement system. 242

Figure 122 Gate leakage measured for the transfer I-V curves in Figure 72 (I_{DS} vs. V_G at V_D=-0.4V) displaying the change in the device performance before and after the completion of the HER2 calibration curve for one device. The black (before) and red (after) curves show the measurement recorded with a bare Au gate, and the blue curve was recorded using the functionalised Biosam gate before the calibration curve measurements are taken. 243

F**igure 123** EGOFET HER2 antibody BioSAM calibration curves of device current ($\Delta I/I0$) response vs ligand concentration covering the range 1 x 10^{-18} M to 1 x 10^{-8} M. The blue squares are the average responses for HER2 ECD as the ligand. The crosses represent the individual device responses. The

green triangles are the responses to a blank assay performed under the same conditions with PBS solutions but no analyte. 244

List of Tables

Table 1 Debye length (λ_D) in electrolyte solutions of various concentrations of monovalent ions (e.g. NaCl).[49] 88

Table 2 Breast Cancer subtypes and generalised therapy management 94

Table 3 Contact angle measurements on glass substrates and thin films deposited on glass substrates of water and various solvents 110

Table 4 A range of HER2 ECD concentrations are shown in ng/ml and the corresponding concentration in M and pM. 123

Table 5 Ratio of co-monomers used in the synthesis of **6A-C** 126

Table 6 Reaction yields from synthesis of PMMA copolymers **6A**-**C** using dioxane as the reaction solvent. 127

Table 7 Loading of COOH containing co-monomer and GPC results for PMMA copolymers **6A**-**C**. 134

Table 8 Water in air contact angle measurements and AFM root mean squared (RMS) surface roughness from of 2 µm scans of DPPTTT/ PMMA COOH 10% thin films during functionalisation process. 137

Table 9 Water in air contact angle measurements on PBTTT thin films on glass substrates 139

Table 10 Affinity constants for OBP GTP_pigF88W against various cannabinoids calculated by fluorescence binding assay by C. Kali which are provided by personal correspondence. 146

Table 11 PBTTT film thicknesses on glass measured by Dektak. The PBTTT solutions where spin coated from DCB solutions at 2000 rpm, displayed is the average thickness over 3 substrates and error as standard deviation. 152

Table 12 Characteristic parameters extracted from transfer hysteresis displayed in Figure 55. The single layer device analysed using the 3 point probe station and a 4µl droplet as the gating electrolyte 158

Table 13 Transfer characteristic parameters of threshold voltage, mobility, on/off current ratio and maximum current, as extracted from the saturation regime of water droplet gated DPPTTT devices with three different gate electrodes. Errors are reported as the standard deviation across 4 devices. 166

Table 14. Characteristic parameters extracted from the transfer hysteresis of a single layer device analysed using the 3 point probe station and a 4µl droplet of DI water as the gating electrolyte. The device was analysed at regular timed intervals and after 10 mins the initial droplet was removed and replaced with a second droplet. Transfer characteristics of the devices are shown in Figure 84. 202

Table 15. Averaged characteristic parameters extracted from the transfer hysteresis of single layer devices. The devices are analysed using the flow cell and characterisation platform with DI water as the gating electrolyte. The devices are tested over 10 sequential analyses over a 10 minute period. Displayed are the averaged values of the 4 devices on the substrate. Transfer characteristics of the devices are shown in Figure 84. 202

Table 16 Averaged characteristic parameters extracted from the transfer hysteresis of bilayer layer devices. The devices are analysed using the flow cell and characterisation platform with DI water as the gating electrolyte. The devices are tested over 10 sequential analyses over a 10 minute period. Displayed are the averaged values of the 4 devices on the substrate. Transfer characteristic of the devices are shown in Figure 89. 206

Table 17. Averaged characteristic parameters extracted from the transfer hysteresis of bilayer devices on 3 different substrates analysed using the flow cell and characterisation platform. 206

Table 18 Characteristic parameters quoted by Mulla *et al* for EGOFET Biosensors at various stages of fabrication.[114] The μ^*C parameter is back calculated from the assumed gate- channel capacitance per unit area of 3 µF cm^{-2} as is used in the paper. 206

Table 19 Averaged characteristic parameters extracted from the transfer curves of DPPTTT/ PMMA COOH devices during the functionalisation procedure. The devices were fabricated with the IDE design and operated in a flow cell with PBS as the electrolyte. The average is taken over 4 different devices. 222

Table 20 Calculated initiator half-life times for Vazo 67 using Equation 31.The reaction length is taken to be approximately three times half-life duration. 237

Table 21 Variation in reaction solvent and duration on polymerisation reaction 237

Table 22 Variation in reaction concentration on polymerisation reaction in toluene 237

Table 23 Variation in initiator concentration and reaction length on polymerisation reaction in toluene 237

Table 24 Variation in initiator concentration on polymerisation reaction in dioxane 238

Table 25 Repeatability of polymerisation reaction in dioxane 238

Table 26 Control of loading of COOH containing monomer in polymerisation reaction in dioxane 238

Abstract

Organic field effect transistors (OFETs) have gained interest as transducers for label-free biosensors as they benefit from intrinsic signal amplification and electrical output to enable outstanding sensing performance. They are easy to interpret and can be fabricated at low cost; allowing the development of disposable electronic sensing systems that are ideal for point of care (PoC) testing. Electrolyte-gated organic field effect transistors (EGOFETs) benefit from a simple device architecture that utilises an aqueous gating solution, a low operating potential (<1 V) and in-situ detection of the analyte in solution. In this thesis EGOFET-based biosensors have been investigated as a platform for the antibody-based detection of the extra cellular domain (ECD) of human epidermal growth factor receptor 2 (HER2), an established blood serum biomarker for breast cancer. In addition, the detection of tetrahydrocannabinol (THC), the psychoactive cannabinoid component of cannabis was investigated using Odorant Binding Proteins (OBPs) as the biorecognition element for the selective detection of the analyte using an EGOFET-based biosensor.

The EGOFET devices utilised solution processed polymeric semiconductors (P3HT, PBTTT and DPPTTT) as the active layer. The superior environmental stability of the DPPTTT-based devices over PBTTT was demonstrated by examining the device performance after prolonged exposure to buffered saline solutions. Device operation was improved by the use of interdigitated source and drain electrodes and gold gate electrodes.

Two strategies where investigated for the functionalisation of EGOFET with the appropriate biorecognition element at the gate electrode or the OSC interface. In the first approach the gold gate electrode was functionalised using established methods that use the formation of a carboxylic acid terminated thiol-based self-assembled monolayer (SAMs) onto the gold surface followed by EDC/NHS coupling of the relevant biorecognition element. The performance of the biosensors was verified by the construction of a calibration curve and the selectivity investigated by the analysis of appropriate controls. This allowed proof of concept for the EGOFET-based detection of ECD of HER2 by a gate electrode functionalised with antibodies. Additionally, the versatility of the technique was displayed by the detection of THC using OBPs attached to the gate electrode and displaying the selective detection of THC over other cannabinoids.

In the second approach, functionalization dielectric copolymers, derived from poly(methyl methacrylate) (PMMA) containing carboxylic acid groups (-COOH), were synthesised for use in bilayer type devices, prepared by spin coating on to the active semiconducting layer of the EGOFET. This bilayer design allowed functionalisation with the HER2 antibody, by covalent attachment to the

dielectric surface by EDC/NHS coupling. The functionalisation procedure was confirmed by fluorescent binding assay, AFM and water contact angle measurements.

The integration of EGOFET devices within a fluidic cell demonstrated robust operation, enabled easy fluid handling, and eliminated problems with water evaporation that hamper the utility of droplet-based devices. The functionalisation process was shown to have negligible impact on device operation. Bias stress induced drift in electrical performance was observed in DPPTTT/PMMA COOH devices. However, increasing the final annealing temperature to above the Tg of PMMA resulted in improved performance and reduced drift. The resulting platform is therefore well positioned for sensing experiments and further development as a biosensor.

Declaration

No portion of the work referred to in this thesis has been submitted in support of an application for another degree or qualification of this or other institute.

Copyright Statement

i. The author of this thesis (including any appendices and/or schedules to this thesis) owns certain copyright or related rights in it (the "Copyright") and s/he has given The University of Manchester certain rights to use such Copyright, including for administrative purposes.

ii. Copies of this thesis, either in full or in extracts and whether in hard or electronic copy, may be made only in accordance with the Copyright, Designs and Patents Act 1988 (as amended) and regulations issued under it or, where appropriate, in accordance with licensing agreements which the University has from time to time. This page must form part of any such copies made.

iii. The ownership of certain Copyright, patents, designs, trademarks and other intellectual property (the "Intellectual Property") and any reproductions of copyright works in the thesis, for example graphs and tables ("Reproductions"), which may be described in this thesis, may not be owned by the author and may be owned by third parties. Such Intellectual Property and Reproductions cannot and must not be made available for use without the prior written permission of the owner(s) of the relevant Intellectual Property and/or Reproductions.

iv. Further information on the conditions under which disclosure, publication and commercialisation of this thesis, the Copyright and any Intellectual Property and/or Reproductions described in it may take place is available in the University IP Policy (see http://documents.manchester.ac.uk/DocuInfo.aspx?DocID=2442 0), in any relevant Thesis restriction declarations deposited in the University Library, The University Library's regulations (see http://www.library.manchester.ac.uk/about/regulations/) and in The University's policy on Presentation of Theses

Acknowledgements

Firstly, I would like to thank my supervisors Prof. Michael Turner and Dr Michelle Webb for giving me the opportunity to pursue these studies and for their generous support throughout this project. I would also like to acknowledge the EPSRC for the funding for this research and hope that many more people continue to be granted the chance to further their scientific interests. In addition a great deal of gratitude is extended to Dr Daniel Tate for his guidance and the synthesis of OSC materials PBTTT and DPPTTT used in this project. Furthermore, I would like to thank Dr Aiman Rahmanudin for lending his expertise in AFM.

I would like to thank all of the wonderful friends I have made during my stay in OMIC. The very many laughs, lunches, drinks and bizarre discussions we have shared during this time are fond memories. Many thanks also go to good gentlemen of Old Mancunians AFC for the enjoyable distractions provided across Lancashire's many sodden fields over the last 4 years. To Steve, thank you for tolerating my questionable flatmate behaviour and thankfully you survived the experience. To Kate, thank you for bringing sunshine to my everyday and backing me on the final stretch. To all these friends and more, thank you for enriching my time in Manchester beyond measure, it has been a blast and I hope we continue to cross paths long into the future.

Finally, my deepest thanks go to my brother and parents for their encouragement, support and inspiration in every way imaginable during my seemingly endless education.

1 Introduction

1.1 Preface

Electronic sensors systems are a critical component of the devices needed to deliver the burgeoning Internet of Things and are essential for a wide range of applications in wearable electronics, healthcare and smart cities. These high-volume sensor applications are pushing the global sensor market towards the introduction of over one trillion units per annum and these devices will allow the routine monitoring of health, exercise and the environment in daily life.

Biosensors are devices that provide effective identification and quantification of a wide range of clinically relevant biomarkers present in biological media such as blood, urine and saliva. They have great potential in the diagnosis, prognosis and therapeutic stratification of diseases and conditions.[1] A biomarker is considered as a measurable substance or characteristic present within the human body that is indicative of a particular disease or biological state of an organism. A biosensor is defined as an analytical device that uses a specific isolated biologically derived element such as an enzyme, immunosystem, tissue, organelle, or whole cell directly coupled to a transducing element for the detection of chemical compounds, usually by producing an optical, thermal or electrical signal.[2] In essence, by utilising the specific complementary interaction between an analyte and a biological recognition element transduction is possible into a distinct measurable signal.

The development of highly sensitive, specific, and portable methods of rapidly detecting and quantifying increasing numbers of relevant biomarkers with Point-of-Care (POC) sensing systems is critical for the advancement of medical care. POC systems are intended to integrate the processing of clinical samples and the quantification of a variety of biomarkers within an inexpensive, user-friendly platform where the underlying technology can reduce the complexity of the test allowing on-site quantification.[3–5] Development of POC technologies will help provide clinicians access to a greater depth of molecular information for disease profiling, to aid and tailor therapy decision making for the advancement of personalised medicine. These sensors are desirable to quickly gather vital patient information and accelerate progress in better understanding the complexities and patterns in managing many diseases. For example, electrical biochips have been developed that enable manipulation and sensing of biological media meet the needs of POC systems by delivering on-chip sample preparation, reduced sample volumes, label-free detection, reduced cost and complexity (ease of use), miniaturisation for portability and integration into multiplexing.[6,7]

Despite the significant increase in new technology platforms and the discovery of potential disease biomarkers reported in the literature the uptake of these into clinical application remains relatively slow.[8,9] The uptake of new techniques and acceptance of biomarker detection has been hampered by the demands for approval by healthcare regulatory bodies. Low cost and easily modifiable assays would aid in the expansion of clinical trials, aiding in discovery and validation of new biomarkers (genomics and proteomics) and the rapid introduction of their testing into clinical practice.

To see widespread use in a clinical setting and an impact on clinical decisions the chosen biomarkers and assay must demonstrate the validity and the utility that the gathered information have on clinical decisions. For a newly developed assay to be approved for use in clinical practice the analytical and clinical validity must be proven and then the clinical utility within a specific setting must be demonstrated.

Analytical validity is determined by the sensitivity, specificity and reproducibility of an assay for the detection of a target analyte, ensuring the accurate and reliable detection and measurement of the desired biomarker. The analytical validity of results is reliant on the limitations of the procedure (methodology), techniques and equipment employed. Clinical validity refers to the accuracy of the measured biomarker to identify a patient's clinical condition, i.e. the state (presence, absence) or risk of a specific disease. Clinical utility identifies the risk and benefits gained from the given test results; specifically, whether the results gained can be used to guide successful clinical actions that improve patient outcomes.

For a novel prognostic biomarker test to gain approval for clinical use, it must demonstrate an improvement relative to its equivalent approved technique allowing more effective clinical actions. Desirable improvements include greater reliability, convenience, cost or less invasive sample collection while not compromising reliability and accuracy, therefore, providing comparable test results to those possible from centralised laboratories. A fully realised POC testing platform aims to achieve all these requirements.[7]

For PoC testing to be realised, advancements in the field of biosensor technologies are necessary and sought after. In this thesis the potential of organic field effect transistor (OFET) devices for use in biosensor devices will be discussed and investigated. To introduce the work this Chapter discusses biosensors and the performance figures of merit, it outlines the role of electrolyte gated field effect transistors (EGOFET) and their mode of operation and highlights recent literature examples of their use as biosensors. Additionally, the urgent need for development of biosensors within the field of breast cancer and unique challenges faced within this field will also be reviewed.

1.2 Biosensors

Biosensors are analytical devices that combine a biological recognition element and a transducer for the detection of an analyte (chemicals). Biosensors are composed of three major components: the recognition element, the signal conversion (transducer) and the output interface. They are generally classified by the bioreceptor and the transducer that is utilised.

The biorecognition element is a biologically derived or biomimetic component that specifically binds to the desired analyte and can be naturally occurring or biologically engineered for example enzymes, antibodies, aptamers and deoxyribonucleic acid (DNA). Therefore, biosensors benefit from the inherently high selectivity of the biological recognition elements to the analyte which is also imparted to the biosensor device. The term bio-recognition is used to describe the binding of the ligand (analyte) to the bioreceptor (biorecognition element) that results in the formation of a biorecognition complex (*R-L complex*) which produces an initial signal such as light, heat, pH change or mass change etc. The affinity between a ligand L (analyte) and a receptor R (such as an antibody) is commonly described by its dissociation constant (K_d) and describes how tightly a ligand binds to its receptor. The formation of the receptor-ligand complex RL in free solution can be simply described as:

$$R + L \rightleftharpoons RL$$

Therefore, giving the corresponding dissociation constant as:

$$K_d = \frac{[R][L]}{[RL]}$$

Where [R], [L] and [RL] are the molar concentrations of the receptor, ligand and receptor-ligand complex. The resulting dissociation constant represents the ligand concentration that occupies half of the receptors at equilibrium. A smaller dissociation constant indicates a more tightly bound ligand and a large affinity between the ligand and the receptor. Therefore the affinity constant (K_a) is inversely related to the dissociation constant (K_d):

$$K_a = \frac{1}{K_d}$$

One of the strongest known affinities is that shared between biotin and streptavidin with a $K_d \sim 10^{-14}$ M and is used extensively molecular biology and biotechnology.[10]

The coupling of a transducer to the biorecognition element allows the conversion of this biorecognition event into a physiochemical response that can be more easily measured as the

transducer signal (the device signal). Transducers are typically categorised by the type of measurable signal that is produced in the detection, these include: electrochemical, optical, thermal and mass/ acoustic (aka piezoelectric) transducers. The electrochemical-based sensors can then be further subdivided into amperometric, potentiometric, coulometric and impedance-based devices.

The transduced signal may require some further processing including conversion from analogue to digital and amplification in order to display the sensing results to the user in a form that is suitable to the context the device is used in. Most transducers used in biosensors produce an optical or electrical transducer signal therefore benefitting from the relative ease of their measurement and processing which improves the utility of the device and reduces complexity and cost of production. Depending on the biosensor it can provide a quantifiable or a qualitative (semi- quantifiable) detection of the analyte, this depends on the purpose and context of the analyte being investigated for example a pregnancy test need only provide qualitative information to the user.

1.2.1 Labelled assays

In general there are two types of detection use in biosensors, those that require a labelled biomolecule and those that are label-free, these are shown in Figure 1.

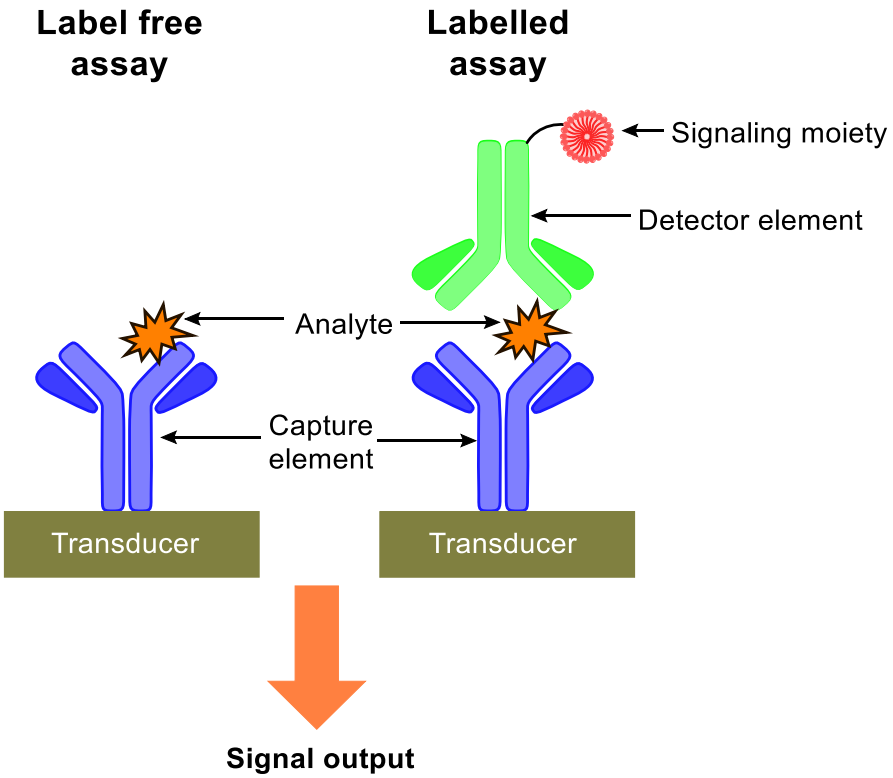

Figure 1 Schematic representation of signal transduction in Label-free (left) and Labelled assays (right). In a Label-free assay (left) a signal is generated directly through interaction with the analyte, and a molecular capturing element (blue) that is immobilised onto a transducer surface. In labelled "sandwich" assays (right) the analyte is sandwiched between a detector and a capture agent (e.g. antibodies), one of which is immobilised on a solid surface (capture element). The signalling moiety attached to the immobilised detector element (green) transduces the formation of the complex into a detectable output signal.

Labelled assays require the application of a separate detecting element in order to transduce the analyte binding event into an output signal. In labelled "sandwich" assays a capture biorecognition element (e.g. antibody) is typically immobilised onto an inert solid surface, such as electrode, glass or chip. The analyte binds to the capture element and is immobilised, and the "sandwich" is formed when the detector agent binds to the analyte. The detector agent is attached to a signalling moiety whose function is to transduce the recognition event into a detectable output signal. The most common assays of this type include Immunohistochemistry (IHC), Polymerase chain reaction (PCR) and enzyme-linked immunosorbent assay (ELISA). Typical signalling moiety include fluorophores, enzymes or dyes, which produce an output as luminescence, electrochemical signal or most commonly in a colourimetric signal, i.e. ELISA. The detection of such tags typically requires an

additional sensor, for example, optical sensors for the detection of fluorescent, colourimetric or luminescent tags and electrochemical sensors for the detection of redox reactions from enzyme tags. These optically based detection techniques are therefore limited by the need for instruments such as colourimeters and spectrophotometers to enable quantification. The required equipment is often expensive, lacks portability and requires trained technicians and a laboratory to perform the multi-step labelling protocols. These factors make them unsuitable for miniaturisation and limit their potential application as point-of-care devices as tests are usually conducted in centralised laboratories resulting in long sample turnaround resulting in delays in acquiring results.

The transduction of the binding event into a quantifiable electrical signal allows the device to benefit from innate high sensitivity and simplicity in its readout and facilitates the effective coupling with miniaturised hardware. There are a variety of recognition elements employed by biosensors for biomarker detection, the most prominent example in current use is the enzymatic biosensor for blood glucose detection.[11]

1.2.1.1 Amperometric glucometers

The benefit of an electrical readout has allowed glucometers to dominate the field of diabetes management since their commercialisation some 25 years ago.[11] Their operation relies on the activity of the highly stable and specific glucose oxidase enzyme (GOx). The enzyme is immobilized under a semi-permeable membrane on the surface of the working electrode. The production of hydrogen peroxide (H_2O_2) as a by-product of glucose-GOx reaction with glucose can cause electrochemical oxidation or form charge carriers at the working electrode upon exposure to an electrical potential (see Equations 1 and 2).[12] Both methods are able to produce a current that is proportional to the concentration of glucose in the sample, allowing the blood glucose concentration in the blood to be monitored.[11]

$$\boldsymbol{Glucose} \xrightarrow[\boldsymbol{GOx}]{} \boldsymbol{Gluconic\ acid} + \boldsymbol{H_2O_2} \qquad (\mathbf{1})$$

$$\boldsymbol{H_2O_2} \xrightarrow[\boldsymbol{0.7\ V\ vs\ SCE}]{} \boldsymbol{O_2} + \mathbf{2}\boldsymbol{H^+} + \mathbf{2}\boldsymbol{e^-} \qquad (\mathbf{2})$$

However, current electrochemical biosensors require redox reactions to produce a signal and the use of enzymes as recognition elements are typically restricted to the detection of metabolites hence, they are not suitable for detecting most protein biomarkers. Metabolites that can be detected in addition to glucose include lactate, urea, uric acid, ammonia. These are useful as

diagnostic indicators of diseases such as diabetes, kidney injury, hypertension, hyperthyroidism, and leukemia.[13–15]

1.2.1.2 Potentiometric biosensors

Electrochemical-based sensors have also been developed for use in labelled assays and one of the most common are potentiometric biosensors in which the transducer produces an electric potential as the analytical output signal. They often rely on biochemical reaction that produces a simple species which is more easily detected electrochemically. (NH_4OH, CO_2, pH, H_2O_2).

In general, potentiometric sensors measure the potential difference (voltage) between two electrodes, under the conditions of no current flow. One of the electrodes in the system is usually a reference electrode that produces a constant potential, the relative variation in potential of the working electrode in response to the activity of the ion in the sample can then be reliably measured. The measured potential may then be used to determine the analytical quantity of interest, which is generally the concentration of some component of the solution.

Enzymatic biosensors are prominent examples that have been used in potentiometric biosensors and rely on selective conversion of the analyte of interest by an enzyme into a chemical species that the sensor detects. Examples include glucose using glucose oxidase, creatinine by creatinine amidohydrolase or urea by urease. For example, the catalytic hydrolysis of urea by the urease enzyme can allow the detection of the hydrolysis products $NH4^+$ and OH^- that can be measured by pH detection and ammonium detection for the quantification of urea. The low cost and stability of urease means it is often the model enzyme of choice for development of new biosensors and new enzyme immobilisation techniques.

Enzymatic pH-mediated potentiometric sensing operates by localising the hydrolysis of the analyte (urea) close to the surface of a pH sensitive layer that the enzyme is often adsorbed on or attached to covalently (usually on the gate). The material must be sensitive to changes in pH and examples include oxide metal and polymer films that can be protonated or deprotonated resulting in a potential shift. However, ammonium mediated biosensors typically rely on the use of an ammonium ion-selective electrodes and the urease is grafted on to the membrane matrix. Both techniques can suffer issues such as buffer capacity for pH sensors and problems due to lack of selectivity from background interferents for ammonium sensors.

1.2.1.3 Immunosensors

Immunosensors rely on the transduction of immunochemical reactions of biorecognition elements (antibodies, aptamers mRNA etc) and their ligands. As a result, immunosensors benefit from significantly wider scope of analytes that can be easily detected whilst also retaining a high level of selectivity. The transduction of the receptor ligand interaction can also be achieved electrochemically in label-based biosensors using either enzymes or nanoparticles tags/label (signalling moiety) that can be readily attached to biorecognition elements. Amperometric immunosensors are amongst the most common reported devices as one of the most extensively used enzyme tags is horseradish peroxidase. This produces compounds that can be easily detected amperometrically and shows low detection limits and high sensitivity. Some potentiometric immunosensors have also been developed using sensing mechanisms based on nanoparticle labelling that release specific ions (such as cadmium) that are detected by ion-selective electrodes (ISE).

1.2.2 Label-free assays

In contrast to the detection methods described in 1.2, label-free detection operates by the recognition process producing a change in a physical variable which is measured directly. In label-free assays, the presence of an analyte is measured directly through interaction with a molecular capturing element immobilised on a transducer surface. The assay design is simplified by requiring only a single recognition element. As the analyte does not require labelling or chemical modification, they benefit from decreased assay cost, lower reagent cost and enable quantification in real time.

Label-free biosensors that rely on molecular recognition elements represent a potential game-changing tool in the field of clinical diagnostics. The relative advantages over comparative techniques including rapid *in-situ* diagnosis in real-time and multiplexed detection, automation and reduced costs make them ideal candidates for point-of-care analysis platforms. The transduction of a chemical binding event into an electrical signal in this manner circumvents many of the disadvantages of labelling by producing an output that is easy to amplify, measure and interpret. Hence, the most promising label-free detection platforms rely on the intrinsic properties present on the target analyte for their direct electrical detection. Recent advances in the field of label-free electrical biosensors were extensively reviewed by Davis *et al.* and Poghossian *et al*, [16,17] where organic field effect transistors are highlighted as a potential solution and are discussed further in sections 1.3 and 1.4.

Non-FET based label-free transducers used in biosesning include piezoelectric sensors such as quartz crystal microbalance (QCM) which utilises a quartz crystal as its piezoelectric material. The device operates through the principle that the analyte will introduce a change in mass on the sensors surface which results in a detectable change in the resonant frequency of the piezoelectric material. As the quartz crystal is covered by a gold or silver electrode this allows its facile functionalisation with biorecogntion elements to give the device same selectivity as alternative transducer-based immunosensors. The biofunctionalisation can be achieved by a number of methods including non-specific adsorption or the formation or carboxylic acid terminated SAMs followed by EDC/NHS to covalently attach the biorecogntion element to the surface. This is often used as an intital method for proof of principle of the immobilisation techniques used to functionalise Gold gate electrodes in some OFET-based devices. Whilst the sensors benefit from high sensitivity, very low detection limits, short response times and low power consumption they can be limited by poor reproducibility and sensitivity to environmental conditions such as temperature and humidity.

Surface plasmon resonance (SPR) is a related technique which can be used for measuring adsorption onto planar metal surfaces (e.g. gold or silver) by an analyte and has seen wide-spread integration into label-free biosensors. SPR immunoassays can be developed by the immobilisation of relevant biorecognition elements (antibodies) onto the sensor surface. The interaction of the antigen at the surface interface can be detected by the change in the surface plasmon resonance angle in the measured interface incident light. The technique has seen applications in various biosensors and in lab-on-a-chip sensors.

1.2.3 Biosensor figures of merit

In order to further discuss the essential attributes of a biosensor the key figures of merit by which a sensors performance is judged are examined below.

1.2.3.1 Calibration curve

A sensor produces an output signal/ response (y) that is described as a function of the input variable, analyte concentration (x). $y = f(x)$ and a calibration curve is typically used to explore this relationship allowing system calibration. The establishment of the relationship between a biosensors output signal (i.e. the response) and calibration standards of known analyte concentration is used to produce a calibration curve as shown in Figure 2. This is carried out by measuring the device response for each standard of known analyte concentration across the specified range. Assessment of calibration can be conducted by preparation and measurement of a blank and at least five standards equally spaced throughout the range of analyte concentrations and ideally covering the

range of concentrations expected to be encountered upon analysis of samples. Measurements should be recorded at least in duplicate (preferably triplicate or more) at each concentration level to allow the precision to be estimated at each of the investigated concentration levels. Typically, calibration standards are prepared from a pure substance of known purity or a solution of known concentration.

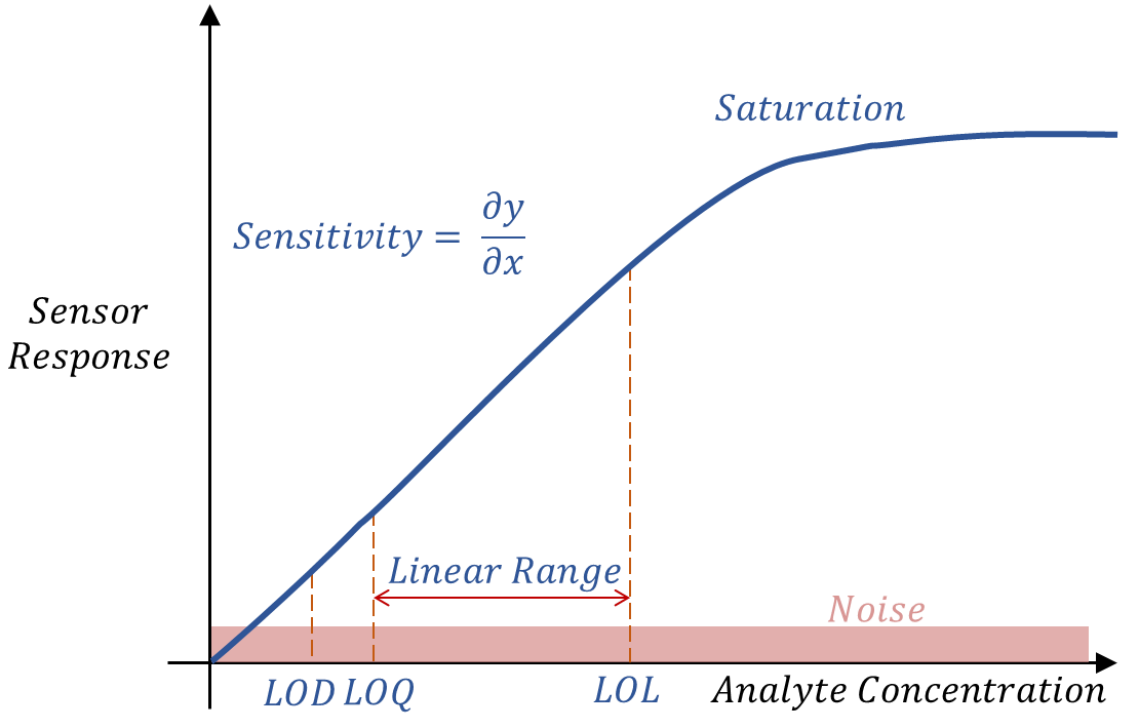

Figure 2 An example calibration curve showing the relative figures of merit that can be extracted.

The solvent used to prepare the calibration standards also requires consideration whether it is a pure solvent or more complex solution mixture that more accurately represents the conditions encountered in the test samples. For example, biological physiological conditions are typically reproduced with phosphate buffered saline (PBS) solutions that simulate pH and ionic strength of biological samples and more complex matrices have been used as the sample solvent such as blood serum devoid of analyte.

The calibration curve itself is obtained by plotting the sensor response (R) on the y axis against the concentration of the analyte standards (x axis) or its logarithm. The response (R) is then typically corrected for the background or blank response (R_0). However, it is often of greater merit to analyse the normalised response as this accounts for any device to device variation which may frustrate meaningful analysis in absolute values.

Normalised response can be calculated as:

Equation 1

$$\Delta R/R_0 = \frac{R_{analyte} - R_0}{R_0}$$

1.2.3.2 Sensitivity

The sensitivity of a sensor describes the ratio of change between the output signal (*Δy*) and the input variable (*Δx*) $S = \frac{\Delta x}{\Delta y}$ and is shown in the gradient (slope) in a calibration plot. Maximising the sensitivity of the senor is a typical aim in the design of a sensor providing that other performance related parameters such as accuracy and precision are not compromised. Increased sensitivity generally aids in improving the measurement resolution in measuring analyte concentrations across the sensors working range. The measurement resolution of a sensor relates to the smallest detectable change in the input variable (analyte concentration) that produces a response in the output signal. Good resolution is desirable in analyte quantification.

Linearity assesses the deviation of the output curve from a specified straight line, in such a case the gradient (and sensitivity) of *y=f(x*) remains constant. The linearity of the device response may be constant and cover the entire concentration range or be limited a range of analyte concentrations where the device response changes linearly to concentration and is termed the linear range. Above the linear range it is common to observe a saturation in the sensor response, the onset of this is referred to as the limit of linearity (LoL). The reduced response sensitivity observed upon the onset of response saturation significantly frustrates reproducibility and accurate quantification of sensing results, therefore unless accurately modelled LoL is considered an upper working limit of the dynamic range.

1.2.3.3 Limit of detection

The limit of detection (LoD) is the minimum concentration of analyte that can be reliably distinguished, from the “background noise” i.e. the response from the blank where no analyte is present (baseline). This is because a blank sample may still produce an analytical signal that unless defined would otherwise correspond to a low concentration of analyte. Assuming a normal distribution about the mean blank value the concept of detection and quantification limits and the distribution and overlap of results at each limit can be visualised (Figure 3).

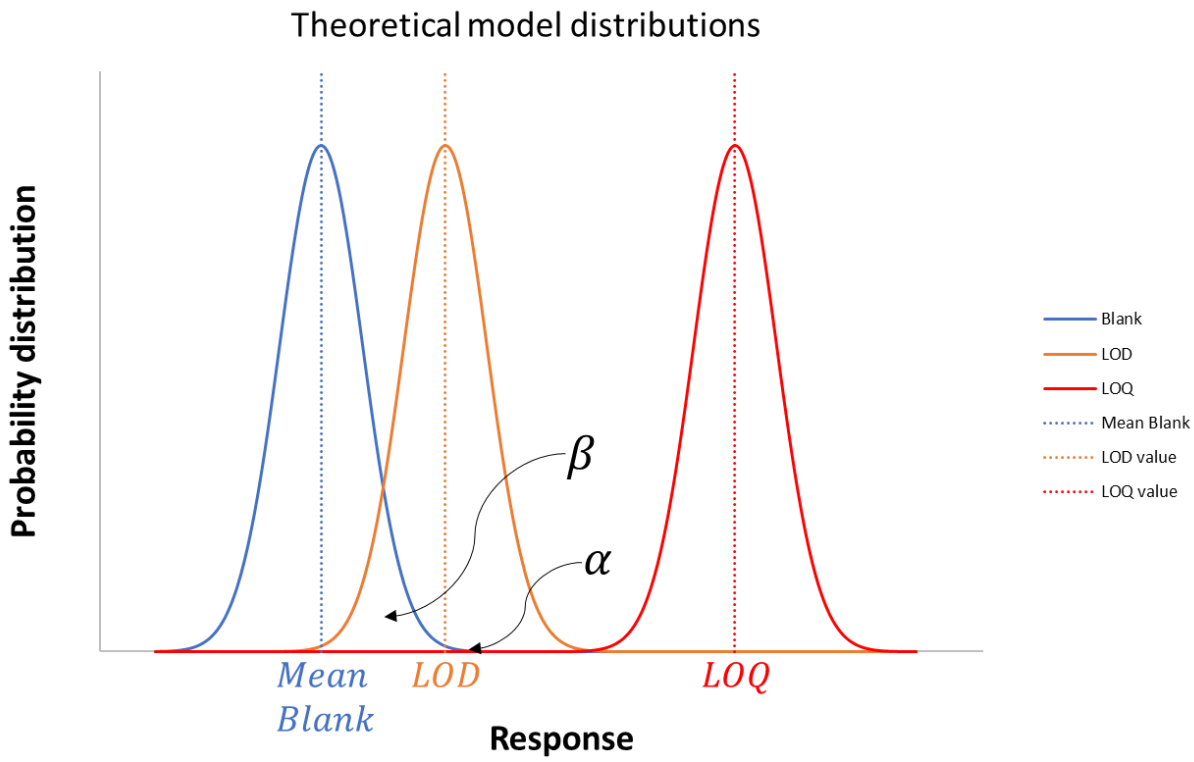

Figure 3 Figure showing normal distribution of a set of blank values and how this effect the separation of the LOD and LOQ. The area under the curves at α signifies the values corresponding to false positives and β signifies the false negatives.

The LoD is typically determined by measuring replicates of blank sample to calculate a mean blank response (R mean blank) and calculating the standard deviation σ(SD) of those values. The standard deviation of a set of results allows statistical measurement of the variation of a set of values (N) from the mean value of the set (μ).

Equation 2

$$\sigma\ (SD) = \sqrt{\frac{1}{N}\sum_{i=1}^{N}(x_i - \mu)^2}$$

The LoD can then be calculated as the concentration that corresponds to that signal within a calibration curve.

Equation 3

$$LoD = Rmean_{blank} + k\sigma_{blank}$$

The value *k* corresponds to an integer related to the confidence interval (conventionally 3) where higher values represent a more conservative approach. Use of a k =3 would define the probability of recording a blank measurement 3 times above the mean at under 1% (false positive). However, the

probability of a concentration value at the LoD falling below mean value would be 50%, this would be a false negative.

The concentration corresponding to the LoD is not necessarily accurately quantifiable by the system and the greater degree of certainty required is often termed the limit of quantification (LoQ). The limit of quantification defines an assays “functional sensitivity” or precision at low analyte levels this defines It sets the limit quantitative results can be obtained within a specified degree of confidence usually 10 times the standard deviation (k=10).

For the performance of biosensors based on biorecognition processes show a direct correlation with underlying dissociation constants of the biorecognition elements to their ligands. A high binding affinity (low dissociation constant) generally results in a lower LoD, and at concentrations below the dissociation constant concentration the biosensor response is lower.

1.2.3.4 Dynamic range

The dynamic range (or working range) of sensor is the range of analyte concentrations values to which a distinguishable system response can be reliably and reproducibly measured and is usually within the linear range of the concentration-response relationship. Below this concentration lies the LoQ and LoD and at above the highest concentration range response saturation is typically observed. For the sensor device to be of use the values of interest for the analyte should fall within this dynamic range.

1.2.3.5 Selectivity

Selectivity is one of the most important characteristics of a biosensor and is the extent of sensors ability to produce a signal response to only the analyte of interest in the analysed sample in the presence of other species that may interact with the sensor. These interfering species can be any mixture or matrix component of the analysed sample such as impurities, metabolites and degradation products etc. When the sensor is selective it should be able to discriminate the analyte from these other components. If one species can be independently determined and all other species give no analytical response then specificity is achieved and would entail an entirely 100% selective response, such cases are rare.

Complex matrices such as blood samples present a significant challenge for selective responses due to the wide variety of components that may interfere with the output signal and frustrate accurate analyte detection. Biosensors typically rely on the inherent selectivity of their biorecognition elements and affinity to only their corresponding ligand. This imparts a high level of selectivity to the coupled transducer and device. Therefore, one of the main considerations in choosing an

appropriate bioreceptor is its selectivity to the desired analyte in addition to taking steps to minimise non-specific interactions. One of the most prominent examples is the interaction between an antibody and antigen that is utilised in immunosensors.

The selectivity of a biosensor is determined by measuring the response of the biosensor against an interfering species (in a simple or complex sample) that otherwise would be expected to produce no response (negative control). The analysis of negative controls usually aims to identify and estimate the sources of non-specific binding and/or response.

Various methods are available for determining the selectivity of a biosensor and one of the two following methods is most frequently used. Plotting a calibration curve for interfering substances for comparison with an identical plot for the analyte which has been performed in an identical manner as that for the analyte performed under the same operating conditions used for the analyte calibration curve. The selectivity of biosensor can then be analysed as the ratio between the output signal produced in response to an equal concentration of analyte and a negative control when these are measured independently under the same operating conditions. An alternative analysis involves spiking the interfering substance at the expected concentration to a solution of known analyte concentration and measuring the resulting variation in response which can be expressed as a percentage.

1.2.3.6 Reproducibility

Reproducibility of a biosensor is an important characteristic related to performance as it provides reliability and robustness and is typically described by the metrics of accuracy and precision. The accuracy of a sensor relates to the ability to report a measured concentration value as close as possible to the true value. This may be defined as an absolute value within the working range.

The precision is the ability to achieve the same value upon repetition of the sample measurement under the same operating conditions. The relative standard deviation (RSD) is a statistical measure which used to express precision and repeatability of a measurement and is often expressed as a percentage (%RSD), where η is the mean of the dataset.

Equation 4

$$RSD = 100 * \left(\frac{\sigma(x)}{\eta}\right)$$

1.2.3.7 Response and recovery time

The response time of a sensor is the amount of time required to achieve equilibrium in the output as a result of a change in the input. In general, the response time can be measured from the point of initial input change to the point where stabilisation of the output signal is achieved. The response time is then frequently reported as the time required for the response to reach a fixed percentage (usually 90%) of the final value.

Conversely recovery analysis investigates the parameters describing the return of a sensors signal to a background value following the removal of the measured variable (the analyte). The recovery time usually defines the time taken to reach 10% of the previous response value. This is particularly important characteristic in continuous measurement systems and the two parameters are collectively known as the system reaction times. However, some systems such as many immunoassays produce irreversible signal responses due to the strength of the binding coefficient of an antibody; and therefore, the response is not expected to recover to the baseline value and the resulting sensors can be considered single use. Alternatively, when recovery is not achieved between sequential analyte detections the baseline drift can be monitored.

1.2.3.8 Stability

The sensor stability relates to the susceptibility of a sensing system to external factors that impact on the ability of a sensor or the sensing system to maintain its previously described performance parameters over time. Stability can encompass a variety of areas but can be broadly grouped into factors concerning the sensor or the samples and the aim is to minimise the impact on the precision and accuracy of results measured.

One factor affecting stability is the susceptibility of the biosensor system to degradation over time either before initial testing (shelf life) or during testing (operational stability), this can be particularly relevant when long incubation steps or continuous measuring is required. The shelf life of a biosensor is determined by the stability and performance of its underlying components over time, namely the transducer and the biorecognition element. Therefore, the stability of the antibody has a pivotal role in determining an immunosensors shelf life and reliability. Proteins such as antibodies are susceptible to various interrelated degradation pathways; they are broadly categorised as resulting from chemical or physical instabilities that result in a reduction or loss of binding activity directly impacting the immunosensors performance.[18]

Chemical instability can include processes such as deamidation, isomerisation, crosslinking through the formation of disulphide bridges and the oxidation of protein residues such as Met, Tyr, Trp, His,

and Cys. Physical instability is exhibited through denaturation or aggregation and may be induced by the previously described chemical instabilities, or environmental conditions such as temperatures or pH. Protein denaturation is the manifestation of a loss of higher-order structure caused by unfolding of the structure. The primary source of physical instability and reduced activity for antibodies in free solution is aggregation, an often-irreversible process.[18]

In contrast, the stability and activity of solid-phase antibodies are thought to be primarily driven by antibody-surface interactions that destabilise the antibody structure and introduce steric interference to antigen binding.[19] The interaction of the antibody with the immobilised surface affects the folding behaviour of fragments which directly impacts the effectiveness of binding to its antigen. Theoretical modelling also suggests that hydrophobic surfaces induce lower stability levels relative to hydrophilic surfaces or antibodies in free solution by inducing a collapsed configuration, causing a denatured structure that is adsorbed onto the surface.[19] The interaction of the antibody with the immobilised surface affects the folding behaviour of fragments and directly impacts the effectiveness of binding to its antigen.

The most common application of solid-phase antibodies is in enzyme-linked immunosorbent assays (ELISA). Shelf-life testing of ELISAs has highlighted that the activity of the antibodies is best preserved by storage in a buffer at low temperatures and should not be allowed to dry. The stability and activity of solid-phase antibodies were demonstrated with a polystyrene substrate functionalised with antibodies by physical adsorption for use in an ELISA by Ansari *et al*.[20] The activity was preserved in a tris-buffer (pH 7.2) for 95 days at 6°C and room temperature. However, a significant loss of activity occurs upon drying, and this loss continues further upon storage of the air-dried solid-phase antibodies.

Additionally, sample stability can also relate to the conditions applied to the samples during processing or storage. This can be analysed by testing replicates of sample once relevant storage conditions or any other variation in sample processing has been applied (e.g. RT for several hours). The results can be analysed against a freshly prepared calibration standard and the variation in the response is indicative of the stability of samples in the nominal concentration response.

1.3 Organic field-effect transistors (OFETs)

1.3.1 Organic electronics

Work on field effect transistors (FET) has progressed significantly since their early 20th century origins to become one of the key components in the electronics industry. FET operation relies on the principle that a charge on a nearby object can attract a charge within a semiconductor channel. Therefore, the application of an external electric field (an applied voltage on a gate electrode) can modulate the flow of charge carriers in the conducting channel between a source and drain electrode. Whilst many FET devices have been developed in the intervening years the most common by far is the metal–oxide–semiconductor field-effect transistor (MOSFET) which uses Si semiconductor and SiO_2 as the gate oxide dielectric material.

Organic electronics seeks to use device structures based on organic (macro-)molecular materials for use as dielectrics, conductors or semiconductors. Organic semiconductors (OSCs) have found promising applications in fields where the electrical properties similar to silicon semiconductors are required and the origins of charge transport in OSCs is further discussed in section 1.3.2.[21] The development of OSCs very active field with synthesis of novel materials reported regularly in prominent journals ranging from small molecules such as rubrene, pentacene, BTBT and to polymers such as P3HT and DPPTTT and is discussed in more detail in section 1.3.4.

The organic toolbox available in organic material design allows gives the opportunity to incorporate different chemical functionalities therefore allowing tuning of the properties to meet those desired in the applications through rational chemical design. As OSCs can be deposited through low temperature solution processing this allows for the use of high throughput techniques such as inkjet or roll-to-roll printing and can enable rapid, sustainable and inexpensive fabrication of devices that are compatible with flexible substrates. This is particularly attractive when compared to the complicated and expensive methods required for inorganic materials that typically require use of ultraclean, lithographic based fabrication facilities.[22]

Historically the commercialisation of organic electronics has been impeded by poor device performance, the challenge being their relatively low mobility of charge carriers and the stability of devices under ambient conditions.[23] However, recent developments in optimising the properties of organic semiconductors has shown improved air stability and charge carrier mobilities comparable to or better than amorphous silicon,[22] opening a new era of low cost and large area applications and providing a viable alternative to a variety of traditionally inorganic based devices and could act as the main component in cheap and flexible electronic circuits.[21] Thin film transistors where first

proposed by Weimer in 1962 and by 1986 the first organic thin film transistor (OTFT) was reported by Tsumura,[24,25] where the flow of electric current is facilitated by an organic semiconductor (OSC) material. OTFTs and OFETs are terms frequently used interchangeably within the field, for simplicity all these devices will be referred to as OFETs from herein. The application of OFETs is further discussed in section 1.3.8.

In addition OSCs have found applications in a wide variety of electronic and optoelectronic devices, such as organic photovoltaic cells (OPVs),[26] organic light emitting diodes (OLEDs)[27] and OFETs.[22,23] Recently organic field effect transistors (OFETs) have gained interest as promising candidates for label-free sensing applications as they combine the function of a label-free transducer and amplifier within one device, whilst benefiting from well-established miniaturisation methods and integration into complex circuits for further signal processing. The inherent signal amplification of OFET-based sensors leads to higher sensitivity and improved LoD in comparison to alternative sensing platforms.[16,28] The sensitivity/amplification of a biorecognition event largely relys on appropriate selection of biorecognition elements and transducers, post-transduction signal amplification is generally not as efficient due to the amplification of accompanying noise therfore the signal to noise ratio is maintained and an improvement in LoD would not be achieved. Furthermore, the simplicity of an electrical output that is easy to interpret combined with low cost fabrication, is advantageous to the development of disposable electronic sensing systems that are ideal for PoC testing.[28,29]

1.3.2 Origin of charge transport in OFETs/OSCs

The term charge carrier is used to describe the particles or quasiparticles that can move freely within a material and carry the electric charge, in a semiconductor these are electrons and holes (travelling vacant sites also called hole polarons). The application of an electric field within conducting media causes a flow of electric charge i.e. an electric current. The degree of conductivity of a material is related to its electronic structure and varies for metals, semiconductors, insulators whether those be organic, inorganic or a hybrid of both. The electronic energy levels of the materials used in OFETs are particularly important to understand the interfaces between the materials and their impact on charge injection and transport during device operation. Therefore, key electronic parameters and their relation to the electronic structures are discussed further below.

The work function (WF) of a solid (usually a metal) is a surface property that describes the energy required to remove an electron at the Fermi level (E_F) of a material to a point of rest in a vacuum near to the surface of the material (E_{vac}). The Fermi level (E_F) is the electrochemical potential of electrons inside the material and describes the hypothetical energy level of an electron, such that at thermodynamic equilibrium it would have 50% chance of occupancy at any given time.

Equation 5

$$WF = -e\phi - E_F$$

ϕ is the local electrostatic potential in the vacuum nearby the surface in V, $-e$ is the charge of an electron, and E_F is the Fermi level.

In an OFET device the Fermi level is typically set by the voltage applied to the Drain electrode. The relative position of the Fermi level is critical in describing the conductive behaviour of different materials and this is usually displayed in a band structure plot showing the filling of electronic states in the different materials when at equilibrium (Figure 4). As conductivity requires the movement of charge carriers and the ability of the charge carrier to move within the material depends heavily on the availability of vacant electronic sites for the charge carriers to move between.

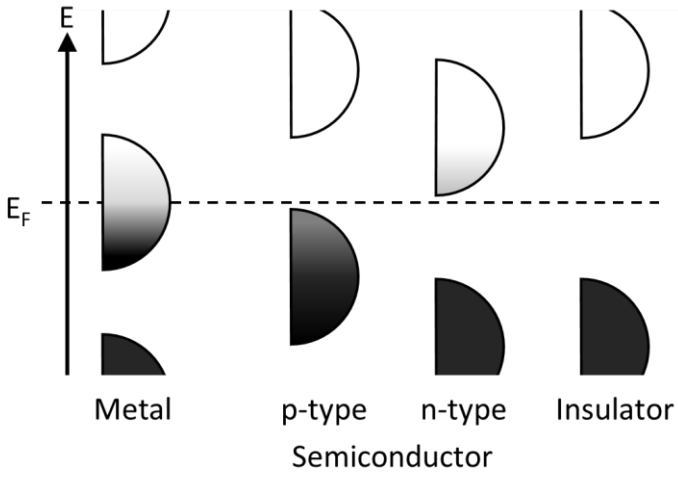

Figure 4 Distribution of available electronic states or energy levels. The y axis represents energy whilst the x-axis represents the density of available states of a certain energy for each material. The shading represents the distribution of filled states (black = all states filled and white = no states filled).

Only charge carriers near or above the Fermi level are free to move within the material as they can move between partially occupied or vacant states in a region. In a metal the Fermi level lies within a delocalised band therefore many energy states are available, and the material is freely able to allow the flow of current.

In contrast for semiconductors and insulators, the Fermi level is located inside the energy band gap (E_g) where few electronic states exist (i.e. between the HOMO and LUMO levels for an organic semiconductor). A material behaves as an insulator when no charges are available, or they are immobilised. Insulators have a sufficiently large band gap (4-15 eV) that the occupied states reside far from the Fermi level therefore the concentration of free charge carriers is close to zero. The

energy barrier to promote a charge carrier into a conduction band is sufficiently high to result in high resistance and insulating behaviour (and when a charge carrier is injected it is trapped).

However, in a semiconductor the band gap lies between that of a conductor and insulator (around 1.5 to 3.5 eV) and the Fermi level is close enough to an energy band that some charge carriers can reside near the band edge and under the appropriate conditions injected charge carriers can flow. For a current to flow in the transistor channel of an OFET charge carriers must be injected from an appropriate source electrode at the OSC/metal interface metal and this is further discussed in section 1.3.5.1.

Organic semiconducting materials are mainly categorised as small molecules or polymers defined by the presence of a π-*conjugated system* of overlapping molecular π-orbitals within their structure. The (macro-)molecular units of organic materials are held together by non-covalent interactions such as Van der Waals forces and π-stacking interactions. This is in contrast with the extended network of covalent bonds that is established in inorganic materials such as silicon. The weak intermolecular forces allow the use of low temperature processing methods and films can be deposited from vapour or solution. OSC's also offer wide-scope for facile chemical modification of the molecular units; modification of the π-conjugated backbone or side groups enables the material to be tailored for the desired electronic, mechanical or biological properties that meet the need of their applications.

Defects and disorder within the OSC material, such as twists and kinks along a polymeric backbone, limits the extent of delocalisation of π-electrons within the material.[30] The variation in conjugation length and interaction energies produces ill-defined delocalised energy bands and forms a Gaussian distribution of statistically variable localised energy states (Figure 5).[31] The distribution of allowed energies gives rise to electronic band structures that can be used to explain the electrical properties of the materials used in solid state devices.

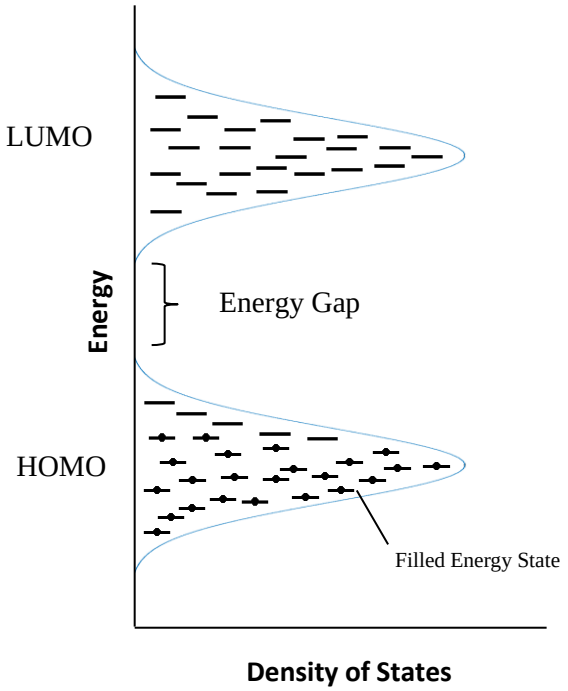

Figure 5 The Gaussian distribution of localised states that form the energy levels of the highest occupied molecular orbital (HOMO) and the lowest unoccupied molecular orbital (LUMO) for an organic semiconductor.

In organic semiconductors these energy states can be described as energy levels where the highest occupied molecular orbital (HOMO) level represents the energy required to remove an electron from a molecule, an oxidative process. Whereas, the lowest unoccupied molecular orbital (LUMO) level represents the energy required in the reductive process of injecting an electron into a molecule. The energy difference between the HOMO and LUMO is the HOMO/LUMO gap and known as the energy band gap (E_g). The HOMO and LUMO levels in OSCs are analogous to the valence and conduction bands of inorganic semiconductors although not as closely packed. The HOMO/LUMO energy levels of a material are conventionally calculated by ultraviolet photoemission spectroscopy (UPS) or cyclic voltammetry (CV). In the solution-based CV method the energy levels are calculated by measuring the electrochemical redox potentials, reduction potential (E_{red}) and oxidation (E_{ox}) relative to an internal ferrocene reference.[32] The electrochemical redox potentials calculated in this fashion are analogous to the charge injection in organic films and the values for ionisation potentials of OSCs quoted in this thesis are calculated by this method.

Semiconductor materials are typically classified by the majority charge carriers that they preferentially transport, and this dictates the type of devices that they are used in. The majority

charge carrier in an OSC is usually a reflection on the ease of charge injection from the electrodes to either the HOMO or LUMO depending on which energy level is more closely aligned with the Fermi level of the electrode. In p-type materials holes are injected into and travel within the HOMO to act as the major charge carrier. In contrast, n-type materials the major carriers are electrons which are injected into the LUMO. However, ambipolar materials allow the injection and transport of both holes and electrons. In organic semiconductors, both intramolecular and intermolecular charge transport may take place: in intramolecular transport, the charge carrier moves within the same molecule whereas intermolecular charge transfer requires the charge carrier to move between molecules. This allows the charge carriers to migrate across the material by hopping between the localised states present in the band gap. The charge carrier mobility (μ) characterises the ability of a charge carrier to move under an external electric field across the semiconductor layer and is usually expressed in cm^2/Vs. The solid phase molecular packing of the OSC strongly affects its electronic properties and charge transport is highly influenced by structural regularity (the degree of order and packing of chains in the solid state), the level of impurities and structural defects which can arise during processing.[23]

Very efficient packing can be achieved in single crystals of vapour deposited materials such as pentacene, resulting in reported charge carrier mobilities of 15 $cm^2/$ V s and higher.[33,34] However, the more disordered morphology of most organic semiconductors when deposited from solution lead to disorders that limits the π-bonding overlap between molecules and give traps such as grain boundaries between crystallites in a polycrystalline film. Therefore, with increasing disorder the conduction of charge carriers becomes more dependent on quantum mechanical tunnelling by hopping transport. As a result, charge carriers are more localised in organic materials and this often limits the mobility at ambient temperature. Despite the lower charge carrier mobility when compared to conventional semiconductors (e.g. Si), field-effect mobilities in excess of 1 cm^2/Vs (exceeding the benchmark for amorphous silicon) for many donor–acceptor co-polymers have been realised,[35–38] and this will likely increase further with the discovery of novel materials and optimisation of fabrication methodology.[39] In combination with soluble organic insulators with high dielectric constants (*k*) the realisation of fully printed electronics is now feasible.[40]

Within the context of low-cost and simple manufacturing process, OFETS are of particular interest due to the potential for tuning properties through rational chemical design.[41] In addition to the properties of the materials used the device performance is influenced by its architecture.

1.3.3 OFET device architectures

An OFET is a layered three-terminal electrical device consisting of an insulator which separates a thin film of organic semiconductor from the gate electrode (G). The metal source (S) and drain (D) electrodes of width *W* (channel width) are separated by a distance *L* (channel length) and are in direct contact with the semiconducting layer. The order of deposition of the electrically active layers in the devices generally classifies devices into one four main device architectures; bottom gate, top contact (BGTC); bottom gate, bottom contact (BGBC); top gate, bottom contact (TGBC); and top gate, top contact (TGTC) (Figure 6). In order to further discuss the mechanism of device operation, the BGBC layered device will be discussed as well as introducing other TGBC architectures that have been developed for use in aqueous sensing.

Generally OFETs operate by similar principle to a conventional MOSFET (metal-oxide semiconductor field effect transistor), where an electrical field is established across a gating medium, that separates the gate from the semiconducting layer (Figure 6a and b).[28] This gating medium can either be a solid dielectric or liquid electrolyte that acts as polarisable electrical insulator and upon application of electric field allows the capacitive coupling of the gate to the semiconducting layer. Electrolyte gated transistors (EGTs) are a group of devices that utilise an electrolyte gating medium, this type of device structure is particularly useful for *in-situ* electrolyte sensing directly from the analyte solution and is particularly sought after in biosensing. The different EGTs are further discussed below (Figure 6c-e).

Dielectric breakdown limits the maximum voltage that can be applied to the gating media during device operation. High voltage applications typically require solid dielectrics that have higher break down voltage due to the susceptibility of electrolyte media to electrolysis. In general, solid dielectrics are more inert and not all materials used in devices are compatible with exposure to electrolyte media and hence they can have negative impact on performance and stability.

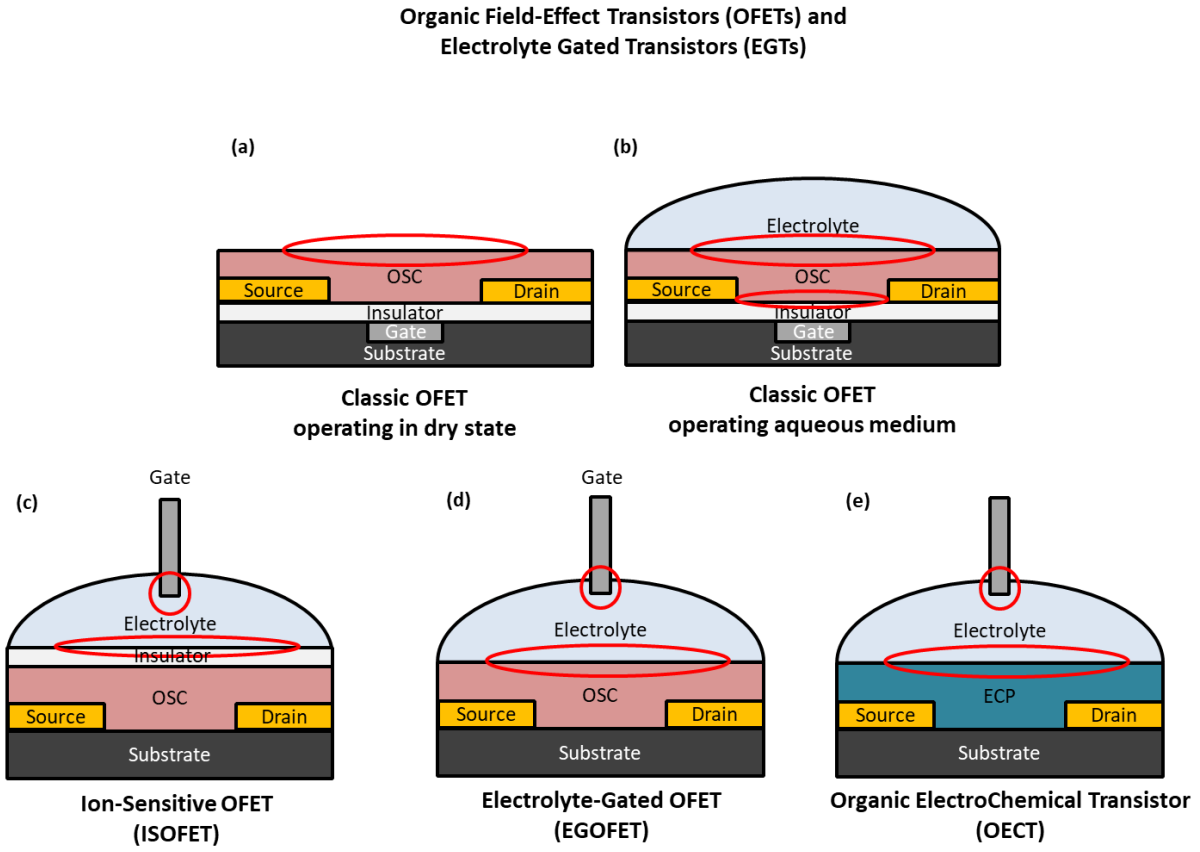

Figure 6 OFET (a and b) and electrolyte gated transistors (EGTs) architectures reported in the literature as possible biosensors: c) ISOFET; d) EGOFET; e) OECT. The red circle indicates the different interfaces involved in the detection of biomolecules.[28]

1.3.3.1 Electrolyte gated organic transistor (EGOFET)

In contrast to other devices, separation of the gate electrode from the semiconductor in EGOFETs is achieved by an electrolyte layer used as the dielectric (which can be solid or liquid as shown in Figure 6d).[42] A variety of electrolytes can be utilised including polymer electrolytes, deionised water and biomimetic aqueous solutions such as phosphate buffered saline solutions (PBS).[42,43] The electrolyte layer permits the movement of ions to produce an accumulation of charge at the interface and a conducting channel is induced when a gate field of sufficient amplitude is applied. An advantage of these devices is the ability to function at very low operating voltages, but they can suffer from slow switching speeds (due to relying on the movement of ions).[28] The low voltage operation of EGOFET devices is due to the formation of an extremely high capacitance electrical double layer (EDL) and is further discussed in section 1.3.7.

1.3.3.2 Ion sensitive organic field effect transistor (ISOFET)

ISOFETs have similar applications to ion sensitive FET (ISFET), a family of silicon-based devices, that have been widely investigated for operation in aqueous media.[44] However the ISFET uses a dielectric

gate medium and ISOFET utilizes an electrolytic gate medium. The architecture of the ISOFET is similar to that of an EGOFET as they have an electrolyte layer in direct contact with a reference electrode functioning as a gate electrode (Figure 6e). However a dielectric layer is also used to isolate the electrolyte from the semiconductor, which can aid in preventing the device from degrading in the presence of environmentally sensitive semiconductors.[45] The channel current is modulated by the potential (caused by the ions) at the electrolyte-dielectric interface therefore making the device a pH sensitive sensor. A variation of this device is the Ion-selective OFET, the ion-selective response of which is achieved by modifying the gate-electrode with a polymeric ion-selective membrane.[46]

1.3.3.3 Organic electrochemical transistor (OECTs)

OECTs belong within a wider class of transistors called electrolyte gated transistors (EGTs) as they share in common with the aforementioned OFET devices the use of an electrolyte gating medium, stable performance in aqueous environments and low voltage operation (below 1V).[28] However, the current modulation in OECTs is achieved by a very different mechanism to OFETs due to the use of an electroactive conducting polymers (ECPs) as channel material (Figure 6e). The different behaviour of EGOFETs and OECTs is further explained by the behaviour at the channel/electrolyte interface. In EGOFETs ideally ions cannot penetrate into OSC channel and the application of a gate voltage results in the formation of an EDL at the interface that is coupled to the induced charge carriers at the interface (hole/electrons etc). However, in OECTs the ions in the electrolyte penetrate into the bulk of the whole conducting polymer channel. Therefore, the application of a variable gate voltage controls the magnitude of the drain current in the channel by electrochemical doping and de-doping of the ECP throughout the bulk of the film. Like the aforementioned EGTs, OECTs also allow *in-situ* electrolyte sensing applications and have seen application in the sensing of various biomarkers including ions, DNA, glucose, cells and application in enzymatic sensing.[47]

1.3.4 Organic semiconductor for use in OFETs

Development of new organic materials for use as the semiconductor in an OFET is a major area of research. The OSC properties that are typically the focus of improvement include increasing the charge carrier mobility, achieving device stability under ambient conditions and operational stability (under bias stress) in addition to the improving the processability of materials, where facile deposition from solution is the most practical technique.[48]

OSCs are generally classified by two main categories, small molecules and polymers, and then further sub-categorised by the type of charge transport that they exhibit (p-type or n-type). EGOFET devices, which are the focus of this work, have so far almost exclusively relied on the use of p-type

OSCs and are therefore the focus of further discussion in this work.[23,49] Additionally, the description of device operation in following sections will focus on the use of a p-type OSCs.

A variety of different p-type OSCs have been applied in OFETs, however the most commonly used include molecular OSCs such as Pentacene, TIPS-Pentacene, BTBT, DNTT, as well as polymeric OSCs such as P3HT, IDTBT, PBTTT and DPPTTT and their molecular structures are shown in Figure 7.[50]

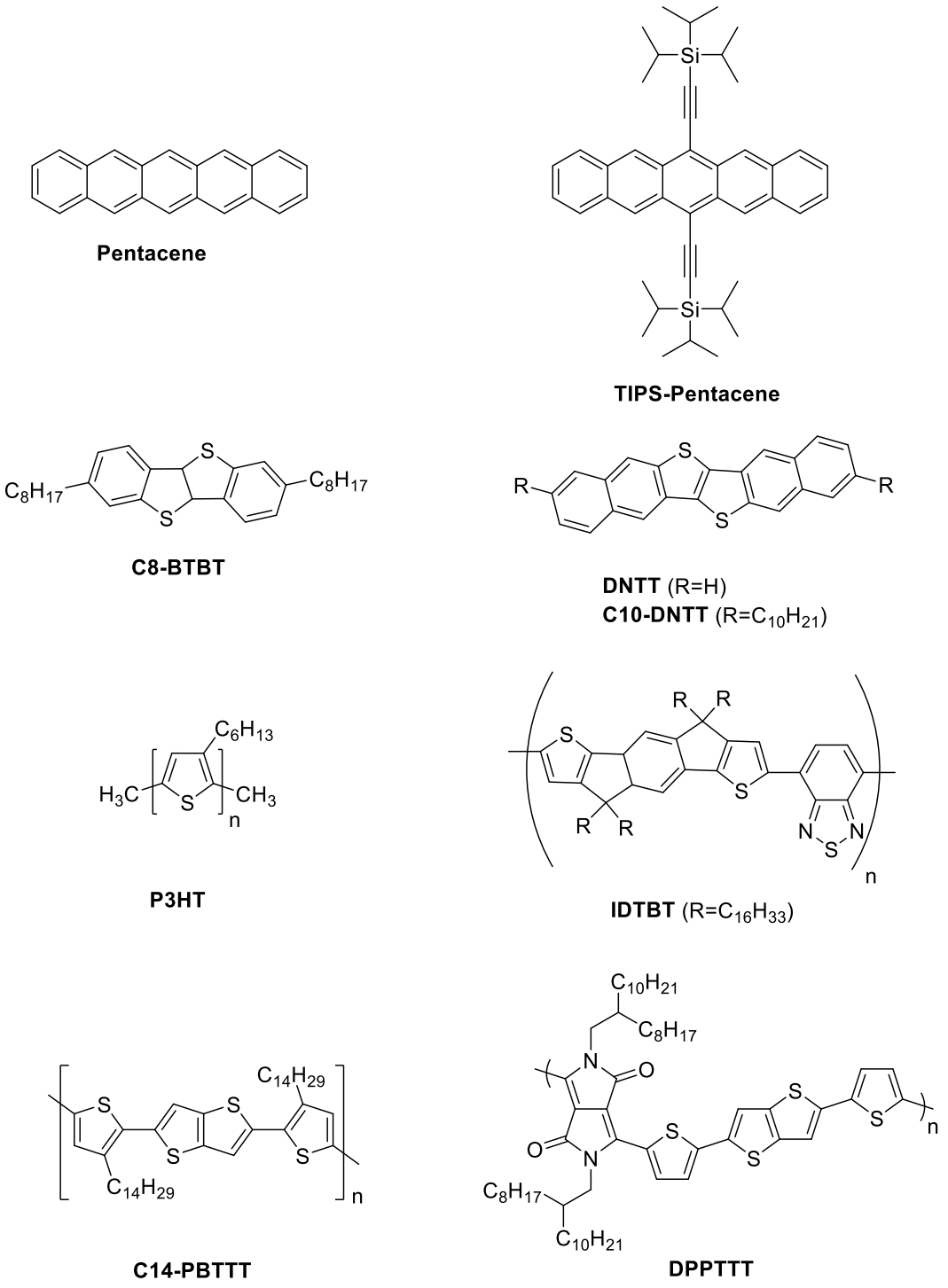

Figure 7 Molecular structures of selected high mobility p-type OSCs.

Small molecules such as rubrene and pentacene can produce highly ordered molecular crystals that display high mobilities but the solution processability is limited by the solubility of these materials and they must be deposited by vacuum sublimation.

One of the most promising and well used building blocks in solution processable p-type semiconductors is the thiophene sub-structure, typically in combination with alkyl substitution to increase solubility. poly(3-hexyl thiophene) (P3HT) is one of the most commonly used p-type conjugated polymer in OFETs displaying hole mobilities up to around 0.1 cm^2/Vs. However, the relatively low-lying HOMO level of (4.8 eV) can make it susceptible to unintentional doping therefore reducing the stability of device operation in ambient conditions. Therefore, design efforts are often made to decrease the conjugation length and therefore slightly increase the ionisation potential whilst maintaining good charge transport.

Further developments include poly(2,5-bis(3-alkylthiophen-2-yl)thieno[3, 2-b]thiophene (PBTTT) which is an example of a alkyl-substituted polythiophenes demonstrating good hole mobilities and improved air stability.[51] Diketopyrrolopyrrole (DPP)-based polymers such as DPPTTT have more recently shown further enhancements in environmental stability and field effect mobility.[35,52–54] Furthermore, other classes of copolymers have also been based on indacenodithiphene (IDT) such as indacenodithiophene–benzo- thiadiazole copolymer (IDT-BT).[55]

1.3.5 OFET Device operation

These devices operate through the modulation of the flow of current between the source and drain electrodes (I_{DS}) by an applied gate voltage (V_{GS}). The gate-contact and the OSC are capacitively coupled by the gating medium hence control of the gate voltage can induce the accumulation or depletion of charge carriers confined within the OSC at OSC/insulator interface to form a conducting channel. In contrast, the channel formation in a MOSFET occurs through the inversion process.[41]

1.3.5.1 Band bending and the field effect

OFETS are interfacial devices and the role of the OSC-insulator interface when subjected to different bias conditions is critical to understanding device function.[56] In an OSC the density of charge carriers (holes or electrons) that respond to an applied field is sufficiently small that the field can penetrate relatively far into the material. The applied field modifies availability and occupancy of energy levels at the surface region of the semiconductor and therefore modulation of the electrical conductivity, this is the *field effect*.

The effect of the applied electric field on semiconductor is best displayed by a *band-bending* diagram that shows a metal-insulator-semiconductor (MIS) junction and the position of the energy states

(band edges) near the interface as a function of depth into the material (Figure 8). The bands of the semiconductor are pinned to Fermi level of the metal electrode and this can be altered by the applied voltage, causing the observed band bending of the energy states near the junction due to space charge effects.

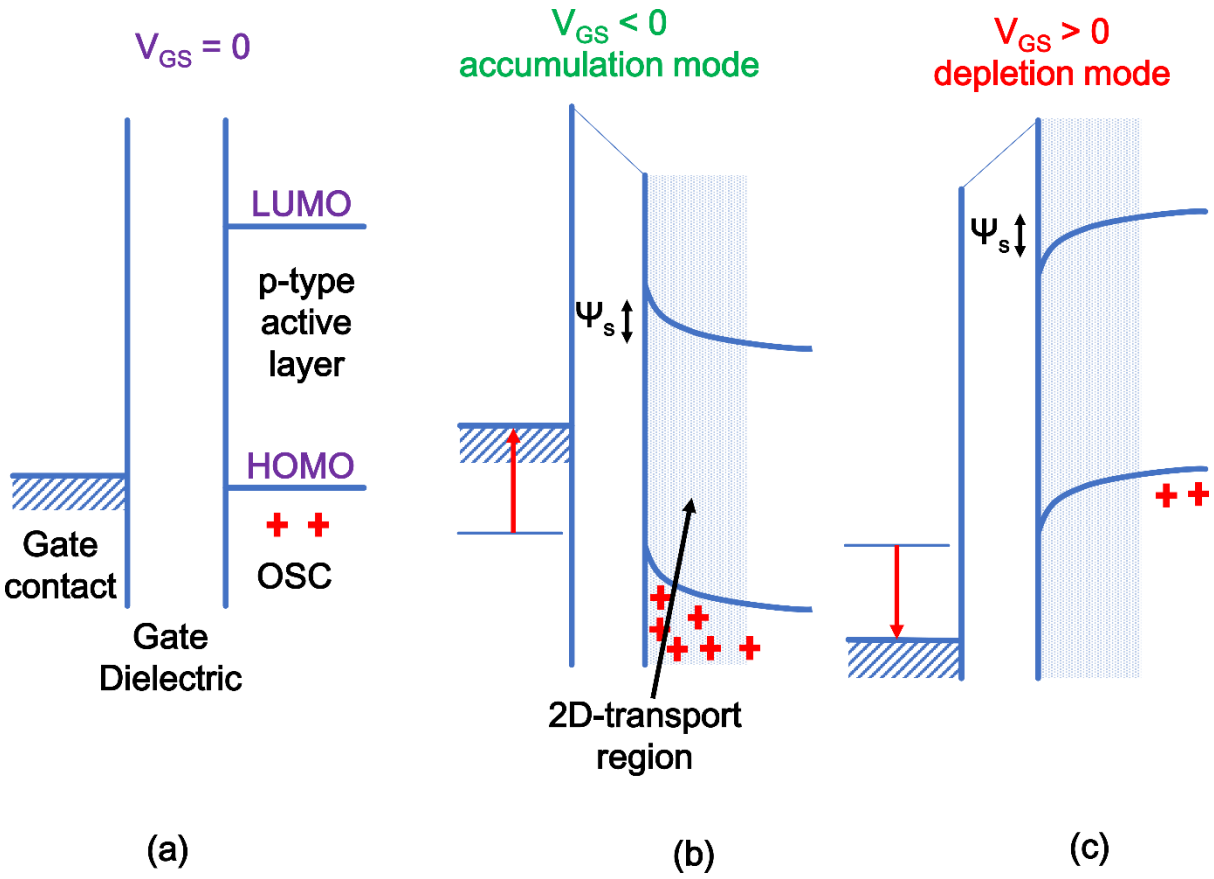

Figure 8, Band structures showing the distribution of holes and the energy level alignment across the metal–insulator–(p-type) semiconductor structure at different gate voltages. (a) zero gate bias (V_{GS} = 0), (b) accumulation (V_{GS} < 0) and (c) depletion (V_{GS} >0) modes.[29] The arrow points towards the region of the accumulated charges at the interfacial channel region where 2D charge transport is confined.

In Figure 8a the band diagram of the metal gate, the insulator (gate dielectric) and OSC are depicted in the absence of a gate bias (V_{GS} = 0). In this condition no band bending (of the HOMO and LUMO levels) occurs which results in the alignment of the Fermi levels of the semiconductor and gate electrode. When in the off state the high resistance of the OSC results in a low I_{DS}. Any transport that does occur is three dimensional (3D) and a result of charge carriers present in the bulk of the OSC film. The presence of any charge carriers in the semiconductor at trace level is a result of doping due to impurities or structural defects that can be hard to control.

The application of a voltage causes the occupancy of the local energy levels to be bent. When a negative gate bias is imposed (V_{GS} < 0) the Fermi energy levels are raised causing upward band-

bending in the OSC (Figure 8b). This generates a potential well and allows the accumulation and confinement of positive charges at the insulator/OSC interface to form a highly conductive channel between the source and drain electrodes.[29] The confinement of charge carriers at the interface (typically within <5nm of the surface) results in two dimensional field-induced transport. The 2D-transport region is highlighted in Figure 8b and forms a conductive path perpendicular to the plane of the paper.[57] This is termed the *accumulation mode* and the I_{DS} current increases when a greater negative gate bias is applied due to the accumulation of a larger charge density bias.

In contrast, when the Fermi level of the electrode is lowered when a positive bias ($V_{GS} > 0$) is applied, causing the bands of the semiconductor to bend downwards (Figure 8c). This results in the depletion of positive charges in the OFET channel region as positive charges are forced towards the OSC bulk and the I_{DS} flow of current is reduced by several orders of magnitude relative to the on-current due to the very low charge density, this is called the *depletion mode*.[29]

1.3.5.2 Role of charge injecting electrodes

One of the key interfaces of semiconductor device is the junction that forms between the semiconductor and a metal (the source and drain electrodes) and its role in the injection of charge carriers into the conducting channel. The efficiency of charge injection is mainly determined by the relative alignment between the work function of the electrode contact (WF) and the HOMO or LUMO energy level of the OSC to which the charge carrier is being injected into. Therefore, the energy level alignment at the metal/OSC interface and the magnitude of any energy misalignment is important in guiding the appropriate choice of contact material and ensuring efficient device operation.

Typical semiconductors of interest in organic electronics have LUMOs and HOMOs in the range of 2–4 eV and 4.5–6.5 eV, respectively. In p-type devices the metal WF aligns with the HOMO and in n-type devices the WF aligns with the LUMO. Ambipolar operation requires the WF lie in between the HOMO/LUMO with a small band gap in order to minimise the injection barrier to both. Optimal charge injection occurs at the junction when the work function of the metal electrode is exactly aligned with the HOMO/LUMO level and an ohmic contact with low resistance is formed.

In contrast, when the energy levels of the metal and HOMO or LUMO are poorly aligned a non-ohmic contact is formed potential barrier is formed, leading to poor charge injection and an extra resistance in the transistor (contact resistance). The size of the potential energy barrier of an electron forming at either side of this metal/semiconductor barrier is the Schottky barrier height (Φ_B). The contact resistance can be measured by various means including four-point probe

measurement or the transfer line method whereby a zero-channel length device is extrapolated by measuring the resistance of transistors of different channel lengths.

This Schottky–Mott model of Schottky barrier formation provides reasonable guidance for the appropriate selection of injecting electrodes by assessing the relative energy levels of the commonly used metals and OSCs which can be complied in an energy band diagram, example materials including those used in fabricated devices are shown in Figure 9.

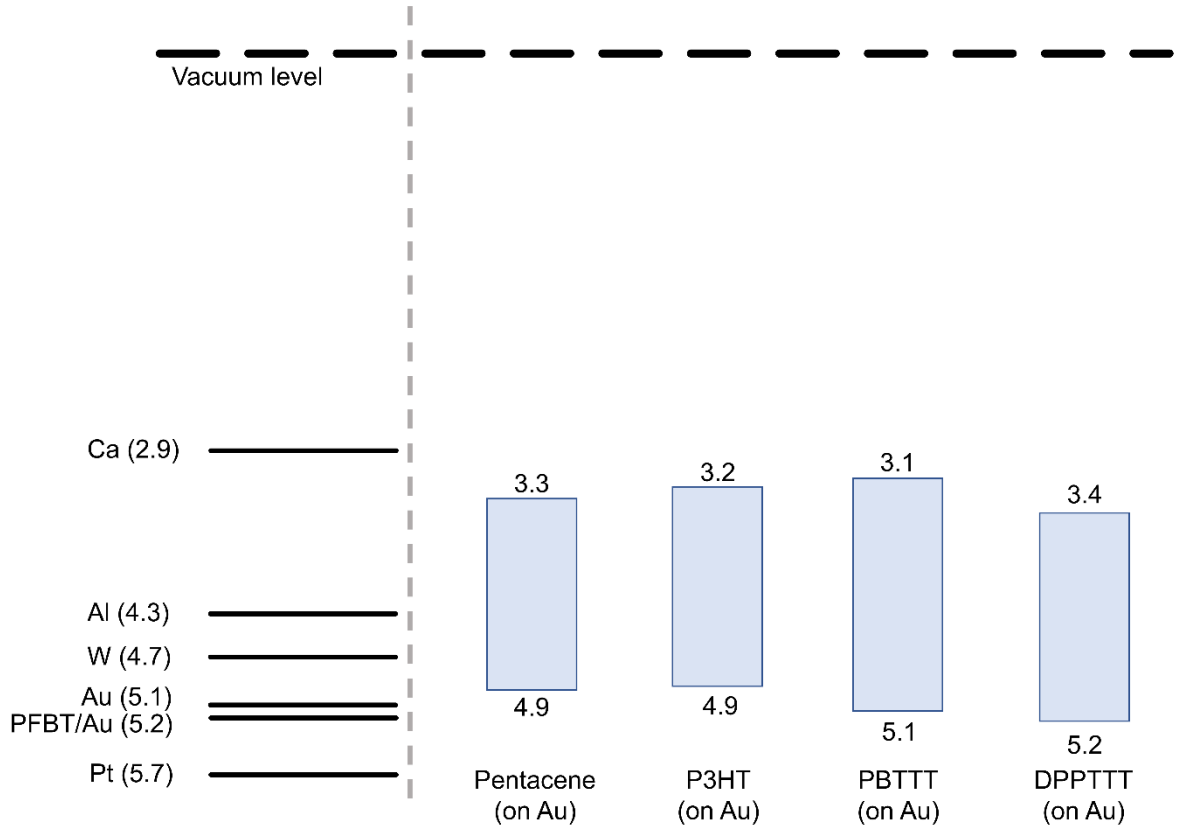

Figure 9 A diagram showing the work function of several metals and the HOMO/LUMO levels of several p-type organic semiconductors relative to the vacuum level in eV.[41]

Metallic contacts are the most frequently used electrodes due to their chemical stability, well-known properties and reproducible processing. Examples include gold, silver, copper, platinum, calcium and aluminium. Gold is the most frequently used electrode contact metal as its work function (4.8-5.1 eV) is closest to the HOMO of most p-type organic materials (4.8-5.3 eV), allowing more efficient of accumulation/injection of charges with minimal injection barrier.[41] Additionally the high environmental stability makes it ideal for stable aqueous operating devices.

The metal thin films used as electrodes are commonly deposited by physical vapor deposition (PVD) techniques such as sputtering, thermal and e-beam evaporation under high vacuum. Electrode

patterning can be achieved for PVD methods by several lithographic techniques such as photolithography, e-beam lithography and stencil (shadow mask) lithography. In pursuit of developing low-cost processing techniques and improved flexibility all-organic and solution processable materials for use in printable devices have also seen use as electrode materials in OFET devices, such as metal particle inks, PEDOT:PSS, carbon nanotubes and graphene.[58]

Chemical modification of the metal contacts can also be used to create conditions for more favourable charge injection into the organic semiconductor, shifting the work function of the electrode and/or influencing the semiconductor morphology. Chemical modification of the electrodes can include metal oxides such as titanium oxide or the formation of SAMs.

A variety of SAMs have been applied for the tuning of the work function, for example thiol-based small molecules. The thiol based SAMs spontaneously adhere to the metal surface due to the formation of covalent bonds between thiol group and metals such as gold. The surface potential and therefore work function is modified (ΔWF) because the SAM changes the local electric field with the contribution of two dipoles; the surface dipole produced by the intrinsic dipole of the molecules that make the SAM layer (ΔV_{SAM}) in addition to the formation of an interfacial dipole created as thiol group binds to the gold surface (BD).

Equation 6

$$\Delta WF = \Delta V_{SAM} + BD$$

The size of the work function shift of the electrode is related to the degree of order and orientation of the formed SAM, in addition to the magnitude and sign of the dipole induced by the SAM. In general alkane terminated SAMs are used to decrease the work function and halogen terminated SAMs are used to increase the work function. An example of this is pentafluorobenenethiol (PFBT) SAM treatment of silver and gold source and drain electrodes, use of this SAM results in a more hydrophobic surface which improves the semiconductor morphology on the contacts whilst also modifying the work function of gold (WF PFBT modified gold 5.4 eV) to allow better alignment with the HOMO of OSCs such as DPPTTT therefore reducing the Schottky barrier height and improving charge injection.[59]

1.3.6 Device characteristics and key parameters

An OFET is typically operated by the application of a potential to the devices gate electrode and the drain electrode whilst the source electrode is held at ground (V_S = 0). Therefore, the resulting voltages used to describe the device operation are the gate-source voltage (V_G) and the drain-source voltage (V_{DS}). In the following discussion the use of a p-type OSC is described and the majority charge

carriers are holes. However, the same behaviour would be observed for an n-type OSC but the polarities would be reversed.

Again, consider a metal-insulator-semiconductor (MIS) structure as the model for an interface when a V_G but no V_{DS} is applied. The application of a negative V_G results in the polarisation of the dielectric and an accumulation of holes in the OSC at its dielectric interface, which are injected from the grounded electrode (source). The density of charge carriers in the channel is proportional to the capacitance of the insulator C_i (dielectric) and the magnitude of the applied field (V_G), i.e. the 'field effect'.

The charges that are induced in the channel must first fill deep trap energy states so that the subsequently injected charges can be mobile and hence establish a conducting transistor channel, the minimum potential required to achieve this is the threshold voltage (V_T).[60] The deep lying traps can result from crystal defects, impurities and interfacial roughness. In order to fill the deep trap sites the applied gate voltage (V_G) must exceed the threshold voltage (V_T), therefore the effective gate voltage (also known as overdrive voltage) (V_G - V_T) must be greater than zero. Hence, when the (V_G - V_T) < 0 the device is effectively "off" and when the (V_G - V_T) > 0 the traps are filled, and charges can accumulate and the device turns "on". Once a V_{DS} is applied the accumulated mobile charge carriers can flow between the source and drain and the drain current (I_D) can be measured. The relationship between the distribution of charge carrier within the conduction channel in different operating regimes and the impact on the drain current with V_{DS} at a fixed gate voltage is depicted in Figure 10.

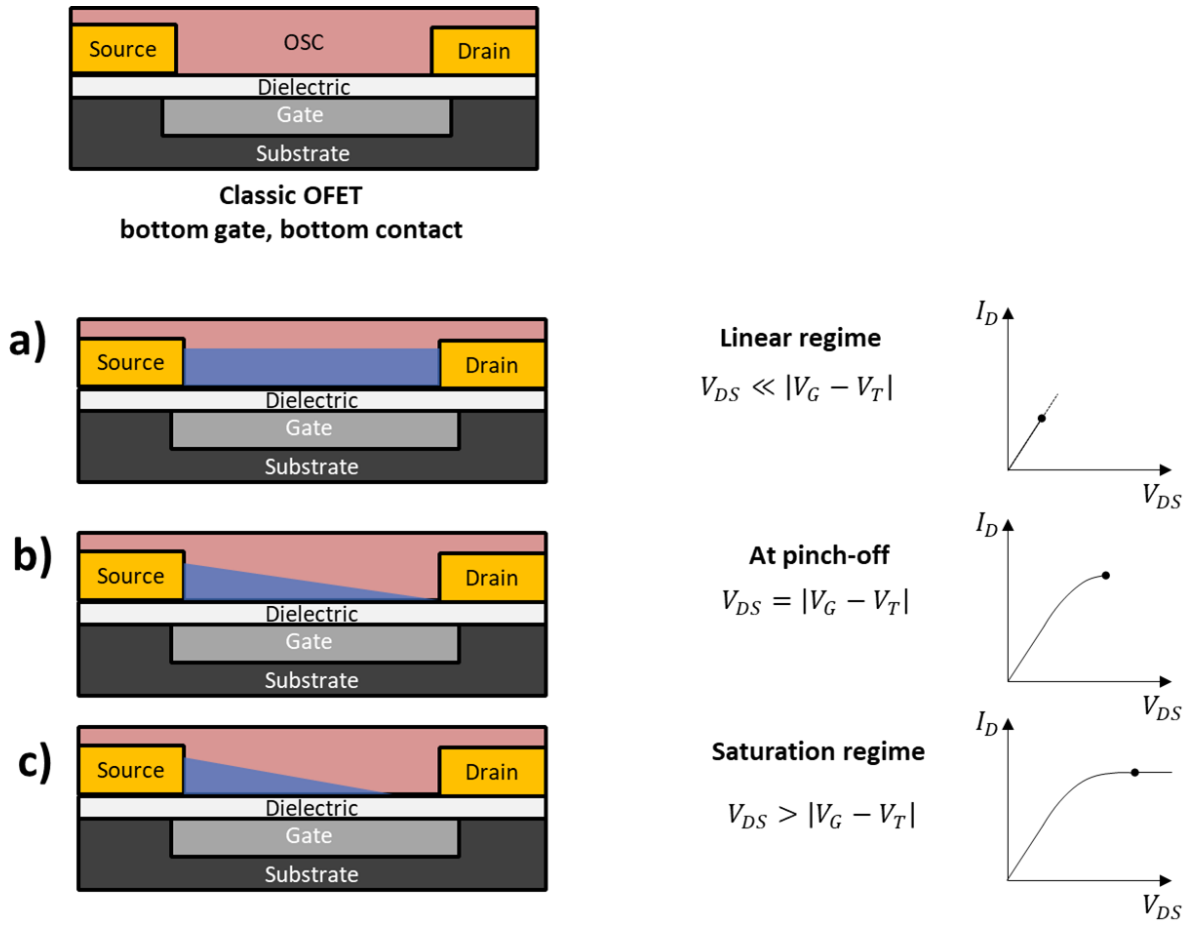

Figure 10 Schematic structure of a classic BGBC OFET showing the shape of the conductive channel in blue, together with the evolution of a current-voltage characteristic for the device with fixed V_G in different operating regimes: a) in the linear regime; b) at pinch-off; d) in the saturation regime.

When V_{DS}=0 a uniform distribution of charge carrier concentration is present in the transistor channel. The application of a small source drain voltage (V_{DS} << $|V_G - V_T|$, Figure 10a) produces a linear gradient of charge density across the channel (charge carriers being present across the entire conducting channel) and the drain current increases linearly with V_{DS}, this is called the *Linear regime*.

As V_{DS} increases and approaches the value of V_G, the interaction of the two potentials results in a change in the shape of the conductive channel and a non-linear I_{DS}-V_{DS} relationship develops at the on-set of the saturation regime. A point is reached when $V_{DS} = |V_G - V_T|$ (Figure 10b) and the channel is "*pinched off*" by the formation of a region near the drain contact that is depleted of free charge carriers as 2D confinement of charges is lost.[61] A space-charge-limited saturation current I_{DS}^{Sat} is still able to flow across this narrow depletion zone as the applied electric field can move charge carriers from the pinch off point to the drain electrode. Further increasing the V_{DS} means the increased potential forcing the movement of charge carriers between the source and drain is offset by the increasing the size of the depletion zone. Therefore, the current saturates towards a limited value (I_{DS}^{Sat}) as $V_{DS} > |V_G - V_T|$, Figure 10c (*Saturation regime*).

Current voltage characteristic relationships in FETs can be represented as chart or graphs (*I-V* curves) depicting I_{DS} current measured as a function of V_{DS} at several different fixed V_G gate voltages producing individual *I-V* curves that are collated in the *output characteristic*. A typical example for a DPPTTT p-channel OFET is shown in Figure 11; the linear regime at low V_{DS} and saturation regime at high V_{DS} are evident.

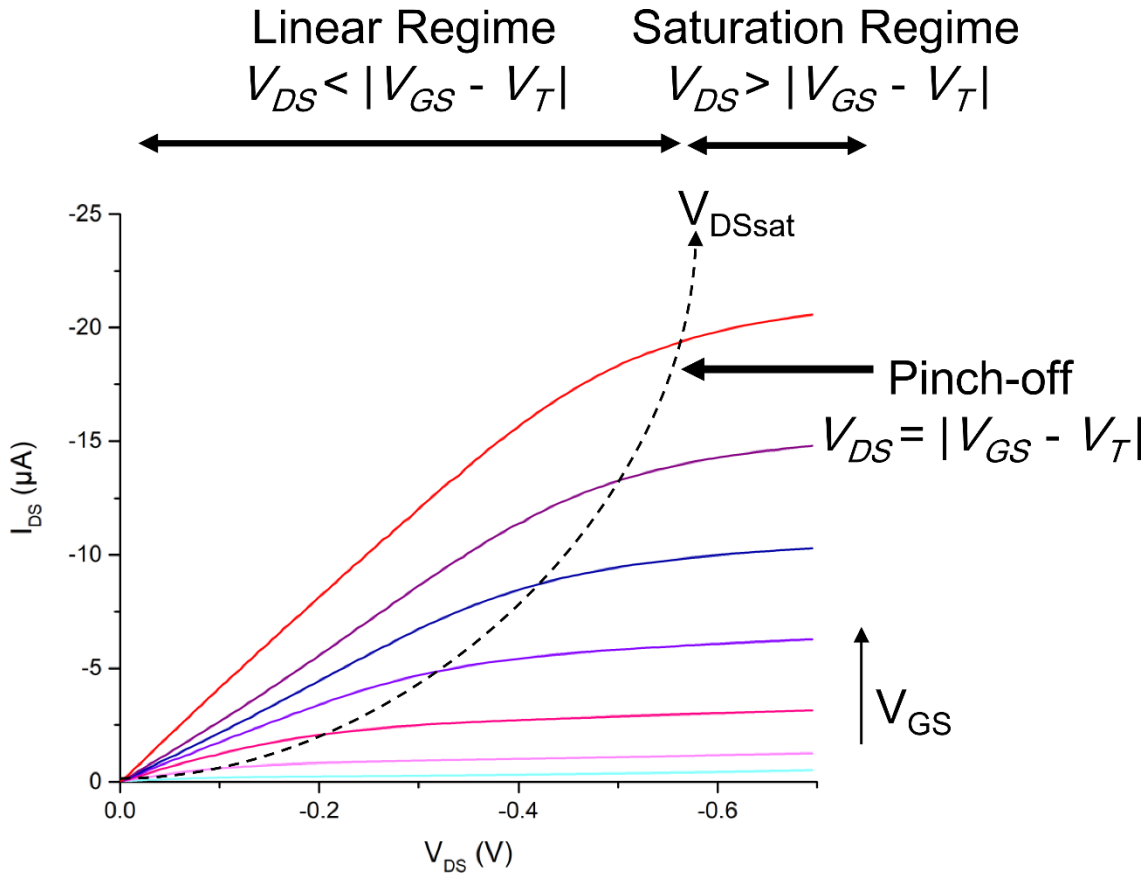

Figure 11 Current-voltage (I_{DS}-V_{DS}) curves of DPPTTT p-channel OFET at different V_{GS} gate voltages. The linear region ($V_{DS}<V_{GS}-V_T$), saturation region ($V_{DS}>V_{GS}-V_T$) and pinch-off at $V_{DS}=V_{GS}-V_T$ are labelled.[29]

The current-voltage characteristics can be approximated for the different operating regimes assuming the *gradual channel approximation* and this gives rise to the following simplified equations:

Equation 7 $\quad$ *linear regime* $\quad V_{DS} \ll (V_G - V_T) \qquad I_{Ds}^{lin} = \frac{W}{L}\mu_{lin}C_i\left(V_G - V_T - \frac{V_{DS}}{2}\right)V_{DS}$

Equation 8 $\quad$ *saturation region* $V_{DS} > (V_G - V_T) \qquad I_{Ds}^{sat} = \frac{W}{2L}\mu C_i(V_G - V_T)^2$

The gradual channel approximation model applies when the electric field between the source and the gate is much greater than the electric field between the source and the gate. This is usually

satisfied when $\frac{L}{d} \geq 10$, although short channel effects can be observed when the channel length is too small and the observed device behaviour deviates from that described by above.

The device behaviour can be further investigated in a "transfer characteristic" by measuring the I_{DS} current measured as a function of V_G at a constant V_{DS} in either the linear ($V_{DS} < |V_G - V_T|$) or saturation regime ($V_{DS} > |V_G - V_T|$). Equation 7 and Equation 8 can describe the I_{DS} relationship to V_G at a fixed V_{DS} and through the manipulation of the equations several useful parameters can be extracted.

The measurement of a device transfer characteristic allows the extraction of the electrical figures of merit that describe the device behaviour and analysis of the device performance can be achieved. The principal parameters of interest are the threshold voltage (V_T), field effect mobility (μ) ratio between max current (I_{on}) and min current (I_{off}) ($I_{On/Off}$) and the method of extraction for a device operating in the saturation regime is shown in Figure 12.

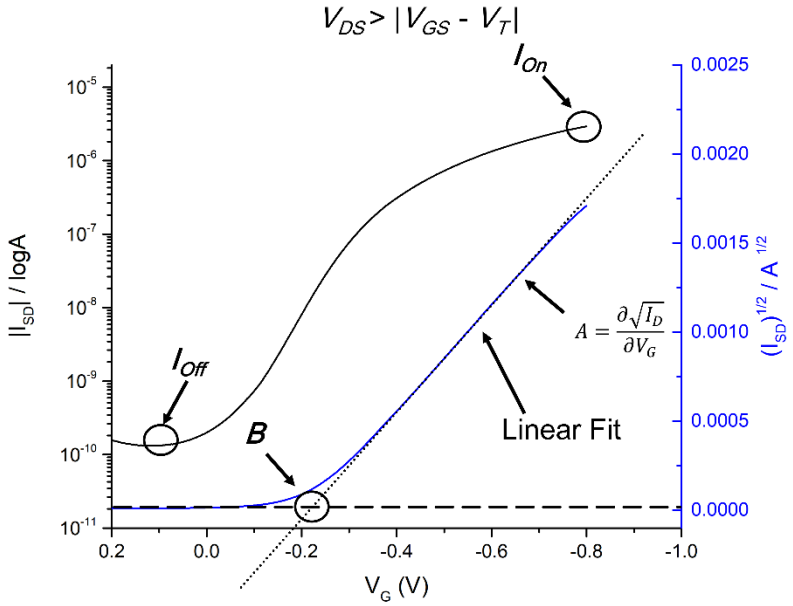

Figure 12 Transfer characteristic of a typical p-type EGOFET device showing the extractable parameters in the saturation regime. I_{SD} (black – solid lines) is plotted in a semi-log scale (left) highlighted are I_{On} and I_{Off} used in calculating the I_{On}/I_{Off} ratio. A linear fit to I_{SD} plotted in a square root scale (blue – right) gives the gradient (A) and intercept (B) from which the mobility (μ) and threshold voltage (V_T) are calculated through Equation 9-5.

The I_{DS} at the maximum V_G during the transfer sweep signifies the maximum current in the transfer hysteresis (I_{on}) and I_{DS} min signifies the lowest current during the transfer forward sweep and when the device is off (I_{off}). The ratio between max current (I_{on}) and min current (I_{off}) gives the on/off current ratio ($I_{On/Off}$). A large on/off current ratio allows the device to present a clear distinction in the on and off states allowing the OFET to behave as an on/off switch and $I_{On/Off}$ >10^6 is considered

good. The switch between on and off performance is indicative of the change between the distinct conduction regimes of the 2D FET transport (on) and 3D bulk transport (off).

I_{off} can be minimised by a number of techniques including: appropriate choice of dielectric material, reduction in the gate leakage (for example by patterning of the gate and the semiconductor layer), reducing the bulk conductivity in the OSC material which can be a result of unintentional doping. Equation 7 and Equation 8 highlight the multiparametric relationship that can control the magnitude of I_{on}. The factors influencing I_{on} can therefore include the operating voltages used in the transfer characteristic, the charge carrier mobility of the semiconductor used, the gate dielectric capacitance, the threshold voltage and density of trap states at the semiconductor-insulator surface.

The saturation regime as described in Equation 8 shows that the square root of the drain current is directly proportional to V_G. The characteristic device parameters, field effect mobility of holes (μ) and threshold voltage (V_T), can therefore be extracted from the transfer characteristics in the saturation regime from the slope (A) and intercept (B) of $I_d^{1/2}$ vs V_G plot (Figure 12, blue line), as shown by the manipulation of Equation 9-Equation 11.[29]

Equation 9 $$\sqrt{I_{DS}} = \sqrt{\frac{W}{2L}\mu C_i}V_{GS} - \sqrt{\frac{W}{2L}\mu C_i}V_T = AV_{GS} - B$$

Equation 10 $$\mu = \frac{2L}{WC_i}A^2$$

Equation 11 $$V_T = -\frac{B}{A}$$

The charge carrier mobilities in different operating regimes can be expressed as:

Equation 12 $$\mu_{lin} = \frac{L}{C_i W V_{DS}}\frac{\partial I_D}{\partial V_G}$$

Equation 13 $$\mu_{sat} = \frac{2L}{WC_i}\left(\frac{\partial\sqrt{I_D}}{\partial V_G}\right)^2$$

In the linear regime, the drain current is directly proportional to V_G, therefore the mobility in the linear regime (μ_{lin}) can be extracted by the gradient of I_D vs V_G at constant V_{DS} as shown in Equation 12. In an ideal device the values calculated for mobility in the linear regime (μ_{lin}) and saturation regime (μ_{sat}) would be the same. However, a significant degree of contact resistance will cause a reduction in the effective V_{DS}, as a result the observed μ_{lin} can be drastically reduced because V_{DS} is relatively small when operating in the linear regime. Contact resistance is particularly important in short channel devices operating at a low V_{DS}.

As described above V_T is the minimum voltage required to turn a device 'on' and is dependent on a variety of factors including: the semiconductor and dielectric used, impurities and particularly on the density/number of trap sites that must be filled by an applied V_G for free charge carrier to contribute to the current.

Equation 14 $V_T = V_{FB} + \frac{qp_0 d_s - Q_i}{C_i}$

V_{FB} flat-band voltage, q charge of each charge carrier, p_0 trap density of semiconductor bulk and semiconductor/dielectric interface, Q_i is the interface charge density, d_s thickness of semiconductor film and C_i capacitance per unit area of gate insulator. Therefore in an ideal trap-free OFET V_T is dependent on the device materials used, summarised by their contribution to V_{FB}; where the work function of gate metal (WF_m) and the ionisation potential (I_p) of a p-type OSC and is broken down by:[62]

Equation 15

$$V_{FB} = WF_m - I_p$$

The threshold voltage dependence on work function (WF_m) of the gate electrode materials is well-established amongst inorganic transistors gated by dielectrics.[61] Work functions of electrode materials are typically measured by either ultraviolet photoemission spectroscopy or capacitance-voltage (*C*-*V*) measurements. Variation of the gate work function or ionisation potential of the OSC layer produces a voltage shift and can be used a sensing parameter as discussed in section….

Additionally, the V_T provides an indicator of the operational voltage of the device, a V_T close to 0 V is desirable for low power applications. The threshold voltage can be reduced by increasing the gate capacitance and therefore increasing the number of charges induced at lower voltages, this is the main reason for the low voltage operation of electrolyte gated OFETs. The incredibly high gating capacitance of the water significantly reduces the V_T close to zero allowing the operation of the device to within the electrochemical window of water (further discussed in section …). It is also of note that when organic devices are operated for significant periods of time a drift in the V_T is generally observed and this is termed bias stress.

When analysing the transfer characteristic, it is often important to investigate the occurrence of a device hysteresis. A device hysteresis is a deviation from ideal behaviour where a significant difference is observed between the forward and reverse voltage sweeps of a current characteristic. This is usually due to the formation of interfacial traps which are held on the forward or reverse sweep or can be due to the use of highly polar dielectrics.

Another figure of interest is the subthreshold slope (*S*), a measure of how quickly a device turns from the off to the on state, this is the quantification of the rate of change in I_D as V_G increases at a fixed V_{DS}. can also be calculated from the following:

Equation 16

$$S = \frac{\partial V_G}{\partial(\log_{10}(I_D))}$$

The subthreshold slope is expressed in units of V/decade therefore expressing the increase in V_{GS} to cause a 10-fold increase in I_D. It is dependent on the capacitance of the gate dielectric and the trap sites present at the interface. A steeper slope signifies a faster transition from the off to on state (this usually happens in devices with a low concentration of shallow traps) and would produce a smaller/larger value for *S*, this is desirable for applications requiring with fast switching speeds.

1.3.7 EGOFET Operation the role of the EDL

As water is an electrolyte, therefore it can be electrochemically oxidised and reduced as shown in Figure 13. These reactions limit the potential that can be applied to the electrodes of OFETs in direct contact with water. Electrolysis begins when a potential difference between source and drain electrodes exceed 1.23 V, therefore establishing the electrochemical window of water (Figure 13). Under such conditions water acts as a conductor and a significant Faradaic current can be measured.[63] Therefore in order to enhance device performance satisfactory operation under 1.23 V is necessary.

Oxidation	$H_2O \rightleftharpoons 2H^+ + {}^1/_2O_2 + 2e^-$	0.571 V
Reduction	$2H_2O + 2e^- \rightleftharpoons H_2 + 2OH^-$	-0.658 V

Figure 13 Electrochemical reactions of water. Standard potentials *vs.* Standardised Hydrogen Electrode (SHE). The difference of these two voltages provides the electrochemical window of water as 1.23 V

Device operation in aqueous media is of critical importance for application in biomedical diagnostics. For such applications the distinct advantages of EGOFETs and ISOFETs make them particularly attractive.[63] In a conventional ion selective OFET or FET (ISFET) the analyte is in direct contact with the solid gate dielectric and the electric field is generated by a metallic bottom gate.[63] However in an EGOFET the organic semiconductor and analyte are in direct contact and the accumulation zone of charge carriers is at the OSC/solution interface. The formation of an electrical double layer (EDL) of very high capacitance (C_i ~ 1- 10 µF cm^{-2}) at the electrolyte-semiconductor interface enables device operation at low voltages, where source-drain currents of a few µA-nA are of more than sufficient

amplitude for further signal processing.[64,65] The inversely proportional relationship between threshold voltage and gating system capacitance established in Equation 14 ($V_T \alpha \frac{1}{C_i}$) results in a significant reduction in V_T to within the electrochemical window of water due to the large capacitance of the EDL, therefore enabling the required low voltage operation. Operation at low voltages becomes increasingly important for stability in aqueous media and to avoid ionic transport through the analyte solution that would limit device performance.[63,66] Furthermore, the direct contact between OSC and water enables water gated OFETs (WGOFETs) to avoid proton trapping and hysteresis allowing stable operation at low voltages.[25,61]

In the case of a p-type EGOFET, positive polarisation of the gate produces an EDL at the gate composed of electrons within the metal and cations in the electrolyte, whereas electrolyte anions and semiconductor holes form the EDL at the semiconductor interface.

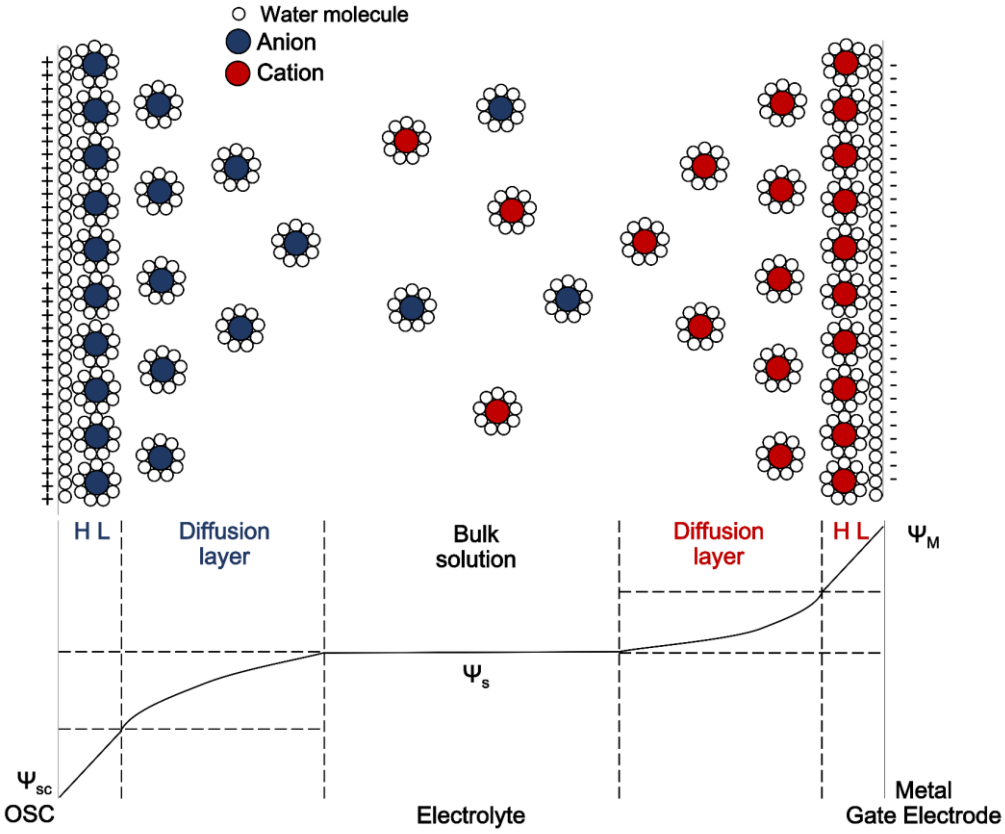

Figure 14 Illustration of the ion distribution in the Stern model. Showing the Helmholtz layer (HL), the Gouy-Chapman diffuse layer and the bulk electrolyte (above), and spatial distribution of the potential between the gate and the semiconductor in an electrolyte-gated transistor (below)[28]

The EDL developed in the Stern model is shown in Figure 14, and combines aspects of the Helmholtz model with the Gouy-Chapman model, resulting in an EDL within the electrolyte composed of two

layers, the Helmholtz layer (internal Stern layer) and the Gouy-Chapman diffuse layer. [28] The Helmholtz layer consists of a single layer of solvent molecules in direct contact with the metal or semiconductor and a single layer of solvated ions. The diffuse layer consists of free ions in solution capable of migration under electrostatic interaction and thermal motion producing a charge distribution of ions as a function of distance from the interface. As the distance increases from the interface (gate or semiconductor) towards the bulk, the excess of ions decreases. As a result, the potential drop at the interfaces only occurs within the double layer. The flow of current across the interface is prevented by the double layer acting as a dipole to generate an electrical field across the interface. In this configuration the EDL functions as a capacitor, where charge separation is minimised by a very thin double layer resulting in very high capacitance values which enables low voltage operation of the OFET. Due to the close proximity of the charged layers a large capacitive coupling is produced. A small difference in potential between the liquid and semiconductor channel induces a significant change in charge density, hence allowing low voltage operation. Additionally, by producing a higher charge density, higher mobility and output currents can be achieved.

Capacitive coupling of the interfaces makes the gating system equivalent to two capacitors in series and the biorecognition elements can be introduced to either interface, to create a third element within this series (Equation 23). The overall gating system capacitance is then controlled by the introduction of this third and smallest capacitor to the series. This capacitance is very sensitive to surface changes which occur upon analyte interaction, allowing for detection of both charged and neutral ligands.

1.3.8 Applications

Although organic transistors typically do not compete with silicon transistors in terms of performance, they still find useful application in devices where inorganic materials are unfeasible or not cost effective. OFETs have traditionally found their main application in display and integrated circuit technology;[67,68] however they have also proven to be excellent candidates for use in chemical and biological sensing applications such as environmental monitoring,[69] detection of explosives,[70] in-situ medical diagnostics,[71] drug delivery[72] and food storage.[73]

The excellent biocompatibility of the organic components lends itself well for use in biomedical applications. In this context, the potential for easy modification with biological components coupled with the chemical similarity of building blocks means organic materials outperform inorganic counterparts significantly. Additionally, the chemical and physical properties of organic compounds can be tuned in order to maximise the selectivity and sensitivity to target analytes.

Moreover, the inherent signal amplification of OFET-based sensors leads to higher sensitivity in comparison to alternative sensing platforms. OFET-based sensors combine the function of a transducer and amplifier within one device whilst benefiting from well-established miniaturisation methods and integration into complex circuits for further signal processing. OFET-based sensors have shown application in the detection of wide variety of analytes ranging from small molecules, vapours to ions and complex biomolecules. Of particular interest in this project is their application in the detection of biomarkers. Their application for sensing has been comprehensively reviewed by Torsi *et al*.[29]

1.4 OFETs as Biosensors in aqueous environments

1.4.1.1 Sensing in OFETs

When applied to sensing applications the OFET current response is modified upon exposure to an analyte which interacts with one of the device interfaces or diffuses into the semiconductor. Depending on the OFET device architecture several interfaces can be utilised for sensing: i) the electrode/semiconductor; (ii) dielectric/semiconductor; (iii) organic/organic interfaces such as grain boundaries; (iv) semi- conductor/ambient interface.[63]

The integration of specific recognition sites into the sensor is essential in allowing the selective detection of target analytes. Various approaches have been used for the immobilisation of recognition elements either at one of the aforementioned interfaces or incorporation directly into the semiconductor film. One of the most popular approaches involves peptide coupling through activation of carboxylic acid groups on the interface surface using EDC/NHS.[74] Functionalised phospholipid bilayers deposited on top of the OSC or gate dielectric have also been proposed as route to surface functionalisation.[75,76] In addition gold-thiol chemistry can be utilised with gold nanoparticles[77] or for directly functionalising the gate electrode.[78]

1.4.1.2 Analysing sensing response in OFET biosensors

As discussed in section 1.3.3, a variety of OFET architectures have been developed and found application in biosensing devices. In order to allow sensing the immobilisation of the biorecognition element to one of the device interfaces is required. The binding of the ligand (analyte) to the bioreceptor (biorecognition element) is a binding event that results in the formation of a biorecognition complex (*R-L complex*). OFET biosensors can transduce the formation of the R-L complex because the electronic properties of the interface where this event occurs are altered and therefore the measured signal and device performance is changed. The location of the functionalised interface plays a fundamental role in determining the electrical parameters that are

altered in sensing in addition to the relevant properties of the analyte such as its electrostatic and electrochemical properties.

The response of OFET biosensors to analytes is typically evaluated by measuring the transfer characteristic of the device, by measuring the I_{DS} vs V_G at a fixed V_{DS} that operates the device in the saturation regime. As OFET biosensors are inherently multi-parametric devices they offer the possibility of simultaneously monitoring the variation of the multiple electrical parameters associated with changes in the measured signal (I_{DS}) due to relationship described in Equation 7 and Equation 8. Therefore, in addition to the measured signal (I_{DS}), the characteristics that are typically also analysed for a sensor response are the field effect mobility (μ), threshold voltage (V_T) and capacitance (C_i).

A transfer characteristic measurement in the saturation regime allows linear interpolation of the $\sqrt{I_{DS}}$ vs V_G curve and extraction of V_T from the intercept and μ*C_i which is equal to the gradient (see section 1.3.6. A representation of the change in measured $\sqrt{I_{DS}}$ vs V_G curves before (blue) and after (red) analyte sensing for different devices (or sensing conditions) is shown in Figure 15. The subscript 0 denotes the values used as the baseline (blank) values from measurement taken in the absence of the analyte (the blue curve).

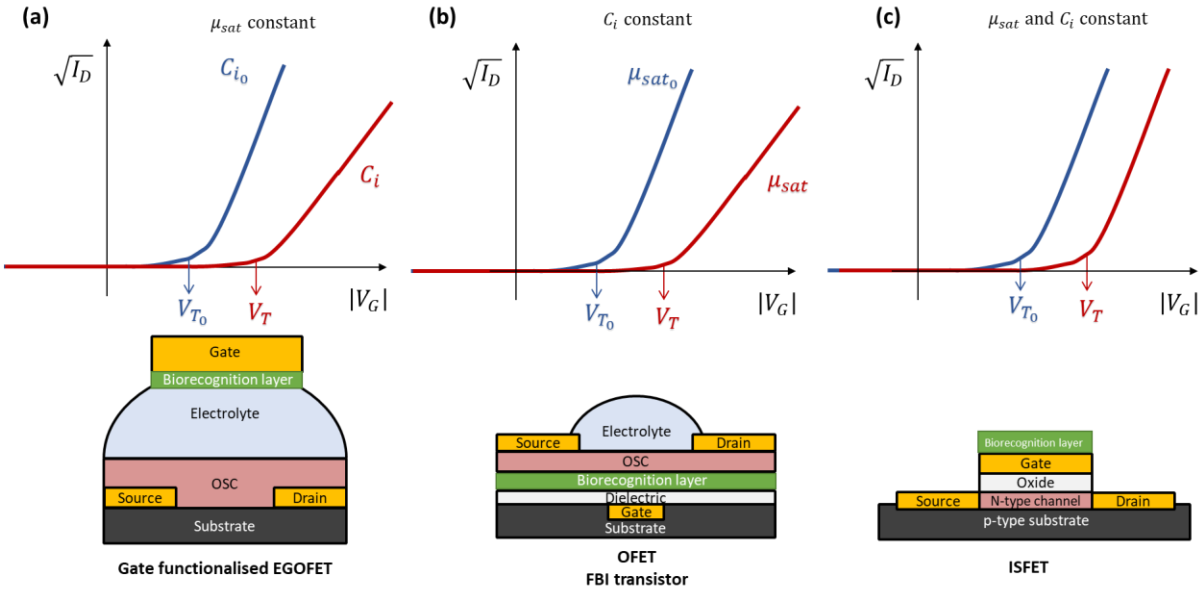

Figure 15 Representation of the change in transfer characteristic and parameters caused by sensing for different FET biosensors. The devices are operating in the saturation regime and the $\sqrt{I_{DS}}$ vs V_G curves represent measurement taken before (blue) and after (red) a binding event. The architecture of each device is shown below. A) An EGOFET device modulated by the change in capacitance of the biolayer and V_T, but μ_{sat} is constant; B) An FBI transistor, the effective gating capacitance remains constant and μ_{sat} and V_T change; C) An ISFET, only V_T varies as μ_{sat} and C_i remain constant.

The change in device characteristic parameters highlighted in Figure 15 depends on the electronic properties altered by the formation of R-L complex during sensing. A change in μ is observed if the formation of the R-L complex affects semiconductor transport. When the R-L complex formation affects the gating capacitance of the system then C_i will change. If the electrochemical potential $\overline{\mu_e}$ of the semiconductor or the metal gate electrode are impacted then a shift in the V_T will be observed. R-L complex formation can impact all the above parameters simultaneously, however some device architectures can allow the parameters to be de-coupled by keeping one or more parameter constant as shown in Figure 15. The decoupling of the parameters that impact on I_{DS} and contribute towards the $\Delta I/I_0$ allows the comparison between the ΔV_T, ΔC_i , $\Delta \mu_{sat}$ to show their relative impact on sensing response.

In the following discussion the examples relate to biosensors that detect the binding of a ligand to a biological recognition element that has been immobilised at one of the device interfaces. However, the same principle and behaviour would be expected for devices sensing the nonspecific adsorption of the ligand to the OSC or gate surface.

A common feature of FET transduction is a biosensing response that produces a threshold voltage shift (ΔV_T) that scales with the logarithm of analyte concentration, such as the ISFET shown in Figure 15c. As previously discussed in section 1.3.6 the V_T is the gate bias required to fill the deep lying traps and enables the device to turn on, it is achieved when the applied gate voltage levels the energy barrier created by the difference between the electrochemical potential of the gate and semiconductor charge carriers ($\overline{\mu_e}$).

The formation of the immobilised R-L complex at the gate interface produces an electrochemical Gibbs free energy for the process ($\overline{\Delta G}$) that changes the electrochemical potential of the gate metal electrons ($\overline{\mu_e}$). The change in $\overline{\mu_e}$ alters the work function of the gate and this results in a shift of V_T due to the relationship described in the equations below:

Equation 17

$$\overline{\mu_e} = \left(\frac{\partial \bar{G}}{\partial n}\right)_{T,,P,n_{j\neq e}}$$

Equation 18

$$\overline{\mu_e} = \mu_e + nF\phi$$

Equation 19

$$\Delta E_F = \bar{\mu}_{e(gate/R-L)} - \bar{\mu}_{e(gate/R)}$$

Equation 20

$$\Delta E_F = -nF\Delta V_T$$

Equation 21

$$\Delta V_T = -\left(\frac{\Delta E_F}{nF}\right)$$

Equation 22

$$\Delta V_T = -\left(\frac{\bar{\mu}_{e(gate/R-L)} - \bar{\mu}_{e(gate/R)}}{nF}\right)$$

The electrochemical Gibbs free energy ($\bar{G}$), differs from the Gibbs chemical free energy (*G*), by the inclusion of effects from the large-scale electrical environment. ΔE_F is the change in electron free energy of the metal-gate acting as the electrostatic contribution to the molar free energy of the R-L complex formation. Where $\overline{\mu_e}$ is the electrochemical potential in J/mol before ($\bar{\mu}_{e(gate/R)}$) and after ($\bar{\mu}_{e(gate/R-L)}$) R-L formation; μ_e is the chemical potential; F is Faradays constant, ϕ is the local electrostatic potential in V, n is the number of moles charges in the phase, ΔV_T is the change in V_T caused by sensing.

Due to the relationship described in Equation 18 $\overline{\mu_e}$ is often dominated by large electrostatic (ϕ) contributions associated with long-range coulombic interactions (10-100 kJ mol^{-1}). This allows typical FET sensors to achieve the sensitive detection of charged species by monitoring ΔV_T. The Gibbs free energy (G) excludes the effects of net charges and monopoles, which are absent in neutral species and accounts for changes in system energy and entropy in the formation of recognition-ligand complex at the interface. ΔG associated with the R-L complex formation is consistent with weaker short-range energies such as dipole-dipole or dispersive interaction involves energies as low as 2 kJ mol^{-1}. The lower energies involved in the detection of neutral species therefore presents a greater challenge in sensors that are solely reliant on ΔV_T for analyte detection.

One method that demonstrated the accurate detection of neutral analytes was reported by Mulla *et al*., they described an EGOFET device that used an odorant binding protein (OBP) based biorecognition layer immobilised on to the gate electrode through a SAM that produces a capacitance-modulated response (Figure 15a).[79]

The gating system capacitance C_i can be described as sum of three smaller capacitances in series. In an EGOFET such as Figure 15a the capacitance series are those that result from the electrical double layer (EDL) of the electrolyte at its interfaces with the gate (C_{EDL-1}), OSC (C_{EDL-2}) and biorecognition layer (C_{Bio}) to give:

Equation 23

$$\frac{1}{C_i} = \frac{1}{C_{EDL-1}} + \frac{1}{C_{EDL-2}} + \frac{1}{C_{Bio}}$$

The bioreceptor layer capacitance (C_{Bio}) can be modelled as a planar capacitor and described by:

Equation 24

$$C_{Bio} = \varepsilon_0 \varepsilon_r d^{-1}$$

with ε_0 and ε_r as the vacuum and relative permittivity, respectively and *d* the distance between the capacitor plates. A typical protein system has ε_r=3 and *d* is the thickness of the monolayer of proteins used in the recognition layer, the capacitance per unit area of most biolayers can therefore be estimated as being in the magnitude of C_{Bio}~0.1 µF cm^{-2}.

As an example, a pOBP-SAM attached to a gold gate electrode with a height of pOBP-SAM *d*~4.22 nm gives an estimated capacitance of C_{Bio}~0.63 µF cm^{-2}. To give further context the reported capacitances per unit area for the Au-gate/water interfaces is C_{EDL-1}~40 µF cm^{-2} and typical water/OSC interfaces are C_{EDL-2}~1-5 µF cm^{-2}.[79]

It is evident from Equation 23 that the capacitance is dominated by the smallest capacitance value in the series (C_{Bio}). Therefore, due to the expected relative magnitudes of these capacitances the whole gating capacitance system C_i can be approximated to the smallest value capacitance C_{Bio} ($C_i \approx C_{Bio}$). The model suggests that the capacitance of the biorecogntion layer can control the output current of the device through its relationship with Equation 23, on the condition that parallel parasitic capacitances are minimised.

The use of relative variation to describe the change in device parameter in sensing provides a robust parameter that normalises device-to-device variation therefore improving the reproducibility of the response. The relative variation of the device current I_{DS} is $\Delta I/I_0$ given by:

Equation 25

$$\frac{\Delta I}{I_0} = \frac{I - I_0}{I_0}$$

The EGOFET configuration in Figure 15a means that the analyte binding event occurs sufficiently far from the semiconductor that the mobility is unaffected and µ remains constant. The change in V_T therefore transduces the electrostatic changes that occur during the analyte detection by probing the change in electrochemical potential ($\overline{\mu_e}$) at the gate electrode. Therefore, the individual contributions from the different performance features can be decoupled when second-order terms

are disregarded (because they are small and have negligible contribution) allowing the response $\Delta I/I_0$ to be expressed as:

Equation 26

$$\frac{\Delta I}{I_0} = \frac{\Delta C_i}{C_{i_0}} - 2\frac{\Delta V_T}{\left(V_G - V_{T_0}\right)}$$

where μ is presumed to be constant and C_i is dominated by the C_{Bio}. Therefore if $V_T \ll V_G$ and $\Delta V_T \ll V_G$ then Equation 26 can be approximated as:

Equation 27

$$\frac{\Delta I}{I_0} \cong \frac{\Delta C_{Bio}}{C_{Bio_0}}$$

This theoretical reliance on a change in capacitance was reinforced by the experimental values reported in the OBP paper, when the relative variation for V_T and C_i at the saturation of sensing response was compared. The work showed that $F(\Delta V_T) \cong 0.1$, whereas $\frac{\Delta C_i}{C_{i_0}} \cong 0.5$ this showed that the sensing output current was more heavily moderated by the C_i term signifying that the device was operating as a capacitance-modulated transistor sensor.

Mulla *et al* hypothesised that the formation of the R-L complex produces subtle conformational changes in the bioreceptor that alter the dielectric properties of the biorecognition layer.[79] Despite the small magnitude of the changes in C_{Bio} the EGOFET is able to transduce them effectively even if no net charges occur allowing the detection of uncharged analytes. This is because instead of sensing relying on a change in $\overline{\mu_e}$ and the change in output current is more heavily dependent on changes in capacitance at the biorecognition layer. The small changes in ΔC_i can be transduced, with high signal to noise as a result of the transistors high current gain.

In contrast, in the functional bio-interlayer (FBI) transistor sensor the capacitance remains constant throughout sensing. In the FBI-OFET geometry an antibody interlayer (bio-recognition layer) is sandwiched between the OSC (above) and the silicon oxide (SiO_2) insulating dielectric (beneath) in a bottom gate device. The analyte can percolate through the voids between OSC grain boundaries to reach the functionalised OSC/gate dielectric interface. There is a direct interface between the biorecognition layer and the OSC electric channel, R-L complex formation produces a direct impact on the charge transport and μ parameter can transduce the analyte interaction.

For the FBI-OFET device shown in Figure 15b, the gating system capacitance C_i can be described as sum of three smaller capacitances in series these are the capacitance per unit area at: the semiconductor (C_{OSC}), dielectric (C_{Diel}) and the immobilised biological layer (C_{Bio}) to give:

Equation 28

$$\frac{1}{C_i} = \frac{1}{C_{OSC}} + \frac{1}{C_{Diel}} + \frac{1}{C_{Bio}}$$

In the FBI-OFET the capacitance of the thick SiO_2 dielectric layer is in the nF cm^{-2} range making it significantly the smallest value in the series and the dominant value in the overall gating capacitance. As a result, in the FBI device system C_{Diel} and the overall gating capacitance C_i remains constant as it which is unaffected by the analyte binding. The device is therefore able to probe the impact of detection in the biolayer on the μ (semiconductor transport), whilst the V_T can again transduce the electrostatic changes that occur during the interaction. This is valid for the FBI device where the assumption is made that C_i is constant and the following relationship holds:

Equation 29

$$\frac{\Delta I}{I_0} = \frac{\Delta \mu}{\mu_0} - 2\frac{\Delta V_T}{\left(V_G - V_{T_0}\right)}$$

An ISFET sensing device is shown in Figure 15c, this is a MOSFET device with a functionalised top gate electrode as shown, also has the gating capacitance system described in Equation 28. In this device the low capacitance of the inert oxide dielectric layer is again the smallest in the series, resulting in a constant capacitance. Additionally, as the semiconductor shares no interfaces with the biorecognition layer it will be unaffected by the analyte binding and μ will also remain constant. Therefore, analyte detection is reliant only on the change to the gate electrons $\overline{\mu_e}$ producing a shift in the V_T. For this reason, ISFETs are usually only employed for the detection of charged analytes.

EGOFET sensors do not require a reference electrode. In an EGOFET the Faradaic current generated by the reference electrode depolarises the EDL, and removes the capacitive series that enables the EGOFET sensing to be driven by changes in capacitance of the biolayer (C_{Bio}). Therefore, EGOFET biosensors perform better with a polarisable electrode, provided that electrochemical processes are avoided within the V_G potential window that the device operates in.

1.4.2 OFETs sensing in the dry state

Through the immobilisation of biological recognition elements the classic OFET architecture (as shown in Figure 6) can be applied to biosensing. For example Yan *et al*. developed bottom gate, bottom contact devices where probe DNA strands where immobilised through thiol chemistry onto the source and drain electrodes.[80] Detection was a result of a change in the work function of the drain and source electrodes upon interaction of a complementary DNA strand. However, in this configuration DNA hybridisation was performed before spin-coating the semiconductor (P3HT) on top, making it unsuitable for practical application.

An alternative approach was described by Lim *et al* through integration of the bio-receptor into the semiconducting layer.[81] The device using a biotinylated semiconducting polymer was capable of protein detection (avidin) at micromolar concentrations. Additionally, Maddalena *et al* showed that an insulating layer modified with a sulfate-binding protein deposited on top of the semiconductor was capable of sulfate ion detection.[82]

Whilst the above examples demonstrate the detection of analytes from aqueous solution, drying is necessary following immobilisation in order to allow characterisation. This is a consequence of the high voltages needed to operate the devices limiting their operation to the dry state.

An electrolyte gating medium such as that in EGOFET allows for low voltage operation due to the exceptionally high capacitance achieved which reduces the V_T required for device operation. The electrolyte gating allows the direct detection of solubilised analytes present within solutions used as the gating medium (e.g. blood serum), this is particularly attractive in the field of label-free biosensors.

1.4.3 EGOFETs as biosensors

In the field of low voltage and low power applications the distinct advantages presented in EGOFETs, provides an interesting alternative to devices based on solid dielectrics such as traditional oxide gate insulators, high-k dielectrics and ultrathin organic layers.[83] Recent literature in the field has reported successful label-free sensing of biologically relevant molecules like DNA,[84] enzymes and proteins,[75,85] in addition to investigations into the effects of pH and ionic strength on device performance.[64] Advances in organic transistor-based biochemical sensing in aqueous media in EGOFETs have been excellently reviewed by Kergoat *et al*[28] and Cramer *et al*.[63]

EGOFET sensing requires the interaction of the detected analyte at one of the devices active interfaces, either the OSC/electrolyte or gate electrode/electrolyte surfaces. The innate sensitivity of the unmodified OSC towards an analyte can be used for a sensor, and they typically rely on the

specific affinity between amines and thiophene-based organic semiconductors to gain a device response. This was shown by Algarni *et al*, and these authors demonstrated the specific sensitivity of PBTTT-based EGOFET towards the detection of water borne amines.[86]

However, in order to allow the detection of biomolecules one of the EGOFETs interfaces must be functionalised with appropriate bio-recognition elements, this can be either the gate electrode or OSC channel. This allows the device to benefit from the greater analyte specificity of the immobilised recognition element. Biosensing demands the integration of specific recognition elements into the sensor to allow the selective detection of an analyte in complex media. The recognition elements, immobilisation method used and interface that is functionalised are therefore of critical interest in EGOFET-based biosensors. A comprehensive review of surface functionalisation strategies for immobilising biomolecules for use in bioanalytical applications was outlined by Jonkheijm and coworkers.[87] Numerous functionalisation strategies have been explored and can broadly be categorised as depending on adsorption, covalent attachment or affinity interactions to immobilise the bio-recognition elements to the desired interface, as shown in Figure 16.[29,88,89]

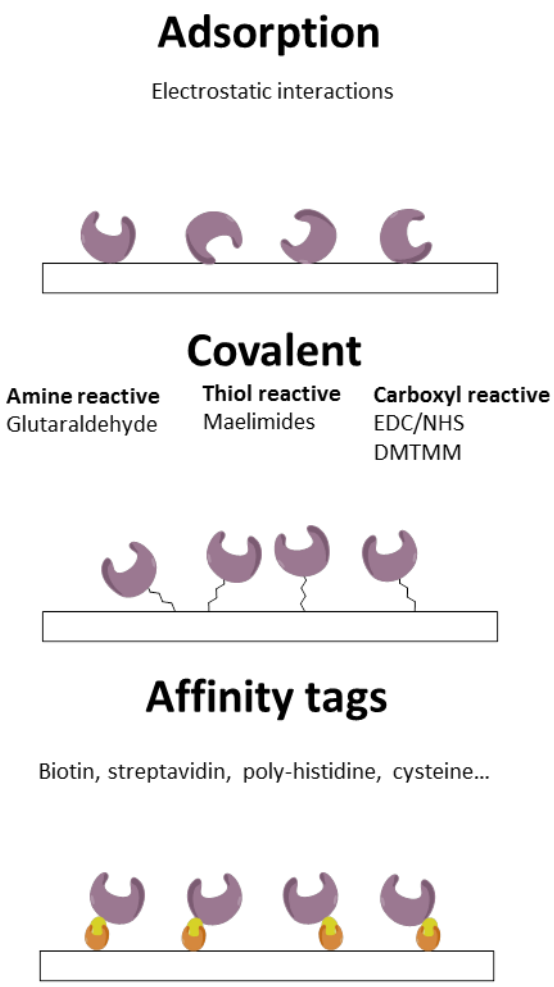

Figure 16 Scheme of the most commonly used immobilisation strategies for bio-recognition elements in biosensors.[87]

Covalent immobilisation requires the formation of chemical bonds between reactive groups on the biomolecules and complementary labile groups introduced to the interface.[90] This can be made possible by introducing functionalities such as hydroxyl (-OH), amine ($-NH_2$), thiol (-SH) & carboxyl (-COOH) groups to the interface surface for use in *in situ* surface confined covalent reactions with bio-recognition elements.

One of the most common strategies for surface functionalisation is through the use of thiol-based self-assembled monolayers (SAMs). SAMs are two-dimensional highly ordered molecular assemblies which form on a surface by chemisorption; in the case of gold this relies on sulphur-containing head groups. The strategy benefits from ease of preparation and the spontaneous formation of the densely packed monolayer, with sufficient chemical and physical stability to allow further modification. Unless the deposited SAMs are pre-functionalised, the terminal group of the SAM contains the reactive chemical functionality which allows the covalent attachment of the recognition elements after monolayer formation. A variety of different known thiol self-assembled monolayers

(SAMs) are capable of anchoring probes to either gold nanoparticles deposited on the OSC channel or directly to a gold gate electrode for use in OFET biosensors.

Gold nanoparticles (AuNP) can be used to introduce binding sites to OFETs, allowing the functionalisation of the device. The deposited gold nanoparticles, shown by Hammock *et al,* used a block copolymer to order large-area arrays of gold nanoparticles with well-defined spacing onto the channel surface of a water stable OFET with back gate operation.[91] The gold nanoparticles where functionalised with a thrombin aptamer capable of specific detection of the corresponding thrombin protein in solution at 100 pM concentration.

Functionalisation of the gate electrode using SAMs has proved the most popular route to functionalisation in EGOFETs. The exceptional selectivity of this technique was shown by the chiral differential detection of carvone enantiomers by Mulla *et al*.[79] Detection was achieved by the attachment of odorant binding protein (OBP) to the gate electrode through EDC/NHS coupling of a free Lysine residue in the OBP to the 3-mercaptopropionic acid (3MPA) SAM functionalised gold gate electrode. [79]

The pinnacle in EGOFET limit of detection was recently demonstrated by Macchia *et al* showing single molecule detection with a highly-packed SAM that is capable of sensing in complex media such as saliva and blood serum.[92] The gold gate functionalisation strategy used in this work relied on a SAM prepared by mixing two carboxylic acid terminated alkanethiols of differing lengths at a molar ratio of 10:1 (3-MPA: 11-MUA). The EDC/NHS coupling of the antibody to the SAM had a preference towards the longer 11-Mercaptoundecanoic acid (11-MUA) due to reduced steric hindrance. The high density of the mixed SAM produces a layer capable of sustaining electro-static cooperative interactions. Detection occurs through cooperation within the hydrogen-bonding network which is densely packed into a monoloayer of 10^{12} recognition elements on the millimetre sized gate, at a density of 10^4 μm^{-2}. The gate work function change was triggered by the binding event and propagated throughout the SAM by the densely packed electrostatic hydrogen bonded network resulting in the exceptional sensitivity and LoD of the device. The current change in the sensor is attributed solely to the shift in V_T displaying a similar response to that of the ISFET described in Figure 15c. This is behaviour is attributed to the high capacitance of the SAM and the gate design which is two orders of magnitude larger in size than the channel area meaning that C_{Bio} is no longer the smallest contribution to the series of capacitances that contribute to C_i (Equation 23). Therefore, the device response is dominated by the electrostatic changes that affect V_T.

A frequent challenge for *in-situ* detection of biomolecules is the sensitivity of many OSC to water. An alternative device configuration proposed by Minamiki *et al*.,[78] applies an extended-gate-type OFET where the main OFET portion of the device is separated from the detection site (the extended-gate), therefore water-induced degradation of the organic transistor is prevented. Surface functionalisation of the extended gate again relies on thiol-gold chemistry for immobilising an antibody for the detection of IgG with a detection limit of 0.62 µg/mL and low voltage operation.

The alternative strategy to functionalisation of the gate electrode requires the immobilisation of the recognition element to the OSC interface, for which a wide range of techniques have been explored.[90] The simplest method developed relies on the adsorption of the recognition element to the pre-prepared devices.[93,94] Physical adsorption uses intermolecular forces such as van der Waals, hydrophobic, and ionic interactions of the biomolecule to the OSC surface for immobilisation, without the need for chemical bonds making it a fast, simple, and inexpensive process relative to covalent attachment.[94] Additionally, adsorption benefits from minimal detrimental impact on the OSC and its electrical performance. However it lacks control of the orientation, homogeneity in coverage and the stability of the immobilised recognition elements compared to other techniques.[90]

In contrast, covalent attachment of the biorecognition elements has the potential to allow optimisation of orientation and coverage, and benefits from a more stable bond between the biomolecule and the functionalised surface. Covalent immobilisation requires the formation of chemical bonds between reactive groups on the biomolecules and complementary groups introduced to the interface.[90] The amine group of lysine and the thiol group of cysteine are the most common targets for reaction with labile epoxides or carboxyl and amino groups through *in situ* formation of reactive carboimide, maleimide and glutaraldehyde intermediates.[82,84,95–97]

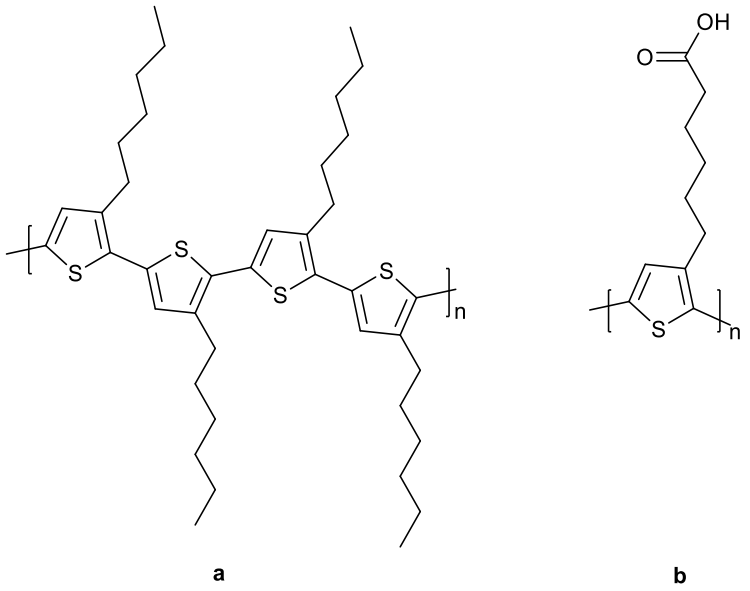

Figure 17 Chemical structure of the regioregular poly(3-hexylthiophene) (P3HT) (a) and the carboxylated poly[3-(5-carboxypentyl)thiophene-2,5-diyl] (P3PT-COOH) derivative (b).

Introduction of reactive functional groups to the OSC interface has been achieved by various methods. For example, the synthesis of OSC with modified structure such as co-polythiophene derivative incorporating functional groups has been used for the immobilisation of DNA probes and antibodies as EGOFET based sensors.[84,98] Kergoat *et al*.[84] demonstrated that this method enabled DNA detection by utilising a carboxylic acid side-chain-containing derivative of P3HT, (poly[3-(5-carboxypentyl)thiophene-2,5-diyl] – P3PT- COOH, Figure 17b). Simple peptide coupling with the carboxyl-groups allowed the DNA probes to be covalently immobilised onto the semiconductor surface of the EGOFET device. Immobilisation and hybridisation of the target DNA resulted in clear measurable changes in the electrical characteristics, causing a shift in threshold voltage and decrease in drain current. However, the signal changes where more pronounced when the device was operated in water compared to an electrolytic solution, indicating the effects of salt screening at higher salt concentrations which reduces the sensitivity in some EGOFETs.

The introduction of non-conductive reactive functional groups to the OSC polymer backbone affects the charge delocalisation of the conjugated system and introduces charge carrier trap sites into the OSC film. This reduces conductivity, which negatively impacts on the electrical performance. Additionally, the polar groups are produced within the bulk of the OSC film instead of being localised at the interface where required for *in situ* covalent reactions; the presence of polar groups within the bulk film can result in OS electro-chemical doping.

The alternative is the deposition of ultra-thin films onto the surface of the OSC, to form the bilayer device structure. This technique avoids chemically modifying the structure OSC whilst still

introducing the labile groups to the electrolyte interface required for *in-situ* covalent attachment of the recognition elements.[99] Sensing can occur in this device configuration as the capacitance of the bio-functionalised dielectric interface is coupled to the OSC layer underneath, which influences the active channel upon analyte interaction.

Plasma enhanced vapour chemical deposition (PE-CVD) is one route to the deposition of hydrophilic layers rich in reactive groups onto the OSC and has been used for both acrylic acid and maleic anhydride.[74,100] The PE-CVD procedure used to deposit a hydrophilic coating on P3HT had only minor impact on the electrical performance. The carboxylic acid rich films produced by this technique allowed the covalent attachment of a phospholipid bilayer through the reactive amino groups of phosphatidylethanolamine. [101] This can be further functionalised with biorecognition elements through affinity interactions, such as a biotinylated phospholipid bilayer used for the detection of streptavidin.

The deposition of thin films by spin-coating directly on to the surface of the OSC provides an easier deposition technique reducing the required equipment and processing. A selection of developed polymers is shown in Figure 18. Acrylic-based polymers are a common choice due to the availability of carboxyl groups for *in situ* functionalisation by EDC/NHS reactions to the amino groups of the target bio-recognition element.[82,97,102]

PAA

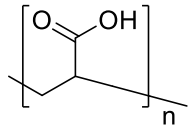

Poly(acrylic acid)

PS-MA

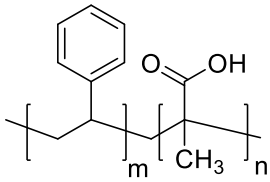

Polystyrene-*co*-metharylic acid

PS-PAA

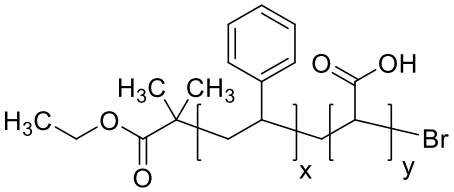

Polystyrene-*block*-poly(acrylic acid)

PMMA-MA

m:n = 1:1

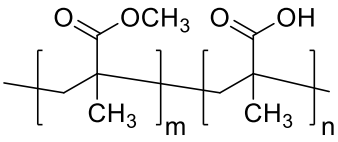

Poly(methyl methacrylate-*co*-methacrylic acid)

PS-MI

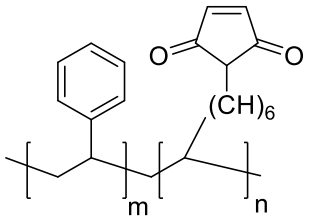

Polystyrene functionalised with maleimide

Figure 18 Polymers used for the deposition of ultra-thin-films onto the surface of the OSC containing the reactive functional groups required for in-situ covalent attachment of the recognition elements.

Mulla *et al* showed that spin-coated poly(acrylic acid) (PAA) films can be used as an immobilisation layer for use in an EGOFET sensors as shown in Figure 19.[97] The soluble spin-coated pAA layer was UV-crosslinked to produce a stable coating with a high density of COOH groups to covalently anchor a biotinylated phospholipid bilayer for detection of streptavidin.

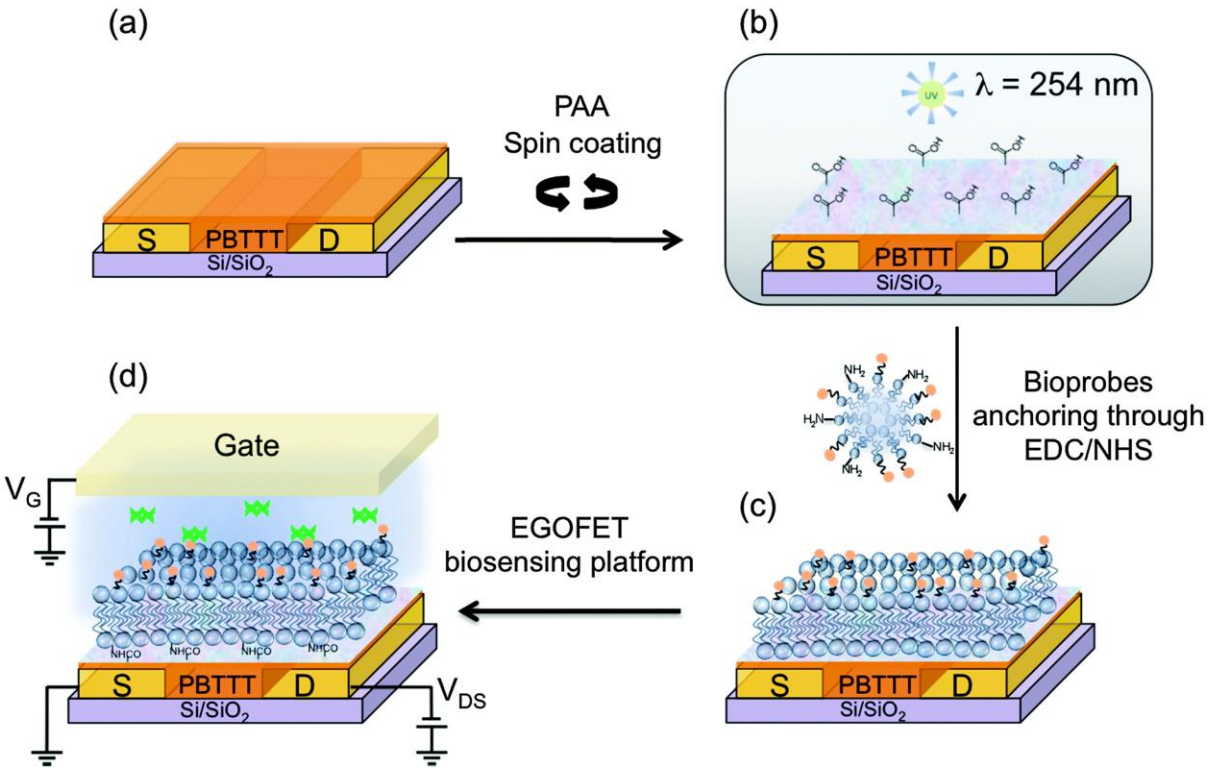

Figure 19 Scheme showing procedure for EGOFET biosensor device fabrication developed by Mulla and co-others.[97] The device uses an Au source and drain contacts and PBTTT deposited as the device organic Semiconductor (OSC). (a) Initial device structure on the substrate. (b) PAA is spin-coated onto the OSC and crosslinked by UV radiation. (c) Biotinalyted phospholipids are covalently attached to the surface using EDC/NHS amine coupling. (d) Aqueous sample containing analyte in PBS is applied and the electrolyte used to gate the EGOFET device using a gold gate electrode. Image reproduced from Ref.[97] with permission from The Royal Society of Chemistry.

Normally activation of the labile group is performed *in-situ* on deposited films during the functionalisation procedure, for example the deposition of the pre-activated polymer, such as the maleimide functionalised polystyrene based co-polymer.[82,95] Similarly the activation of the carboxylic acid on PS-PAA copolymer (molar ratio of styrene: acrylic acid is about 2 : 1) was achieved using EDC/NHS in solution (CH_2Cl_2– DMF mixed solvent) to allow the spin-coating of the activated co-polymer onto the device surface. An antibody for a brain injury biomarker was then immobilised onto the extra insulating layer with high yield and surface coverage to allow the specific detection of the target protein in solution.[103]

The influence of layer structure was investigated in a side-by side study of different carboxylic acid bearing co-polymers for immobilising antibodies in OFET-based biosensor. [103] The PS-MA and PMMA-MA polymers proved most stable to repeated washing with greatest adhesion leading to most efficient immobilisation of antibody. A higher ratio of the hydrophilic acrylic acid subunits further decreased the aqueous stability of the polymer films.[103]

Conventionally, detection relies on the interaction of the analyte with the biorecognition element at one of the device interfaces to produce a sensing response. A novel alternative approach

demonstrated by Piro and co-workers is the use of a competitive displacement immunoassay to elicit field-effect transduction (Figure 20).[104,105] This approach proved effective for designing immunoassays with both gate electrode and OSC functionalised interfaces. In this competitive exchange immunoassay the antibody specific to the analyte is immobilised by affinity interaction with a target mimic which is attached to the desired interface (gate or OSC). The target mimic is a molecule that is chemically similar to the analyte that it is able to weakly bind to the antibody but with a lower binding affinity than the intended analyte. Upon target analyte addition to the electrolyte solution, a competitive exchange occurs with the target mimic due to more energetically favourable complex formation of the analyte-antibody complex. This is results in the dissociation of the antibody from the interface surface leading to the reorganization of the electrolyte interface and produces a sensing response by variation in the output current.

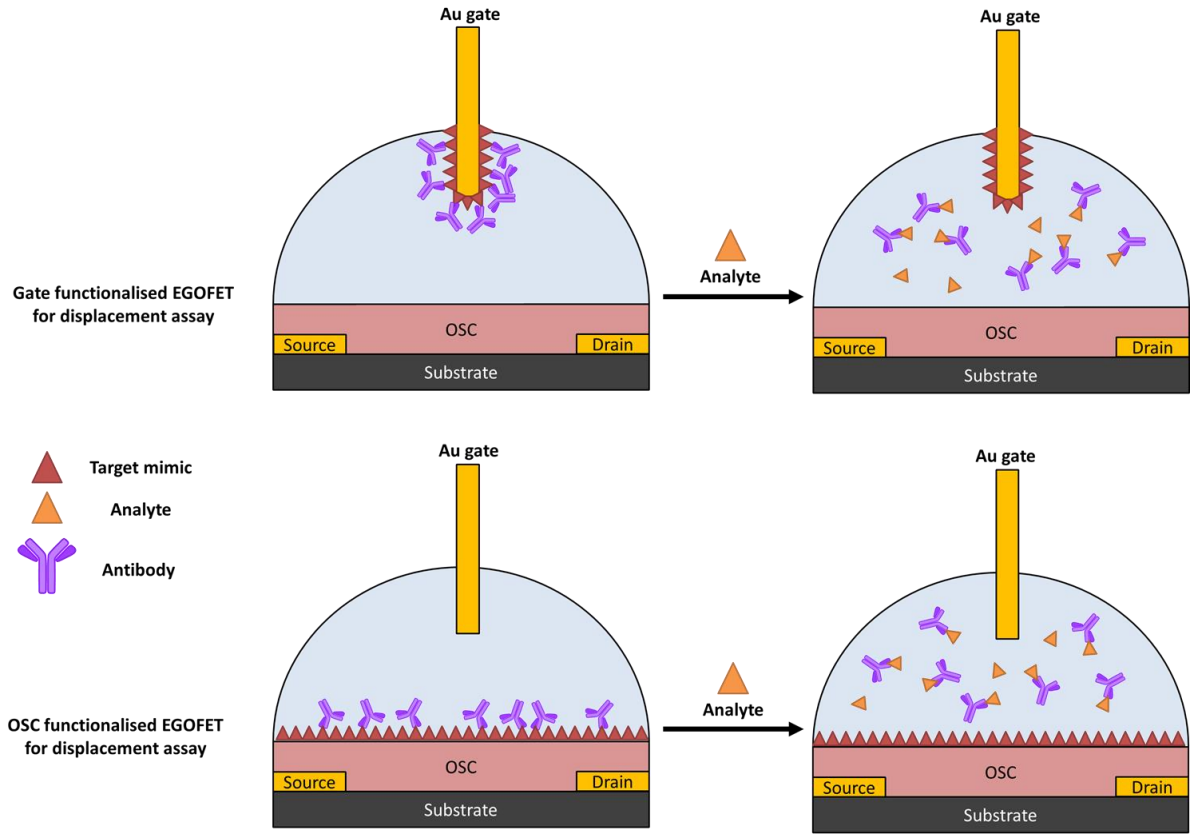

Figure 20 Schematic representations of gate (top) and OSC functionalised (bottom) EGOFET sensors demonstrated by B. Piro and co-workers used in displacement immunoassays.[104,105]

1.4.4 Improvements to device operation

In OFET-based sensing systems the active organic semiconductor in the channel plays a critical role in device performance. Whilst a variety of small molecules and single crystals have recently been employed as the active layer,[64,84,106] few solution-processable semiconducting polymers have been reported in electrolyte-gated devices largely limited to P3HT and its derivatives.[43,84] One of the main

challenges currently facing EGOFETs is the well documented environmental instability due to water, oxygen and light exposure.[107] Issues relating to the instability of the OSC can be problematic when the device functionalisation requires long incubation steps that can be detrimental to OSC performance. Additionally, instability in performance that occurs during the calibration curve measurements can cause a drift in performance and increase the background noise, this frustrates accurate sensing. Evidence of degradation on device behaviour can include increased hysteresis and gate leakage (I_G) in transfer curves, a shift in threshold voltage and a decrease in on current overtime.

The hysteresis observed in transfer curves can be influenced by the scan rate of the applied potential and potential window that measurement is taken. The application of a pulsed voltages of alternating polarities for V_G has been demonstrated as a method for acquiring hysteresis free transfer curves in P3HT based FETs.[108] Water-gated P3HT FETs operated the pulse-mode measurements resulted in hysteresis free transfer curves and doubled the I_D/I_G ratio relative to the conventional DC-mode (R. Picca *et al.* 2019).[109] R. Picca *et al*. also observed that P3HT-based EGOFET devices displayed a double exponential decay in current, with a very large initial decrease in current followed by a significantly slower steady state of decay which is reached after a prolonged period of incubation in water after 18 hours. Once the steady state has been reached the current drift is significantly reduced to around 1% per hour and this allows the incubated device to be highly suited for highly sensitive biosensing experiments. The pre-biosensing incubation protocol in water has been used in various recent biosensing experiments.[110,111]

Higher sensing sensitivities have also been achieved through the use of large surface-to-volume ratio nanostructures or low dimensional non-molecular materials such as silicon nanowires,[112–114] carbon nanotubes[115–118] and graphene.[119,120] However these approaches are often hindered by high cost and demanding fabrication procedures. Additionally, carbon nanotubes and graphene can suffer from significant non-specific protein adsorption caused by hydrophobic and electrostatic interactions.

Blending of a semiconductor with an organic insulator has been demonstrated as a method for improving the device performance.[107] This P3HT/PMMA blend, used as the semiconductor layer in a water gated OFETs (WGOFETs), showed that up to 70% of insulating polymer could be used without affecting mobility but lowering off-current by an order of magnitude, resulting in an enhanced on/off ratio. In other work, it has been shown that blending can also improve air stability of the semiconducting layer.[121]

Different OSC as the active semiconducting layer for EGOFET sensing application have been explored. R. Porrazzo *et al*.[66] have reported on a poly(2,5-bis(3-hexadecylthiophen-2-yl)thieno[3,2-b]thiophene) (pBTTT) based EGOFET showing promising electronic performance and improved electrochemical stability. A charge carrier mobility of 0.08 cm^2/Vs was achieved, comparable with single-crystal based water-gated devices and solid- state polymer dielectric transistors, whilst maintaining low voltage device operation (~ 1V).

Recently new polymers have been investigated for application including in EGOFET devices including BTBT[122] and DPPTTT.[35,52–54] DPPTTT is particularly promising for application in EGOFET devices due to its relatively high hole mobility (ca. 1 cm^2 /Vs), low HOMO (-5.2 eV) and exceptional environmental stability which was shown to be superior to PBTTT.[105,123] As the field of OSC continues to mature newer materials with improved properties for OFET applications are being developed and it is expected they too will find applications in EGOFETs and eventually biosensing.[35]

1.4.4.1 Challenges in protein detection

Significant challenges remain if OFETs are to realise their potential as inexpensive sensors for diagnostic and monitoring systems. If label-free OFET biosensors are come to the forefront of the field for chemical and biological detection they must first display excellent performance in specificity, sensitivity, reproducibility and stability. Outlined below are some of the issues, which must overcome in order to achieve this.

(i) To satisfy clinical diagnostic and prognostic criteria the need for detection of more than one biomarker is clear. Many diseases, including cancers, have more than one associated biomarker and many blood bound tumour markers have typically low cancer type and organ specificity.[124–126] Therefore the ability to multiplex, i.e. the parallel assay of multiple analytes, can increase the diagnostic value of biomarker detection whilst also reducing time, cost and sample volume. The individual functionalisation of an array of transistors with different receptors is one route into multiplexing. However, multiplexed label free detection of biomarkers, particularly in complex fluids, remains a considerable challenge in which only a few examples have been reported.[127–129]

The integration of microfluidic devices with micro-diagnostic systems complements optical and electronic based detection systems is as an ideal platform for the multiplexed analysis of biomarkers and miniaturisation of complex assay for use in POC setting.[4,130] Serial washing and incubation with reagents and analytes simplifies fabrication, sample processing and fluid handling whilst also reducing the required sample volume and duration of analysis.[4,130–132] An ELISA integrated system demonstrated HIV diagnosis within 20 mins requiring only a few microliters of unprocessed blood.[4] Whereas a surface-enhanced Raman scattering (SERS) integrated microfluidic device has shown

multiplexed detection of a panel of four breast cancer biomarkers, including HER2, directly from biofluids.[132]

(ii) A second challenge is translating the detection of analytes in laboratory solutions to their native biological media such as blood, serum and urine. Phosphate buffered saline (PBS) solutions and analyte spiked blood serum samples are typically used in sensing experiments to simulate physiological conditions of biological samples. Displaying device operation and sensing from physiological simulated solutions shows the potential to use the devices in POC biosensing.[66] Clinical samples are a complex mixture of proteins, hormones, ions and other chemicals (including directly electroactive compounds), which can result in non-specific binding and anomalous background signals. For example charge-based label free biosensors are highly sensitive to changes in ionic strength, pH and environmental temperature.[16,133] Non-specific adsorption may contribute to measurable signals which are indistinguishable from specific target analyte signal. A variety of strategies have been proposed to minimise sample matrix effects;[16,133] a popular approach being hydrophobic 'antifouling' surfaces, many of which are based on polyethylene glycol and its dervatives.[134] Blocking agents have also been used to reduce non-specific adsorption onto the biosensing surface such as bovine serum albumin,[135] OH-terminated self-assembled monolayers, surfactants (such as Tween)[136] and zwitterionic polymers.[137,138] An alternative method for reducing non-specific binding and lower background noise is through on chip pre-filtering. [139]

(iii) OFETs for sensing applications function on the principle that charges or potential changes caused by molecular interactions upon target binding influences the (gating) electric field seen by the current carrying element, resulting in an variation in the operating characteristics of the device.[16]

As antibodies and antigens generally carry an intrinsic molecular charge, their detection relies on modification of the electric field generated by the binding event being seen at the surface. It is known that electrostatic interactions in electrolyte solutions are limited to within the Debye screening length (λ_D), beyond which charges introduced by the analyte are shielded by electrolyte ions.[115,140] As a result some sources suggest that detection in OFET sensors is limited to within the Debye length, were recognition event takes place within λ_D.[91,141,142] Therefore it is suggested that OFET detection is only possible at salt concentrations where λ_D is suitably large to encompass the analyte. Therefore, when high ionic strength electrolytes are used and the Debye length is significantly reduced, detection techniques that depend on electrostatic detections can be significantly frustrated. In contrast to this rule recent reports have shown EGOFET sensing of analytes beyond the Debye length. [75,95,143,144]

The Debye length in electrolyte solutions is inversely proportional to ionic strength, therefore as ionic strength increases the distance in which the analytes charge can be seen decreases, some relevant λ_D are shown in Table 1. Complications arise when large recognition elements such as antibodies are used, whose dimensions (ca. 10-12 nm)[133] are much larger than the Debye length (λ_D ~ 0.8 nm) in physiological solutions such as blood serum (~150mM). Therefore in order to reduce screening effects and improve sensitivity many assays are performed in low ionic strength solutions, which may require physiological solutions to be diluted or desalting processes prior to analysis.[145]

Table 1 Debye length (λ_D) in electrolyte solutions of various concentrations of monovalent ions (e.g. NaCl).[17]

Ion concentration (mM)	Debye length - λ_D (nm)
1000	0.3
150	0.8
100	1
10	3
1	10

The above assumes antibodies are rigid bodies, which bind solely to the surface through the C3 terminus domain (Schenk model) to produce a distance of around 10 nm (Figure 21a).[146] This common misconception is discussed by Casal *et al*,[133] it is highlighted that antibodies are highly flexible and capable of adsorption to the surface in variable orientations.[147] As a result the bound analytes can be orientated at an angle to the substrate, some of which are expected to be within the Debye length (Figure 21b), hence providing a rational for devices with successful FET sensing.[78,148,149]

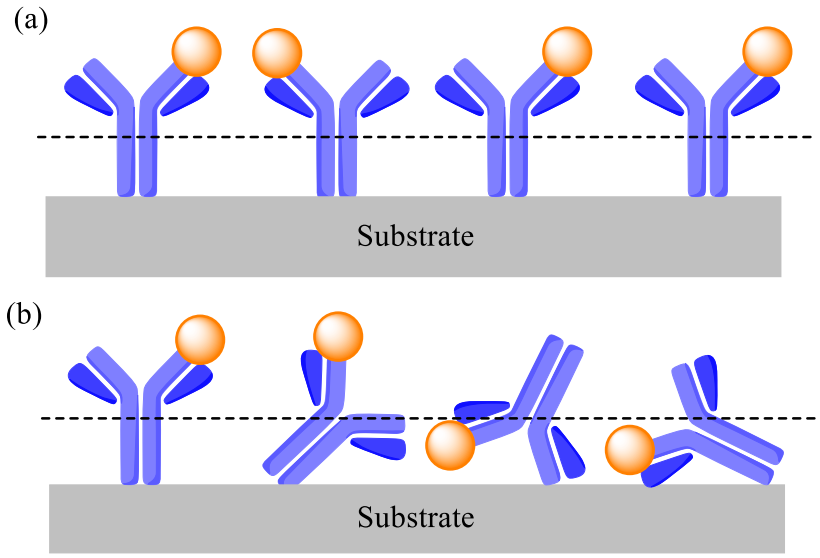

Figure 21 (a) Cartoon representation of antibodies (blue) immobilised on a sensing interface and bound to an analyte (orange) in Schenk model.[150] Approximate Debye length shown by dashed line. (b) A more realistic representation of antibody alignment, depicting a more random orientation relative to the surface.

Pallazo *et al* demonstrated an EGOFET sensor in high salt concentrations capable of detecting at distances 20-30 nm (30 x λ_D) from the transistor channel surface. The EGOFET device displays a capacitance modulated response that operates independently from the Debye length. [144] The sensing mechanism relies on the formation of a Donnan equilibrium within the biorecognition layer, (in series to the gate capacitance) that can operate regardless of the ionic strength of the electrolyte and therefore independent of Debye length.

One alternative to circumvent issues with charge screening is to use smaller recognition probes whose dimensions permit the recognition event to take place in closer proximity to the sensing surface, falling within the Debye length. These could include probes such as aptamers (1-2 nm),[151] short peptide ligands,[152,153] and antibody fragments.[145,154,155] Additionally, Elnathan *et al*.[145] demonstrated that fragmentation of antibody-capturing units can produce size reduced fragments capable of effectively sensing proteins in untreated blood and serum sample at sub-pM concentrations. The antibody-fragments which contained free amine groups were covalently immobilized to the aldehyde terminal groups of flexible alkyl linkers using sodium cyanoborohydride in a reductive amination reaction. The effects of controlling antibody surface coverage were also investigated, showing that greater sensitivity can be achieved by using a comparatively lower antibody surface density and long flexible linkers. At lower surface densities of antibody fragments the flexible nature of the connecting linkers can be exploited to allow them to easily adopt conformations closer to the sensing surface hence reduce the screening effects of the electrolyte solution.

(iv) The addition of functional groups to OSC is commonly used in order to allow the direct surface functionalisation at the interface. However, this can often compromise electronic performance as introducing a non-conductive region to the polymer backbone inserts charge carrier traps to the OSC film, reducing conductivity. The use of bilayer devices has been noted as a technique to help alleviate inferior charge-transport,[99] with "un-modified" OSC at the dielectric interface and the "modified" component at the OSC-surface /analyte interface. Additionally, sensitivity and response can be further enhanced by ultra-thin-films of semiconductor blends.[156]

(v) The suitability of p-type OSCs synthesised by Pd(0) organometallic Stille coupling catalysed reactions was brought into question for use in biosensing EGOFETs by T. Althagafi *et al*. due to the reported innate cation sensitivity the material displayed.[157] Pd(0) is used as the catalyst for the synthesis of PBTTT and DPPTTT and the post-synthetic removal of residual Pd(0) may not always be successful. As a result, the authors demonstrate the divalent cation sensitivity (including Ca^{2+}) of their PBTTT-based devices synthesised by the Stille catalysed reaction. This innate divalent cation sensitivity was however absent in rrP3HT devices which they ascribe as its polymerisation is catalysed by Ni dppe rather than $Pd_2(dba)_3$. The investigation probed changes in device performance of simple aqueous salt solutions relative to DI water. A comparison against buffered salt solutions (e.g. 0.1 M PBS) spiked with additional cations would provide a better comparison to physiological conditions of biosensing samples and reducing the overall variation of ionic strength and pH in the previous investigation.

Divalent cations such as calcium can be present in blood serum samples from which biosensing devices aim to be able to quantify the target biomarker. The serum calcium concentrations in healthy individuals are normally maintained in the range of 8-10 mg dl^{-1} (2-2.5 mM) with a range of 4 mg dl^{-1} (1 mM) in Hypocalcaemia patients and 16 mg dl^{-1} (1 mM) as an upper limit that would present an immediate medical emergency. Therefore Ca^{2+} has the potential act as an interferant that may increase the noise associated the real-world sample analysis by producing a non-specific response and frustrate accurate sensing.

Whilst the proposed cation sensitivity of these Pd(0) catalysed OSCs doesn't present an immediate risk to proof of principle for analyte detection, it has the potential to frustrate real-world sample analysis from blood serum where the analyte sample comes into direct contact with the OSC. In such cases processing of blood serum samples to remove ions may be necessary. Alternatively, the use of other OSCs such as rrP3HT may be required. Biosensing systems that do not directly expose the OSC to the analyte may also be beneficial such as extended gate architecture or the BioSAM system developed by Torsi et al.[92] which exposes the gate to the analyte solution separately and the gate is

then moved back to the EGOFET device and the sensing response is measured independently in DI water.

In most EGOFET based biosensors at the proof of principle stage focus on investigating the sensing performance associated with novel: device architectures, immobilisation techniques, the interface chosen for functionalisation, biorecognition elements and analytes being detected. The OSC can be easily swapped for an alternative OSC material on the condition that it is orthogonal to the processes previously used, therefore allowing for the integration of new OSC.

1.5 Cancer

One area where biosensor-based technologies for use in PoC analysis can find urgently needed application is within the field of cancer.[8] Cancer is a leading cause of mortality globally with 14.1 million new cases and for 8.2 million deaths in 2012, accounting for 1 in 6 deaths that year.[158] Approximately 70% of deaths occurred in low to middle-income countries but only 26% of low-income countries reporting accessible pathology services in public sector. Application/testing in resource-poor settings is exceptionally desirable and may help narrow the widening global disparity in patient outcomes. The incidence rates of cancer are more prevalent in older age, and the developing global demographic and epidemiological shifts forecast an ever-growing cancer burden over coming decades, with over 20 million cases expected by 2025.[159] In addition to minimising risk factors, earlier detection and more efficient patient management are the main strategies to reduce the cancer burden where novel sensing platforms can contribute.

Cancer is a generic term for a family of over 100 diseases affecting different organs of the human body affecting tissue growth regulation. They are defined by unregulated proliferation of abnormal cells due to genetic and epigenetic alterations affecting gene activity and expression. The resulting disruption of normal cell signalling pathways produces cancer cells that exhibit higher growth rates than normal mammalian cells and the characteristic lack of tissue growth regulation.

As a result, the typical features of neoplastic disease include: unlimited cell division by sustained proliferative signalling which, activates the invasion of nearby tissues and metastasis to distant organs, resistance to antigrowth signalling, and apoptosis resistance (regulated cell death), inducing angiogenesis and evading immune destruction.[160]

Mutations arising in cells can be influenced by a range of factors and are frequently caused by the interaction of a person's genetic factors with external carcinogens (environmental factors), ranging from ionising or ultraviolet radiation, chemicals and carcinogenic infections from certain viruses or bacteria such as Human papillomavirus (HPV) and hepatitis B virus. Other factors in diet and lifestyle

may also play a role in cancer. Furthermore, ageing is a fundamental factor in cancer development due to the accumulation of overall risk and a tendency towards reduced effectiveness for cellular repair mechanisms with increased age.

Cancer is a polygenic disease; its heterogeneous nature means that there can be a considerable variation in alterations in oncogenes and tumour suppressor genes across the pool of patients making single biomarker analysis ineffective. Genetic and epigenetic changes depend on tumour location (e.g. organ) and vary amongst those in the same location leading to different subtyping. In addition to genome-related changes, molecular alterations produced during the progression of a tumours development include gene over/under-expression and (mRNA changes) or protein over/under expression. These biomarkers can be present in tumour tissues or bodily fluids (e.g. blood serum and urine) and cover a plethora of molecules, including transcription factors, cell surface receptors, and secreted proteins.[124] Monitoring their levels can aid in the diagnosis of early-stage cancers (diagnostic), response to treatment (predictive), tumour state and progression characteristics (prognosis).[124] Demand for effective tumour markers is high since they have the potential to improve cost-efficiency, survival rates and disease prognosis by facilitating early diagnosis and helping tailor personalised treatments.

Therefore, a wide range of molecular biomarkers have the potential for use in sensing platforms to aid in tumour classification and guide diagnosis, prognosis, monitoring treatment and disease recurrence. Biomarkers for cancer are varied ranging from mutations in gene fragments DNA; expression levels of gene activity by messenger RNA; quantification of proteins in serum or circulating tumour cells.[124,161,162]

The ability of the cancerous cells to grow beyond regular boundaries and invade other parts of the body and to other organs is also a defining feature of cancerous cells. This process is referred to as metastasis and occurs when cancerous cells from the primary tumour break away and travel through the bloodstream or lymphatic system forming new tumours (metastatic tumours) at distant site but of the same cancer type to the primary tumour. For example, for a breast cancer patient, breast cancer cells present in a metastatic tumour in the lung is referred to as “metastatic breast cancer”. This process is regarded as advanced cancer or “stage 4 cancer” and is the major cause of cancer-induced death, i.e. not caused by the primary tumour, accounting for ~90% of deaths. The progression of cancerous to metastasis is therefore a critical stage in patient management, as prognosis is often poor with no curative treatments currently available. Different types of cancers preferentially metastasise to specific organs, but overall the most common metastases locations are the lungs, liver, brain and the bones.[163]

Globally 32.6 million people are living with cancer within five years of diagnosis.[158] Relapse following primary treatment is a pertinent threat for many patients and long-term recurrence relatively common, making monitoring patients during remission desirable. Relapse is frequently a result of cancerous cells surviving the initial phase of treatment or not entirely removed after surgery. Therefore, adjuvant therapy (treatment in addition to primary treatment such as chemo or radiotherapy), is often prescribed to minimise the risk of recurrence. Recurrence of cancer in patients is usually a return of the primary cancer; local recurrence has good therapy options however metastatic relapse has poorer outcomes with currently available treatments. Within this context, it is proposed that earlier detection from more frequent monitoring could yield more effective treatment strategies and improved survival.

Whilst cancers can affect many different organs the most common causes of cancerous death are cancers of the lung, liver, prostate, stomach and breast. Incidence rates for different types of cancer vary among men, women and world regions. Breast cancer is by far the most frequent cancer diagnosed among women, with an estimated 1.67 million (25%) new cases in 2012.[158]

1.5.1 Breast Cancer

Breast cancer is a cancerous disease which affects the breast tissue, and the highly heterogeneous nature of tumour biology produces a variety of pathological features and clinical implications. Therefore, the heterogeneity of the biology associated with the disease should be accounted for in its risk assessment and treatment. Stratifying (or grouping) cancer patients based on the specific characteristics of the cancer is the first step towards personalising cancer treatments and the reliable assignment of breast cancers into these clinically relevant subtypes is crucial for therapeutic decision making and is urgently required.

Traditional decision making for patient prognosis and management is based on the analysis of clinicopathological variables such as tumour size, tumour grade and nodal involvement known as tumour node metastases (TNM) system.[162] The TNM system is reliant on the examination of macroscopic or microscopic morphology of pathological tissue samples which have been acquired by biopsy or during surgery. However, the techniques used are limited in identifying disease subtypes, which have different disease outcomes.

The advent of gene expression profiling has allowed the elucidation of the 'molecular profiles' of cancers where expression levels of key biomarker genes allow classification into at least five intrinsic subtypes which demonstrate distinct clinical outcomes. Classification rational is that the molecular

profiles of the cancers reflect the fundamental differences of the tumours at a molecular level accounting for their differing biological behaviour and likely therapeutic response.

This intrinsic subtyping requires investigating the tumour's intrinsic properties through biomarker analysis. Assignment of subtype requires determining the expression status of oestrogen receptor (ER), progesterone receptor (PR), HER2 and Ki67 and it is typically performed through immunohistochemistry (IHC) assays. The five basic IHC-defined subtypes, and their IHC status, prevalence and typical clinical prognosis and therapy are summarised in Table 2.

The exception is for normal-like tumours (7.8% of lymph-node-negative cohort) which shares similar IHC status to luminal A subtype and requires additional characterisation by standard breast tissue profiling due to different expression patterns.

It is important to identifying tumours with the most aggressive biology that necessitate the use of adjuvant/additional chemotherapy versus those where endocrine therapy alone is sufficient and avoiding unnecessary cytotoxicity. This is a frequent challenge for ER-positive/HER2-negative cohort of patients and is the most common challenge in contemporary breast cancer patient management, which provides the clinical motivation for developing most gene expression-based assays.

Table 2 Breast Cancer subtypes and generalised therapy management

Intrinsic subtype	ER Status	PR status	HER2 status	Ki67 status	Grade	Prognosis	Prevalence	Typical therapy
Luminal A-like	+	+	-	-	1|2	Good	23.7%[a]	ET alone in most cases
Luminal B-like (HER2-)	+	+	-	+	2|3	Intermediate	38.8% [a]	ET + CT most cases
Luminal B-like (HER2+)	+	+	+	+		Poor	14% [a]	CT + anti-HER2 therapy +ET
HER2 over-expression	-	-	+	#	2|3	Poor	11.2% [a]	CT + anti-HER2 therapy
Basal (triple negative)	-	-	-	#	3	Poor	12.3% [a]	CT
Normal-like	+	+	-	-	1|2|3	Intermediate	7.8% [b]	

ER oestrogen receptor, PR progesterone receptor. #: not in the definition criteria CT, Chemotherapy; ET, endocrine therapy

Prevalence: [a]data from ref [164], [b]data from ref. [165],Prognostic: data from ref. [166], Typical therapy from ref.[167]

1.5.2 Breast Cancer Biomarkers

As the cancer biomarkers are indicative of the biology and fundamental mechanisms causing the cancerous behaviour. Therefore, biomarker analysis and monitoring allow the identification, development and effective use of the relevant targeted therapeutic agents such as hormone receptor signalling, HER2 and angiogenesis. Commonly administered targeted therapies include Imatinib (Novartis' Gleevec), Trastuzumab (Roche's Herceptin) and Rituximab (Roche's MabThera).[168] The combined biomarker profiles have proven to be more accurate and reproducible indicators for prognosis and therapeutic response than anatomical prognostic factors alone, providing improved stratification and therapeutic decision making, therefore driving the need for biomarker analysis for therapeutic selection.[169]

1.5.2.1 ERs/PRs

The estrogen receptor (ER) is a member of the steroid hormone receptor family acting as ligand-activated transcription factors. The receptor is activated by its ligand, the hormone estrogen; once bound it can translocate into the cell and bind to DNA regulating the activity of different genes. Overexpression (i.e. overactivity) of the ER receptor, therefore, interrupts processes that dictate the normal cell cycle, apoptosis and DNA repair ultimately leading to tumorigenesis (cancer). Therefore, drugs that interrupt the ER function in breast cancer cells can provide effective treatment and ER status is used to determine the sensitivity and suitability for these targeted therapies. Targeted therapies include selective oestrogen receptor modulating (SERM) or disrupting (SERD) agents like Tamoxifen or aromatase inhibitors such as Anastrozole.[168]

The progesterone receptor (PR) is also a member of the steroid hormone receptor family and is activated by progesterone. It is a downstream regulator of ER signalling making PR expression highly dependent on the presence of ER. In combination, ER/PR expression statuses have proven as effective prognostic factors with ER-positive/PR-positive status indicating a favourable outcome.[168,170]

1.5.2.2 Ki67

Ki67 is a nuclear protein associated with ribosomal RNA transcription and commonly used as a marker for cell proliferation. The clinical validity of Ki67 is often questioned because of assay reproducibility concerns. Insufficient standardisation is the chief culprit and results in poor interlaboratory concordance due to variation in protocols, reagents and equipment.[171,172] When appropriately used Ki67 can provide useful prognostic value for survival and tumour recurrence for stratifying patients, for example, identifying subsets of ER-positive breast cancer patients who will benefit from adjuvant chemotherapy.[173]

1.5.2.3 HER2

HER2 is a member of the human epidermal growth factor (EGF) receptor family, which contains EGFR, HER2/neu (c-erbB2), HER3 and HER4. They are responsible for the regulation of processes including cell proliferation, differentiation, migration and survival. The HER2/neu gene encodes for a 185kDa transmembrane receptor with three domains: intracellular tyrosine kinase domain, transmembrane lipophilic segment and an extracellular domain (ECD) of 105kDa, Figure 1.[174,175] In addition to cancerous cells, low levels of expression are present from epithelial cells of healthy tissues of other organs such as lung, kidney, ovary gastrointestinal tract and placenta.[174,176]

Overexpression of HER2 occurs in 12-15% of breast tumours. Tumours showing Her2/neu amplification or receptor overexpression have accelerated growth rate and a higher incidence of recurrence. Therefore, relative to other subtypes have lower patient survival and are associated with an aggressive disease with poor prognosis. However, they respond well to anti-HER2 treatments, commonly monoclonal antibodies such as Trastuzumab with significantly improved outcomes.[177]

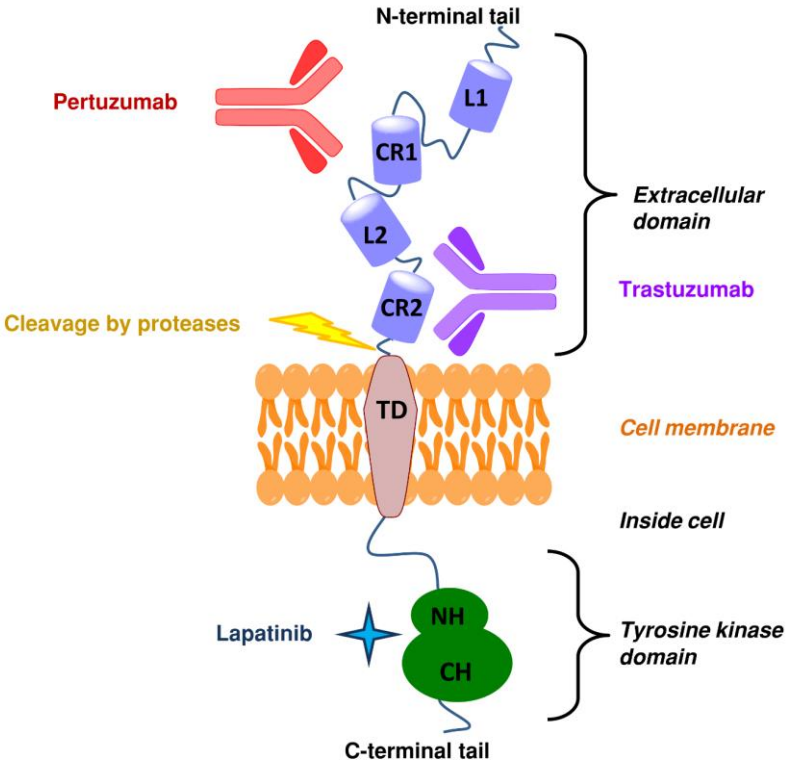

Figure 22 The cellular domain structure of HER2, composed of an extracellular domain (ECD), transmembrane domain (TD) and a tyrosine kinase domain which is the target for the drug Lapatinib.[174] The ECD is itself composed of four individual domains and the two cysteine-rich domains CR1 and CR2 are the targets for monoclonal antibody therapies Pertuzumab and Trastuzumab. HER2 can be cleaved by proteases at specific sites to produce the soluble ECD and a truncated receptor.

Cleavage of ECD or "shedding" of the HER2 produces a truncated receptor which dramatically increases tyrosine kinase activity, producing 10-100 times more oncogenic behaviour than the full-length protein by promoting the growth and survival of cancer cells.[174] The cleaved ECD domain can be detected at elevated levels in the blood serum of patients with breast cancer but also from other cancers such as ovarian, lung and prostate cancer. In addition, moderately high levels are possible despite the absence of cancer and can be associated with liver disease, pre-eclampsia and chronic heart failure.[176] Chronic heart failure is long term (chronic) heart condition where the heart is not able to effectively pump blood around the body.

1.5.3 Additional biomarkers

Beyond the standard IHC-defined biomarkers, a few other biomarkers have demonstrated enough clinical validity and clinical utility to translate into a clinical setting. Within a clinical context, individual tumour biomarker status holds limited value as they lack the specificity of being tumour specific and can be associated with multiple diseases in addition to the varying levels present in disease free-patients collectively increasing the risk of false positive/negative diagnoses.

As many biomarkers can be associated with the same disease, assessments are of much higher value when multiple biomarkers can be analysed, as many biomarkers have shown increased prognostic value when considered within the context of other results, particularly for biomarkers and assays whose individual validity remains questioned. In combination, these independent breast cancer biomarkers profiles (presence and concentration) can hold greater clinical value making multi-biomarker analysis essential and multiplexed analysis (simultaneous detection of analytes) more efficient. This has seen the spread of various commercial auxiliary tests which aim to help further deciphering the heterogeneity of breast cancer disease and provide a better 'picture' of disease state.

1.5.3.1 Genomic testing

Genes altered in cancerous cells can be classified as oncogenes or tumour suppressor genes. Modification or mutations to oncogenes stimulate abnormal cell survival and division, whereas tumour suppressor genes can be lost and result in loss of control of cell growth. The interaction and activity levels of these genes effect the tumours behaviour and can be probed by gene expression profiling (GEP) assays.

GEPs such as Oncotype DX and MammaPrint are the most well-established auxiliary tests for molecular diagnostics in breast cancer.[178] Oncotype Dx utilises reverse transcription polymerase chain reaction (RT-PCR) in an mRNA based panel of 21 gene assays on a tissue biopsy sample, to

generate a Genomic Health Recurrence Score (GHI-RS), informing accurate prognosis and cost-effective treatment.[179] The information gained can be of particular use in the identification of women at sufficiently low risk of recurrence that chemotherapy is envisaged to provide no benefit. Whilst the method has found extensive use in the US, its application elsewhere is impeded by its significant cost, retailing at $3,650 USD.[179]

1.5.3.2 Circulating biomarkers

In addition to tissue biomarkers, numerous circulating breast cancer tumour biomarkers present in the blood serum from a 'liquid biopsy' have been suggested although few have been adopted into clinical practice.

It is important to note that the classically defined breast cancer biomarkers outlined in Table 2 and section 1.5.2 are typically identified and analysed by IHC tissue staining methods therefore quantitative threshold values for detection are not defined. In contrast circulating biomarkers are soluble therefore readily quantifiable and clinical utility can be gained from specifying cut-off values for detection.

The detection of soluble biomarkers in circulating biological media is attractive as sample collection is minimally invasive. Conventional status assessment via the established IHC and FISH methods requires a biopsy or surgery to collect breast tissue sample, which hinders the practicality of frequent screening. Therefore, liquid biopsies make frequent biomarker analysis viable as a tool for real-time monitoring of tumour progression and follow up with the aim of improved patient management.

With this regard, various biomarkers present in circulating media have been identified ranging from circulating tumour cells (CTC) and DNA to proteins. For example, it has been suggested that high levels of CTC (e.g. ≥5 CTC per 7.5 mL of blood) can act as an independent predictor of adverse prognosis in patients with either early or advanced breast cancer.[180]

The utilization of blood-based circulating tumour cell-free DNA(cfDNA) has also been recently demonstrated as a powerful biomarker for simultaneous multi-cancer detection and localisation. The incredible utility of these biomarkers has recently been clinically validated in an assay using bisulfite sequencing of the methylation signatures in plasma cfDNA fragments. The remarkable genetic sequencing technique is capable of accurately detecting over 50 types of cancer and the assay has recently been launched for clinical trials as a cancer detection diagnostic tool.[181]

The genetic sequencing of cfDNA fragments combines fluorescently labelled nucleotides and PCR amplification and the bisulfite sequencing (a Next Generation Sequencing method to determine the

pattern of methylation) is used to evaluate site-specific DNA methylation change (targeted methylation analysis of cfDNA).

1.5.3.3 HER2 ECD, CEA and CA 15-3

As HER2 ECD is indicative of the process that causes cancerous behaviour, it has the potential for use as a biomarker in monitoring tumour HER2 status by quantifying the serum HER2 concentrations.[174] HER2 ECD levels can provide insight into specific areas for evaluating cancers that overexpress HER2, most notably in the detection of recurrence and metastasis. Elevated levels are considered to be ≥15 ng/ml with an absolute change of $^{+}/_{-}$ 20% from threshold value considered to be of significance, with normal individuals median of 12 ng/ml and lower range down to 7 ng/ml.[182] There is a correlation between tumour markers, tumour size and nodal involvement, with significantly higher concentrations of HER2 ECD in patients with larger tumours or patients with nodal involvement.

However, several factors bring into question the clinical validity of HER2 ECD (especially when considered in isolation) including the lack of specificity. Correlation between tissue and serum HER2 levels is the principal concern in determining suitability as a prognostic factor and consideration for guiding therapy, with contrasting opinions stated. Considering the uncertainty surrounding the validity of HER2 ECD, the consensus is that it cannot be used as a substitute for direct tissue analysis by IHC/ FISH for determining tumour HER2 status but could be used to complement the assays and provide real-time status updates of patients. Periodic HER2 ECD testing may be useful to identify patients who have been erroneously categorised (for example HER2+ as HER-) or whose HER2 status is unknown. Serial evaluation by IHC/FISH is beneficial to determine eligibility for HER2 targeted therapies and provide a real-time picture of status for those undergoing therapy.[183]

The prognostic value of HER2 ECD can be increased when used in combination with the detection of cancer antigen 15-3 (CA 15-3) levels. CA 15-3 is a detectable circulating biomarker protein in blood serum derived from MUC-1 gene. The genes regular function is cell protection and lubrication, and it is frequently overexpressed on breast tumour cells, resulting in elevated levels CA 15-3, where 25 U ml^{-1} is considered a threshold. [182] However, elevated levels are also common in various other advanced adenocarcinomas such as lung, ovarian, pancreatic or gastric cancers.

Carcinoembryonic antigen (CEA) refers to a collection of glycoproteins involved in cell adhesion, this is produced by some types of cancer cell and is also detectable in blood serum; Normal range for CEA is typically < 2.5 ng/ml, however levels > 20 ng/ml suggest metastatic disease. Whilst CEA levels are more commonly associated with cancers of the gastrointestinal (GI) tract, increased levels are also found in breast cancer but they may also be raised in non-cancerous conditions, such as liver disease and inflammatory bowel disease (Crohn's disease and ulcerative colitis).

CEA and CA15-3 have been shown to detect 40–60% of breast cancer recurrences before clinical or radiological evidence of disease with a lead-time between 2 and 18 months.[184] Simultaneous detection of both serum markers allows the early diagnosis of metastases in up to 60– 80% of patients with breast cancer. [1–3]

HER2 ECD, CEA and CA 15-3 provide strong independent indicators on disease-free survival (DFS) and cancer-specific survival (CSS) in untreated early breast cancer patients, in addition to indicators for worse outcome in patients with high pre-therapeutic value levels of these markers.[18–21] In addition, they are useful surveillance biomarkers for early diagnosis of relapse and predicting progression to metastasis of breast cancer, with increased prognostic value when used in combination. They are therefore valuable in identifying high-risk patients aiding disease management and a potential predictor of treatment.

1.5.4 Current Breast Cancer biomarker detection techniques

Combining clinical and molecular markers improves their prognostic value for distant recurrence probabilities beyond that of classical clinic-pathological factors such as age, nodal status, tumour size and grade.[185] Breast screening involves a triple assessment involving a manual inspection, ultrasound and breast X-ray (mammogram). Magnetic resonance imaging (MRI) of the breast tissue frequently supplements screening with the aim of identifying tissue abnormalities which are often too small to be seen or felt, such as small areas of calcium in the tissue (calcification) which can also occur in non-cancerous tissue. Upon identification of an abnormality, a sample of tissue (biopsy) is collected and further testing within a pathology laboratory can confirm the diagnosis and identify the cancer subtype. This is typically undertaken using a sample of the tissue biopsy and biomarkers analysis is performed using an IHC test or FISH test, both of which are types of labelled assays. Both use staining processes that require a label to produce a visualised response on the tissue sample that must be analysed by a trained operator.

1.5.4.1 Immunohistochemistry (IHC) test

Histopathology involves the microscopic analysis of biopsy or surgical specimens by a pathologist following fixation and processing (staining), where the shape and pattern of cells in the tissue are used to diagnose the subtype. The staining agents used in processing allow the visualisation of components within the tissue, so their localisation and distribution can be analysed. IHC utilises selective staining by labelled antibodies which allow for the visualisation of the antibodies corresponding antigens (inc proteins, lipids and carbohydrates) within the tissue sample to aid cell categorisation by identifying the presence or elevated expression of the desired biomarker.

In order to visualise the antibody-antigen interaction, the antibody must be attached to a moiety that elicits a signal (signalling moiety). These can vary from enzymes which catalyse a colour inducing reaction such as peroxide (immunoperoxide staining). Alternatively, the antibody can be tagged with a fluorophore (immunofluorescence).

Analysis of well-established biomarkers ER, PR, HER2 and Ki-67 on tumour biopsies by IHC is common practice in most centres and is the technique of choice used in diagnostic pathology for subtyping due to its relatively low cost. The useful prognostic and predictive information gained from their analysis is well-recognised.[170,186]

IHC4 is an immunohistochemical assay and recurrence scoring method analogous to GHI-RS, combining the information from the aforementioned four IHC markers. Studies have shown that IHC4 scoring based on the results of the four assays can be at least as informative for distant recurrence as GHI-RS.[185] However, IHC suffers from issues in reproducibility caused by observer variability, non-standardised assays protocols and scoring systems with erroneous results of HER2 IHC assays reported to be around 12-20%.[185] As reproducibility for IHC measurements is a concern, label-free biosensor detection platforms such as OFETs may compete with the added benefits of reduced cost over GHI-RS.

1.5.4.2 Fluorescent *in situ* Hybridisation (FISH) test

Fluorescent *in situ* Hybridisation (FISH) is a cytogenetic technique used to detect and monitor the genetic abnormalities associated with certain cancers. The method detects and locates the presence of specific nucleotide sequences (DNA or RNA) in tissue samples by utilising complementary fluorescently labelled sequences; a typical image is shown in Figure 23.[187]

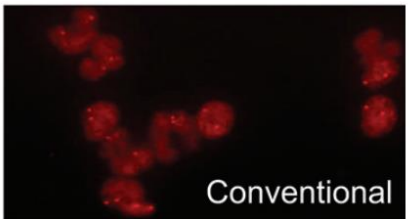

Figure 23 Fluorescence image of a typical pattern of immobilisation. Picture taken from conventional interphase FISH protocol completed on a patient sample with a microscope slide after 14 hours of hybridisation. The probe used was LSI D13S319 for detecting 13q14.3 deletions, present in malignant cells.[187]

The clinical utility of FISH for disease management lies in its high specificity, and selectivity providing a more conclusive assessment of HER2 status than IHC, and it is considered as the 'gold standard' for detection of HER2.[188,189]

Labelled assays in current use for *in vitro* diagnostic tests have well-recognised benefits and also limitations. The requirement for multiple binding events results in high specificity, as the capture and detector elements can specifically bind to the analyte at different sites, as illustrated in Figure 1. However, they can suffer from assay design complications, for example ensuring the signalling moiety does not interfere with the antibody-antigen reaction.[190] Additionally labelling procedures (especially fluorophores) are often expensive (probes are around $90/test), time-consuming and require large sample volumes.[190187] Additionally, IHC and FISH require tissue biopsy to collect the required tissue samples for analysis, impeding the speed of information delivery and making monitoring disease progress and response to treatment difficult.

Some immunoassays have been developed to address these problems to produce POC devices.[191] However, they frequently prioritise speed and ease of use over quantification; lateral flow tests are a prominent example of a simple platform that meets these requirements. Whilst in some applications such as pregnancy test qualitative results are sufficient, clinically relevant results for cancer-related diseases require quantification.[191] Optically based detection techniques are therefore limited by the need for instruments such as colourimeters and spectrophotometers. The required equipment is often expensive, lacks portability and requires trained technicians and a laboratory to perform the multi-step labelling protocols. These factors make them unsuitable for miniaturisation and limit their

potential application as point-of-care devices as tests are usually conducted in centralised laboratories which delay decision making in clinical treatment.

2 Aims and Objectives

EGOFETs are a promising biosensing platform as they benefit from a simple device architecture utilising an aqueous gating solution that allows a low operating potential (<1 V) and in-situ detection of the analyte in solution. In addition, they allow label-free biosensors by benefiting from intrinsic signal amplification and electrical output to produce high sensing performance. The signal is easy to interpret combined with low cost device fabrication, allowing the development of disposable electronic sensing systems ideal for PoC testing.

We seek to investigate the proof of principle for the novel label-free detection of new analytes using an EGOFET-based biosensor. The initial target is the detection of the ECD of HER2, a blood serum biomarker for breast cancer using an appropriate anti-HER2 antibody as the device biorecognition element. The application of Odorant Binding Proteins (OBPs) as the biorecognition element in an EGOFET biosensor for the selective detection of Tetrahydrocannabinol (THC), the psychoactive cannabinoid component of cannabis, is also investigated.

In order to allow the analyte detection two strategies for the functionalisation of the device are investigated through the immobilisation of the biorecognition element to either the gate electrode or the OSC interface.

The gold gate electrode is suitably functionalised using carboxylic acid terminated thiol-based self-assembled monolayer (SAMs) followed by EDC/NHS coupling of the relevant biorecognition element. The performance of the biosensors is verified by the construction of a calibration curve and the selectivity investigated by the analysis of appropriate controls for both the antibody-based detection of HER2 ECD and the OBP-based detection of THC. This is discussed in section 7.

Additionally, to investigate the functionalisation of the OSC interface of the EGOFET device, PMMA copolymers containing reactive carboxylic acid groups are synthesised for deposition *via* spincoating onto the active layer of the device. The polymers are synthesised by radical polymerisation and the reaction conditions optimised. The molecular weight of the polymers and their dispersity are analysed by GPC and the ratio of free carboxylic acid groups ascertained by NMR. The deposition of the polymer on top of the OSC allows the device to be functionalised by appropriate biorecognition element. The method of choice for this functionalisation is the *in situ* covalent attachment of the HER2 antibody by EDC/NHS coupling. The effectiveness of this strategy is assessed by investigating the surface morphology and the bioavailability of the immobilised antibodies is assessed by fluorescent binding assay as shown in section 5.

Different OSCs are compared for use in the bilayer device by the analysis of the electrical performance for both pristine OSC and bilayer devices in section 6. Strategies are examined to optimise the device electrical performance to deliver a low V_T and sufficient I_{DS} for effective operation including the investigation of different gate materials. To create a platform of optimal biosensing capability it is important to minimise any variation in device performance that is not associated with the analyte interaction, such as device stability and reproducibility. Therefore, the development of reproducible devices stable to the exposure to aqueous solutions for at least as long as the duration of the functionalisation procedure are investigated.

The integration of EGOET devices within a flow cell is particularly attractive as it allows more reliable device operation, enables easy fluid handling and reduces sample and reagent consumption and cost. Therefore, the development of an EGOFET biosensor within a flow cell is investigated in section 8. In order to investigate the suitability of the bilayer device for biosensing, control experiments are performed that mimic a sensing assay in the absence of analyte, this allows the investigation of the baseline response and efforts made to minimise any unwanted variation in section 8.3.4 and 8.3.5.

3 Materials and Methods

In this work two different functionalisation strategies have been investigated for use in EGOFET biosensors through the immobilisation of the relevant biorecognition element to either the gate electrode or OSC interface. The gold gate electrode was functionalised through the formation of carboxylic acid terminated thiol-based self-assembled monolayer (SAMs) followed by EDC/NHS coupling of the relevant biorecognition element. The SAMs used are based on previously verified techniques. A mixed SAM consisting of 3-mercaptopropionic acid (3MPA) and 11-Mercaptoundecanoic acid (11MUA) at a 10:1 ratio which was used for antibody immobilisation and is based on the system developed for EGOFET biosensing by Torsi *et al.*,[92,110,192–194] and a lipoic acid based SAM which has recently been demonstrated the selectivity of OBPs by QCM.[195]

P3HT is the most frequently used OSC for OFET devices and the polymer and has found frequent application for use in EGOFET biosensors that operate using gate functionalised sensing systems. Due to P3HTs proven ability to operate well within these conditions we have used this OSC proof of principle devices that use the gate functionalised sensing system. The performance of the biosensors for both the antibody-based detection of HER2 and the OBP-based detection of THC are discussed in chapter 7.

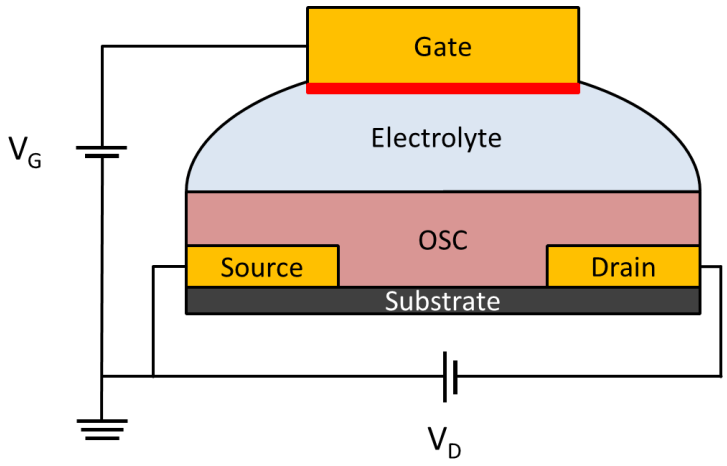

Figure 24 Schematic representation of the developed gate functionalised EGOFET biosensor devices. The gold gate electrode was functionalised using carboxylic acid terminated thiol-based self-assembled monolayers (SAMs) followed by EDC/NHS coupling of the relevant biorecognition element. The resulting biorecognition layer is shown in red and schematic structures of the two different SAM layers used are shown in Figure 45 and Figure 46. Au source and drain electrodes are patterned onto a glass substrate followed by spin-coating of the OSC.

A bilayer EGOFET device was also investigated for use as a biosensor by depositing a thin layer of PMMA-based co-polymer containing carboxylic acid groups on to the surface of an OSC by

spincoating, as shown in Figure 25. The labile carboxylic acid groups introduced to the surface of the interfaces device allowed for the immobilisation of the antibodies by *in-situ* covalent attachment, as described in chapter 5.

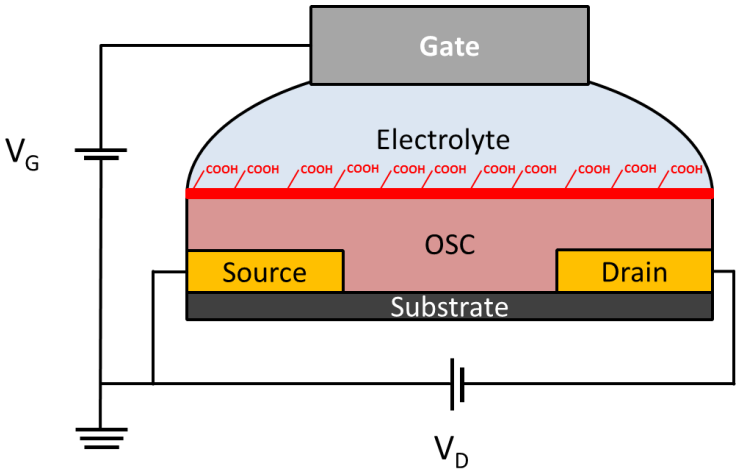

Figure 25 Schematic representation of the developed bilayer EGOFET device. Au source and drain electrodes are patterned onto a glass substrate followed by spin-coating of the OSC and PMMA-based co-polymer containing carboxylic acid groups (shown in red).

The chemical stability of the OSCs used in EGOFET devices is key to ensuring effective and long-lasting device operation, in what is considered a challenging environment for organic semiconductor operation, *i.e.* exposure to water and oxygen. As a result, to widen the scope of OSCs in EGOFET devices we have investigated PBTTT and DPPTTT for use in our bilayer systems. PBTTT (Figure 26a) has been used as an alternative semiconductor to P3HT in several EGOFET type devices.[79,86,97,104,196,197] Relative to P3HT, PBTTT benefits from enhanced environmental stability due to a higher ionisation potential, of around 5.1 eV and improved hole mobility of 1 cm^2 /Vs in thin film transistors compared to 0.1 cm^2/Vs of P3HT.

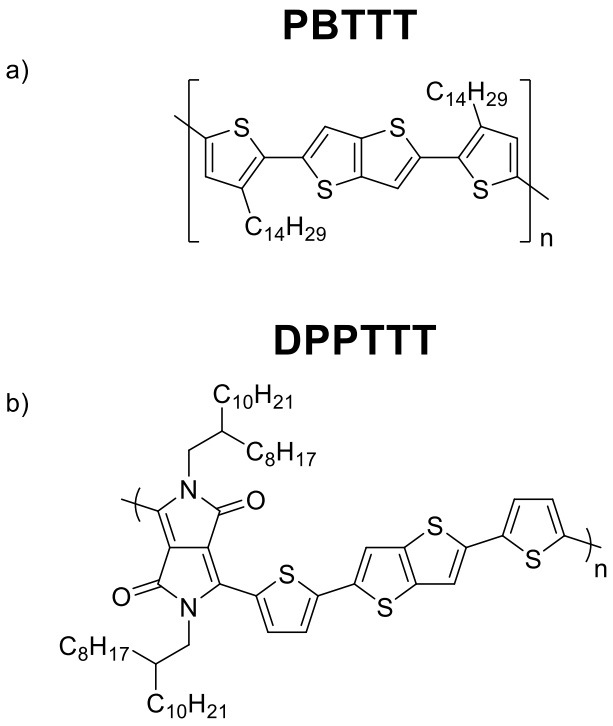

Figure 26 Chemical structures for p-type OSC used in devices. a) PBTTT-C14 b) DPPTTT.

There have only been a few reports of the use of poly(N-alkyl- diketopyrrolo-pyrrole dithienylthieno[3,2-b]thiophene) (DPPTTT) (Figure 26b) as the OSC in EGOFET devices since its first discovery by Li *et al* [54] DPPTTT shows improved environmental stability and mobility relative to PBTTT.[35,52–54] The semiconductor is particularly desirable for EGOFET application due to its relatively high hole mobility (ca. 1 cm^2 /Vs) and low HOMO (-5.2 eV) and well-ordered compact lamellar structure contributing towards its exceptional environmental stability. [105,123] When applied to EGFOET devices the DPPTTT has shown a field-effect mobility of 0.09 cm^2/Vs in water and 0.13 cm^2/Vs in saline solution.[123]

However, in EGOFET devices the gate material has a direct influence on device operation and the extracted figures of merit, in particular V_T due to its relation the gate work function as discussed in section 1.3.5, therefore the nature of the gate metal has also been examined in section 6.3. [62,198]

3.1 Thin film deposition

Device fabrication utilised spin-coating to deposit organic semiconducting films on to pre-defined gold source (S) and drain (D) patterns on glass substrates for use in EGOFET devices. Spin coating is a commonly used deposition technique for the production of uniform thin films (in the range of several nm to µm thickness) through the application of a solution of the desired material to a substrate and rotating at a fixed high speed of up to several thousand revolutions per minute (rpm).

The spin coating process is desirable due to the simplicity of solution based deposition techniques relative to other techniques such as evaporation for the production of uniform thin films. Relative to thermal evaporation, spin-coating procedures require reduced thermal workloads, therefore, limiting thermal degradation of the material, but issues can be encountered with the solubility of the materials in volatile solvents.

In spin coating an initial excess of solution is applied to a substrate and spinning at high speed spreads the material outwards to reduce the thickness. The exerted centripetal force and surface tension of the solution causes the material to spread evenly. The airflow during high-speed rotation is usually sufficient to evaporate most of the residual solvent to leave the desired uniform thin film. If the process is correctly optimised it produces thin films consistently at both the macroscopic and nanometer length scales. Film thicknesses can be measured by surface profilometry (Dektak), the resulting data points can be used to calculate a spin thickness curve with reasonable accuracy and parameters adjusted to give the desired thickness.

Provided the solution sufficiently wets the substrate surface the final film thickness *d*, displays an inversely proportional relationship with angular velocity (*ω):* [199,200]

Equation 30

$$d \propto \sqrt{\frac{1}{\omega^2}}$$

The range of thicknesses achievable from a given concentration covers a relatively narrow range due to the dependence of film thickness on the inverse of spin speed (a factor of around 3-4) and a recommended operating spin speed window of around 600 – 6000 rpm. At lower concentrations, the film thickness can have a more linear dependence on solution concentration whereas at higher concentrations a non-linear relationship can develop due to the effects of solution viscosity.

In order to optimise the spin-coating deposition procedure the film thicknesses and surface properties of the deposited films were investigated by surface profilometry and contact angle measurements. Film thicknesses were evaluated using a Dektak Profilometer to give the thicknesses described in Figure 27 and Figure 28. The instrument operates with a stylus to measure a one-dimensional height profile (with a height resolution of ~ 1nm), in a similar fashion to a one dimensional AFM. In order to quantify the thickness of the soft films a scratch of a few µm is made using a needle tip, the resulting trench depth is equivalent to the thickness of the film.

The water contact angle (WCA) of a water droplet on a solid surface is a useful probe for the hydrophobicity of surfaces on a macroscopic scale to provide qualitative information on the surface properties of surfaces and deposited films. A more quantitative assessment of surface properties is through calculation of the surface free energy (SFE) through extrapolation from the static contact angles of two or more liquids with known values for surface tension.

Many factors need to be considered to produce a film with the desired quality including: spin speed, solution concentration and solvent evaporation rate. In addition the interfacial interaction of the various interrelated components of the spin coating system are also vital in dictating behaviour including the interactions between solvent, material and substrate. Therefore we investigated the variation of the contact angle with various solvents on glass substrate to decipher a good match to ensure efficient film deposition and adhesion during the spin coating procedure (Table 3).

Table 3 Contact angle measurements on glass substrates and thin films deposited on glass substrates of water and various solvents

Surface	Droplet Solvent	Contact Angle (°)
Glass	Water	17
Glass	DCB	35
PMMA film	Water	72
DPPTTT film	Water	104
DPPTTT film	Anisole	42
DPPTTT film	MEK	7
DPPTTT film	Toluene	12
DPPTTT film	n- butyl acetate	11
DPPTTT/PMMA film (from n-butyl acetate solution)	Water	72
DPPTTT/PMMA COOH film (from n-butyl acetate solution)	Water	69
PBTTT film	Water	104
PBTTT film	Anisole	33
PBTTT/PMMA film (from anisole solution)	Water	104
PBTTT/PMMA COOH film (from n-butyl acetate solution)	Water	70

The strong intermolecular interactions and rigidity of the polymer backbone that ensure an OSC shows high mobility in an OFET can hinder processability by limiting the solubility of these polymers. Processing is particularly problematic for higher molecular weight OSC polymers, and the low

solubility at room temperature, necessitates high-temperature processing. To enable processing at elevated temperatures high boiling point chlorinated solvents such as chlorobenzene and DCB were used in device fabrication. High-temperature polymer processing is problematic as oxidation is accelerated in ambient conditions; therefore devices were fabricated in the inert atmosphere of a nitrogen-filled glovebox. Additionally, the poor adhesion of polymer thin films to the substrate at elevated temperature is further complicated by the high viscosity and roughness at lower temperatures, presenting a problem in obtaining consistent electrical properties from the deposited OSC films.

The substrates were sequentially cleaned by sonication in acetone, iso-propanol and methanol, and they were then treated with UV ozone for 25 mins. After the cleaning process the glass surface had a WCA of ~ 17°, indicative of a highly hydrophilic substrate. The OSC were heated in 1,2-dichlorobenzene (DCB) at various concentrations ranging from 3 – 7 mg/ml. The OSCs were processed immediately from the hot solutions in order to avoid precipitation and filtered through a 0.45 µm PTFE filter in order to limit the presence of large aggregates in the deposited film.

An annealing step is usually added to promote crystallisation between semiconductor molecules and remove any residual volatile materials such as solvent, therefore, improving device performance. The use of higher boiling point solvents is known to act as a plasticiser as residual solvent molecules in the film increases the free void space between chains to facilitate movement of polymer chains and orientation and crystallisation during the annealing process.[201]

Thermal annealing was carried at 160 °C for 20 mins for PBTTT and at 140 °C for 1 hour for DPPTTT to yield the finished OSC thin films. The film thicknesses were measured as between 30 - 50 nm by Dektak. This was deemed sufficient to allow complete coverage of the source and drain electrodes, for efficient charge injection while limiting gate leakage. WCA measurements of 104° indicated that the deposited OSC films were highly hydrophobic.

In order to develop the desired bilayer device architecture, the deposition of the PMMA-based polymers was investigated. Initially, the deposition of PMMA on to glass from an anisole solution was effective and confirmed by the shift in WCA to 72° after PMMA deposition. By varying the concentration of the solution good control of the film thickness was achieved, as shown in Figure 27. The 5 mg/ml anisole-based solution was therefore deemed viable for subsequent use in the fluorescent binding assay as it gave reproducible films of 10 nm thickness.

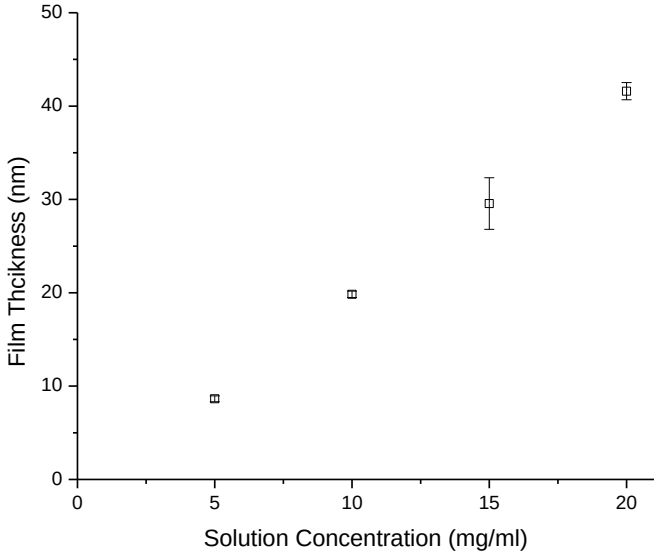

Figure 27 Film thicknesses determined by Dektak of PMMA COOH 10 % in anisole deposited on glass substrates at 2000 rpm.

It was determined that anisole was not an effective solvent within the same concentration regime when depositing on top of the OSC films, as the spin-coating trials returned an unchanged WCA. The high contact angle of anisole on the OSC was indicative of a poor interfacial contact resulting in poor film adhesion; therefore a more hydrophobic solvent orthogonal to the underlying OSC was investigated. Toluene and n-butyl acetate produced good wetting on DPPTTT films as characterised by the low contact angle, subsequent spin-coating of PMMA solutions from both solvents produced film coatings with the expected WCA of ca. 70°, to confirm effective deposition.

The WCA value measured for the pristine OSC films highlights the expected hydrophobicity of these polymers, in accordance with their chemical structures. In contrast, OSC/PMMA COOH produces a less hydrophobic surface as a result of the deposited coating. As demonstrated by the low WCA value of OSC/PMMA COOH surface signifying their relatively hydrophilic character (WCA<90°).

The thickness of the deposited dielectric layer in bilayer type devices can strongly influence the electrical performance of the EGOFET device.[100] Thicker coatings produced an adverse effect on transistor characteristics, with a considerable reduction in drain current observed in the output curves. Therefore the PMMA solution concentration used in spin-coating was investigated as a route to controlling the thickness of the deposited layer (Figure 28). Film thicknesses of varying solution concentrations of PMMA and PMMA COOH 10 % were investigated by spinning the PMMA solutions on top of existing DPPTTT films and then measuring the overall film thickness before and after deposition. It was concluded that concentrations of 7.5 mg/ml for PMMA and 10 mg/ml for PMMA COOH 10 % would achieve devices with reproducible coatings of thickness 15 nm $^{+}/_{-}$ 5 nm.

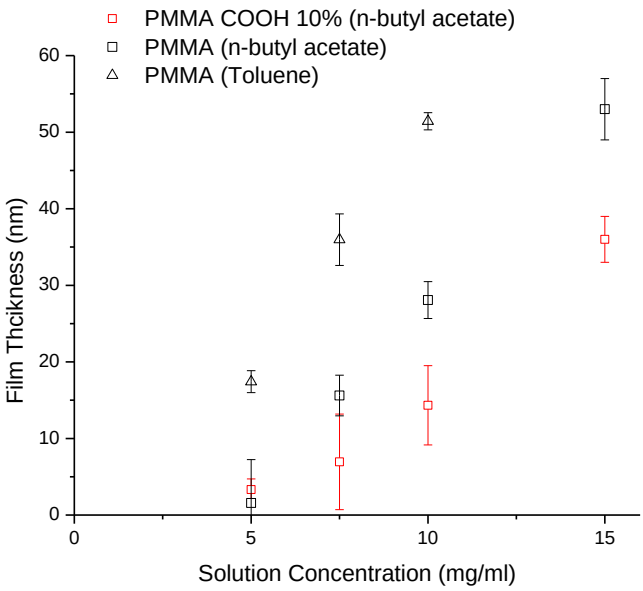

Figure 28 Film thicknesses determined by Dektak of Commercial high molecular weight PMMA and PMMA COOH 10 % in n-butyl acetate and toluene. The samples were prepared by spinning PMMA solutions on DPPTTT films on glass substrates.

The surface morphologies of the deposited films were further investigated by scanning electron microscopy (SEM) and Atomic force microscopy (AFM).

3.1.1 DPPTTT

The AFM topology of the annealed pristine DPPTTT film shows a polymer film consisting of intertwined crystalline nanofibers that create interconnected polymer chain networks (Figure 30a), in agreement with previously observations.[54] The highly ordered nature of the deposited films is indicative of the ability of the polymer chains to self-assemble into ordered lamellar structures in a thin film, which is driven by the strong intermolecular forces from π-π stacking and donor-acceptor interactions. Formation of these interconnected polymer chain networks contributes to the formation of highly efficient pathways for charge carrier transport through the polymer film, which results in the characteristically high charge carrier mobility for this material. Additionally, good film uniformity was achieved with a low root mean squared (RMS) surface roughness of 1.2 nm. While few aggregated nano-particles are visible on the surface indicating the effectiveness of the 0.45 µm PTFE filtering of the solution before deposition. This is also shown by the lack of aggregates on larger scale in the optical microscope images in Figure 29.

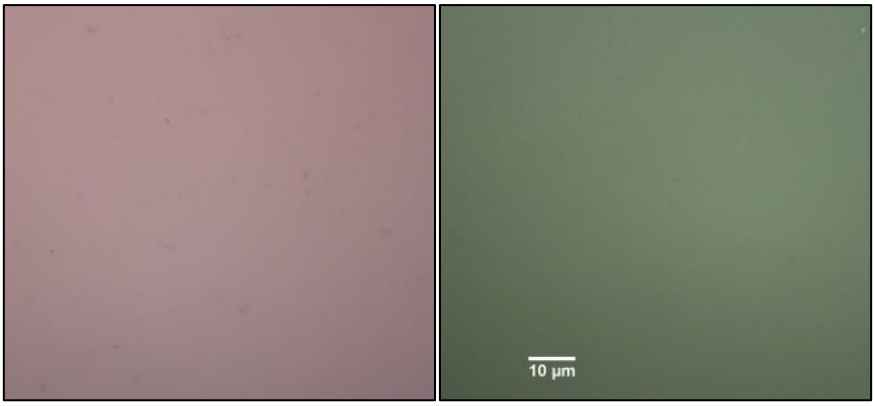

Figure 29 Optical microscope images at x100 magnification of a pristine DPPTTT (left) and a DPPTTT / PMMA COOH 10 % film (right).

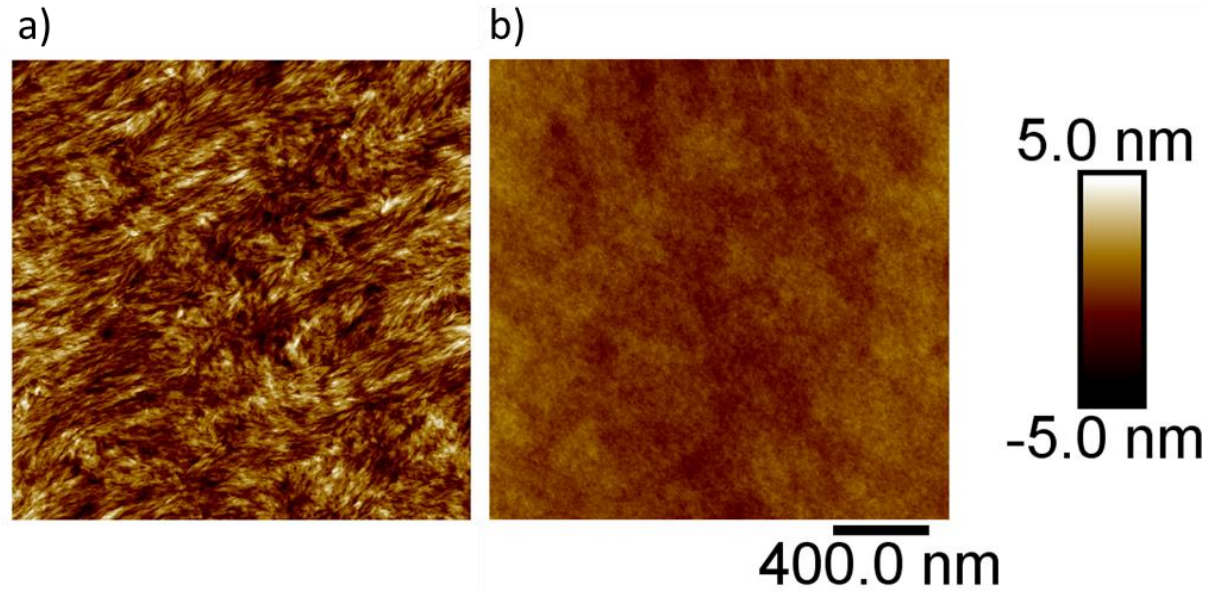

Figure 30 AFM tapping mode 2 µm scans of spin-coated thin films on glass substrates of a) Pristine DPPTTT (RMS roughness = 1.2 nm); b) DPPTTT / PMMA COOH 10 % film (RMS roughness = 0.6 nm).

AFM data was also acquired to investigate the surface morphology of the thin films and the effect of the deposition of a thin film of PMMA COOH copolymer onto the surface of the OSC film. Deposition of PMMA COOH on to the OSC is characterised by a significant reduction in surface roughness and a relatively homogeneous smooth surface morphology, with RMS roughness of 0.6 nm (Figure 30b). This is in line with observations made following PAA coating deposition which showed the planarising effect on the OSC surface of the polymer coating.[97]

In this thesis PFBT treatment was performed onto the gold source and drain electrodes prior to DPPTTT deposition. This allowed the formation of a highly hydrophobic surface for more favourable thin film formation in addition to a constant work function for the contact electrodes aiding in more reproducible device preparation. The successful PFBT SAM formation was noted by the hydrophobic WCA of 90° relative to the hydrophilic untreated gold.

3.1.2 PBTTT

PBTTT typically displays larger crystalline domains in the order of several hundreds of nanometres relative to those of DPPTTT as evidenced by AFM images (Figure 31). Due to the thermotropic liquid crystalline nature of PBTTT, thermal annealing of films within the LC mesophase (120-180 °C) allows a degree of re-organisation of the molecular chains in the LC phase and retention of this degree of structural order through gradual cooling as the structure crystallises.[51] Therefore by annealing at 160 °C allows control of the semiconductor microstructure resulting in the formation of the larger crystalline domains observed, which can enhance charge carrier mobility.[51]

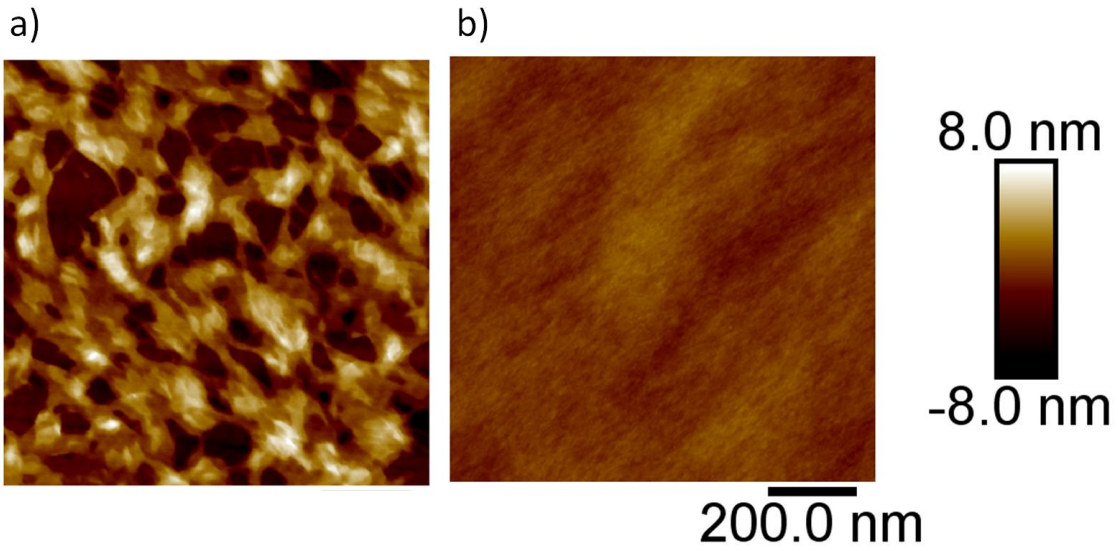

Figure 31 AFM tapping mode 1 µm scans of spin-coated thin films on glass substrates of a) Pristine PBTTT (RMS roughness = 2.7 nm); b) PBTTT / PMMA COOH 10 % film (RMS roughness = 0.6 nm).

SEM surface characterisation was also performed to investigate the surface morphology of the thin films on a larger scale (Figure 32). The SEM of PBTTT film, Figure 32a, shows the grain like features indicative of the crystalline domains in the order of hundred nm previously reported by Manoli et al,[202] and Mulla et al.[97] The absence of aggregated nanoparticles on the deposited thin film again indicates the effectiveness of PTFE filtering of the solution before deposition. Whilst the planarising effect on the OSC surface of the polymer coating is again clearly observed on a larger scale in Figure 32b.

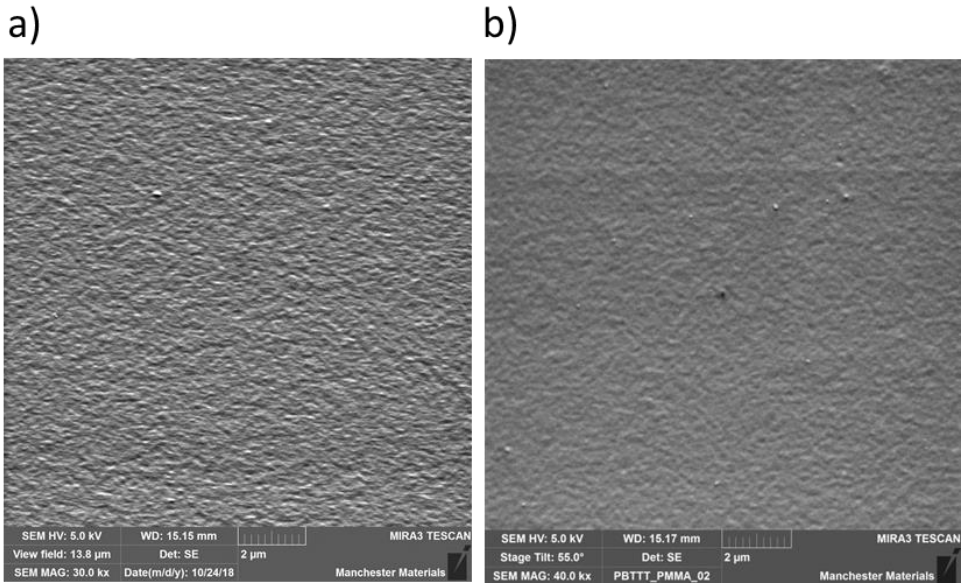

Figure 32 SEM images of spin-coated PBTTT films deposited on glass substrates (a) Pristine PBTTT film; (b) PBTTT film covered by a PMMA COOH layer (b). The samples were prepared by spinning PMMA COOH 10% in n-butyl acetate on PBTTT. The images were obtained by tilting the sample by 55°.

4 Experimental

4.1 Materials

All reagents were obtained from commercial sources and used as received without further purification, unless stated. The OSCs PBTTT-C14 (Mn 39.2kDa; Mw 77.1kDa; PDI 1.99) and DPPTTT (Mn 113kDa; Mw 268kDa ; PDI 2.4) were synthesised by Dr D. Tate in OMIC following previously published procedures.[51,53] rrP3HT was purchased from Sigma Aldrich and used as received without further purification (Mn 31.4kDa; Mw 62.1kDa ; PDI 1.98). The molecular weights of the OSCs were determined by GPC in trichlorobenzene at 140 °C. Poly(methyl methacrylate) (PMMA) (Mw = 996,000) was purchased from Sigma Aldrich and PMMA-COOH polymers were synthesised as outlined in chapter 4.7. Template-stripped ultra-flat gold films was purchased from Platypus Technologies LLC, Nobel Drive, Madison, USA and used immediately after stripping without further cleaning. The gold wire used as the functionalised gate electrodes had diameters of 0.5 mm and 1mm (99.99% purity). The OBPs used in this thesis where raised by Dr K. Cali by methods reported K. Cali *et al*.[195] The gate electrode used for the OBP sensing experiments where prepared by K. Cali for use in this research using the methods validated in this paper. The OBP was immobilised onto the 1mm gold gate electrode via lipoic acid SAM using EDC/NHS coupling.

Water used throughout this thesis was milliQ (type 1) DI water with a specific resistance of 18.2 MΩcm. The PBS solutions used have an ion concentration and osmolality that matches that found in the human body (isotonic). PBS solution was prepared by dilution from DI water from x10PBS solution purchased from Sigma Aldrich. This gave a PBS solution of 0.01 M phosphate buffer, 0.0027 M potassium chloride and 0.137 M sodium chloride in deionized water, pH 7.4. PBS-Tween solution was prepared by the addition of 0.05% (v/v) Tween-20 to the 0.1M PBS solution. The Bovine serum albumin (BSA) used in blocking has a molecular weight of 66 kDa.

4.2 Equipment and measurements

Contact angles: The contact angles were measured using a Kruss DSA-100 goniometer. The contact angles measurements were extracted by using Young Laplace, sessile drop fitting using the Kruss DSA-100 software.

Atomic Force Microscopy (AFM): AFM images were recorded on a Bruker Multimode 8 in Peak Force tapping mode at a resolution of 512 × 512 pixels. The cantilevers had a spring constant of approximately 0.350 Nm^{-1} with a resonant frequency of approximately 50–80 kHz. A modulation frequency of 2 kHz was used.

Fluorescence Microscopy: Images were collected on a Olympus BX51 upright microscope using a 20x objective and captured using a Coolsnap ES camera (Photometrics) through MetaVue Software (Molecular Devices). Specific band pass filter sets for FITC were used for the fluorescein labelled secondary antibodies to prevent bleed-through from one channel to the next. The exposure time was set to 1.5 seconds for HER2 antibody assay. Images were then processed and analysed using ImageJ software.

Spin coating: The solutions were spin-coated onto pre-prepared substrates using a Laurel WS-4003-6NPP/LITE spin-coater inside a nitrogen filled glove box, unless stated otherwise.

Device analysis: electrical measurements of the EGOFET devices were carried out using a semiconductor parameter analyser (Agilent B1500A) equipped with 3 SMUs and all measurements were taken in ambient air. The droplet-based devices were analysed using a 3 point probing station. A droplet of water or electrolyte was applied over the channel area to act as the gating electrolyte in the EGOFET device. 4 µl droplets were used for shadow mask design devices and 8 µl droplets for the IDE design devices. A tungsten-tip, gold or platinum wire was dipped into the droplet and used as the gate electrode. The flow cell devices were analysed by flooding the cell chamber with water or PBS using a syringe pump.

The characteristic device parameters, field effect mobility of holes (μ) and threshold voltage (V_T), were extracted from the transfer characteristics in the saturation regime. Mobility is estimated from the slope of $I_d^{1/2}$ vs V_g curve, but is presented as the parameter ($\mu * C$) combined with capacitance (C_i), which was not determined.

4.3 Device Fabrication

Devices using Shadow Mask designed Source and drain electrodes:

Glass Corning 7059 polished plates (20mm x 20mm x 0.7mm thick) were used as the device substrate. The substrates were sequentially cleaned by sonication with acetone, iso-propanol and methanol (Sigma Aldrich reagent grade) for 10 minutes each. The substrates were then rinsed with acetone and dried with a stream of N_2 and then treated with UV-Ozone for 25 mins (Bioforce Nanosciences UV/Ozone Procleaner Plus). Source and Drain electrodes were deposited using Cr/Au (5/40 nm) using a thermal evaporator under 2 x 10^{-6} Torr at room temperature. The electrode dimensions were defined by using a shadow mask with a set channel width and length (L= 60 µm / W= 1mm). The prepared substrates were then stored in the glove box until further use. Prior to OSC deposition the substrates were sequentially rinsed with acetone, iso-propanol and methanol dried

with a stream of N_2 and then treated with UV-Ozone for 25 mins and were ready for immediate PFBT treatment.

Devices using IDE designed Source and drain electrodes:

The substrates were fabricated by the Centre for Process Innovation (CPI). Corning Eagle glass plates (20mm x 20mm x 0.7mm thick) were used as the device substrate. Ti/Au layers (5/50nm thickness) were sputtered onto the substrates and the source and drain electrodes were patterned by photolithography. A variety of channel lengths were fabricated to give devices with channel lengths of L= 60 µm, 40 µm, 20 µm and 10 µm and with the same channel width of W= 16.9 mm. The substrates were sequentially cleaned by sonication with water, acetone, iso-propanol and methanol for 10 minutes each. The substrates were then rinsed with acetone and dried with a stream of N_2 and then treated with UV-Ozone for 25 mins and were ready for further processing or immediate PFBT treatment for DPPTTT devices.

PFBT treatment

Following the cleaning procedure, the substrates were immersed in a 10 mM solution of 2,3,4,5,6-pentafluorothiophenol (PFBT) in toluene, for 15 minutes. The substrates were then rinsed in toluene and dried with a stream of N_2 and immediately transferred to the nitrogen filled glovebox for further processing.

PBTTT-based device fabrication

A solution of PBTTT of the desired concentration between 3-7 mg/ml was dissolved in dichlorobenzene with stirring overnight at 100 °C in a nitrogen filled glovebox. The solution of PBTTT was then heated to 120 °C and filtered through a 0.45µm filter directly onto the prepared substrate and spin-coated at 2000 rpm for 1.5 min. The samples were immediately annealed at 160 °C for 20 mins on a hot plate and allowed to cool slowly to room temperature.

DPPTTT-based device fabrication

A solution of DPPTTT (7 mg/ml) in dichlorobenzene was prepared by stirring overnight at 100 °C. The solution was heated to 140 °C, filtered through a 0.45 µm filter and spin-coated directly onto the prepared substrate at 1500 rpm for 90 seconds. The samples were then immediately annealed at 140 °C for 60 mins on a hot plate.

P3HT-based device fabrication

A solution of P3HT (5 mg/ml) was dissolved in chlorobenzene with stirring for 3 hours prior to use at 80 °C in a nitrogen filled glovebox. The of P3HT solution (100 µl) was then applied directly onto the

prepared substrate and spin-coated at 2000 rpm for 2 min. The samples were immediately annealed at 90 °C for 60 mins on a hot plate.

Bilayer device fabrication

Bilayer devices where fabricated by spin-coating a 0.45µm filtered PMMA 10% COOH co-polymer solution (10 mg/ml) in n-butyl acetate on top of the semiconductor layer at 2000 rpm for 2 mins after annealing. Samples were annealed at 80 °C for 1 hours on a hot plate. All spin-coating and subsequent annealing was performed in a N_2 filled glove box.

Evaporated gold substrates for AFM

A Gold layer was deposited onto a SiO_2 substrate (10 mm x 10mm) using the same cleaning method described for shadow mask designed source and drain electrodes. The substrate was patterned with Cr/Au (5/100 nm) using a thermal evaporator under 2 x 10^{-6} Torr at room temperature. The substrates were then sequentially rinsed with acetone, iso-propanol and methanol dried with a stream of N_2 and then treated with UV-Ozone for 25 mins and were ready for immediate SAM treatment.

4.4 Fluorescent binding assay

4.4.1.1 Substrate preparation

Oxidised silicon wafers with a thermally grown oxide layer (300 nm thickness) were cut into 1 cm x 1 cm sized pieces for use as the substrate in the assay. The substrates were cleaned by sonication with acetone and iso-propanol, for 10 and 5 minutes respectively. The substrates were then rinsed with isopropanol, ethanol and acetone and dried with a stream of N_2. The substrates were then treated with O_2-plasma for 2 min at 25 °C. Solutions of 40 µl of 5 mg/ml PMMA co-polymer in anisole was applied to the substrate and spin coated at 2000 rpm for 1 min under ambient conditions in a laminar flow cabinet. Each substrate is then annealed on a hot plate for 2 hours at 100 °C.

A solution of 0.4M EDC and 0.1M NHS in water was prepared. Each substrate was then incubated with 40 µl of the solution in the dark at RT for 30 min and then rinsed with 0.1M PBS solution. A 270 nM solution of primary antibody in 0.1M PBS-Tween was prepared. Each substrate was incubated with 25 µl of primary antibody solution in the dark at RT for 2 hours and then rinsed with 0.1M PBS-Tween.

The substrate was then incubated with 60 µl 30 µg/ml BSA blocking solution/ in 0.1 M PBS for 1h at RT in dark. Following incubation substrates are washed with PBS-Tween, water and dried with a stream of N_2. A 75 nM solution of fluorescently labelled secondary antibody in sample buffer (0.1 M

PBS, 0.05% (v/v) Tween-20, pH7.4) was prepared, and the substrate incubated with 60 µl in the dark at RT for 1 hour. Following incubation substrates are washed with PBS-Tween, water and dried with a stream of N_2, then stored in the dark for analysis by fluorescence microscopy.

0.1 M Phosphate-buffered saline (PBS) (pH 7.4) was made in the laboratory and was prepared using 150 mM NaCl, 68 mM Na_2HPO_4, 32 mM NaH_2PO_4 and pH adjusted with 1M HCl and 1M NaOH. PBS-Tween solution was prepared by the addition of 0.05% (v/v) Tween-20 to the 0.1M PBS solution.

4.5 Gate functionalised EGOFET biosensors

The devices described in Chapter 7 where measured using the chambers developed and discussed in Figure 69 - Figure 71. Each chamber was filled with ~30 µl of aqueous liquid used as the gating medium and the gold gate electrode was held in place directly above the channel using the PTFE holder. The electrical measurements where then performed in a probe station using an Agilent B1500A Semiconductor Parameter Analyser (Figure 121). The devices were prepared with interdigitated source and drain electrodes with a channel lengths of L= 20 µm and channel width of W= 16.9 mm, P3HT was used as the organic semiconductor.

4.5.1 Gate functionalisation with 3MPA/11MUA and HER2 Antibody

Before functionalisation the 0.5mm diameter gold wires used as the gate electrodes were cleaned by immersing in piranha solution (H_2SO_4/H_2O_2, 3:1, v/v) for 10 min and then washed thoroughly with DI water. The cleaned electrodes where then used immediately to chemisorb the self-assembled monolayer using a 10 mM solution consisting of a 10:1 molar ratio of 3-mercaptopropionic acid (3MPA) to 11-Mercaptoundecanoic acid (11MUA). The cleaned gold surface was immersed in the 3-MPA and 11-MUA solution and kept in the dark under N_2 for 18 h at RT. After functionalization the SAM-modified gold electrodes were rinsed with absolute ethanol to give the chemSAM.

The carboxylic groups of the chemSAM were then activated by immersion in an aqueous solution of 200 mM EDC and 50mM sulfo- NHS for 2 h at RT. Following activation, the gold wires are rinsed with DI water and then placed in a solution composed of 0.54 µM (0.1 mg/ml) of HER2 monoclonal antibody in PBS, incubated for 2 h at RT and then rinsed with water. The wires were then immersed in a solution of ethanolamine 1M in PBS for 1 h and then rinsed with water. The formation of the BioSAM functionalised electrodes was completed by immersion in a 1.5 µM (0.1 mg ml^{-1}) BSA solution in PBS 10mM for 1 h then rinsed with water.

4.5.2 Gate functionalisation with Lipoic acid SAM and OBP

The gate electrode used for the OBP sensing experiments where prepared by K. Cali for use in this research using the methods validated in the paper.[195] The OBP (GTP_pigF88W) was immobilised onto the 1mm diameter gold gate electrode via lipoic acid SAM using EDC/NHS coupling.

4.5.3 Calibration curve measurements

The EGOFET device is first incubated in water for 18 hours in DI water in order to stabilise the device performance. The I_{DS} was further stabilised by repeating the measurement of the transfer curve of the P3HT EGOFET using a bare gold gate electrode until three successive curves perfectly overlap. All the subsequent data are recorded on devices that where cycled until the traces overlap. The bare gold electrode is then replaced with the functionalised gate electrode which had been incubated in the blank sample solvent for 10 mins and then rinsed with water.

The transfer curve measurement is recorded immediately before the start of the assay and recorded as the baseline value (I_0) from which the relative device response to the analyte is recorded. Prior to the initial analyte concentration, the functionalised gate was incubated in sample solvent with no analyte (blank) in order to verify the stability of the baseline value before further testing which was only continued when $\Delta I/I_0$< 5%. The analyte measurements are recorded in order of sequentially higher concentration.

The HER2 ECD detection assay is performed by measuring the transfer characteristics of the EGOFET device after incubation of the functionalised gate electrode in PBS standard solutions of HER2 ECD ranging from 1 x 10^{-18} M (attomolar, 1 aM) to 1 x 10^{-8} M (10 nM) nominal concentrations. PBS is used as the sample solvent. All the electrical measurements using the BioSAM electrodes are performed in DI water. The gate electrode is incubated separately in the analyte solution for 20 mins, rinsed in DI water and then returned to the EGOFET for electrical measurement.

The cannabinoid sensing assays were performed by measuring the transfer characteristics of the EGOFET device after incubation of the device including the functionalised gate electrode in 2% IPA in DI water solutions spiked with analyte concentrations covering the range 1 x 10^{-14} M (10 fM) to 1 x 10^{-7} M (100 nM). 2% IPA in DI water is used as the blank or sample solvent throughout the experiment. The analyte measurements are recorded using the analyte solution as the gating medium after incubation of the functionalised gate in the analyte filled device well for 5 mins.

4.6 Procedure for flow cell functionalization and measurements

The set up shown in Figure 120 was used for the control of fluids and electrical measurements in the flow cell experiments described in chapter 0. A three-way stopcock tap was used to connect to two syringes containing the prepared fluids needed for the experiment. The syringes were mounted to separate syringe pumps so that the flow rate could be controlled but only one syringe pump was used at a time. The fluid was introduced into the cell through by PTFE tubing connected to the stainless-steel inlet tube. The system dead volume (including the three-way stopcock and tubing) was ~150 µl. For electrical measurements the flow cell was filled with the appropriate electrolyte solution at a flow rate of 70 µl/min. The electrical measurement is recorded in a 'static' environment, with no flow of electrolyte.

The functionalization procedure carried out with the flow cell involved the same reagents and procedure that was described in section 4.4. However, all fluid handling (rinsing, incubation and introduction of new solutions) was performed within the flow cell set up. The steps in the procedure using PBS and PBS Tween (rinsing) was performed at 70 µl/min for 2.5 mins (175 µl). The steps in the procedure that involved the chemical reagents such as antibodies, blocking and analyte were performed at 85 µl/min for 3.5 mins (300 µl). Subsequent electrical measurements were then taken. In the calibration curve experiment each analyte concentration was prepared in 0.1M PBS. Each analyte was introduced to the cell and then incubated for 20 mins, followed by rinsing with PBS and the measurement was taken in the 'static' environment. The next analyte concentration was then investigated in sequential order from the lowest to the highest concentration. The baseline experiment described in section 8.3.4 follows the same procedure however the analyte samples were replaced with PBS solution (blank samples). For clarity the HER2 ECD concentrations that were investigated are shown in Table 4.

Table 4 A range of HER2 ECD concentrations are shown in ng/ml and the corresponding concentration in M and pM.

ng/ml	M	pM
0.1	1.41E-12	1.41
1	1.41E-11	14.1
10	1.41E-10	141
100	1.41E-09	1410
1000	1.41E-08	14100

4.7 PMMA – COOH synthesis

All reagents were obtained from commercial sources and used as received without further purification, unless stated. If not mentioned otherwise, reactions were carried out under an argon atmosphere using standard Schlenk techniques. ^{1}H NMR NMR spectra were recorded at 400 MHz on a Bruker Avance AV 400 MHz Ultrashield spectrometer with the stated solvent at 25 °C.

Gel permeation chromatography (GPC) was carried out in THF using a Viscotek GPCmax VE2001 solvent/sample module with 2 _ PL gel 10 lm MIXED-B + 1 _ PL gel 500A columns, a Viscotek VE3580 RI detector and a VE 3240 UV/VIS multichannel detector. 1 mL/min flow rate was used and the system was calibrated with polystyrene standards and *n*-dodecane as a flow marker. Fourier transform infrared (FT-IR) spectroscopy was performed on a PerkinElmer SpectrumRX 1 FT-IR spectrometer.

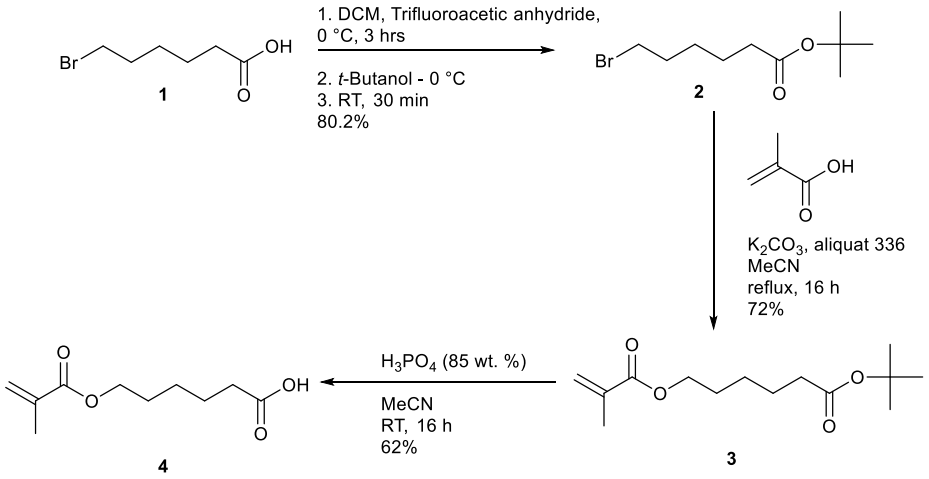

Scheme 1 Reaction scheme for the synthesis of carboxylic acid functionalised co-monomer

4.8 Synthesis of tert-butyl 6-bromohexanoate (2)

6-Bromohexanoic acid (20 g, 102.5 mmol) was dissolved in anhydrous dichloromethane (250 ml) under an inert atmosphere and the vessel cooled to 0 °C. Trifluoroacetic anhydride (48.1, 31.8 ml, 229 mmol) was added dropwise and stirred for 3 hours. *tert*-Butanol (25.7 g, 33.2 ml, 347 mmol) was added to the solution dropwise at 0 °C and after allowing to warm the reaction mixture was stirred at room temperature for 30 min. The reaction mixture was then quenched washed with water (200 ml) and extracted with DCM (2 x 200ml). The combined organic layers where washed with brine (2x 200 ml) and then dried over magnesium sulfate before removing the solvent *in vacuo*. The crude product was separated *via* flash silica column chromatography (light petroleum ether/ ethyl acetate, 95:5) to yield *tert*-butyl 6-bromohexanoate **2** as a colourless oil (20.7 g, 80.2%).

^{1}H NMR (400 MHz, $CDCl_3$) δ ppm 1.48 (9 H, s and 2H, m), 1.62 (2 H, m), 1.88 (2 H, m, *J*=7.2 Hz), 2.24 (2 H, t, *J*=7.4 Hz), 3.42 (2 H, t, *J*=6.8 Hz).[203,204]

4.9 Synthesis of tert-butyl 6-(methacryloyloxy)hexanoate (3) [203,205]

Methacrylic acid (3.37 g, 25.2 mmol), **2** (4.49 g, 18.0 mmol) and Aliquat 336 (4.00 g, 9.90 mmol) were dissolved in anhydrous acetonitrile (80 ml) under an inert atmosphere. Potassium carbonate (4.18 g, 30.2 mmol) was added in portions and the reaction mixture was refluxed for 16 hours. The reaction mixture was allowed to cool to room temperature, water (80 ml) was added and the product extracted with dichloromethane (80 ml). The combined organic layers were washed with water (3 x 80 ml) and brine (80 ml) and then dried over magnesium sulfate before removing the solvent *in vacuo*. The crude product was separated *via* flash silica column chromatography (light petroleum ether/ diethyl ether, 7:2) to yield *tert*-butyl 6-(methacryloyloxy)hexanoate **3** as a colourless oil (3.31 g 72%). In order to stabilise the monomer against polymerisation 30 ppm of hydroquinone monomethyl ether was added.

^{1}H NMR (400 MHz, $CDCl_3$) δ ppm 1.41 (9 H, s and 2H, m), 1.66 (4 H, m), 1.94 (3 H, s), 2.23 (2 H, t, *J*=7.4 Hz), 4.14 (2 H, t, *J*=6.5 Hz), 5.54 (1 H, m), 6.09 (1 H, d, *J*=0.5 Hz). [203]

4.10 Synthesis of 6-(methacryloyloxy)hexanoic acid (4) [203,205]

Compound **3** (3.00 g, 11.7 mmol) was dissolved in acetonitrile (2.21 mL) and aqueous phosphoric acid (85 wt. %, 2.21 mL, 30.4 mmol) was added dropwise whilst stirring. The reaction mixture was stirred for a further 16 hours at room temperature. Water (50 ml) was then added and the product extracted with ethyl acetate (3 x 50 mL). The combined organic layers were dried over magnesium sulfate before removing the solvent *in vacuo*. The crude product was separated *via* flash silica column chromatography (ethyl acetate/light petroleum ether, 1:3) to yield 6-(methacryloyloxy)hexanoic acid **4** as a colourless oil (1.36 g, 62.2%).

^{1}H NMR (400 MHz, $CDCl_3$) δ ppm 1.46 (2 H, s), 1.71 (4 H, m), 1.95 (3 H, s), 2.39 (2 H, t, *J*=7.4 Hz), 4.16 (2 H, t, *J*=6.5 Hz), 5.56 (1 H, m, *J*=3.1 Hz), 6.10 (1 H, m).[203]

Polymerisation reaction.[203]

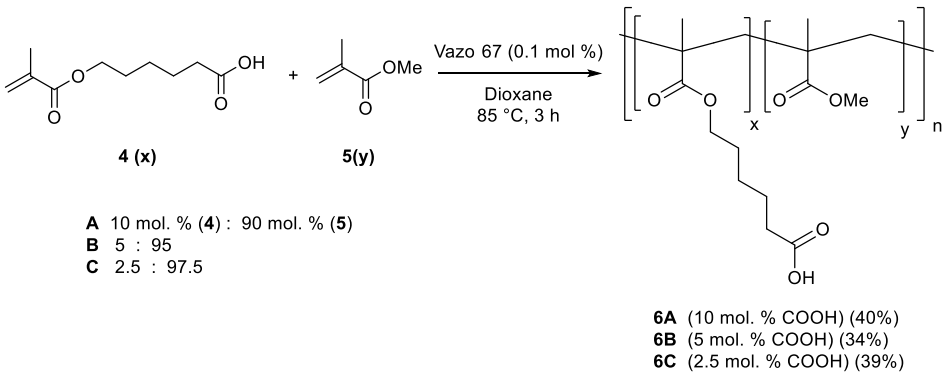

Scheme 2 Reaction scheme for polymerisation reaction of PMMA co-polymers

The three different PMMA based carboxy co-polymers where synthesised by free-radical polymerisation reaction in a variety of solvent, (THF, toluene and dioxane) using Vazo 67 as an initiator. The abbreviations for the co-polymers relate to the initial theoretical molar ratio of carboxylic acid containing monomer (**4**) present in the co- polymer. The same procedure was used for the synthesis of each co-polymer only varying the ratio of monomers, methyl methacrylate (MMA) (**5**) and 6-(methacryloyloxy)hexanoic acid (**4**), used as shown in Table 5.

Table 5 Ratio of co-monomers used in the synthesis of **6A-C**

Polymer	Mass of MMA (5) (g)	Moles of MMA (5) (mmol)	Mass of (4) (mg)	Moles of (4) (mmol)
6A	0.90	9.0	200	1.00
6B	0.95	9.5	100	0.50
6C	0.98	9.8	40	0.20

The monomers (MMA) (**5**) and 6-(methacryloyloxy)hexanoic acid (**4**) were dissolved in the reaction solvent (20 ml) and degassed by freeze-pump-thaw cycles. A separate solution of Vazo 67 was degassed by 3 freeze-pump-thaw cycles and was added to the reaction mixture.

The reaction mixture was heated to 85 °C and the reaction was allowed to proceed for 3h. The reaction mixture was allowed to cool to room temperature and the polymer precipitated through dropwise addition to 200 ml of n-hexane. The crude polymer was collected by filtration before washing by Soxhlet extraction with n-hexane for 16 hours followed by drying in a vacuum oven at 40 °C to yield the copolymer as a white solid in the yields reported in Table 6.

^{1}H NMR (PMMA-COOH (10%) **6a**, 400 MHz, $CDCl_3$, δ): 3.96 (s, 2H), 3.61 (s, 27H), 2.38 (s, br, 2H), 2.1-1.6 (22H), 1.42 (s, br, 4H), 0.78-0.96 (m, 30H); IR: ν = 2986, 2947, 2115, 1730, 1487, 1447, 1268, 1237, 1193, 1147, 991, 963, 751 cm^{-1}

Table 6 Reaction yields from synthesis of PMMA copolymers **6A**-**C** using dioxane as the reaction solvent.

Polymer	Weight of product (mg)	Yield (%)
6A	434	39.7
6B	357	34.0
6C	400	39.3

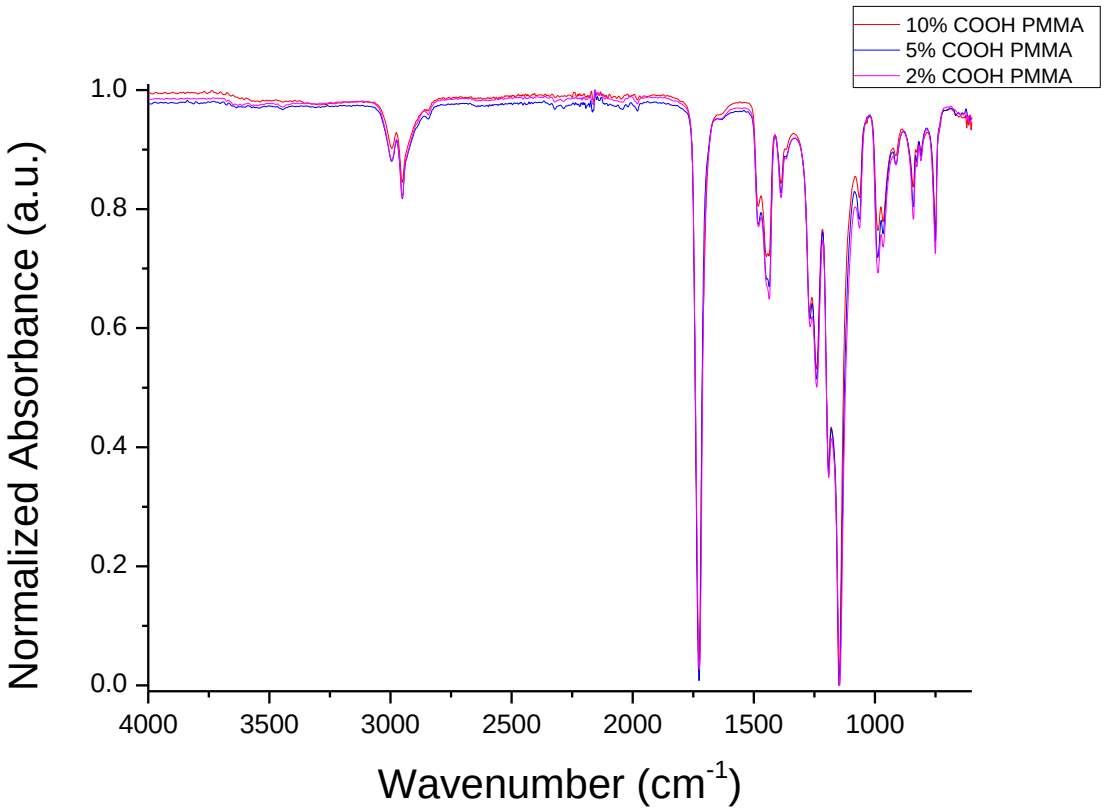

Figure 33 FT-IR spectra of PMMA/PMMA-COOH. (**6A, 6B, 6C**).

5 Immobilisation strategies

OFETs have been identified as a promising platform for the development of low-cost point-of-care biosensors. The *in-situ* detection of biomarkers in biological media is vital in producing a point-of-care device, therefore aqueous operation in water and biomimetic solutions, as shown in Figure 34, are of particular interest. However, OFETs with classic architecture have limited performance in aqueous operation.[29] In contrast, EGOFETs benefit from a simple device architecture which uses an aqueous gating solution allowing a low operating potential and compatibility with well-established biorecognition processes for *in-situ* detection of the analyte in solution.[88]

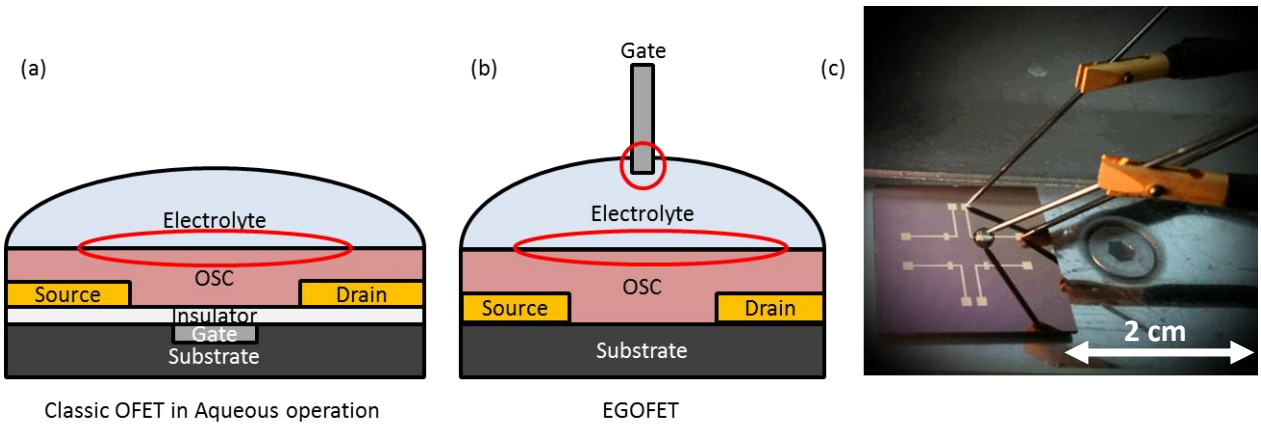

Figure 34 OFET biosensor architecture (a & b). The red circle indicates interfaces available for functionalisation and detection of biomolecules. Picture of water gated field effect transistor as fabricated in OMIC (c).

In order to allow the detection of biomolecules a device interface must be functionalised with appropriate bio-recognition elements. EGOFET biosensors therefore rely on the immobilisation of biorecognition elements to either the gate electrode or the OSC interface, as indicated in Figure 34. Numerous functionalisation strategies have been explored and can broadly be categorised as depending on adsorption, covalent attachment or affinity interactions to immobilise the bio-recognition elements to the desired interface.[29,88] In this work the functionalisation of both the gate electrode and the OSC interface are investigated for use in EGOFET biosensor devices. The development of the immobilisation methods used for the biosensor devices is discussed in this chapter and separated into sections which discuss the strategy for either gate electrode (section ….) or the OSC interface for which a bilayer system is developed (section 5.1).

5.1 Bilayer functionalisation

The immobilisation of the biorecognition element to the OSC interface is a strategy for which a wide range of techniques have been explored.[90] Optimisation of the orientation and surface coverage of the immobilised biorecognition elements are needed in order to maximise their effectiveness and retain specificity. Additionally, it is desirable for the deposition process to have minimal detrimental impact on the OSC and its electrical performance, as well as being simple, fast and inexpensive. With this regard, physical adsorption holds an advantage,[94] however it lacks control of the orientation, homogeneity in coverage or the stability of other techniques.[90]

In contrast, covalent attachment of the biorecognition elements has the potential to allow optimisation of orientation and coverage. Whilst a pertinent risk is denaturing the biomolecules during the anchoring step by covalent reactions, strong electrostatic interactions from physisorption can also have similar effects on antibodies conformational structure.[94] Additionally, covalent immobilisation presents a more stable and robust attachment to withstand the required washing procedures necessary for biosensor and assay integration within a flow cell system.

Covalent immobilisation requires the formation of chemical bonds between reactive groups on the biomolecules and complementary labile groups introduced to the interface.[90] This can be made possible by introducing functionalities such as hydroxyl (-OH), amine ($-NH_2$) & carboxyl (-COOH) groups to the interface surface for use in *in situ* surface confined reactions with bio-recognition elements.

Introduction of reactive functional groups to the interface has been achieved through deposition of a second layer on top of the OSC,[79,97] blending the OSC with another material or modification of the OSC structure.[84,203] Each method is recognised to have its limitations. Pre-attachment of the biosensing element may not be suited for use with all biomolecules (e.g. antibodies) which lack stability in the harsh organic solvents needed for processing. The introduction of non-conductive reactive functional groups to the bulk OSC introduces trap sites which negatively impact on the electrical performance.

The use of bilayer devices has been noted as a technique to avoid chemically modifying the structure OSC whilst still introducing the labile groups to the electrolyte interface,[99] although at the compromise of increasing the distance of the sensing element from the active channel, which may reduce sensitivity. Sensing can occur in this device configuration as the bio-functionalised dielectric surface coating is capacitively coupled to the OSC underneath, which influences the active channel upon analyte interaction.

PMMA is a cost-effective material which is in mass production for use in a variety of applications including Perspex glass, medical implants and thin film dielectrics.[206–208] PMMA can also be used as a device insulator/dielectric in OFET devices.[107,208] The commercially available products are inert materials that do not contain reactive functional groups and therefore frequently require treatment in order to impart some functionality to allow covalent immobilisation of bio-recognition elements. Physical and chemical treatment methods of PMMA include plasma processing, surface reactions using wet chemistry (hydrolysis and aminolysis) and UV treatment.[97,209–211] However these are limited by ageing effects, instability of newly formed functional groups and difficulty in controlling surface etching which can result in the formation of irregular surfaces.[209–211] Additionally, the required harsh treatment is likely to cause some damage to the underlying OSC within the EGOFET device structure.[100] Therefore there is a need for the development of stable and robust materials with a high level of control of the surface concentration of functional groups.

The alternative is the deposition of ultra-thin-films onto the surface of the OSC, to form the bilayer device structure, with materials that already contain the reactive functional groups required for *in-situ* covalent attachment of the recognition elements. PE-CVD is one route to the deposition of hydrophilic layers rich in reactive groups onto the OSC.[100] Whilst UV-crosslinked spin-coated poly(acrylic acid) (PAA) films have also been utilised as an immobilisation layer in to produce the stable coating with a high density of COOH groups demonstrated its use in EGOFET sensors.[97] However both techniques require processing steps which have the potential to damage the underlying OSC. The development of solution processable polymers for use as dielectric film, requiring minimal further processing following spin-coating, is therefore highly desirable.

Co-polymer based surface coatings have been well studied for use in applications in surface protein immobilisation for other biosensing assays, such as ELISA.[210,212–217] Acrylic-based polymers are a common choice due to the availability of carboxyl groups for *in situ* functionalisation by EDC/NHS reactions to the amino groups of the target bio-recognition element.

The main advantages of using PMMA co-polymer are its low cost relative to a functionalised semiconductor co-polymer such as P3HT it is therefore more realistic for the large-scale production of cheap disposable devices. The insulating bilayer may also the benefit of protecting the lower layers from the electrolyte improving device stability; also, it can be used in combination with any conjugated polymer in the active layer provided an orthogonal solvent is used during deposition, allowing scope for easy improvements in device production and performance in terms of processability, mobility, air and moisture stability.

Different loadings of COOH bearing methacrylic acid monomer within PMMA-MA co-polymers have been studied for their effectiveness in protein surface immobilisation for various applications including ELISA, but no comparative study has yet been reported for their effects in OFET based sensors.[211,212,215,218,219] A higher ratio of hydrophilic groups, such as acrylic acid subunit, in the receptor layer decreased the stability of the polymer film to the multiple aqueous washing steps used in functionalisation.[103] Therefore it is important to optimise the concentration of carboxyl groups within the receptor layer to provide a balance of stability to washing and the coupling capacity for biofunctionalisation.

In order to facilitate post polymerisation bio-conjugation monomers incorporating pendant carboxylic acid side groups on a 6-carbon spacer where used to reduce steric crowding of the reactive site and provide more accessible COOH groups. Tethering a bioactive compound via spacer can improve bioactivity by reducing the steric constraints and shielding the compound from hydrophobic interaction induced denaturation.[210] The surface concentration of functional groups can lead to protein de-activation by steric repulsion (over-functionalisation) or protein denature in close proximity of the polymer surface (low surface coverage of functional groups).[210] Therefore a variety of monomer concentrations were explored in order to allow investigation into the optimum number of surface COOH groups. Previous PMMA-MA co-polymers containing a 10% loading of COOH containing monomers demonstrated the highest sensitivity in ELISA based assays, we will also synthesise polymers with lower loadings to gauge their effectiveness in EGOFET devices.[211,212,215,218]

5.1.1 PMMA co-polymer synthesis

Polymers for use as thin film coatings that can act as a modified dielectric layer, derived from poly(methyl methacrylate) (PMMA) containing carboxylic acid groups (-COOH) were synthesised to allow the active channel of EGOFET devices to be functionalised with sensing elements.

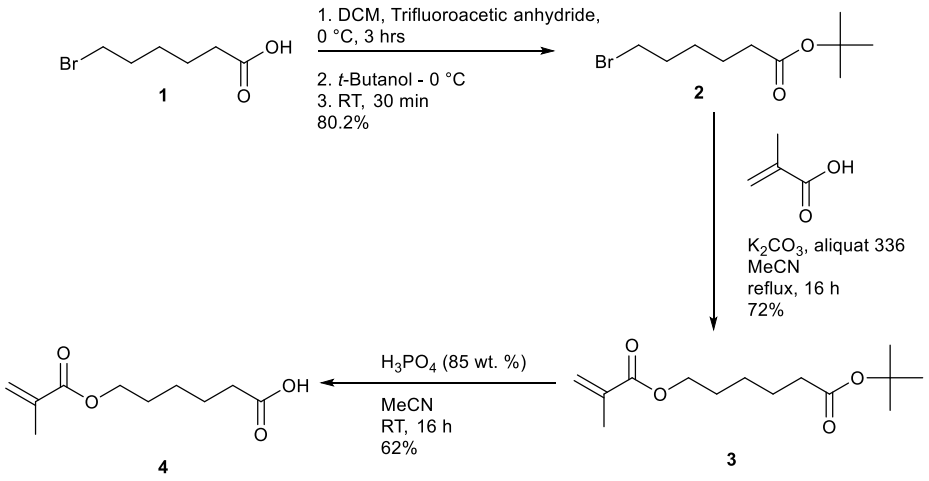

Scheme 3 Reaction scheme for the synthesis of carboxylic acid functionalised co-monomer

In order to achieve this tailored monomer **4** was synthesised by the route shown in Scheme 3. An improved method for protecting the carboxylic acid group of 6-bromohexanoic acid with *tert*-butanol utilising trifluoroacetic anhydride was also developed, resulting in improved yield (from 73% to 80%) and efficient reaction scale up (4.70 g to 20.7 g), relative to performing the reaction with DCC/DMAP, as shown in Scheme 4.

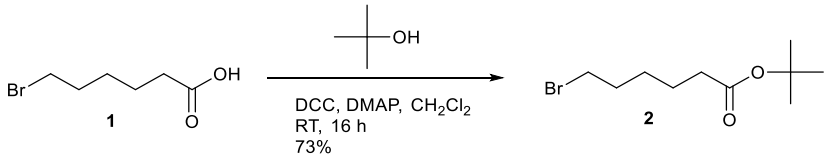

Scheme 4 Reaction scheme for the synthesis of *tert-butyl 6-bromohexanoate (**2**)*[203,205]

Using a well-established free-radical polymerisation synthesis protocol (Scheme 5) co-monomer, **4** was reacted with **5** in different ratios to produce co-polymers with 10, 5 and 2 mol % loadings of carboxylic acid allowing control over the number and density of bio-recognition elements that can be immobilised onto the surface. Control of the polymerisation reaction and surface chemistry was based on the following assumptions: varying the initial ratio of monomers would produce a polymer with control over the number of COOH containing segments and the COOH groups introduced to the polymer would be present at the spin-coated polymer surface.

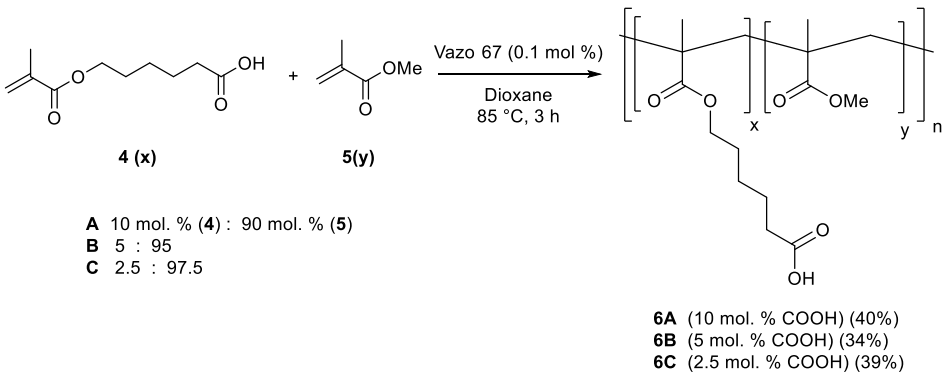

Scheme 5 Reaction scheme for polymerisation reaction of PMMA co-polymers

The structural composition of the final polymers was determined by ^{1}H NMR spectroscopy indicating successful copolymerisation (Figure 35). In addition, the actual mol. % of carboxyl-containing monomer incorporated into the polymer was calculated and are comparable to the theoretical values, shown in Table 7, indicating a successful synthesis of the intended polymers.[203] The actual mol % of carboxyl calculation was achieved by calculating the ratio of the integrals unique to each of the monomers (Figure 36). The resonance at 3.91 ppm was assigned to the C*H*$_2$COOH containing co-monomer and the resonance at 3.53 ppm to the methyl of the methacrylate group co-monomer, as illustrated in Figure 36.

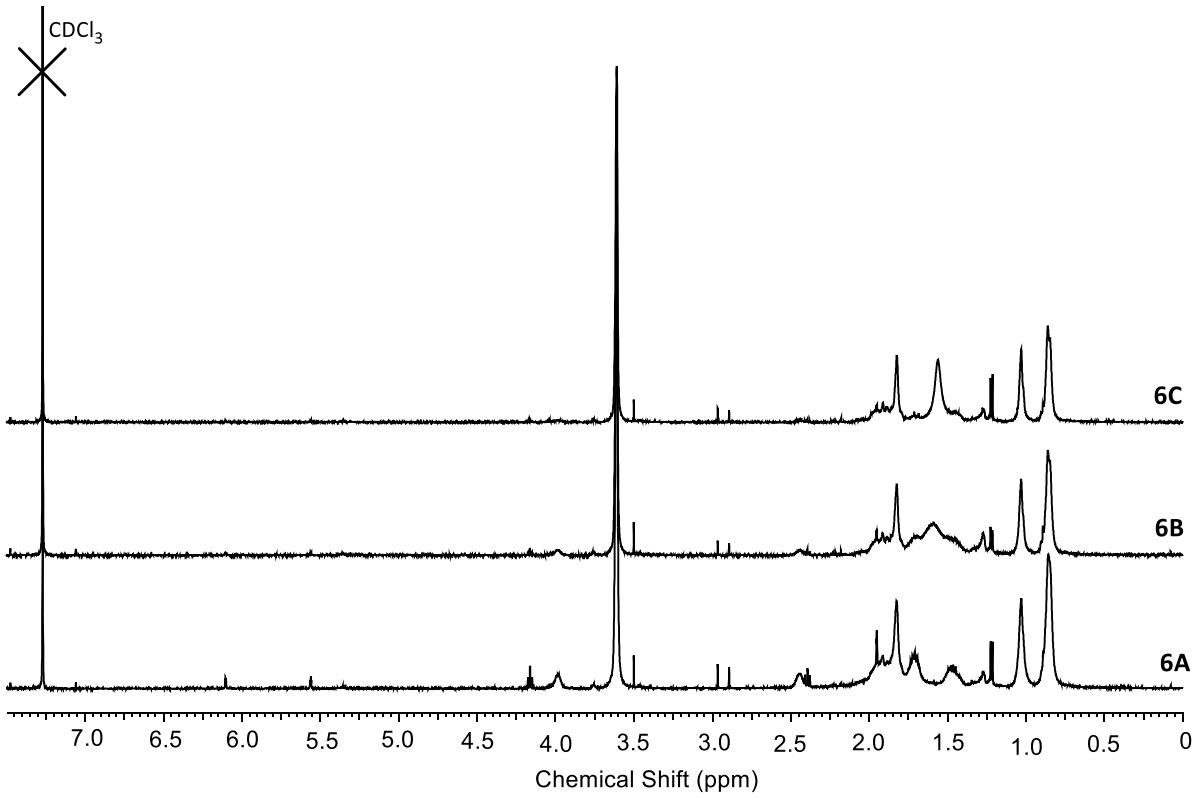

Figure 35 ^{1}H NMR spectra of PMMA COOH copolymers 6A-C.

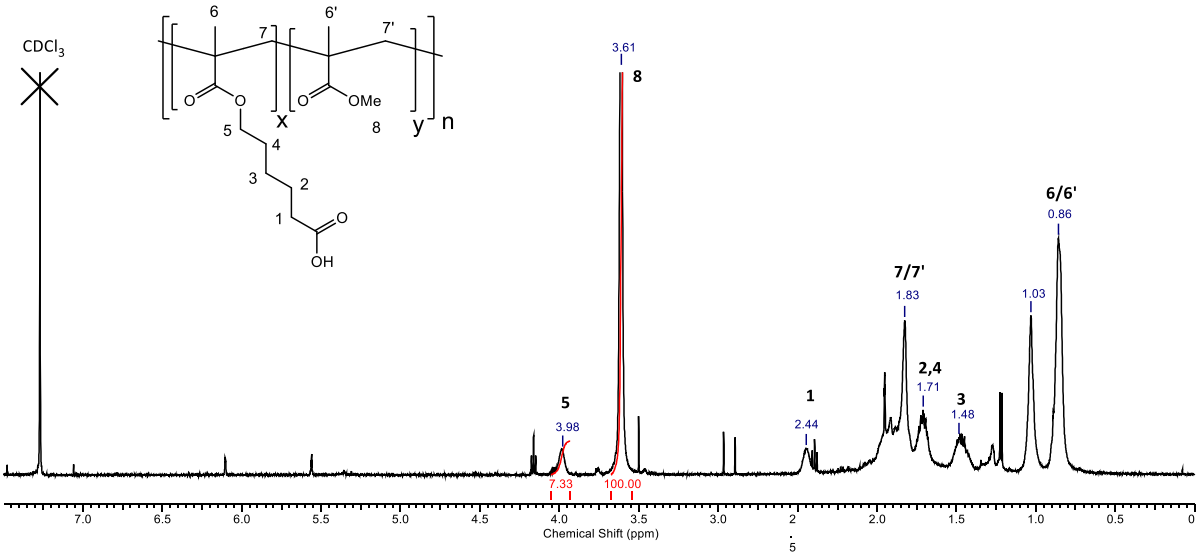

Figure 36 ^{1}H NMR spectra for PMMA 10% mol. (6A), showing the showing the resonances compared to calculate the experimental loading in the polymer.

Table 7 Loading of COOH containing co-monomer and GPC results for PMMA copolymers **6A**-**C**.

Polymer	Theoretical loading of COOH (%)	Loading of COOH from NMR (%)	Mn (kDa)	Mw (kDa)	Đ (Mw/Mn)
6A	10	9.6	46.1	80.4	1.7
6B	5	4.6	49.4	87.0	1.8
6C	2	2.2	50.3	92.8	1.8

The presence of the carboxylic acid group could not be confirmed by FT-IR analysis as the carbonyl stretching frequency of the esters of the polymer backbone (1724 cm^{-1}) masked the expected signal from the carboxylic acid (expected at 1707 cm^{-1}), as shown in Figure 33.

The molecular weights of the PMMA co-polymers was determined by GPC and were comparable to molecular weights produced in previous work.[203] The molecular weights of all synthesised polymers covered the range of 10.4-50.2 kDa and polydispersity indexes (Đ) in the range of 1.7 - 3.1, indicating successful synthesis of the polymers (see Table 7 and Table 21 to Table 26).

Whilst the reaction was successfully completed initially; it was characterised by low yields as shown in Table 1, which was attributed to inefficient polymerisation caused by running the reaction in THF at sub-optimal temperature (65 °C) and short duration (3 hours). The yield in THF was significantly improved by increasing the reaction length to 48 hours (65 °C) closer to $3*t_{1/2}$, as shown in Table 21-B; however, Đ increased and the polymer had a lower Mw (Figure 113). Therefore to further

optimise the reaction it was investigated under optimal conditions of 85 °C, which required a higher boiling point solvent with solvation properties similar to THF, namely toluene and dioxane.

An improved yield was achieved in toluene at 85 °C (Table 21-B) with a reduced reaction length of 3 hours, without compromising Đ. Additionally, an increase in reaction concentration correlated with improved yield and increased Mw, as shown in Table 22. The effect of varying initiator concentration in toluene is shown in Table 22 and Figure 115, with no noticeable increase in yield after 3 hours and no significant change in Mw. A lower initiator concentration produced a higher Mw polymer due to a reduction in the number of propagating chains. However control of COOH containing monomer loading was lost, as is seen by comparing Table 21-A vs Table 22 and Table 23, therefore the use of a solvent with solvation properties closer to THF but retaining a higher boiling point was investigated. The desired loading of COOH containing monomer was recovered when using dioxane as the reaction solvent, in addition to improved yield relative to toluene (Table 23-B vs Table 24-A). The effect of initiator concentration on the reaction in dioxane, Table 24, was similar to that in toluene, a lower initiator concentration produced a higher Mw polymer, but reduced yield, and pleasingly the bimodal distribution was also lost, as shown in Figure 116. An initiator loading of 0.1 mol.% was preferred and these reactions were shown to be reproducible (Table 25 and Figure 117). These conditions were then used to synthesise co-polymers of 10, 5 & 2 mol % loading of carboxylic acid bearing monomer; the theoretical loading was comparable to the values determined by NMR quantification indicating the successful synthesis of the intended polymers (Table 26, Figure 118).

5.1.2 Thin film surface functionalisation and characterisation

The pendant carboxylic acid side chains of the PMMA co-polymers enable the covalent immobilisation of bio-recognition elements via simple peptide coupling.

The carboxylic acid containing co-polymer can be functionalised through condensation reactions with primary amine groups. EDC is a water-soluble carbodiimide and well known crosslinking agent when used with NHS which can be used to generate activated surfaces by *in situ* surface conversion of –COOH groups to intermediate ester groups.[210]

The intermediates formed are highly reactive towards the primary amine ($-NH_2$) groups of peptides and proteins therefore result in covalent immobilisation of biomolecules to the surface, as shown in Figure 37. The sulfo-NHS serves as to extend the half-life of the unstable 'activated' carboxylic acid intermediate formed by EDC which can also be hydrolysed.[210] This technique for covalent

immobilisation of proteins has been applied in both biomaterials and surface designed biosensors.[84,97,102,215,218,220]

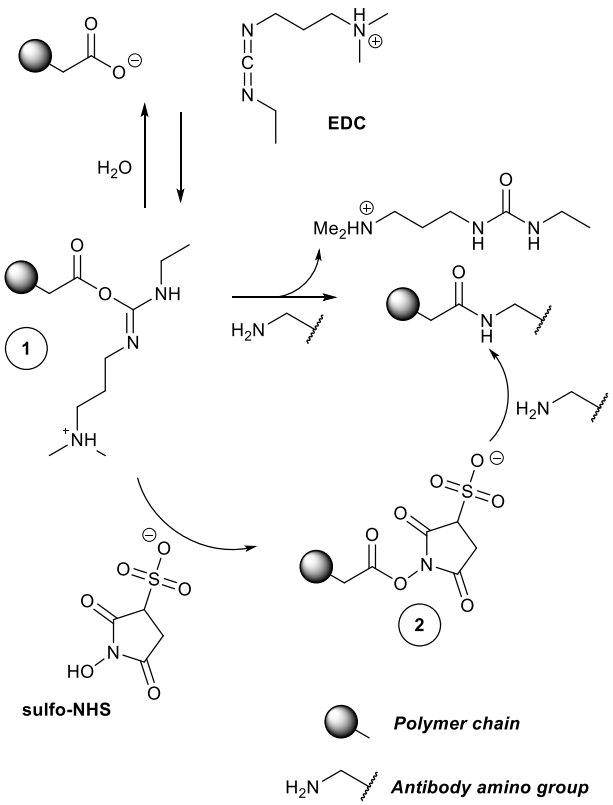

Figure 37 Formation of amide bonds can be achieved by EDC/NHS coupling reaction through the formation of highly reactive intermediates *1* and *2*.

In order to allow the specific detection of biomarkers in an EGOFET biosensor, the biorecognition element must be immobilised onto the surface of the device channel. The extracellular domain (ECD) of HER2, a blood-bound protein which can be found in blood serum was identified as a viable initial target to develop the biosensor platform. Therefore, in order to allow HER2 detection, a procedure was developed to covalently immobilise HER2 specific antibodies to the device surface utilising EDC/NHS chemistry. In order to verify the surface immobilisation technique of bio-recognition elements changes in film surface were monitored and the subsequent activity of immobilised antibodies was probed in a fluorescent binding assay.

5.1.2.1 AFM and Contact angle measurements

The effectiveness of the EDC/NHS based antibody binding protocol was initially investigated by monitoring changes in surface properties of the DPPTTT / PMMA COOH 10 % bilayer films during the functionalisation process using AFM (Figure 38-Figure **39**), to investigate the surface morphology, supplemented by WCA measurements (Table 8), to probe changes in hydrophobicity/hydrophilicity.

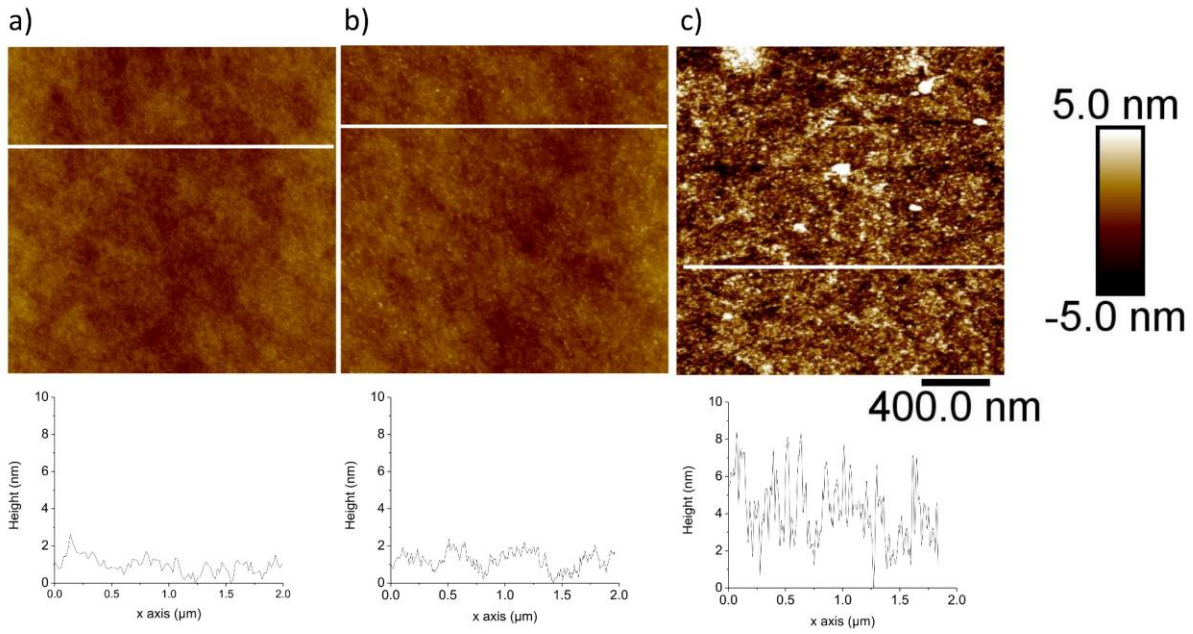

Figure 38 AFM tapping mode 2 µm scans of the DPPTTT / PMMA COOH 10 % films; a) Pristine; b) after incubation in PBS for 2 hours; c) after antibody functionalisation by EDC/NHS. White lines on the images signify the areas displayed below in line scans. Root mean squared (RMS) roughness of the films is shown in Table 8.

The AFM topology of the bilayer surface was characterised by low surface roughness and a relatively homogeneous smooth surface morphology, with RMS roughness of 0.6 nm (Figure 38a). Incubation of the film in PBS for 2 hours was performed as a control to mimic the duration of functionalisation process. The incubation induced no significant alteration in surface morphology supported by minimal changes in both WCA and surface roughness as shown in Table 8, indicating excellent stability of the deposited bilayer system.

Table 8 Water in air contact angle measurements and AFM root mean squared (RMS) surface roughness from of 2 µm scans of DPPTTT/ PMMA COOH 10% thin films during functionalisation process.

Surface Material	Surface Treatment	Contact Angle (°)	Error (+/-)	Roughness (RMS /nm)
DPPTTT / PMMA COOH 10%	None	71.2	0.2	0.6
DPPTTT / PMMA COOH 10%	2 hours in PBS	71.3	0.5	0.6
DPPTTT / PMMA COOH 10%	Antibody functionalised with EDC/NHS	65.2	2.2	2.2

The HER2 antibody was then covalently attached to the surface of the PMMA COOH film in the bilayer structure via *in situ* EDC/NHS coupling reaction to mimic the procedure carried out in subsequent binding assays. The film topologies following antibody functionalisation are displayed in Figure 38c and Figure 39b, and highlight significant alteration in surface morphology indicative of successful attachment of the antibodies, comparable with antibody functionalised surface observed elsewhere.[94,135,217]

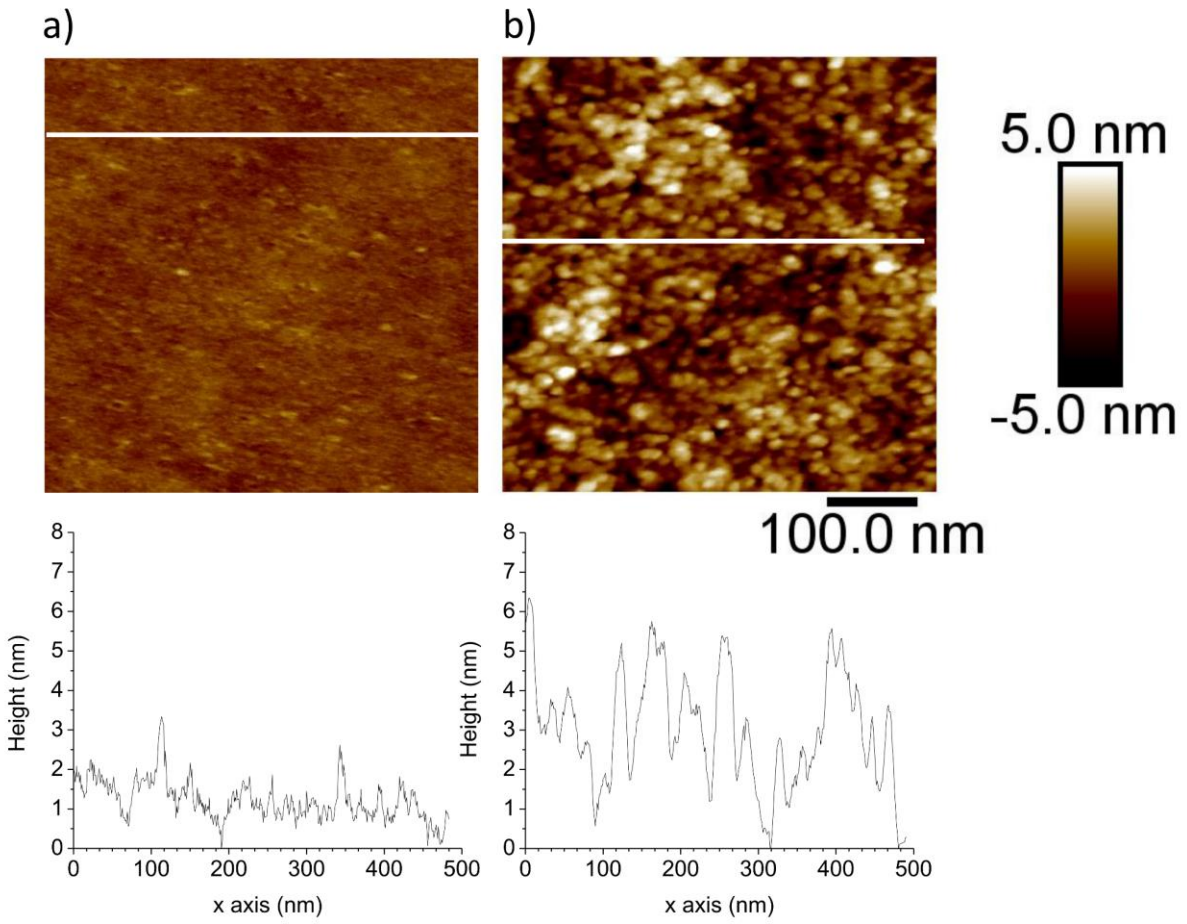

Figure 39 AFM tapping mode 500 nm scans of the DPPTTT / PMMA COOH 10 % films; a) after incubation in PBS for 2 hours (RMS roughness = 0.4 nm); b) after antibody functionalisation by EDC/NHS (RMS roughness = 1.7 nm). White lines on the images signify the areas displayed below in line scans.

Antibodies can be approximately modelled as ellipsoid structures, with a diameter of 15-20 nm and thickness of roughly 3 nm.[94,221] Higher resolution scans in Figure 39 reveal the morphology of the functionalised surface in greater detail, where globular features of comparable dimensions are identifiable, indicating substantial coverage. The visible change in surface morphology is quantified by the significant increase in RMS surface roughness.

An identifiable alteration in the WCA further supplements the morphological evidence following the functionalisation process, which could either be attributed to an increase in hydrophilicity of the deposited antibodies relative to the unmodified surface or the change in surface roughness caused by their deposition. Surface roughness has the effect of further adjusting the contact angle of the surface away from 90.[222] In the case of hydrophilic surface an increased surface roughness will

decrease the contact angle by promoting wetting on the surface, as water penetrates into the hollows of voids to extend the water interface making θ tend to zero.

The same investigation was also performed using the PBTTT/PMMA COOH % bilayer system which showed comparable results and supports the relative reproducibility of the surface modification induced by the functionalisation procedure, Table 9.

Table 9 Water in air contact angle measurements on PBTTT thin films on glass substrates

Surface Material	Treatment	Contact Angle (°)	Error (+/-)
PBTTT	None	102.0	0.4
PBTTT	2 hours in PBS	101.7	0.7
PBTTT / PMMA COOH 10%	None	70.8	0.5
PBTTT / PMMA COOH 10%	2 hours in PBS	70.5	0.3
PBTTT / PMMA COOH 10%	Antibody functionalised with EDC/NHS	65.3	1.3

5.1.2.2 Fluorescent Binding Assay

Following confirmation of antibody immobilisation by AFM, the effectiveness of the protocol for analyte detection was further investigated by a fluorescent binding assay. The assay procedure is schematically shown in Figure 40 and began by spin-coating a thin layer of the PMMA-COOH onto the substrate surface, in this case, a SiO_2 wafer, to mimic that of a functionalised EGOFET channel. The HER2 antibody was then covalently attached to the surface via EDC/NHS coupling reaction and BSA was used to block all non-specific binding sites. A fluorescently labelled secondary antibody was then applied and the substrate imaged using fluorescent microscopy. The data extracted is the average pixel intensity of fluorescence in arbitrary units from the fluorescence microscope images using imageJ. The extracted data fluorescence intensity is related to the number of occupied sites and is not fully quantitative but does provide a qualitative data for comparison.

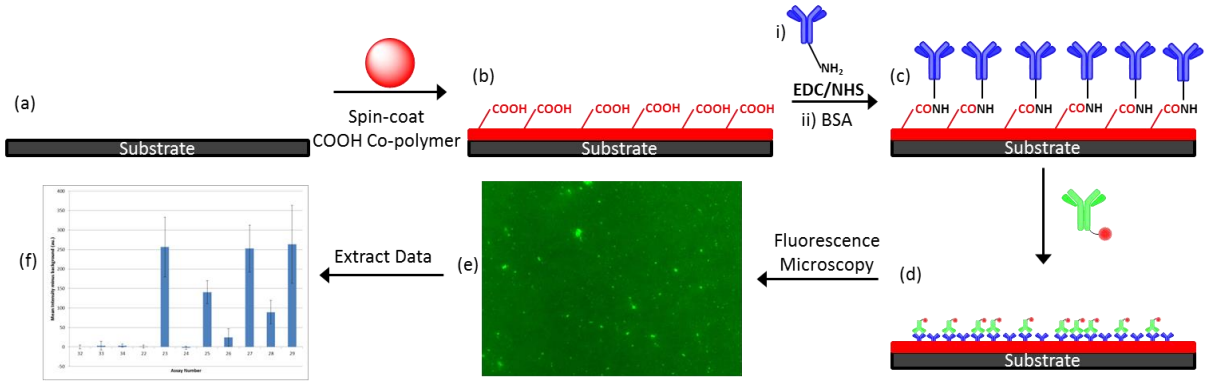

Figure 40 Scheme showing the procedure for fluorescence binding assay. (a) Cleaned SiO_2 substrate. (b) COOH functionalised Co-polymer spin-coated onto the substrate surface. (c) Primary HER2 antibody covalently attached to the surface. (d) Fluorescently labelled secondary antibody immobilised. (e) Substrates are probed by fluorescent microscopy. (f) Relative intensity of the fluorescence is extracted from images in imageJ.

The biomolecular binding capability of the immobilised recognition element can be approximated by measuring the fluorescence intensity relative to that of various controls, after binding with the fluorescently labelled secondary antibody. As shown in Figure 41, the *Z*-axis represents the relative fluorescence emission signal in arbitrary units plotted as a function of the 2D substrate surface. For the purposes of qualitatively assessing the signal an average fluorescent intensity value for the image was calculated. Relatively uniform signals can be observed indicating the degree of surface coverage, whilst bright spots corresponding to peaks in *Z* height can be attributed to aggregates.

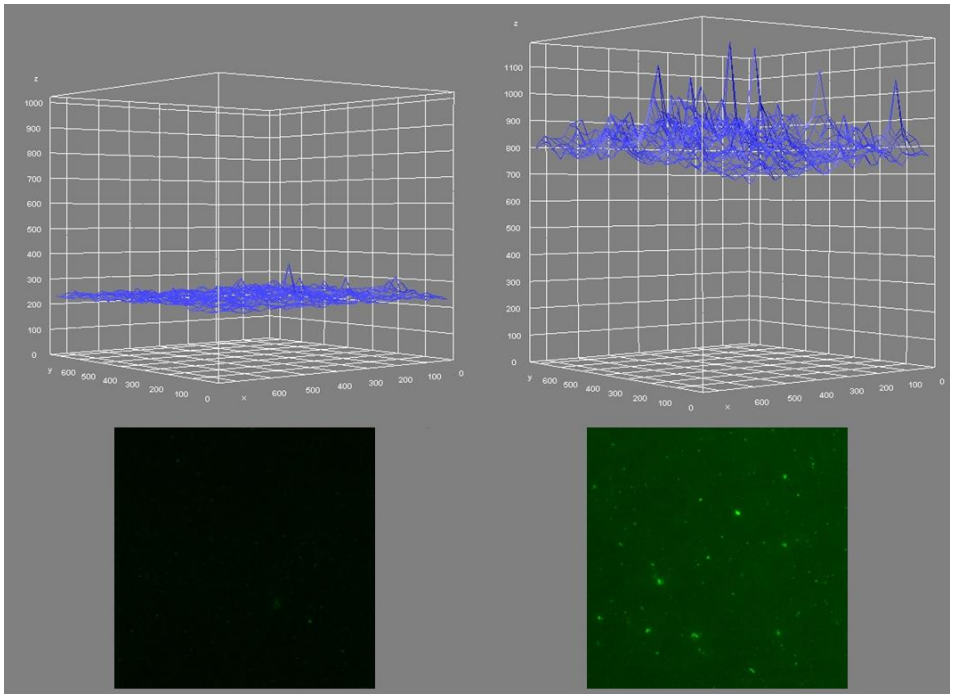

Figure 41 Fluorescent microscope images and corresponding 3D plots of intensity: left, FITC-labelled secondary antibody (no primary antibody) on PMMA COOH 10% (control); right, FITC-labelled secondary antibody after primary antibody immobilisation on PMMA COOH 10% surface. Z axis represents the fluorescence emission intensity; X and Y axes are the 2D substrate surface in units of pixel from the original image.

Previously reported investigations suggest that increasing the concentration of antibody to too high a concentration can impede efficient antigen binding; this effect was attributed to steric hindrance caused by overlapping biorecognition elements which reduce the bioavailability of the immobilised antibodies.[94,223] Therefore the concentration of primary antibody immobilised to the surface as the recognition element was investigated.

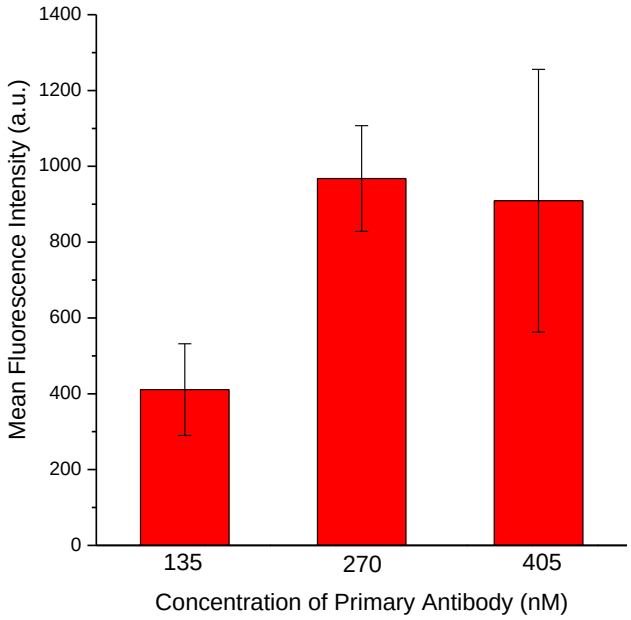

Figure 42 Results from fluorescent binding assay to determine the concentration of primary antibody used in immobilisation procedure.

The concentration of primary antibody used in the assay was also evaluated covering a range of 135-405 nM (25 - 75 µg/ml). As reported in Figure 42 the highest fluorescent intensity recorded was obtained at 270 nM of HER2 antibody (50 µg/ml); this was in loose agreement for previously conducted similar assays which investigated the efficiency of immobilising antibodies finding the range 50-70 µg/ml most effective. No significant improvement was observed in secondary antibody binding by increasing the concentration of primary antibody any further.

As controls, the same experiment was performed omitting various stages of the assay, as well as using non-complementary secondary antibodies & a PMMA polymer substrate absent of carboxyl groups therefore only allowing non-covalent attachments. The results of the studies are shown in Figure 43.

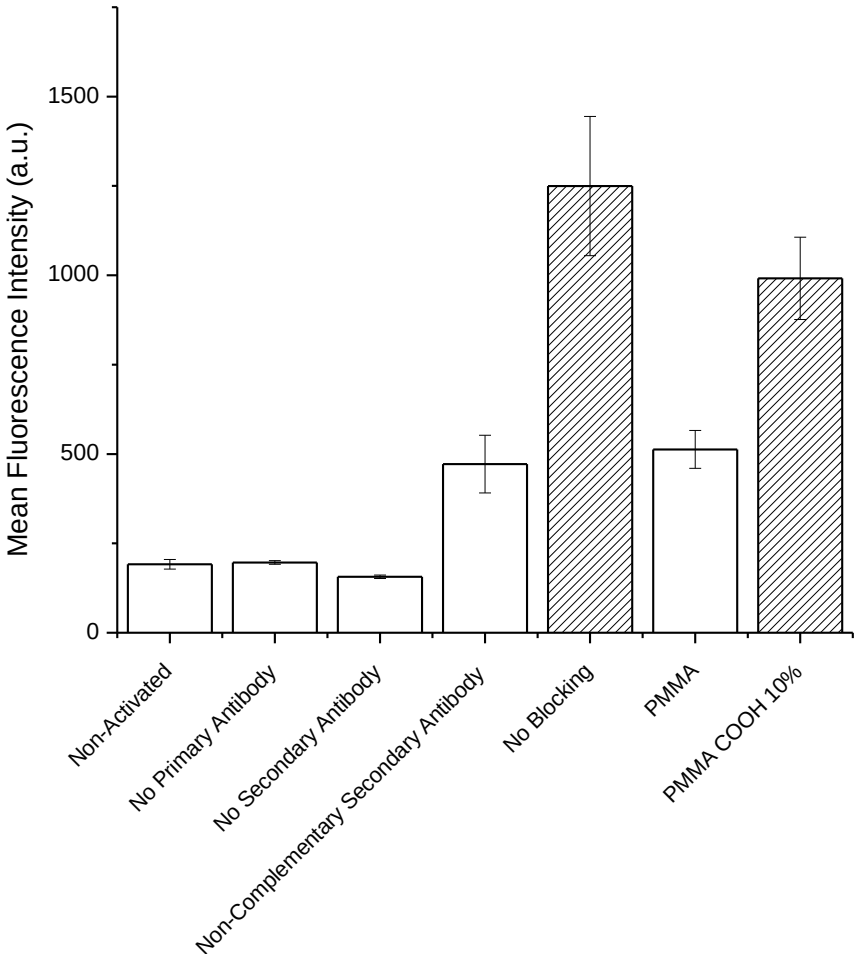

Figure 43 Results from controls in the fluorescent binding assay for PMMA co-polymer. Negative controls are shown as unfilled bars and hash filled bars indicate assay where strong fluorescence signal is expected. The assay used a 270 nM solution of HER2 antibody as the primary antibody and a 75 nM solution of fluorescently labelled secondary antibody.

Where no fluorescently labelled secondary antibody was applied, it can be assumed that any fluorescence observed can be attributed to the background for the experiment. Any fluorescence observed in the negative controls (unfilled columns in Figure 43) with higher intensity relative to the background is attributed to non-specific adsorption of the secondary antibody. Non-specific adsorption could be caused by physical adsorption of the primary or secondary antibody to the surface due to favourable hydrophobic attractions and electrostatic interactions, such as H bonding.

The intensities of the assay with non-activated substrate and assay performed in the absence of primary antibody is comparable to background levels; this signifies that physical adsorption and non-specific interactions are negligible in both cases.

Some fluorescence intensity was observed in assays performed with a non-complementary antibody and on a commercial PMMA thin film that contained no carboxylic acid; this can be attributed to non-specific interactions with the surface such as physical adsorption. Results which can be attributed to non-specific adsorption are in line with those observed in literature, which also showed

the ability of commercial PMMA to immobilise antibodies but as shown here less effectively than covalent attachment using carboxylic acid containing copolymers.[224]

The results showing the highest response can be seen from the activated surface with the COOH containing co-polymer with a complementary pair of primary and secondary antibodies are used resulting in specific immobilisation as shown in red. In the case where the assay was carried out without blocking the highest intensity is observed; this is due to covalent binding between the free amine groups of the secondary antibody with EDC/NHS activated COOH groups of the polymer, resulting in non-specific attachment to the surface.

In order to test the specificity of the system further assays where performed using a pair of complementary primary and secondary antibodies as shown in Figure 44. The use of complementary and non-complementary antibody pairs was used to investigate the non-specific binding that occurs during the assay and is common practice in immunologic tests such as ELISA, western blots and immunofluorescence. The investigation therefore shows that the specificity of the immobilised antibodies was retained. Antibodies are raised as an immune response in a host species (e.g. Sheep) to bind to the corresponding antigen. However, an anti-antibody is a 'secondary antibody' that specifically binds to other antibodies, for example a Rabbit-Anti Sheep antibody is raised in a rabbit but specifically binds to sheep antibodies. The non- complementary pairs of antibodies, shown in green and purple, are of comparable intensity to that of the background signal. It is significant that the complementary pairs of antibodies, shown in blue and red, are considerably stronger in intensity signifying that the system has retained its specificity.

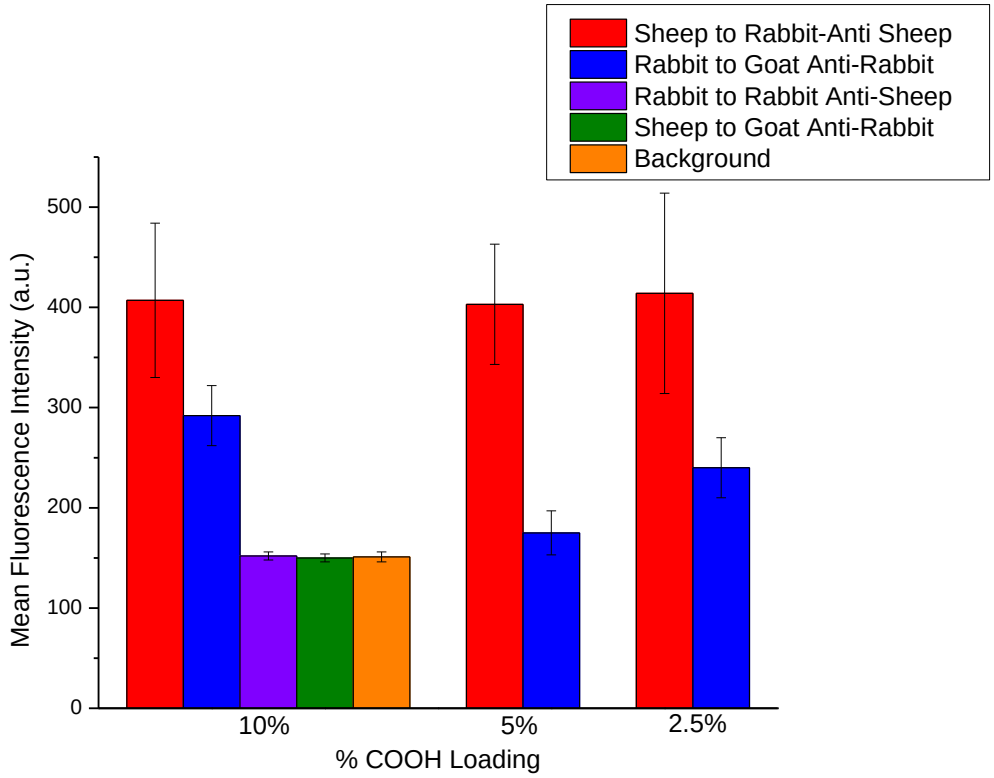

Figure 44 Results from fluorescent binding assay for PMMA co-polymer, comparing fluorescence between COOH loadings in PMMA co-polymer and use of complementary and non-complementary pairs of antibodies. The assay used 270 nM solutions of primary antibodies and 75 nM solutions of fluorescently labelled secondary antibodies.

It has been demonstrated in literature that the surface concentration of reactive functional groups can have a significant impact on the performance of the immobilised biorecognition elements.[224] Ideally a higher surface concentration of reactive COOH groups would lead to an increase in the number of immobilised biorecognition elements resulting in a higher output signal. However, it has been suggested that a high concentration of surface COOH groups can also increase the likelihood of a biomolecule being anchored to the surface by multiple sites which may distort the biomolecule impacting on its ability for complementary binding.[224,225] Alternatively it has been hypothesised that too low a concentration may result in a loss of activity as the biomolecule interacts with the polymer surface.[225,226]

Therefore it was of interest to investigate the effects of varying the surface concentration of COOH groups by performing the assay with the copolymers produced with different loadings of COOH, the results of which are shown in Figure 44. Results in literature investigated the same behaviour identifying a PMMA-MMA copolymer with 10% COOH loading for optimal performance in an ELISA assay; however copolymers with lower loading were not investigated.[211,224] However in the assay performed here no clear trend relating to the loading of COOH groups can be identified; this

behaviour could be due to limitation in the fluorescent assay performed and it will be of interest to investigate the effects when the polymers are used in functioning EGOFET devices.

5.2 Gate functionalisation strategy

Functionalisation of the gate electrode is typically achieved using Self Assembled Monolayers (SAMs) of thiolates deposited on to the gold surface, exploiting well known gold-thiol chemistry.[79,227,228] Terminal labile groups on the SAMs can introduce functionalities required for covalent attachment of biorecognition elements through *in-situ* reactions. This method has proved the most popular and versatile route to functionalisation in EGOFETs and devices with exceptional LoD reported down to the single molecule.[92] However some limitations have been noted for example the sensing measurements are typically performed with pure water as gating medium due to the ion-permeable nature of the bio-SAMs. The resulting reduction in Debye length in higher ionic strength solutions causes charge screening and can result in the limitation in device analyte sensitivity, especially when the detection of an analytes intrinsic charge is the main method of transduction for R-L complex formation.

In these devices the gate functionalisation is performed separately and then used to fabricate the EGOFET device. The easily interchangeable nature of the components in this sensor set up makes the investigation of new sensor components relatively straightforward as the gate or OSC can be modified separately from the rest of the device; therefore allowing straightforward investigation of new biorecognition elements and analytes, gate immobilisation techniques and the use of novel OSCs.

In this thesis the versatility of the gate electrode functionalisation is demonstrated by investigating two different SAM systems for the immobilisation of the relevant biorecognition element enabling the detection of two new analytes with EGOFET biosensors. The gold gate electrode is first functionalised through the formation of carboxylic acid terminated thiol-based self-assembled monolayer (SAMs) followed by EDC/NHS coupling of the relevant biorecognition element. The lipoic acid and 3MPA/11MUA SAMs used in this work are based on previously established biosensing systems.

5.2.1 Lipoic acid-based SAM for THC sensing

Odorant-binding proteins are small soluble proteins located in the olfactory receptor neurons of invertebrates and vertebrates and are involved in the perception of odor. In contrast to antibodies they are significantly smaller, more stable and display the ability to reversibly bind odorants and pheromones (small chemicals) as opposed to large proteins. Recently these proteins have gained

interest for use as biosensing elements for small molecules.[195,229] A lipoic acid-based SAM and EDC/NHS coupling was recently used for the immobilisation of OBPs onto gold QCM electrodes by C. Kali *et al*.[195] The resulting QCM-based biosensors were used for the selective detection of a variety of drugs of abuse including tetrahydrocannabinol (THC). Therefore, in this thesis the application of the aforementioned method was investigated as a proof of concept for use in an EGOFET biosensor. This investigation uses GTP_pigF88W OBPs, these were produced and immobilised on to the gold gate electrodes using the reported lipoic acid-based protocol (Figure 45). Functionalised gate electrodes where supplied by C. Kali for use in the EGOFET device measurements in section 7.2.

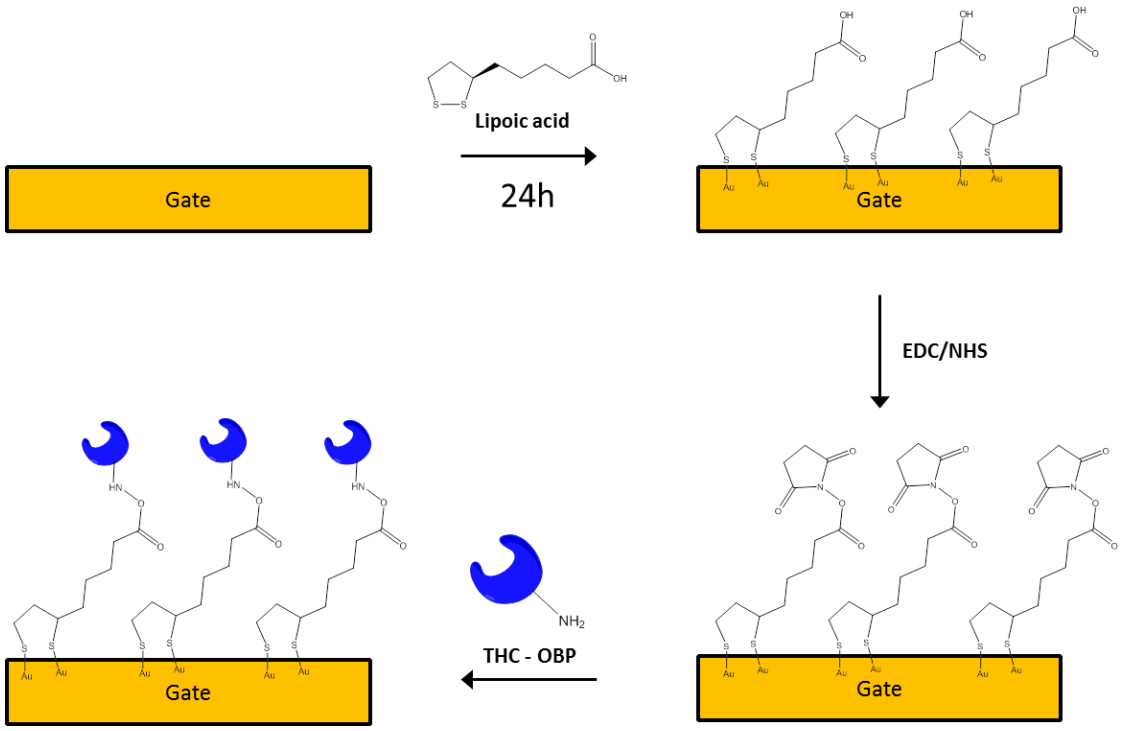

Figure 45 Scheme showing the procedure for the immobilisation of the THC sensing OBP onto the gold gate electrode used in the EGOFET sensor. A self-assembled monolayer (SAM) is prepared on the surface of the bare gold gate electrode. The OBPs are then covalently attached to the carboxylic acid bearing SAM by EDC/NHS coupling with a free amine group on the protein.

The ability of the OBP to discriminate THC from other common cannabinoids was examined in solution through fluorescence binding assay (Table 10). Therefore, the ability of the immobilised OBP in the EGOFET sensor to allow the selective detection of THC was also investigated.

Table 10 Affinity constants for OBP GTP_pigF88W against various cannabinoids calculated by fluorescence binding assay by C. Kali which are provided by personal correspondence.

	Affinity constants [$K_a(\mu M^{-1})$]	**±**
Tetrahydrocannabinol (THC)	1.31	0.26
Cannabinol (CBN)	0.06	0.01
Cannabidiol (CBD)	0.08	0.01

5.2.2 3MPA/11MUA-based BioSAM for HER2 ECD sensing

In this thesis, the EGOFET-based detection of HER2 ECD was also investigated by the application of gate functionalisation method developed by E. Macchia et al.[92,110,192] The gate electrode in this device was functionalised through the formation of a SAM on the gold surface of the electrode consisting of a 10:1 ratio of 3-MPA to 11-MUA and the resulting monolayer is referred to as the chemSAM. The amine group on the relevant antibody were then covalently attached to the carboxylic acid groups of the chemSAM by EDC/NHS coupling, to produce the BioSAM layer as shown in Figure 46.

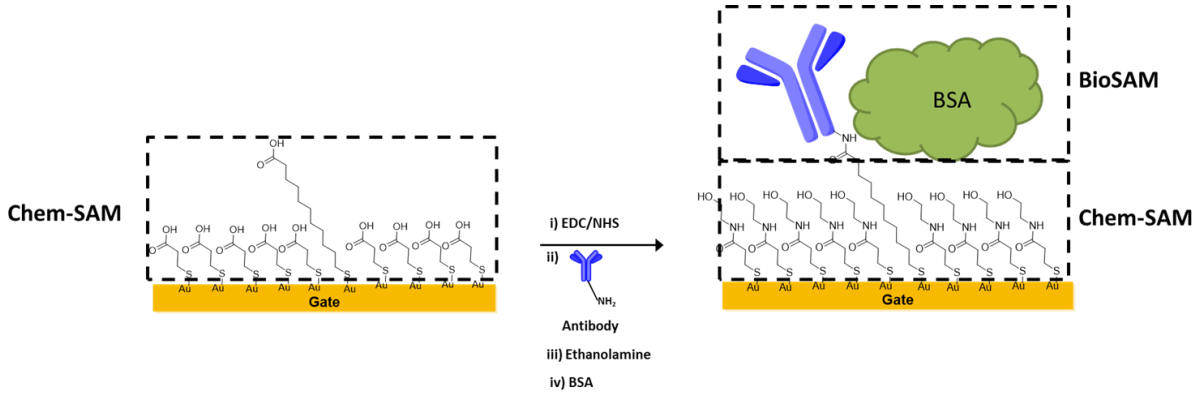

Figure 46 Scheme for the formation of the BioSAM from the chemSAM.

The mixture of different chain lengths used in the chemSAM allows more effective immobilisation of the antibody. The longer 11 MUA chain is preferred by the antibody for covalent attachment therefore reducing the steric hinderance imposed by the surface onto the antibody that may cause conformational changes. Subsequently the unreacted activated functionalities of the chemSAM are blocked with ethanolamine and finally BSA is applied to further reduce non-specific binding.

The amide groups which are formed in the BioSAM following the reaction with ethanolamine allows for the formation of hydrogen bonds between the oxygen and hydrogen of neighbouring chains amide groups, as depicted in Figure 47. Each hydrogen bond has an associated dipole moment therefore generating an electrostatic network on the gold interface mainly composed of the dense layer of 3MPA chains. The dipole moment associated with the 3MPA H-bonded layer is ~ 3.7 D which is larger and has a greater impact on the electrostatic interactions of the chemSAM compared to dipole associated with Au-S bond (1-2 D).[230] The electrostatic impact of formation of an R-L complex is therefore allowed to propagate over a large area giving a large irreversible response. The

biosensors ability to achieve extremely low limits of detection has been attributed to the electrostatic cooperative interaction that occurs through the extended network of hydrogen bonds.

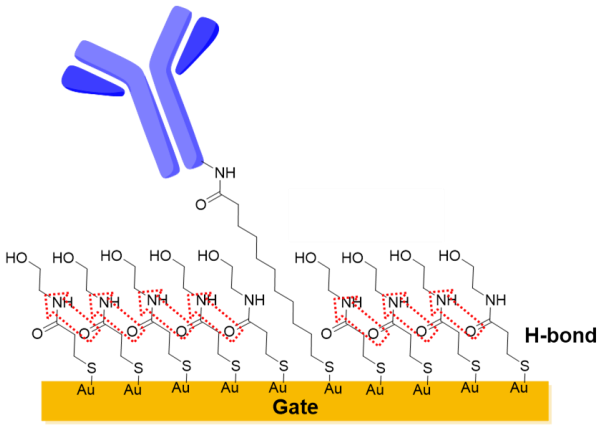

Figure 47 2D schematic representation of the BioSAM on gold gate electrode and the formation of hydrogen bonds between the amide groups of neighbouring chains (red arrows), leading to a dipole moment.

The BioSAM system has demonstrated proof of concept for the single molecule detection of immunoglobins with an EGOFET biosensor, in addition to the selective label-free detection of C-reactive protein in both PBS and saliva.

In this thesis we investigated the use of HER2 antibody as the biorecognition element to examine the application of this system for the label-free detection of HER2 ECD. The effectiveness of the BioSAM procedure for the immobilisation of HER2 antibodies was initially investigated by monitoring changes in surface properties of gold substrates during the functionalisation process using AFM to investigate the surface morphology. In these experiments two types of bare gold substrates were used gold substrates prepared by thermal evaporation (Figure 48) and template-stripped ultra-flat gold films (Figure 49).

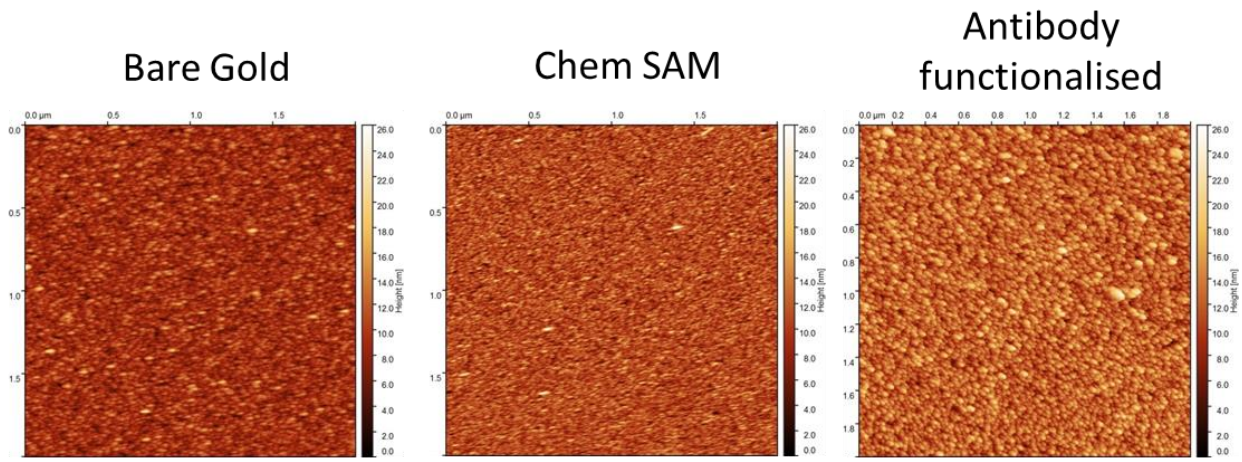

Figure 48 AFM tapping mode 2 µm scans of the thermally evaporated gold substrates; left) as prepared gold substrate (RMS roughness = 2.13 nm); middle) after ChemSAM formation (RMS roughness = 2.39 nm); right) after antibody functionalisation by EDC/NHS (RMS roughness = 2.7 nm). White lines on the images signify the areas displayed below in line scans.

The deposition of the chemSAM and BioSAM each cause a sequentially larger relative increase in the calculated RMS roughness which is evident in both Figure 48 and Figure 49 and is in agreement with the findings of Macchia et al.[92] However, the thermally evaporated gold exhibited a high starting surface roughness relative to the size of typical biomolecules, therefore ultra-flat gold films were also used. The ultra-flat films exhibit exceptionally low roughness typically around 0.2 nm therefore the changes in the surface features during the investigation are more easily visible.

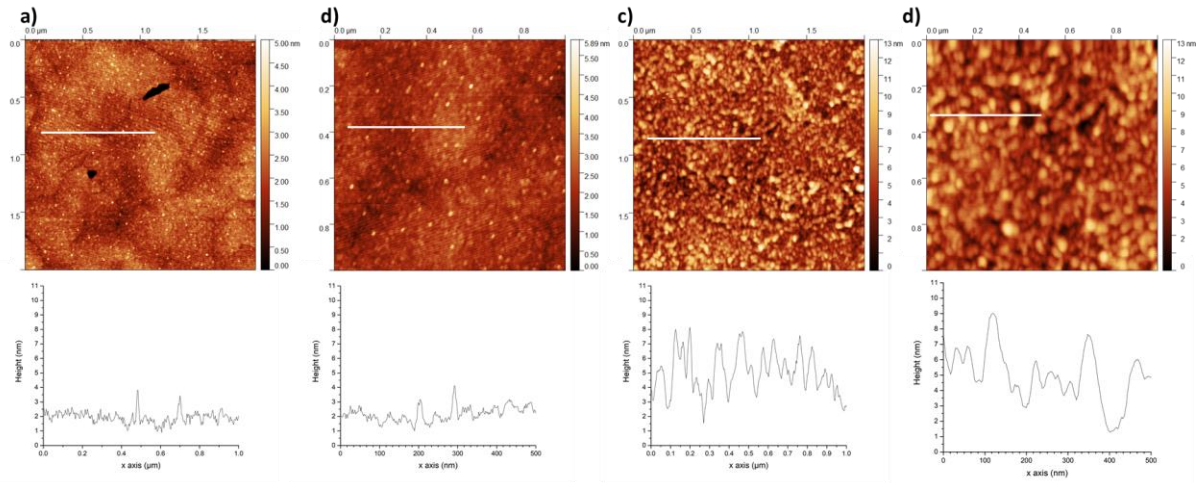

Figure 49 AFM tapping mode 2 µm and 1 µm scans of the template-stripped ultra-flat gold films; a) after ChemSAM formation, 2 µm scan (RMS roughness = 0.49 nm); b) after ChemSAM formation, 1 µm scan (RMS roughness = 0.46 nm); c) after antibody functionalisation by EDC/NHS, 2 µm scan (RMS roughness = 1.62 nm); d) after antibody functionalisation by EDC/NHS, 1 µm scan (RMS roughness = 1.81 nm). White lines on the images signify the areas displayed below in line scans.

The AFM topology of the chemSAM was characterised by low surface roughness (RMS roughness of 0.49 nm) and a relatively homogeneous surface morphology with some interspersed small peaks which is indicative of a well packed chemSAM (Figure 49a and b).

The film topologies following antibody functionalisation are displayed in Figure 49c and Figure 49d, and highlight significant alteration in surface morphology indicative of successful attachment of the antibodies, consistent with antibody functionalised surfaces observed in section 5.1.2.1 and elsewhere.[94,135,217] Globular features of comparable dimensions to antibodies are identifiable, Figure 49d indicating substantial coverage. The visible change in surface morphology is quantified by the significant increase in RMS surface roughness. The procedure for antibody gate functionalisation was therefore used for EGOFET biosensor devices, where the formation of the gate is further supported by the substantial -0.1 V shift in V_T.

5.3 Summary

Morphology from SEM images of the deposited PMMA COOH films on the OSC indicated complete coverage on the microscale. Additionally, the shift in water-air-contact angle probes the physical properties on a macro-scale upon thin film deposition from the more hydrophobic coating of the OSCs to a relatively more hydrophilic coating exhibited by the PMMA COOH film.

SEM images suggest the planarising effect of the deposition of the PMMA COOH film onto the OSC resulting in a relatively flat homogeneous topography. This was confirmed by AFM analysis, by the reduction in surface roughness when compared to the uncoated samples. The same observations have been made in previous publications using comparable systems.

The AFM measurements and fluorescence binding assay indicate a high surface coverage of HER2 antibody deposited onto PMMA COOH films which retain their bioavailability in good agreement with that reported by others using similar polymer coating for covalent immobilisation. Additionally, the binding assay indicates that with the use of BSA as an effective blocking agent limiting non-specific interactions as shown by negative control experiments. The resulting assay is therefore well positioned for investigation for use in EGOFET biosensor systems utilising PBTTT and DPPTTT as OSC, using the protocol validated in the fluorescence binding assay.

In addition, the procedures for functionalisation of the gate electrodes was established for the investigation of two SAM-based strategies: the Lipoic acid-based system for the detection of THC using OBPs; and 3 MPA 11 MUA-based BioSAM system for the detection of HER2 ECD using antibodies. The later was investigated by AFM which showed successful high surface coverage of the antibody onto the gold through the BioSAM. Therefore, prompting the biosensing experiments in section 7.

6 Droplet-based EGOFET devices

EGOFETs benefit from a simple device architecture that uses an aqueous gating solution allowing a low operating potential and *in-situ* detection of the analyte in solution. This is of particular interest for developing low cost point-of-care biosensors. The sensing ability is a consequence of changes in the capacitance generated at the device interfaces being very sensitive to the interaction of analyte at these interfaces. The relative change in device performance is probed in sensing for these devices.

Covalent immobilisation of recognition elements requires the formation of chemical bonds between reactive groups on the biomolecules and complementary groups introduced to the interface of a transducer.[90] Introduction of reactive functional groups has been achieved through deposition of a functional layer on top of the OSC,[79,97] blending of this material with the OSC or modification of the OSC structure.[84,203]

The protocol for deposition of a thin PMMA COOH co-polymer layer on to the OSC and effective use of this thin layer for immobilisation of the antibodies was established in the previous Chapter. A thin layer of PMMA copolymer was spin-coated directly on to the OSC of the EGOFET device to form a bilayer structure, which can then be post-functionalised with the HER2 antibody for use in sensing. The closest reference point for a bilayer architecture is presented by Mulla *et al*, where a biosensing platform was fabricated from a thin layer of poly(acrylic acid) (pAA) spin-coated directly on to a PBTTT OSC that was subsequently crosslinked by UV radiation.[97,100] However, in contrast to directly functionalising the carboxyl group of the deposited layer with antibodies, a biotin functionalised phospholipid bilayer was covalently anchored by EDC/NHS chemistry. The device architecture developed in this work removes the need for UV curing that can damage the OSC and also reduces the distance of the recognition element from the interface surface.

Only a few conjugated polymers have demonstrated reproducible operation in water-gated devices, with even fewer used with gating by physiological media, clearly desirable for biosensor application. We therefore aimed to widen the class of organic semiconducting materials employed as the active material and test the feasibility of using these in a bilayer structure and with the assay procedures. However in order to develop effective bilayer devices we first investigated the performance of the devices using pristine OSC. The role of the semiconducting polymer for use as the active material is pivotal in producing EGOFET devices with good and reproducible electrical performance, which is particularly desirable for an effective platform for biosensing.

6.1 PBTTT Tungsten-gated water droplet devices

We first investigated the use of PBTTT as the p-type OSC in EGOFET devices as an alternative to P3HT that has been extensively reported.[66] PBTTT shows enhanced environmental and electrochemical stability over P3HT and relatively high charge carrier mobility in OFETs of ca. 1 cm^2/Vs.[231]

A wide variety of procedures for fabricating devices using PBTTT as the OSC have been reported in the literature with variations in the concentration of the spin-coated solution, solvent and spin speed parameters.[66,79,97,202] Due to the potential for optimising device performance, stability and cost, the effects of varying the spin-coated solution concentration were investigated, covering the previously reported concentration range of 3-7 mg. The polymer was deposited by spin-coating from DCB solutions directly onto the shadow mask defined source and drain gold electrodes on glass substrates, to achieve film thicknesses as described in Table 11. A film thickness at least comparable to the source and drain heights (45 nm) would be desirable to ensure complete coverage of the source and drain electrodes and reduce gate leakage. However difficulties were encountered in reproducing the thickness, such as the 50 +/- 5 nm film yielded from a 3 mg/ml solution of PBTTT in 9:1 DCB: Chloroform.[97] The significant deviation in the film thicknesses previously achieved could be due to differences in unreported processing conditions used, such as solution temperatures, spin coating equipment and polymer Mw.

Table 11 PBTTT film thicknesses on glass measured by Dektak. The PBTTT solutions where spin coated from DCB solutions at 2000 rpm, displayed is the average thickness over 3 substrates and error as standard deviation.

PBTTT Concentration (mg/ml)	Film Thickness (nm)	Error (+/-)
3	11	2
5	18	1
7	33	2

We therefore investigated the effect of concentration on device performance and reproducibility of the fabrication process over different substrates. Initially EGOFET devices were tested using a 3 point probing station by applying a 4 µl droplet of water over the channel area to act as the gating electrolyte and a tungsten tip as the gate electrode. A typical saturation transfer characteristic for a PBTTT device is shown in Figure 50, solid and dashed lines represent the source-drain (I_{SD}) and gate leakage (I_G) currents respectively. The transfer characteristics are carried out by sweeping the gate-source voltage (V_G) at a fixed drain-source voltage (V_{DS}). The devices show good p-type characteristic

behaviour, which displays minimal current hysteresis between the forwards and backwards sweeps and near-ideal shape typified by the linearity of the I_{SD} square root plot. The low gate leakage, several orders of magnitude below the maximum I_{SD}, indicates the absence of electrochemical reactions. Leakage current is typically identified as a specific characteristic of the transistor geometry in contact with water and the measurement scan rate.[197]

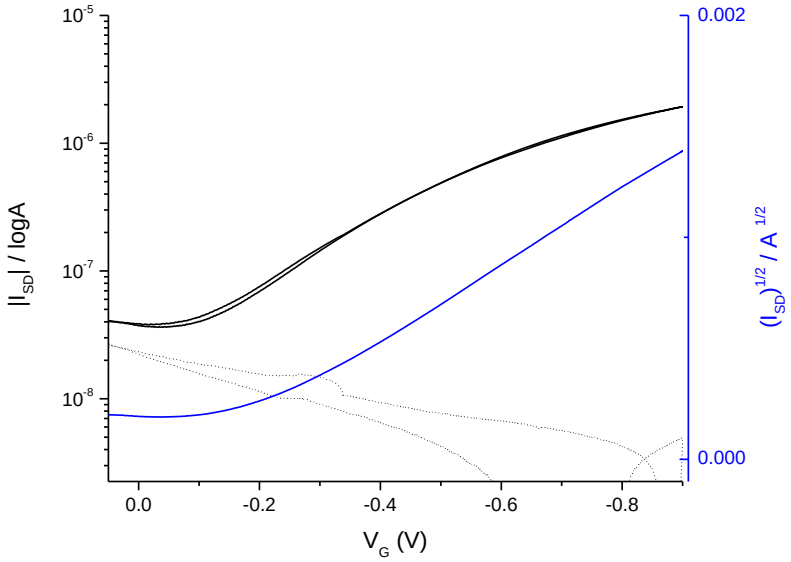

Figure 50 Transfer characteristic of a representative PBTTT EGOFET device using water droplet and W pin as the gate electrode. Source and drain electrode where patterned using a shadow mask. I_{SD} (black – solid lines) and I_G (black – dotted lines) plotted in a semi-log scale (left). I_{SD} plotted in a square root scale (blue – right) from which characteristic parameters are extracted from the saturation regime.

Device performance is analysed through the transistors electrical figures of merit. The principal parameters of interest are the threshold voltage (V_T), field effect mobility (μ) ratio between max current (I_{on}) and min current (I_{off}) ($I_{On/Off}$) and their method of extraction is described in section 1.3.6. The source-drain current at certain voltages (I_{DS}) are quoted in the results tables, as these values are used in calculating the devices $I_{On/Off}$. The I_{DS} at the maximum V_G during the transfer sweep signifies the maximum current in the transfer hysteresis (I_{on}) and I_{DS} min signifies the lowest current during the transfer forward sweep and when the device is off (I_{off}).

Mobility (μ_{sat}) is presented throughout this thesis as the capacitance-mobility product in the saturation regime (I will use the term $\mu*C$ for ease), the parameters are combined as the specific areal capacitance (C_i = cap/unit area) has yet to be determined for our system. The capacitance of the structure used in the device can be measured by electrochemical impedance spectroscopy (EIS)

with a potentiostat by measuring the capacitance of the Au/water/polymer/Au structures.[197] Additionally the extracted capacitance is highly dependent on the device (electrode metals, OSC and electrolyte used) and measurement set up (measurement frequency and scan rate) to calculate the effective capacitance of the system, therefore the calculated values are frequently not universal for the OSC used. In general at low frequencies (< 1 Hz) the capacitance value saturates due to the formation of the high capacitance Helmholtz double layer and the capacitance value for the devices in saturation mode are calculated from within this regime. The hydrophobic semiconductors used usually display a high capacitance of between 0.5 µF/cm^2 and 10 µF/cm^2 at their dielectric interface which typify EGOFET devices and allows low voltage operation.[197,232,233]

The characteristic device parameters are sensitive to the effects of analyte interaction and it is their relative variation which is of interest, typically it is the change in I_{on} and V_T that demonstrates the clearest response upon analyte exposure.[29,93] This relative analyte induced variation can be normalised as shown by Mulla *et al*, to account for device to device variation of the absolute parameters.[97] However, to create a platform of optimal biosensing capability it is important to minimise any variation in device performance that is not associated with the analyte interaction, such as device stability and reproducibility. Of particular interest is the reproducibility of the forward sweep from which the electrical figures of merit are extracted. The variation in performance of the four devices fabricated on one substrate is demonstrated in Figure 51, which shows a small variation across the substrate (see Figure 51 and Figure 52).

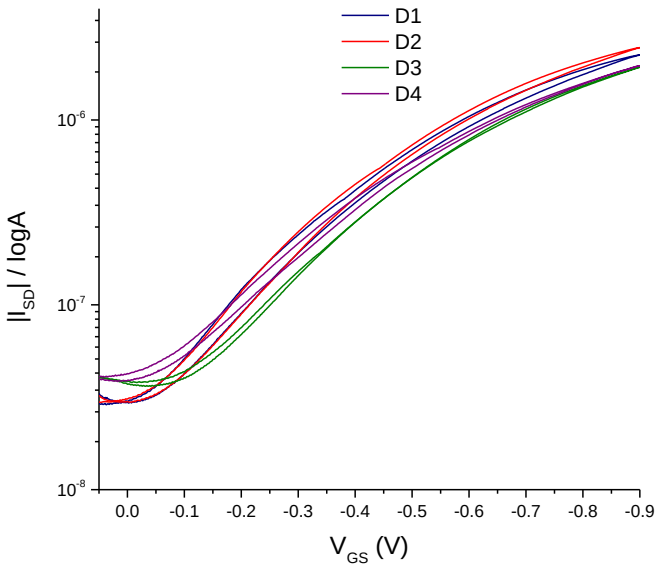

Figure 51 Transfer characteristics showing the variation of performance of four PBTTT EGOFET devices fabricated on the same substrate with I_{SD} and plotted in a semi-log scale. The devices were operated using

water droplet and W pin as the gate electrode and source and drain electrode were patterned using a shadow mask.

To further this investigation, the reproducibility of the fabrication process and impact of PBTTT concentration used was assessed by compiling the characteristic parameters from the transfer characteristics of the 16 devices fabricated over 3 substrates for each concentration. The extracted parameters for the various concentrations of PBTTT devices are gathered in Figure 52.

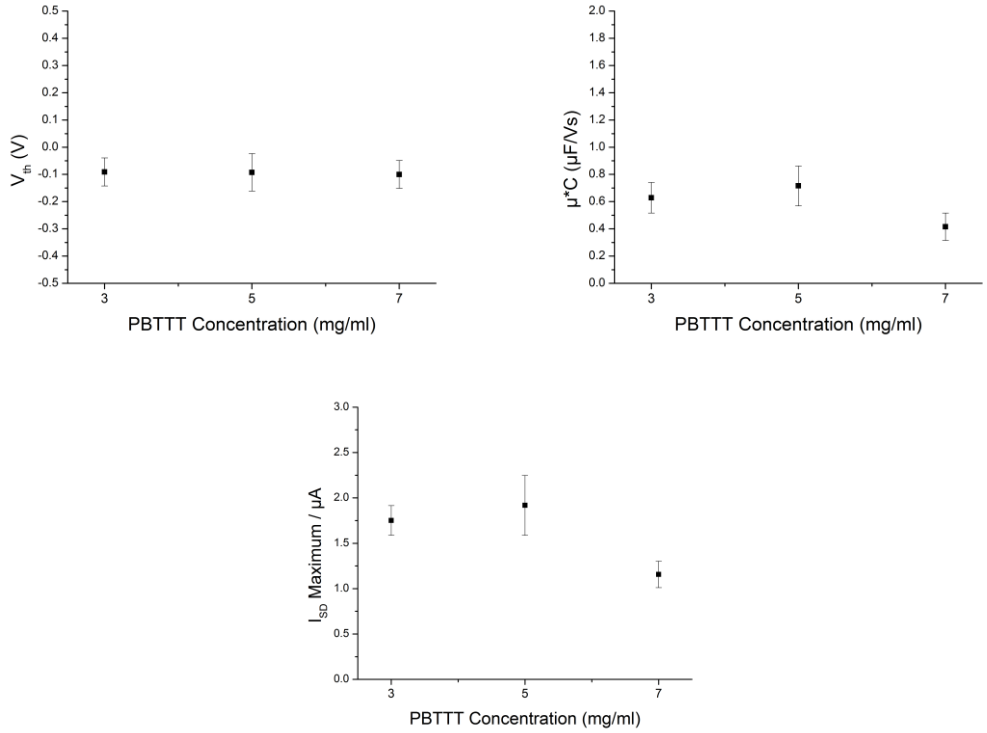

Figure 52 Variation in device parameters extracted from transfer characteristics of fabricated from concentrations of PBTTT varying from 3 -7 mg/ml. The EGOFET water droplet gated devices were measured using a W tip as the gate electrode. The averages and errors are taken from 12 devices fabricated on 3 different substrates for each concentration.

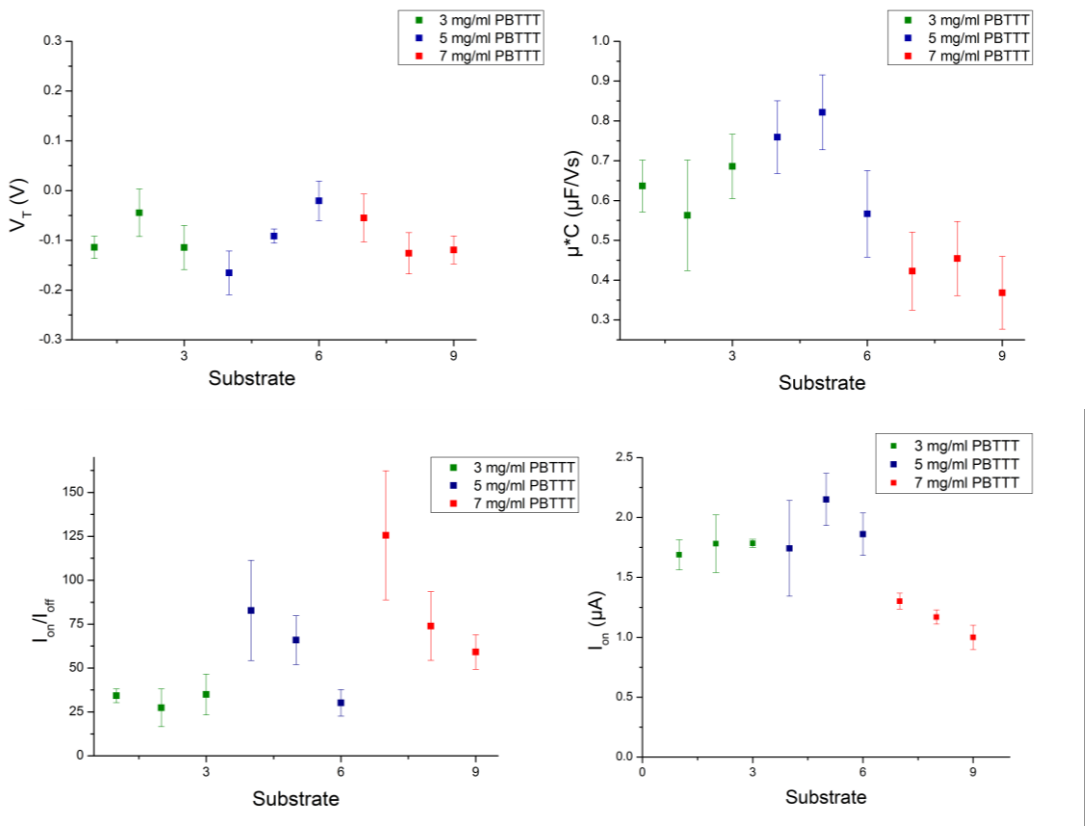

Figure 53 Intra-substrate variation in device parameters extracted from transfer characteristics of fabricated from concentrations of PBTTT varying from 3 -7 mg/ml. The EGOFET water droplet gated devices were measured using a W tip as the gate electrode. The averages and errors are taken from 4 devices fabricated on 3 separate substrates for each concentration.

The investigation highlights the variation in the extracted critical parameters both in terms of intra-substrate variation (devices on the same substrate shown by the standard deviation error bars in Figure 53) and inter-substrate variation (variation between different substrates). The variation in parameters is of critical importance when the devices are applied for sensing applications as it will impact directly on the reproducibility, hence reliability, of analyte detection and quantification.

The $\mu*C$ calculated from the saturation regime of our PBTTT devices typically fell in the range of 0.4 – 0.8 µF/Vs, one order of magnitude higher than previously reported PBTTT water gated EGOFETs operated with tungsten gate electrode with a value of approximately 0.05 µF/Vs.[197] Other device set-ups utilising Au gate electrodes typically quote the device $\mu*C$ within the same order of magnitude.[97] The capacitance of PBTTT in water gated EGOFET is typically quoted as 0.6 µF/cm^2 measured within a Au/water/polymer/Au set up by EIS, to give a calculated μ of 0.08 cm^2/Vs;[197] elsewhere μ has been reported within the same order of magnitude (0.02 +/- 0.01 cm^2/Vs).[97] Assuming a similar capacitance of 0.6 µF/cm^2 for our OSC/electrolyte interface would give a μ of 0.7 to 1.3 cm^2/Vs, which is a significant improvement on previous studies. No significant trend could be observed in the

hole mobility using different solution concentrations as shown in Figure 52. The V_T values were consistently around -0.1 V, in close agreement for other PBTTT EGOFET devices.[97,197]

The variation in extracted parameters at different concentrations of spin coating solution used is negligible, with little benefit clearly identifiable in terms of either absolute value improvement or an improvement in the reproducibility as shown by reduced error bars. Ultimately it was decided to use devices fabricated from 7 mg/ml DCB solutions as this gave thin film thicknesses at least comparable to the source and drain heights (45 nm) in order to ensure complete coverage, with the aim of minimising the potential for gate leakage in subsequently developed devices.

Various operating voltages for V_{DS} and V_{GS} were investigated through the output characteristic (Figure 54). This demonstrated that V_{DS} > 0.5V resulted in non-linear behaviour in current after saturation. It can be observed that the output characteristic does not intersect the x axis at the origin and at V_{GS} > 0.5V the intersect shifts to higher V_{DS}. As a result, V_{DS} > 0.5V and V_{GS} > 0.5V were deemed unsuitable for device operation. The voltage window for device operation was reduced to 0.05 to -0.5V when sweeping the V_{GS} with the aim of minimising device degradation caused by electrochemical reactions in the OSC, which is more in line with the device operating regimes used elsewhere for PBTTT devices.[97]

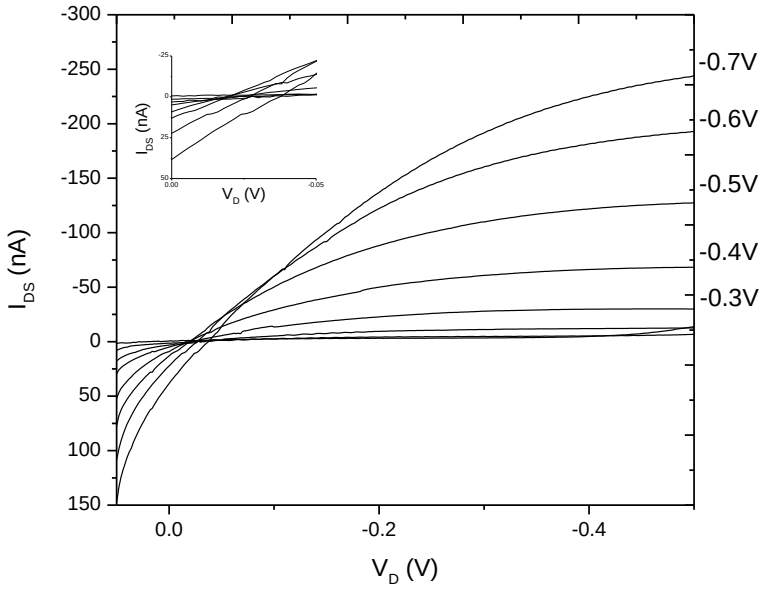

Figure 54 Output characteristic for PBTTT bilayer device in DI water V_{DS} 0.05 to -0.5V and V_{GS} 0 to -0.7V in 0.1V steps. The migration in x axis intercept at higher gate voltages is highlighted in the inset.

As highlighted, variation in inter- and intra-substrate device performance limits the reproducibility of analyte detection and accurate device calibration. The device performance was analysed over 10 sequential transfer hysteresis analyses over a 5 minute period in order to ascertain short term stability and reproducibility under repeated stress with the initial W gate water droplet measurement set-up (Figure 55). The forward sweep of the devices on the substrate showed a large variation in I_{SD} however the variation in the characteristic parameters extracted from the transfer curve are less pronounced (Table 12).

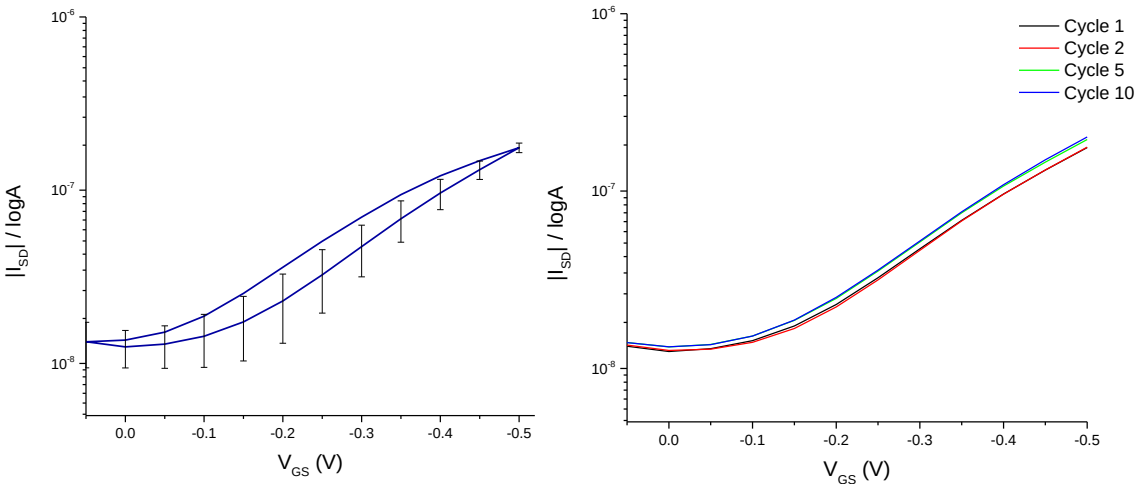

Figure 55 Transfer hysteresis performance of single layer device analysed using the 3-point probe station and a 4µl droplet as the gating electrolyte. (Left)-Averaged transfer hysteresis and standard deviation of 4 devices on the same substrate. (Right)- Averaged transfer hysteresis of 4 devices over 10 repeat cycles. The extracted parameters are shown in Table 12.

Table 12 Characteristic parameters extracted from transfer hysteresis displayed in Figure 55. The single layer device analysed using the 3 point probe station and a 4µl droplet as the gating electrolyte

Cycle Number	V_T (V)	Error (+/-)	µ*C (µF/Vs)	Error (+/-)	$I_{On/Off}$	Error (+/-)	I_{on} (nA)	Error (+/-)
1	-0.08	0.06	0.24	0.05	15.0	3.5	176	11
2	-0.09	0.05	0.24	0.05	14.7	2.7	177	9
5	-0.09	0.06	0.27	0.08	15.3	2.5	195	17
10	-0.09	0.05	0.28	0.06	15.8	1.9	202	30

The operational stability of the devices was then tested over this short bias stress window, as shown in Figure 55. Due to the frequent occurrence of bias stress effects devices are usually continually swept until reproducible transfer curves are produced and a stable operation window for measurements is established and necessary measurements are taken in sensing assays.[234] Over this

short period of stressing the device performance demonstrated reasonable stability with only slight decrease in I_{on} observed.

Overall it is evident that sufficient inter-device variability in performance exists in order to frustrate sensing from absolute values. This highlights utility of normalising the response to give the relative variation when describing the change in device parameter in sensing as shown in Equation 1; as this provides a robust parameter that normalises device-to-device variation therefore improving the reproducibility of the response.

6.1.1 EGOFETs using PBTTT – PMMA blends

Blending is a technique often used to modify the desired properties of a material. Blending can be used to improve the processability of solutions and enhance the film forming properties resulting in more homogeneous films producing devices with improved and more uniform performance.[235] Whilst blending is not particularly common practise in EGOFET fabrication, improved air stability, mobility of charge carriers and I_{on}/I_{off} ratio has been shown for OSC/insulator blends in OFETs.[107,235–238] Blending has even exploited self-organisation to allow facile one-step procedure for formation of semiconductor and dielectric layers,[235,236] and nanowire networks.[238]

Favourable phase separation of the blended OSC/insulator solutions during processing can deliver greater control of the microstructure through control of the thin film morphology.[235] The formation of continuous layers of highly crystalline OSC across the transistor channel drives improved performance and as charge transport in OFET devices is limited to a thin layer at the OSC/dielectric interface, any improvement in OSC order at this interface improves performance. Therefore, improved performance is typically achieved by inducing favourable vertical phase separation or the formation of nanofibrillar networks within the insulating polymer network.

Kergoat *et al*, demonstrated the improved device performance for P3HT/PMMA EGOFET devices operating in water.[107] Work within the research group has also exploited P3HT blended with bio-functionalised PMMA with a peptide in EGOFET sensing.[203] However devices using PBTTT as the OSC have shown improved hole mobility and stability relative to P3HT,[66] and insulator blends of PBTTT/PS and DPPTTT/PS have been investigated in simple OFETs.[237,238] In general the insulating polymers act as a plasticiser to provide a mobile environment allowing greater order in the OSC through formation of crystallites with better inter-chain ordering.[239,240]

However PBTTT insulator blends have not yet been reported for the EGOFET device architecture. Therefore it was of interest to see if the benefits of blending extend to PBTTT/PMMA blends in EGOFETs to the same extent as those demonstrated for P3HT/PMMA, which exhibited an order of

magnitude improvement in I_{on}/I_{off}.[107] Therefore a range of blend ratios of PBTTT and PMMA, varying from 20% - 100% PBTTT, where investigated as shown in Figure 56.

All EGOFETs showed typical p-channel behaviour and the extracted parameters for the various blend ratios are gathered in Figure 56. Overall no blend of PBTTT/PMMA produced a device with any significant simultaneous improvement in all 3 critical parameters relative to pristine PBTTT, whilst the improvements observed were less pronounced and restricted to higher concentrations relative to those seen in P3HT/PMMA.[107]

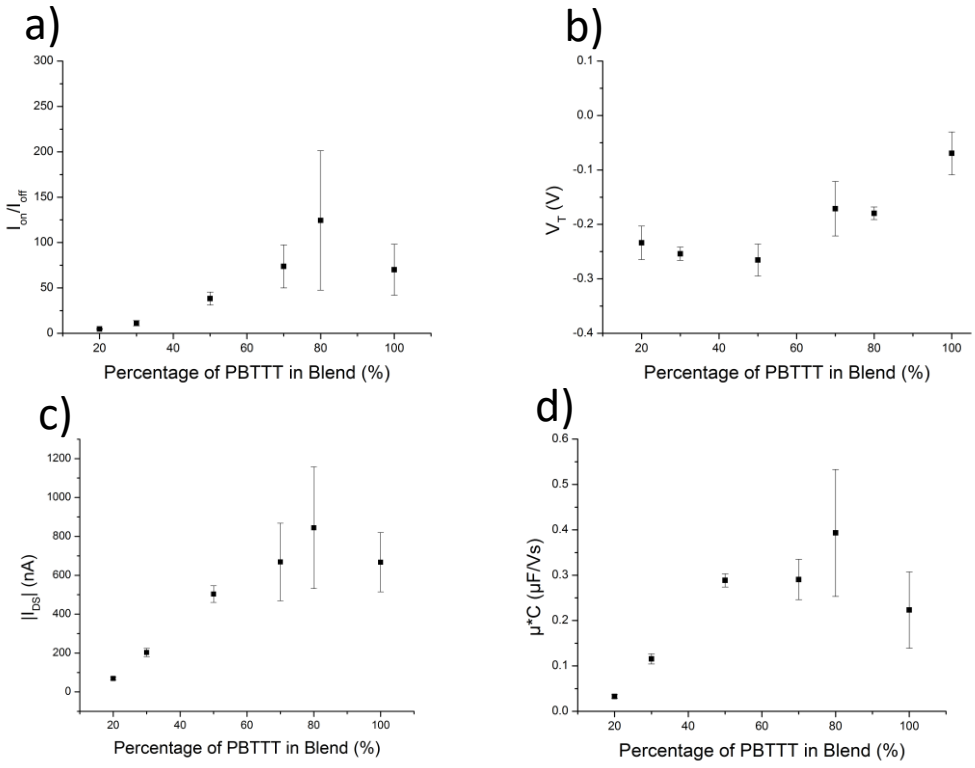

Figure 56 Charts showing mean device performance as a function of PBTTT ratio. The devices have different blends of PBTTT and PMMA, with standard deviation shown across the 4 devices on each substrates a) I_{on}/I_{off} ratio; b) V_T ; c) I_{on} d) mobility expressed as μ^*C.

Optimal images of blends with varying PBTTT/PMMA concentrations are displayed in Figure 57 and show clear phase separation for the 1:1 ratio on the µm scale with lateral phase separation and two distinct networks, in agreement with that previously observed in P3HT/PMMA.[107] As with P3HT, the mobility remains roughly constant over a broad range of PBTTT/PMMA ratios (Figure 56(d)), up to 50% PMMA, indicating that despite lateral phase separation the percolation path can still provide good charge carrier transport through the blend. However, in agreement with P3HT blend, the hole mobility decreases with low PBTTT content (30% and below) probably due to the formation of more isolated islands and discontinuous paths.[107]

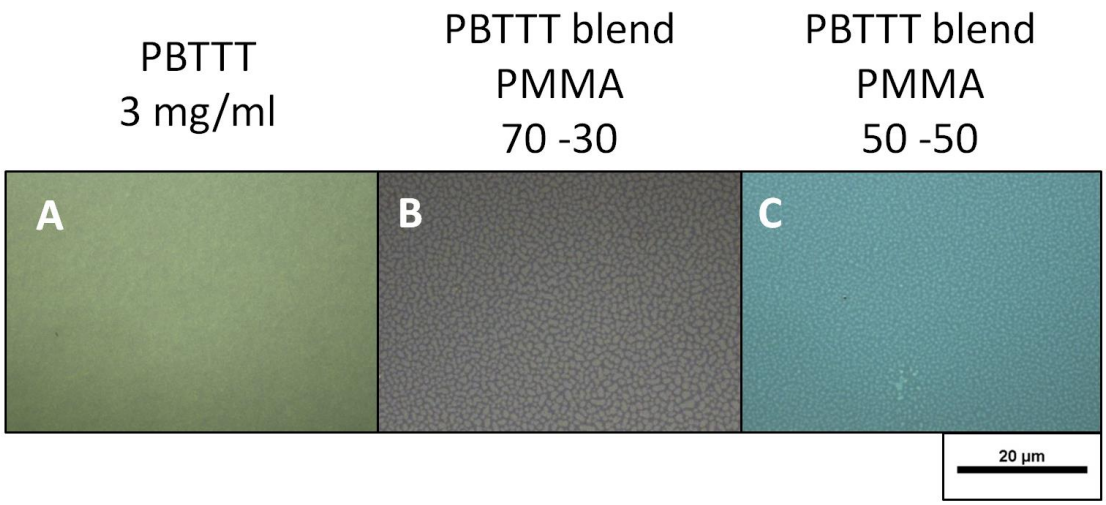

Figure 57 Optical microscope images of phase separation in devices. A) 100% PBTTT; B) 70% PBTTT/ 30% PMMA Blend; C) 50% PBTTT/ 50% PMMA Blend.

Whilst there was negligible change in on-current, off-current can be reduced under certain conditions resulting in an increase in I_{on}/I_{off} and the dependence on PBTTT ratio is shown in Figure 56a). However unlike P3HT where I_{on}/I_{off} was improved by an order of magnitude with as little as 30% OSC, PBTTT performance relative to pristine OSC was reduced below 70% PBTTT, whilst improvements were also less pronounced in comparison. Finally, Figure 56b shows variation in threshold voltage as a function of PBTTT. A threshold voltage close to 0 V is desired for low voltage applications, a shift to more negative V_T is observed with decreasing PBTTT but remaining at a low level.

Overall no blend of PBTTT/PMMA produced a device with a significant simultaneous improvement in all 3 critical parameters relative to the use of pristine PBTTT and the improvements observed were less pronounced than those for P3HT/PMMA. The difference is most likely driven by poor phase morphology control where undesirable macro-lateral phase separation appears prevalent.

The PMMA blending with PBTTT was used initially to investigate the possibility of blending as a pathway to blending with PMMA-COOH which would allow the attachment of biorecognition elements. As the anticipated vertical phase separation was not achieved and the effectiveness and reproducibility of macro-sized islands in immobilisation was unknown, in addition to the large hysteresis behaviour of the devices, therefore the use of PBTTT/PMMA blends was not pursued any further.

6.2 DPPTTT Tungsten-gated water droplet devices

Following the successful fabrication of PBTTT-based devices the use of DPPTTT was investigated for use as the OSC. The initial DPPTTT EGOFET devices were tested using a 3 point probing station by applying a 4 µl droplet of water over the channel area to act as the gating electrolyte and a tungsten tip as the gate electrode and a typical transfer curve is shown in Figure 58.

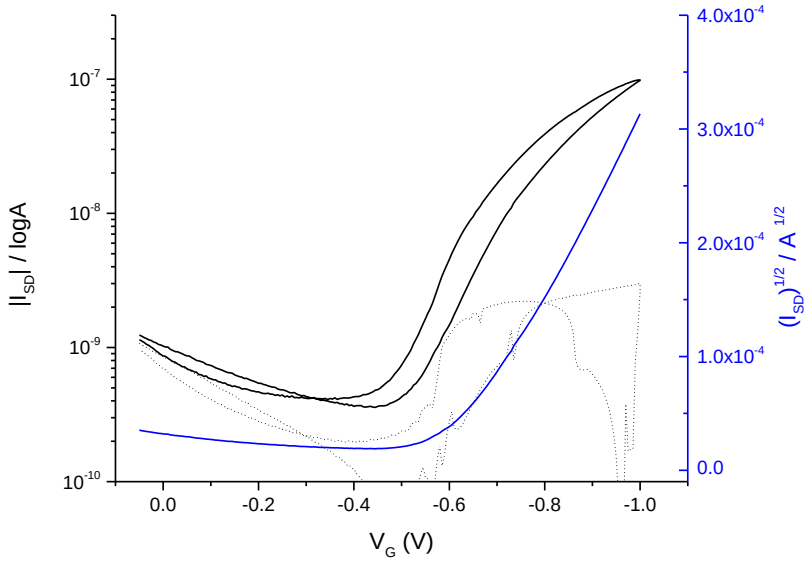

Figure 58 Transfer Characteristic DPPTTT EGOFET device using water droplet and W pin as the gate electrode. Source and drain electrode where patterned using a shadow mask. I_{SD} (black – solid lines) and I_G (black – dotted lines) plotted in a semi-log scale (left). I_{SD} plotted in a square root scale (blue – right) from which characteristic parameters are extracted from the saturation regime.

The DPPTTT devices gave a $\mu*C$ of approximately 0.1 µF/Vs and V_T of -0.6 V (+/- 0.02), a significantly more negative V_T relative to that of PBTTT which is closer to 0V. The electrolysis of water typically limits the safe device operation in EGOFETs to <1V, therefore the effective operational window for DPPTT EGOFET devices is significantly reduced by the high V_T.[29]

Bilayer devices were fabricated by depositing PMMA films on to the DPPTTT layer by spin coating from n-butyl acetate solutions. Initial experiments checked that n-butyl acetate was truly orthogonal to the underlying OSC and had minimal impact on the electrical performance. The neat solvent was spin coated on to the device and annealed in replication of the bilayer deposition process. The electrical performance was measured before and after by operation, as shown in Figure 59, showing minimal alteration in performance.

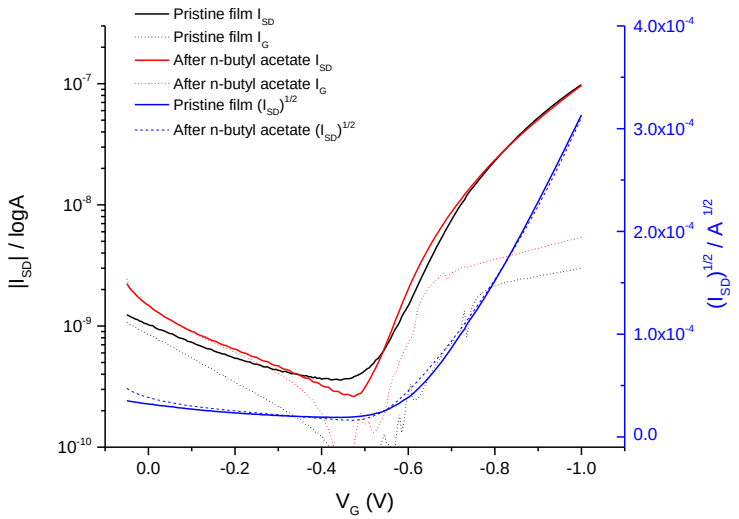

Figure 59 Transfer characteristic displaying the effect on electrical performance of spin-coating n-butyl acetate onto a DPPTTT device. The device was operated using 4 ul water droplet and W tip gate electrode.

Consequently devices DPPTTT based bilayer devices utilising both PMMA and the PMMA COOH co-polymer where fabricated following the previously validated procedure described in section 3.1 The electrical performance relative to pristine DPPTTT was assessed by measuring the transfer characteristic, shown in Figure 60.

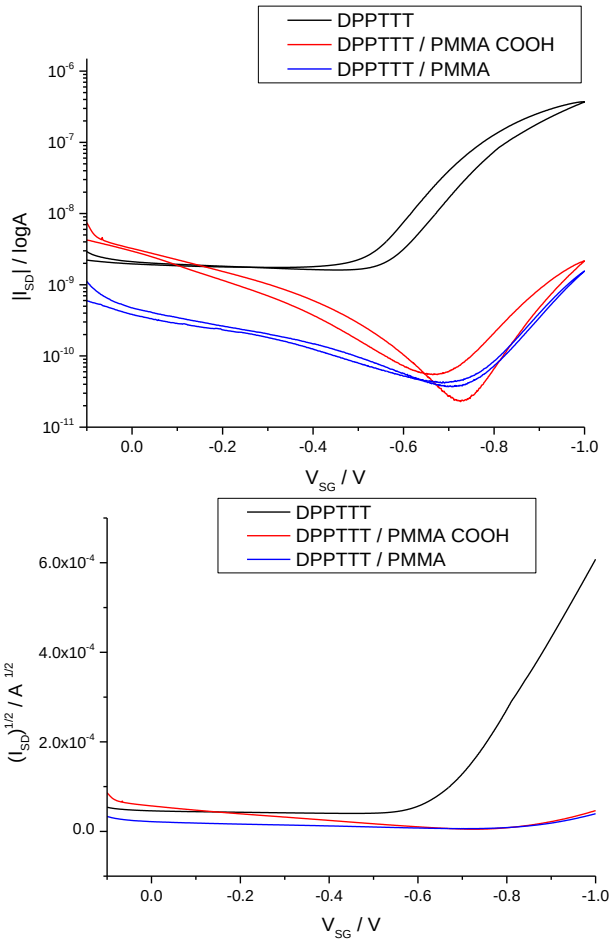

Figure 60 Transfer characteristics of water droplet gated DPPTTT devices operated with a tungsten gate electrode. Displayed are pristine OSC device and bilayer devices: DPPTTT (black), DPPTTT / PMMA COOH bilayer (red) and DPPTTT / PMMA bilayer (blue). a) I_{SD} plotted in a semi-log scale. b) I_{SD} plotted in a square root scale from which characteristic parameters for V_T and $\mu*C$ are extracted from the saturation regime.

It is evident that deposition of the PMMA layer on to the DPPTTT caused a significant negative shift in V_T from -0.6 V to -0.8 V further reducing the window for device operation under -1V. Additionally the deposition of the second layer also caused a one order of magnitude reduction in the observed mobility, which was also observed by Mulla *et al* after PAA deposition on PBTTT.[97] The increase in V_T and reduction of $\mu*C$ can be explained by the introduction of a lower capacitance system to the OSC/dielectric interface, as the PMMA layer replaces the extremely high capacitance of the EDL and the lower capacitance system dominates the device behaviour.[231] The combination of these high V_T and lower mobility therefore logically resulted in the very low maximum currents observed. The observed device performances within the existing measurement set up was not deemed effective for device operation or suitable for use in biosensing application. However previous studies have shown that the choice of gate electrode material can be an effective tool for V_T tuning and presents an opportunity shift the device operation into a more suitable regime.[43,62,241]

6.3 EGOFET devices using different gate metals

Whilst the gate metal is not in direct contact with the OSC and charge carriers, the threshold voltage is dependent on the gate work function, as shown in *Equation 14*. Therefore in an ideal trap-free OFET V_T is dependent on the device materials used, summarised by their contribution to V_{FB}; where the work function of gate metal (φ_m) and the ionisation potential (I_p) of a p-type OSC and is broken down by *Equation 15*.[62]

The threshold voltage dependence on work function (φ_m) of the gate electrode materials is well-established amongst inorganic transistors gated by dielectrics.[61] Work functions of electrode materials are typically measured by either ultraviolet photoemission spectroscopy or capacitance-voltage (*C*-*V*) measurements. Variation of the work function, either through modification of the gate electrode or use of another material, produces a voltage shift in the *C*-*V* characteristics of the metal-insulator-semiconductor stack. The effect of varying the electrode work function of the gate electrode could be used to shift the V_T of the devices into a more appropriate window for *I*-*V* characterisation in water.

Therefore the dependence of *I*-*V* characteristics of water-based EGOFET devices on the gate metal was investigated for both PBTTT and DPPTTT, using different gate electrodes immersed into the water droplet as previously demonstrated by Kergoat *et al* for P3HT-based EGFOET devices.[43] The transfer curves were recorded for each material and the characteristic parameters extracted from the saturation regimes and the values are displayed in Table 13. The chosen gate materials have previously been applied in EGOFET devices as gate electrodes and cover a range of work functions, namely W (φ_W 4.65 eV), Au (φ_{Au} 5.4 eV), and Pt (φ_{Pt} = 5.65 eV).[43] DPPTTT devices were initially tested with the various gate materials sequentially immersed into water droplets used as the electrolyte in the EGOFET devices, the measured transfer characteristic are displayed in Figure 61. The $\sqrt{I_{SD}}$ shows the expected trend in gate work function induced V_T shift producing the observed shift towards a more positive (or less negative) threshold voltage, allowing the devices to turn on at lower voltage. Additionally the lower V_T resulted in an increased I_{on} by extending the operational window of the device operation during the same V_G sweep range. In contrast, the μ^*C remained relatively unchanged by gate metal as shown by the similar gradients of the $\sqrt{I_{SD}}$ in Figure 61.

Table 13 Transfer characteristic parameters of threshold voltage, mobility, on/off current ratio and maximum current, as extracted from the saturation regime of water droplet gated DPPTTT devices with three different gate electrodes. Errors are reported as the standard deviation across 4 devices.

	DPPTTT					PBTTT			
	V_T (V)	μ*C (μF/Vs)	I_{on}/I_{off}	max I_{DS} (nA)		**V_T (V)**	**μ*C (μF/Vs)**	**I_{on}/I_{off}**	**max I_{DS} (nA)**
W	-0.60 (±0.01)	0.20 (±0.04)	10	270 (±60)	W	-0.27 (±0.02)	0.06 (±0.01)	10	250 (±90)
Au	-0.15 (±0.03)	0.19 (±0.02)	10^2	1100 (±90)	Au	0.07 (±0.11)	0.13 (±0.03)	10^2	700 (±100)
Pt	0.14(±0.08)	0.15 (±0.07)	10	1000 (±300)	Pt	0.23 (±0.13)	0.12 (±0.05)	10^2	750 (±200)

	DPPTTT/PMMA-COOH					PBTTT/PMMA-COOH			
	V_T (V)	**μ*C (μF/Vs)**	**I_{on}/I_{off}**	**max I_{DS} (nA)**		**V_T (V)**	**μ*C (μF/Vs)**	**I_{on}/I_{off}**	**max I_{DS} (nA)**
W	-0.82 (±0.01)	0.007 (±0.002)	10	2 (±1)	W	-0.30 (±0.01)	0.006 (±0.001)	10	30 (±10)
Au	-0.38 (±0.02)	0.025 (±0.007)	10^2	80 (±20)	Au	-0.16 (±0.06)	0.028 (±0.007)	10	150 (±20)
Pt	-0.16 (±0.06)	0.031 (±0.001)	10^2	200 (±30)	Pt	0.44 (±0.02)	0.011 (±0.003)	10	130 (±30)

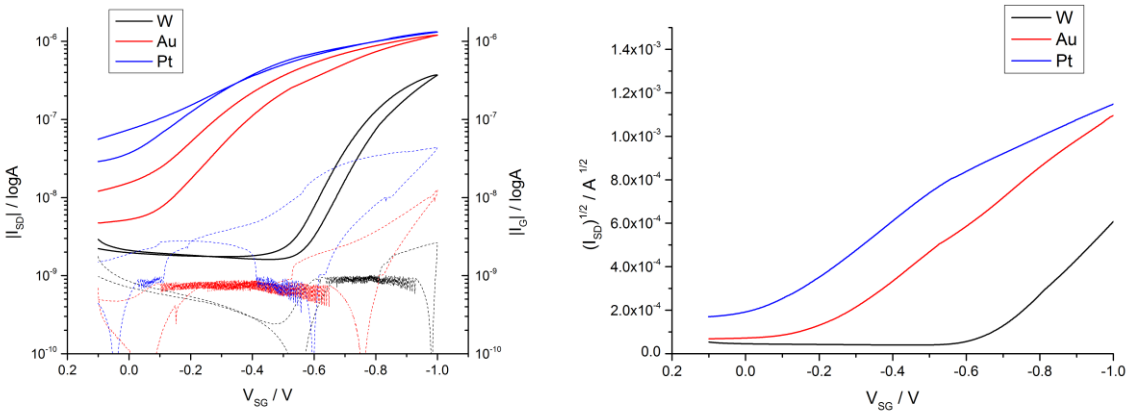

Figure 61 Transfer characteristics of water droplet gated DPPTTT devices with three different gate electrodes: Pt (blue), Au (red), W (black). a) I_{SD} (left – solid lines) and I_G (right – dotted lines) plotted in a semi-log scale. b) I_{SD} plotted in a square root scale from which characteristic parameters for V_T and μ^*C are extracted from the saturation regime. The extracted parameters are displayed in Table 13.

The trend is again repeated for PBTTT-based devices with a more positive V_T yielding higher I_{on} values, as shown in Figure 62, however the initial V_T for the PBTTT devices operated with W electrode are significantly less negative, resulting in overall more positive V_T values relative to DPPTTT.

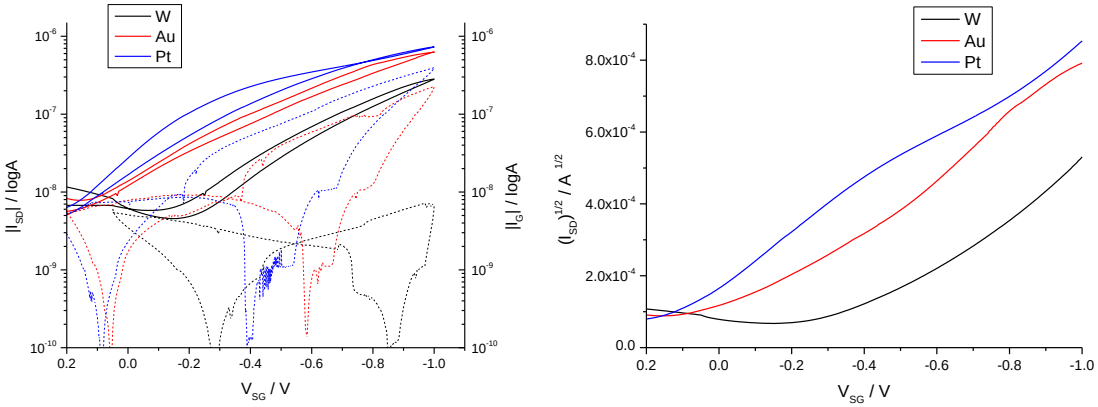

Figure 62 Transfer characteristics of water droplet gated PBTTT devices with three different gate electrodes: Pt (blue), Au (red), W (black). a) I_{SD} (left – solid lines) and I_G (right – dotted lines) plotted in a semi-log scale. b) I_{SD} plotted in a square root scale from which characteristic parameters for V_T and $\mu*C$ are extracted from the saturation regime. The extracted parameters are displayed in Table 13.

Subsequently the influence of the gate material was investigated for the bilayer devices; the transfer curve for the DPPTTT/PMMA COOH device is displayed in Figure 63. The same trend is again observed and the desired V_T is closer to 0V for Au and Pt electrodes. The device operational window is sufficiently large to allow more effective device performance achieving I_{on} of around 100 nA. Additionally an increase in $\mu*C$ was also observed to around 0.03 µF/Vs when the devices were operated with Au and Pt electrodes, a one order of magnitude reduction relative to the unmodified DPPTTT EGOFET device, which is more in line with that observed by Mulla *et al* for PAA devices.[97] The reduction in mobility could be explained by the addition of lower capacitance PMMA dielectric layer to the OSC/electrolyte interface.

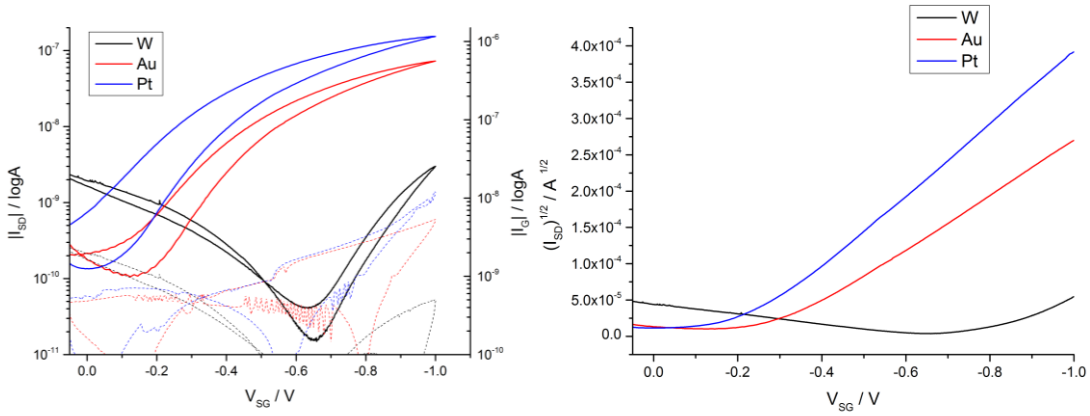

Figure 63 Transfer characteristics of water droplet gated DPPTTT/PMMA COOH devices with three different gate electrodes: Pt (blue), Au (red), W (black). a) I_{SD} (left – solid lines) and I_G (right – dotted lines) plotted in a semi-log scale. b) I_{SD} plotted in a square root scale from which characteristic parameters for V_T and $\mu*C$ are extracted from the saturation regime. The extracted parameters are displayed in Table 13.

The threshold voltage is plotted as a function of the gate electrode in Figure 64. Theoretically threshold voltage of FETs should have a linear correlation to the work function of the gate metal electrode with a slope of 1.[29,43] The correlation is qualitatively as expected, with an increase in work function producing the observed shift towards a more positive (or less negative) threshold voltage in the devices; however an exact quantitative trend is not observed in our data. Deviations appear in the trend, which can be attributed to variation in the expected gate electrode work functions as a result of contamination of the material which can result in a different work function to that theoretically expected and can result in a significant reduction in the effective work function of high work function metals, in particular for Au and Pt.[43] In ideal conditions Au and Pt are known to exhibit similar work functions of around 5 eV but both are known to display a wide variety of effective work functions depending on operating conditions (Au ~ 4.7-5.5 eV, Pt ~ 5.1-5.9 eV).[242,243] Photon electron spectroscopy measurements point toward a reduction of the work function of Au from 5.4 eV to 4.7 eV due to contamination under ambient conditions.[244]

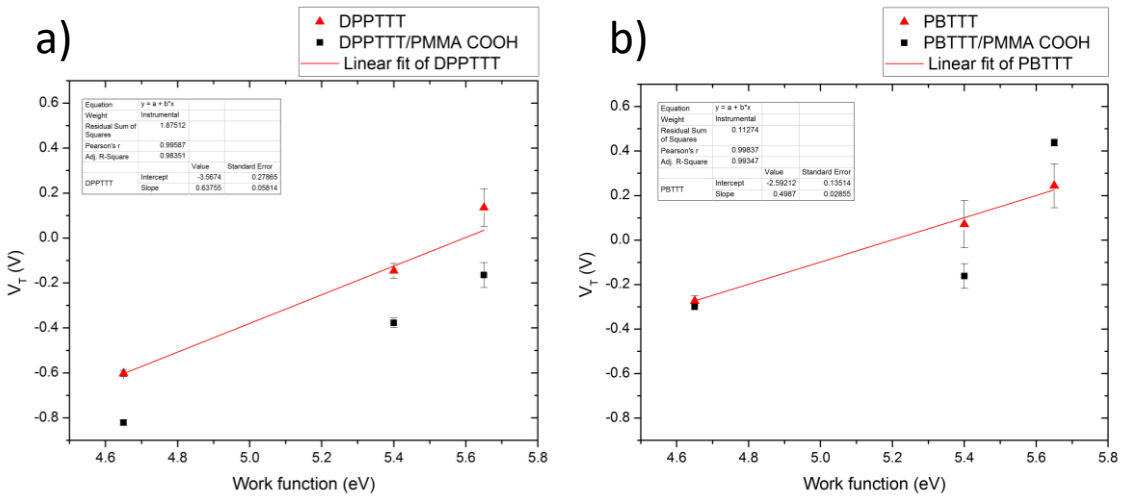

Figure 64 Threshold voltage as a function of the theoretical work function of the gate material used in water droplet gated EGOFET devices with three different gate electrodes: Pt (5.65 eV), Au (5.4 eV), W (4.65 eV). a) DPPTTT based devices. b) PBTTT based devices. A linear fit is plotted for both OSCs. Pristine OSC devices are plotted in red and OCS/ PMMA COOH 10% bilayer devices are plotted in black. Errors are displayed as the standard deviation across 4 devices.

The difference in the effective work function of Au and Pt by around 0.6 eV could also be caused by compression of the high surface electronic density tail as a result of Pauli repulsion with the electron density that extends beyond the gate metal surface.[43] The large polarizable electron density of Au can lead to a significant reduction of the work function due to the formation of this highly polarised

layer at the water/metal interface.[232] In contrast tungsten has a less polarizable surface density and the effective decrease in work function would be small, as is observed for carbon or oxides.[43]

Contamination of the W gate electrodes is also common upon exposure to air and DI water through the formation of an oxide layer which increases in thickness upon anionic polarisation, and its dissolution can occur below 1V.[245–248] The electrochemical reaction in water within the 5-7 pH range is expressed as:[247]

$$W + 4H_2O = WO_4^{-2} + 6e^-$$

The formation of an oxide layer on the gate is undesirable, as it will lower the capacitance of the gate electrode potentially lowering the output current, as well as changing the gate electrode work function. Additionally, dissolution of the oxide can contribute to increasing the ionic strength of DI water.

The understanding of the interfacial properties and the modelling of EDLs on metals such as Pt are complicated by difficulties in achieving reproducible surface conditions for device operation due to the impact of cleanliness and adsorbed impurities. An alternative EGOFET configuration which negates gate electrode contamination utilises a reference electrode such as Ag/AgCl and the instability of device performance caused by the gate electrode has previously been demonstrated by EGOFET devices showing a potential drift of the Au electrode against a Ag/AgCl reference electrode.[42] The reference electrode operates at a fixed potential by working as a redox electrode, meaning all observed changes are only related to changes at the OSC/electrolyte interface and any interaction at the gate is negated. The use of other gate metals as electrodes means they operate as more of a quasi-reference electrode with the presumption that the potential of electrodes and bulk solution remains unchanged.[42]

The appropriate choice of metal gate electrode work function has also been shown to allow tuning of the contact resistance experienced at the *S* and *D* electrodes by over one order of magnitude, where low work function materials are particularly undesirable.[241] Gold is the most frequent and convenient electrode material in EGOFET devices due to the good work function match to the HOMO level of most p-type OSCs minimising potential energy mismatch and charge injection barriers[241]. Additionally the relative stability to electrochemical reactions in the aqueous electrolytes is desirable for device operation. In this work effective DPPTTT/PMMA COOH operation with a low V_T was achieved by using Au as gate electrode, making it the preferred gate material in our biosensor development. In addition to this the use of gold gate electrodes allows for use of SAM based functionalisation techniques for the biosensor which are investigated further in chapter 7.

6.4 Interdigitated electrodes with Au gated EGOFETs

The EGOFET devices initially produced by shadow mask evaporation typically displayed a relatively low I_{on} of around 100 nA (V_{DS} = -0.7 V and V_{GS} = -1 V). This can be attributed to the low geometry factor of the shadow mask design used during source and drain metal deposition by high vacuum thermal evaporation (L= 60 µm, W = 1 mm), through its relation to I_{SD} described in Equation 8. The use of interdigitated electrodes is a facile method to significantly increase the width of the device channel that results in a larger I_{SD} due to the increased geometry factor. However, the features that can be formed through use of a shadow mask defined design are relatively restricted in their geometry as the mask must be self-supporting, and this limits the feature sizes that can be achieved preventing the fabrication of inter-digitated electrode designs with small channel lengths.

Therefore in order to maximise the possible I_{SD} current of the devices, interdigitated electrode (IDE) devices were produced by photolithography.[249] A variety of channel lengths where fabricated to give devices with channel lengths of L= 60 µm, 40 µm, 20 µm and 10 µm and the same channel width of W= 16.9 mm. Devices were fabricated from the 60 µm channel lengths utilising the IDE design and the original low geometry factor shadow mask design, and the performances of these devices utilising DPPTTT and PBTTT as the OSC are directly compared by their respective transfer characteristics in Figure 65.

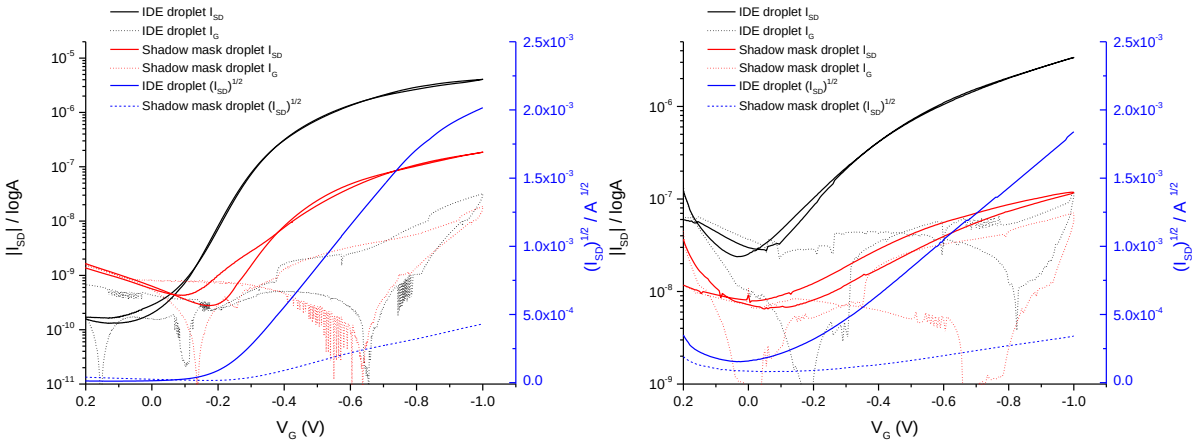

Figure 65 Transfer characteristics comparing typical DPPTTT (left) and PBTTT (right) EGOFET devices using source and drain electrodes patterned by evaporation using a shadow mask (red) and photolithography defined IDE design (black), with 60 µm channel length. Devices operated with water droplet and Au wire as the gate electrode. I_{SD} (solid lines) and I_G (dotted lines) plotted in a semi-log scale (left). I_{SD} plotted in a square root scale (blue – right) from which characteristic parameters are extracted from the saturation regime.

In both DPPTTT and PBTTT the expected increase in I_{SD} due to the increased geometry factor is clearly observed, with µA currents achieved. The small hysteresis observed can be attributed to

charge polarisation and ion movements in the electrolyte.[42] Interestingly the gate leakage (I_G) remains within the same order of magnitude despite the large relative increase in I_{SD}; this is indicating that the increased current is due to good charge transport within the active material and not a corresponding increase in electrochemical reactions.

In both cases the use of IDE results in a more ideal transfer characteristic in particular a reduction in the relative level of hysteresis between the forward and backward sweep. A high relative level of I_{SD} to I_G correlates with an increased hysteresis, especially with regard to the PBTTT devices and an improvement in the relative ratio of I_{SD} to I_G gives improved device performance.

The impact of varying the device channel length in the DPPTTT devices was investigated and the transfer curves and output characteristics of devices with varying lengths (L = 60, 40, 20, 10 µm) and the same channel width are displayed in Figure 66. In all cases, good overall device performance and p-type OSC behaviour is typified by the well-shaped linear and saturation regimes for the I_{DS}– V_{DS} curves and low hysteresis of the device characteristics of the devices in addition to good modulation with V_G of the transfer curves displayed in Figure 66. The output characteristics show that even at the shortest channel good saturation in the output curves is displayed, with no significant short-channel effects observable.[250] Short channel effects in EGOFETs are usually inhibited by the high transversal field generated by the high capacitance of the exceptionally thin EDL.[251] Additionally EGOFET devices are also typically less prone to contact resistance issues and at all channel lengths none are clearly identifiable.[252]

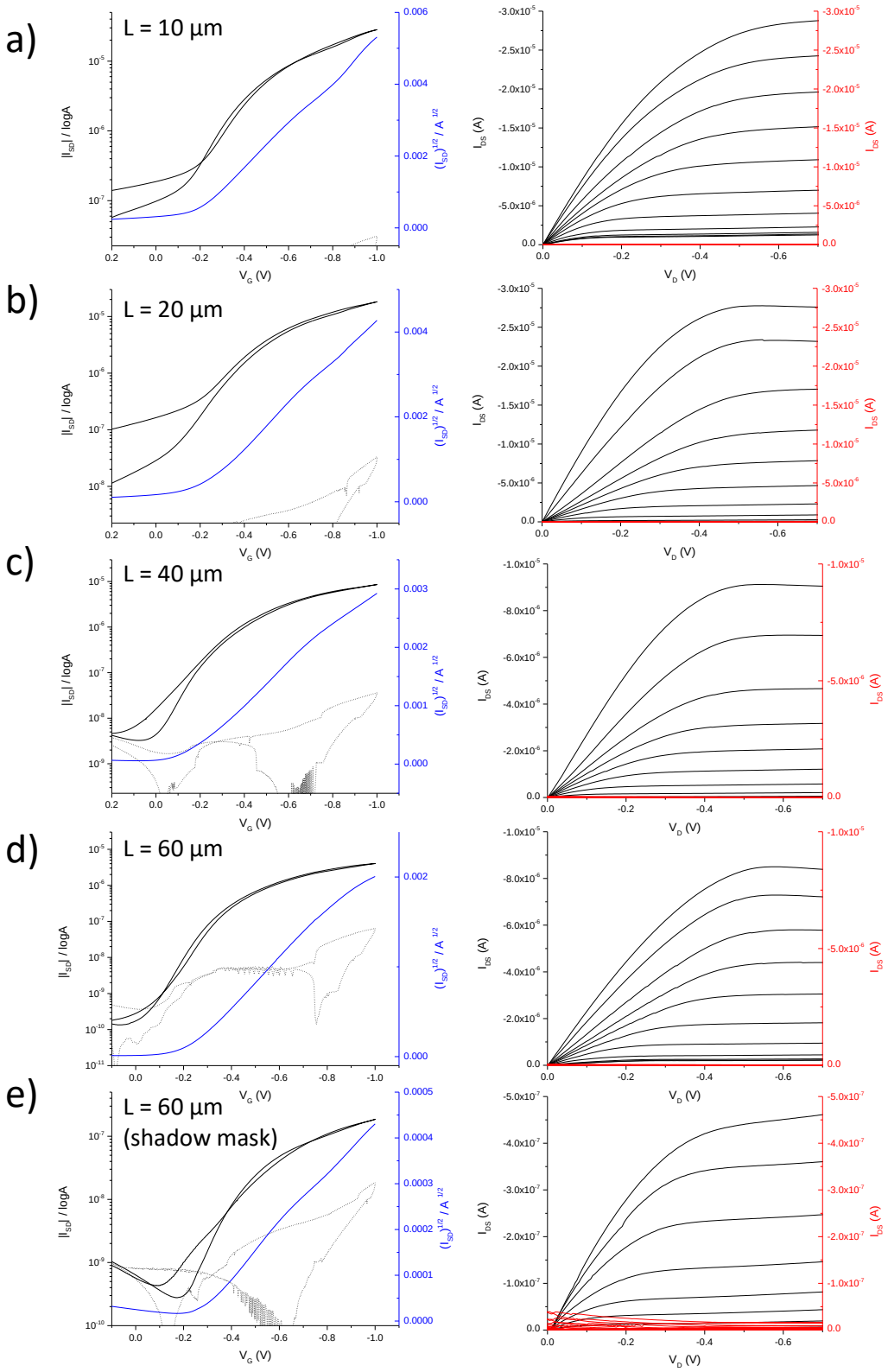

Figure 66 Transfer characteristics and output characteristics of typical DPPTTT EGOFET devices using an 8 µl water droplet and Au wire as gate electrode with varying channel lengths: a) 10 µm IDE; b) 20 µm IDE; c) 40 µm IDE; d) 60 µm IDE; e) 60 µm shadow mask design.

As is expected the increased geometry factor at shorter channel lengths results in a significant increase in I_{on} for the devices as shown in Figure 67. The trend is further investigated through the averaged extracted parameters from the transfer curves as a function of varying channel length, displayed in Figure 68. The relation between I_{SD} in the saturation regime is related to the channel length through the device geometry factor ($^{W}/_{2L}$) through Equation 8, which in theory should follow a linear correlation, Figure 68a shows that the trend is observed although with some deviation caused by processing variations.

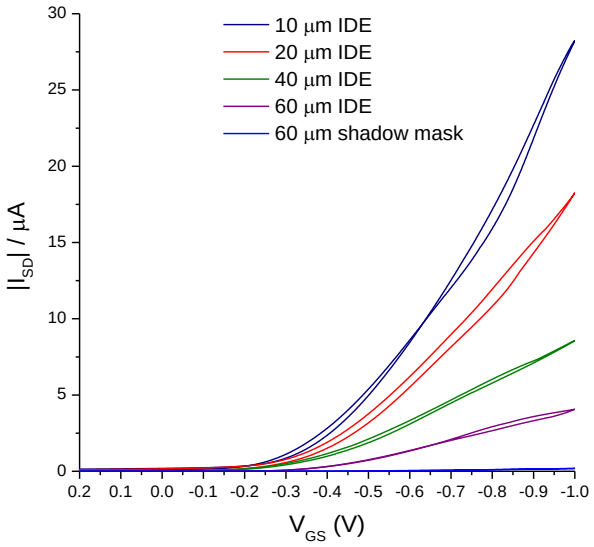

Figure 67 Transfer characteristic comparing typical DPPTTT EGOFET devices of varying channel lengths using source and drain electrodes patterned by photolithography defined IDE design (L= 60, 40, 20, 10 µm, W = 16.9 mm)and evaporation using a shadow mask (L= 60 µm, W = 1 mm). Devices operated with DI water droplet and Au wire as the gate electrode.

Under ideal operation both V_T and mobility should be independent of the device channel length and for both parameters Figure 68b-c no identifiable trend is observed, again a good indicator for a lack of short channel effects or contact resistance, and variations observed can be ascribed to the processing techniques used. The V_T for the devices is consistently around -0.1V with $\mu*C$ of around 0.05 µF/Vs. In previous DPPTTT EGOFET devices the measured capacitance at V_{GS} = -1V was calculated as 1.8 µF/cm^2 in water, giving a μ of 0.13 cm^2/Vs.[253] Using the same capacitance value we can estimate the μ of our devices to be around 0.03 cm^2/Vs.

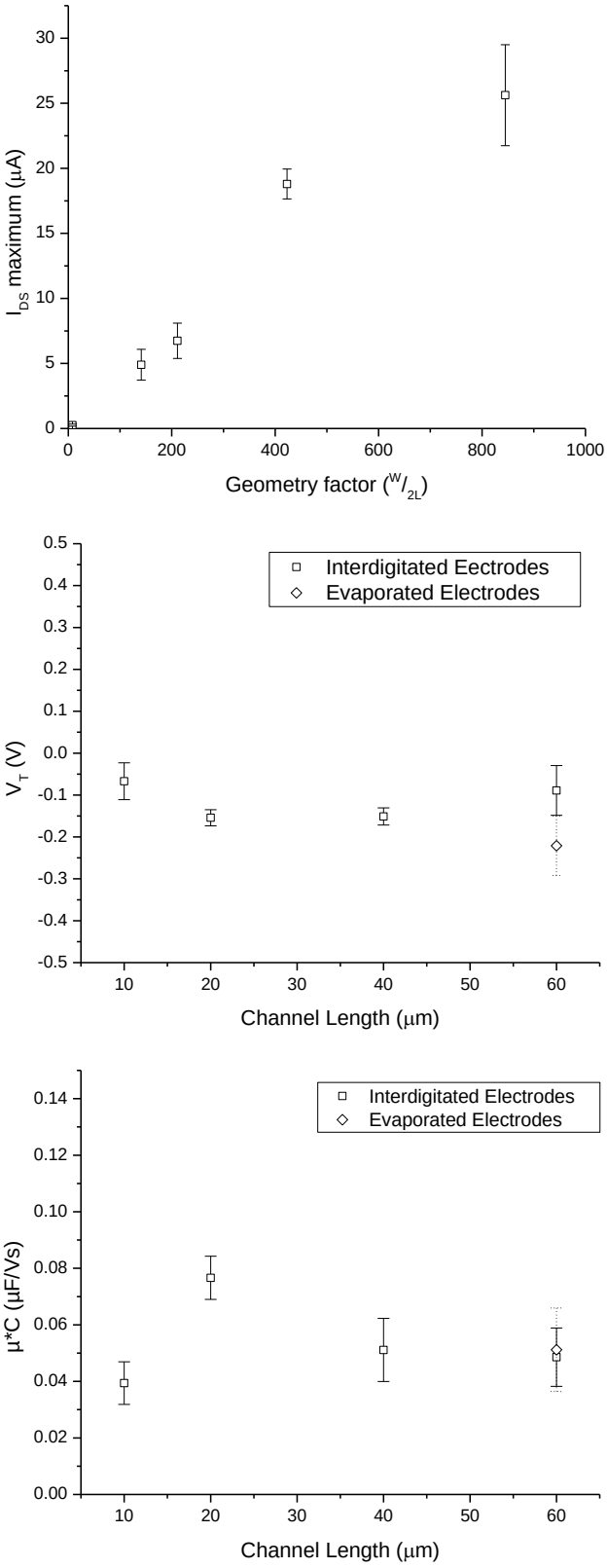

Figure 68 Variation in key transfer characteristics parameters DPPTTT EGOFET devices of varying channel lengths: a) Variation of maximum I_{DS} as a function of device geometry factor; b) Variation of V_T against device channel length; c) Variation of μ^*C against device channel length. Errors are displayed as the standard deviation across 4 devices.

6.5 Summary

Following the improvement of the device operation by successful implementation of Au gate electrodes and photolithography defined IDE, the devices are well positioned for further investigation in the biosensing platform.

In order to create a platform of optimal biosensing capability it is important to minimise any variation in device performance that is not associated with the analyte interaction, such as device stability and reproducibility. Of particular interest is the reproducibility of the forward sweep from which the electrical parameters are extracted; these parameters are sensitive to the effects of analyte interaction and it is their relative variation which is of interest. Variation in inter- and intra-substrate device performance limits the reproducibility of analyte detection and accurate device calibration, although the relative variation can be normalised.[97]

Initially EGOFET devices were tested using a 3 point probing station by applying a 4 µl droplet of water over the channel area used as the gating electrolyte and a tungsten tip as the gate electrode. The device performance was analysed over 10 sequential transfer characteristic analyses over a 10 minute period in order to ascertain short term stability and reproducibility under repeated stress (Figure 55). The forward sweep of the devices on a single substrate showed a large variation however the variation in the extracted characteristic parameters was less pronounced (Table 12).

There are several factors in the measurement process that can lead to variation in the device performance when using the droplet-based measurement set-up. For instance, human error in positioning of the gate electrode and electrolyte droplet, relative to the channel area, both in terms of lateral positioning (x, y) and vertical positioning (i.e. gate height). Greater control over the positioning of the gate electrode can be gained through use of a flat gold square, covering the entire channel area and at a controlled height as the gate electrode.[42,75,97] This also allows the generation of a more homogeneous electrical field to cover the entire channel area. Another factor contributing towards device performance variation is through evaporation of the gating electrolyte during analysis which causes an increase in the relative concentration of salts and analyte over time as well as a change in the size and shape of the analyte droplet.

7 Gate functionalised EGOFET biosensors

In order to facilitate the investigation of gate functionalised electrodes for use in EGOFET biosensors, a setup was developed to reliably hold the relevant components of the device in place during the electrical measurements. After the deposition of a P3HT thin film onto a glass substrate, a 30 µl well is made to hold the aqueous gating medium above the interdigitated source and drain electrodes (Figure 80). The well design was patterned from 3 mm thick acrylic and double-sided adhesive using a laser cutter and is stuck onto the substrate with the double-sided adhesive. A PTFE block holds the four gold wire electrodes in the wells and the resulting EGOFET device is constructed as shown in Figure 70. The wells hold a larger volume of liquid for use as the gating medium than is reasonably practicable with a droplet, whilst reducing the rate of evaporation to allow more accurate sensing results. Similar wells have been reported in other EGOFET biosensors but are usually made from PDMS.[42,123,254]

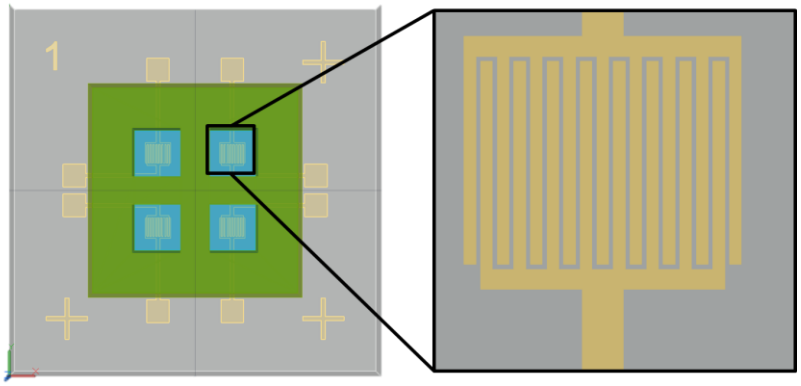

Figure 69 Schematic showing a patterned glass substrate with four separate wells of 30 µl for holding the aqueous gating medium in the EGOFET device (left). Inset the photolithographically defined interdigitated source and drain electrodes with a channel length of L= 20 µm and channel width of W= 16.9 mm used in these devices.

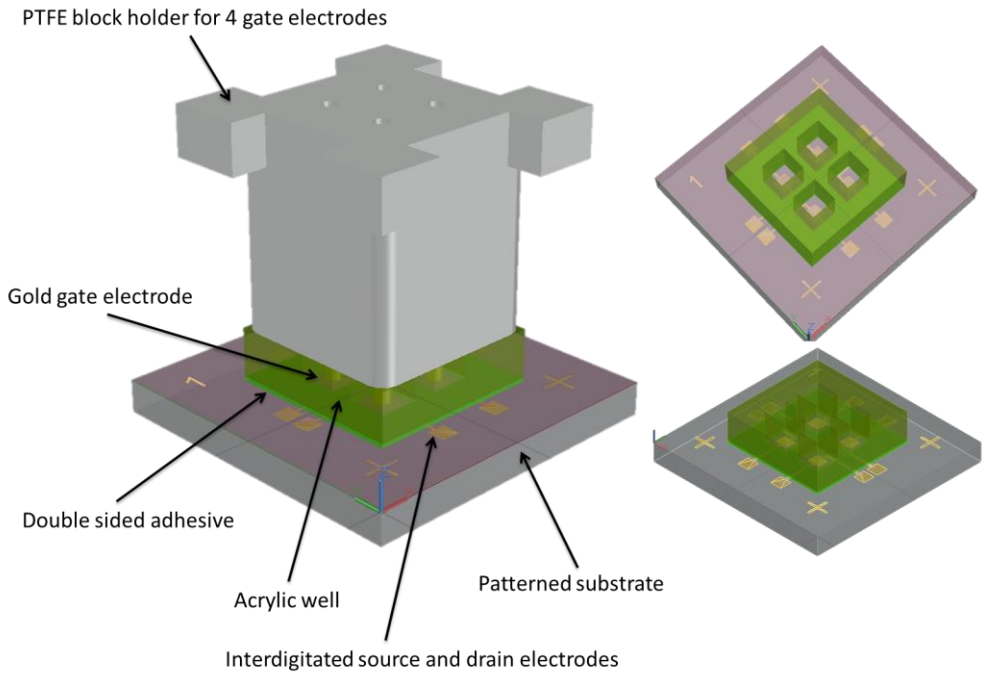

Figure 70 Three-dimensional structure of the constructed Electrolyte-gated OFET device.

A PTFE block was also designed to hold all the required components in place (Figure 82). This enabled the controlled and reproducible positioning of the gate electrodes over the channel area at a consistent height in order to minimise related variation in electrical measurements. The gate electrode is a gold wire that is stably held ~ 1mm over the channel area inside the electrolyte filled well. The PTFE blocks also house spring loaded micro-pins for contacting the source and drain contact pads for easy measurement within the microprobe station with an Agilent semiconductor analyser for device analysis (Figure 121).

Figure 71 Exploded view of all the components – left PTFE block with gate electrodes, lower right the sensing chamber that contains 4 compartments that form 4 EGOFET devices, top – block containing spring loaded contacts that make the electrical connections to the devices. Inset- PTFE block holding 4 gate electrodes.

The device structure enables the gate electrode to be easily removed for the application of different aqueous solutions required in calibration curve experiments. In the BioSAM sensing experiments (reported in section 7.1) the gate electrodes must be removed entirely from the device for the separate incubation in the relevant analyte solutions. The gate electrodes are then rinsed and returned to the EGOFET device for electrical measurement in DI water.

7.1 HER2 ECD sensing with 3MPA/11MUA-based BioSAM

The BioSAM system has previously been utilised for the selective detection of immunoglobins and C-reactive Protein (CRP) with EGOFET biosensors. Therefore, using monoclonal HER2 antibodies as the biorecognition element the detection of HER2 ECD, a biomarker associated with breast cancer, was investigated with BioSAM functionalised gold gate electrodes for use in an EGOFET biosensor as discussed in section 5.2.2. The experimental protocol used for the sensing measurements was performed in accordance to those reported elsewhere for BioSAM devices.

The EGOFET device is first incubated in water for 18 hours in DI water in order to achieve a steady state of decay that results in a stabilised device with low I_{on} current drift. The I_{DS} was further

stabilised by repeating the measurement of the transfer curve of the P3HT EGOFET using a bare gold gate electrode until three successive curves perfectly overlap. Stabilising the device in this manner fills the low mobility trap states of the OSC which leads to a stable V_T and device performance. The subsequent shifts in V_T can therefore be attributed to changes in the work function which may be altered in the presence of an analyte. The transfer characteristics for the devices in this section were taken by measuring the I_{DS} as a function of V_G ranging from 0.1 to -0.6V at a constant V_D of -0.4V. All the subsequent data discussed in this section was recorded on devices that where cycled until the traces overlap and the transistors operational stability was reached for each measurement. Following the stabilisation of the device with the bare gold electrode the final measurement is retained as a reference value and is shown by the black curve in Figure 72. The gate leakage current (I_G) was also recorded over the same range of V_G and shown to be two orders of magnitude lower than the I_{DS} (Figure 121). The operating voltage range used excludes potentials where electrochemical process occur that could produce desorption or degradation of the SAM which would be evidenced by large I_G.

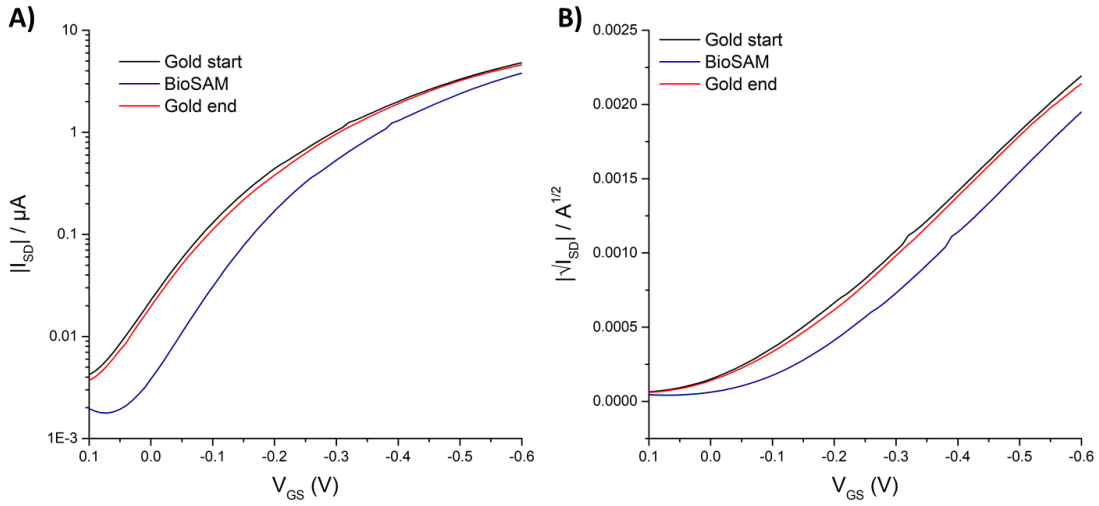

Figure 72 Transfer I-V curves (I_{DS} vs. V_G at V_D=-0.4V) displaying the change in the device performance before and after the completion of the HER2 calibration curve for one device. The black (before) and red (after) curves show the measurement recorded with a bare Au gate, and the blue curve was recorded using the functionalised Biosam gate before the calibration curve measurements are taken.

The bare gold electrode is then replaced with the functionalised gate electrode which had been incubated in PBS for 10 mins and rinsed with water. Following the stabilisation of the current through cycling of the transfer curves, the measurement is recorded as the baseline for the calibration assay (I_0) and is shown by the blue curve in Figure 72. A shift in V_T of -0.1 V relative to the bare gold is observed for the functionalised electrode and agrees with that reported elsewhere for this BioSAM system, providing further evidence for successful functionalisation.[110] The shift in V_T to a more negative potential is a result of the decrease in the work function of gate electrodes caused by

the electrostatic effects of the surface dipoles introduced by the immobilised chemSAM and BioSAM systems at the electrode/electrolyte interface.

The HER2 ECD detection assay is performed by measuring the transfer characteristics of the EGOFET device after incubation of the functionalised gate electrode in PBS standard solutions of HER2 ECD ranging from 1 x 10^{-18} M (attomolar, 1 aM) to 1 x 10^{-8} M (10 nM) nominal concentrations. The PBS solution is used as the solvent in order to reproduce the physiologically relevant environment of blood serum giving the solution an ionic strength of 162 mM and pH of 7.4. **Figure 73**a shows the typical sensing transfer characteristics of an EGOFET device after incubation of the functionalised gate electrode in sequentially higher concentrations of analyte. Prior to the initial analyte concentration, the functionalised gate was incubated in PBS with no analyte (blank) in order to verify the stability of the baseline value before further testing. The sensor response to no analyte is shown in **Figure 73** by the black (I_0) and blue (blank) curves and shows negligible variation. **Figure 73**a shows that the incubation of the gate electrode in HER2 ECD results in a decrease in I_{DS} relative to the baseline and the reduction in in I_{DS} becomes larger with progressively higher concentrations of analyte.

In theory the responses measured in the calibration curve are as a result of the analyte irreversibly binding to antibodies on only the gate electrode. Therefore, when the original bare gold gate electrode is returned to the cell and the transfer characteristic is recorded, the drift in the performance of the EGOFET can be assessed. The transfer characteristic for the gold electrode acquired after the completion of the calibration curve is shown by the red curve in Figure 72 and shows very similar performance to the stored reference level from the start of the experiment (black). Overall the bare gold gate electrode has the following average relative variation (across the three devices) between the measurements recorded before and after the completion of the calibration curve of HER2 concentrations: $\Delta I/I_0$= -4.9% (±0.1%), $\Delta V_T/V_{T_0}$= 1.3% (±1.0%) and $\Delta \mu C/\mu C_0$= -1.5% (±1.7%). This demonstrates that only a negligible change in these parameters occur during the calibration curve which is associated with a steady degradation of the underlying P3HT device. In order to ensure that only devices displaying current variations associated with the ligand interactions at the gate electrode where included, a cut off value of $\Delta I/I_0$< 8% was deemed acceptable for use of the data in alignment with the protocols established for other BioSAM based assays.

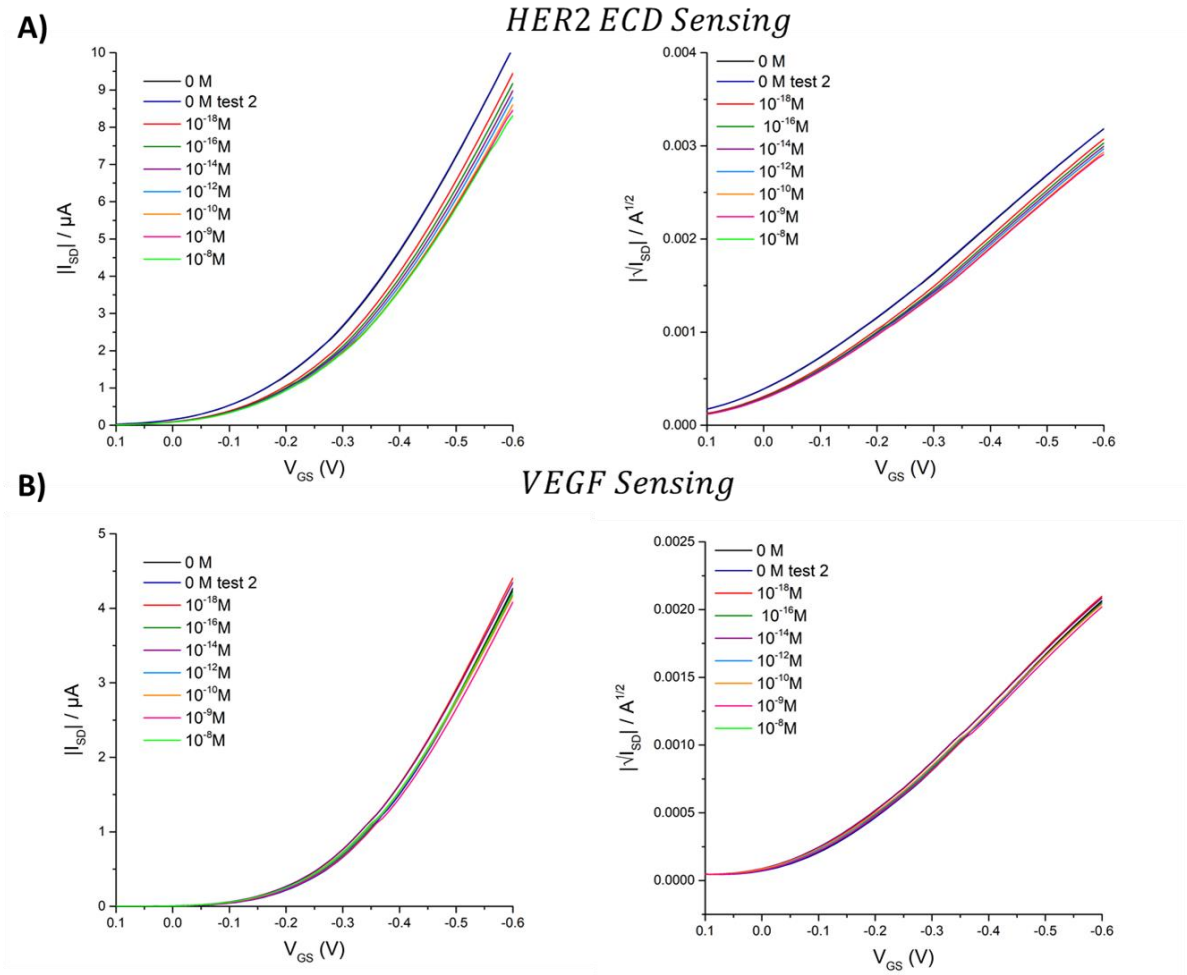

Figure 73 EGOFET HER2 BioSAM sensing transfer characteristics (I_{DS} vs. V_G at V_D=-0.4V). Displayed are the measurements collected for the calibration curve for one of the devices in response to increasing concentrations of analyte covering the range 1 x 10^{-18} M to 1 x 10^{-8} M for HER2 ECD (a) and negative control VEGF (b). The measurements are displayed with I_{DS} in the linear scale on the left and as $\sqrt{I_{DS}}$ on the right which is used to extract V_T and µ*C.

The extraction of the characteristic parameters for the device at each point in the calibration assay allows the evaluation of the device response in changing I_{DS}, V_T and µ*C caused by sensing the analyte. The changes in I_{DS} monitored here is the current value when V_G is maximised at -0.6V. In order to reduce the device to device variation the normalised response is evaluated for each parameter according to Equation 1, where R_0 is the value extracted from the baseline measurement. The normalised responses for each parameter were calculated to give the calibration curve in **Figure 74** and this enables the establishment of the relationship between the biosensor response and calibration standards of known HER2 ECD concentrations which are shown in blue. Each data point plotted in the calibration curve represents the average response over three replicates, each replicate is measured on a separate device using a different gate electrode. The reproducibility of response at each concentration level is shown on the graph by the error bars which display the relative standard deviation across the separate devices. The individual $\Delta I/I_0$ response of each device is shown in the appendix as further information (Figure 123).

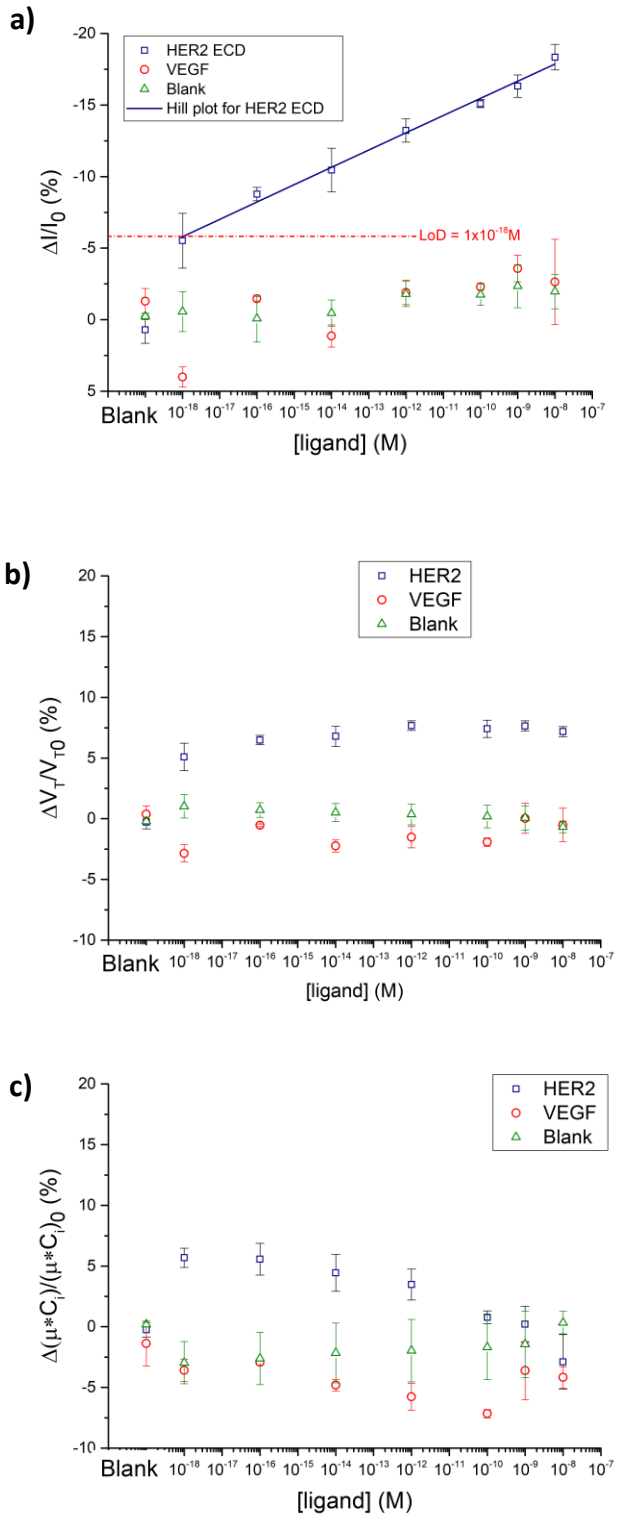

Figure 74 EGOFET HER2 antibody BioSAM calibration curves of device response vs ligand concentration covering the range 1 x 10^{-18} M to 1 x 10^{-8} M. a) The relative change of the I_{DS} current ($\Delta I/I_0$); b) the relative change of the V_T ($\Delta V_T/V_{T_0}$); c) the relative change of the μ*C ($\Delta\mu C/\mu C_0$). The blue squares are the responses for HER2 ECD as the ligand. The red circles are the responses to VEGF protein used as a negative control. The green triangles are the responses to a blank assay performed under the same conditions with PBS solutions but no analyte. A trend line has been fitted for the HER2 ECD responses (blue) using the Hill equation. From this the LoD is calculated as ~1 x 10^{-18} M from the concentration equating to a signal response of -5.8%.

A negative control assay was also performed by measuring the device response to a PBS solution containing no analyte (blank sample) by the same gate incubation procedure as used for the analyte sensing. The procedure was repeated in the same manner used to construct the calibration curve by measuring eight consecutive incubations of the gate in PBS. The normalised relative variation in the device characteristic parameters across the full experiment where shown to be as low as $\Delta I/I_0$ = -1.5 ± 0.6% for a single device. The average over the full calibration range for three replicates of the negative control assay are shown in green in **Figure 74**, the reproducibility error at each point is given as one standard deviation across the three measurements. The reproducibly low variation in the characteristics is further evidence of a stable EGOFET biosensor which displays little drift and is comparable to the drift reported in other P3HT-based BioSAM devices throughout a calibration experiment.

The $\Delta I/I_0$ response (**Figure 74**a) is used as the main parameter to analyse the sensor response to different concentrations of HER2 ECD analyte and allows a quantification of the decrease in current as a function of increasing analyte concentration which is visible in **Figure 73**. A trend line was fitted for the HER2 ECD responses (blue) using the Hill equation, this highlights that the $\Delta I/I_0$ response remains roughly linear over the concentration range investigated in the assay. The investigating higher concentration of analyte above $1x10^{-8}$ M may result in the expected saturation of response which was observed in previous BioSAM based EGOFET biosensors.

The LoD was calculated as the level of concentration that produces a response equal to the average noise level plus three times the standard deviation of the noise. The values gathered for the blank response assay (shown in green in **Figure 74**) were used to calculate the system noise by taking an average over all the individual blank response values for $\Delta I/I_0$. The mean relative current variation in the negative control blank assay was -1.4% (noise level) with a standard deviation of ±1.5%. Therefore, the computed LoD in the assay corresponds to the analyte concentration at a $\Delta I/I_0$ signal response of -5.8%, for HER2 ECD results this gives an LoD of approximately $1x10^{-18}$M by extrapolation of the fitted plot for the data set. This concentration of HER2 ECD is equivalent to approximately 0.0000001 ng/ml which is significantly below the lower range of the concentrations found in the blood serum (7 ng/ml ~ $1x10^{-10}$M).[182] Furthermore, the dynamic range of the device response to HER2 ECD detection covers the range of concentrations relevant for clinical analysis. The system achieves the proof of principle for HER2 ECD detection using an EGOFET biosensor however the level of sensitivity and reproducibility displayed may impair accurate quantification at the concentrations levels typically found in blood serum samples.

The extraction of the device response in both V_T and μ*C as a function of concentration (**Figure 74** b and c) allows the evaluation of the underlying cause of the $\Delta I/I_0$ sensing response due to the relationship described in Equation 26. The assumption is made for this system that μ remains constant throughout the assay and is unaffected by the analyte binding process which occurs at the gate electrode, a sufficient distance to not impact the channel. Therefore, the changes in the measured μ*C are solely a result of variation in capacitance at the gate electrode. Inspection of Figure 74b and Figure 74c shows that both V_T and μ*C have some degree of concentration dependent response and therefore are both likely contributors to the observed $\Delta I/I_0$ sensing response.

In the previously reported BioSAM EGOFET biosensors the $\Delta I/I_0$ sensing response is a result of a pronounced concentration dependant shift in V_T, however no relative variations in the sensing response such as those in Figure 74b and Figure 74c are reported for V_T and C_i to allow direct comparison. The current change in their sensors is attributed solely to the shift in V_T because the effective C_i of the device is assumed to remain constant throughout the sensing. This is expected due to the high capacitance and ion-permeable SAM and as a result of the gate electrode design which is two orders of magnitude larger in size than the channel area. The changes of the C_{Bio} are then no longer detectable and the device response is dominated by the electrostatic changes that affect V_T. The biosensors ability to achieve extremely low limits of detection has been attributed to the electrostatic cooperative interaction that occurs through this extended network of hydrogen bonds and is sustained by the field, resulting in a large sensitivity at low concentration levels and a very LoD in zM range. The electrostatic impact of one R-L complex formation is therefore allowed to propagate over a large area giving a large irreversible response for each binding event over the entire domain. The extent of the propagation of the work function change and response is therefore limited by the size of the SAM domains which will be reduced by defects. The reduced magnitude of signal response and lowered sensitivity can be attributed to the inhomogeneous surface of gold wire gate electrode. The previous BioSAM sensors used large smooth gold electrodes that give compact, uniform and electrostatically connected SAM layers.

However, the gate wire electrode used in this work has significantly extended the dynamic range of the sensor due to the reduced size of the domains therefore limiting the propagation of the work function change for each binding event. The use of pre-defined isolated SAM domains therefore presents an opportunity to tune the dynamic range of the device sensing performance. Additionally, the use of a more homogenous flat gate electrode for example produced by e-beam deposited gold would improve the quality of the SAM to allow for improved HER2 sensing performance.

In order to evaluate the selectivity of the biosensor assay response to a non-specific protein, vascular endothelial growth factor (VEGF) protein was also investigated. VEGF is a protein biomarker involved in the metastatic process of breast cancer which can be overexpressed in blood serum with concentrations over 100 pM.[255] The protein has been used as a negative control in other HER2 based biosensor assays.[256,257] This negative control experiment was performed using the same EGOFET bioSAM-based biosensor and measuring the dose response relationship for VEGF protein across the same concentration range that was investigated for HER2 ECD. The transfer characteristics measured at each point in the calibration assay are shown for one device in **Figure 73**b and can be compared to the measurements taken for the detection of HER2 ECD. The graph suggests that the distinctive decrease in drain current with respect to HER2 concentration is not repeated with VEGF protein. The device parameters from the transfer characteristics of three devices are extracted and the average normalised responses for each parameter as function of concentration are displayed by the red markers in **Figure 74**. No significant response or trend is observed for any of the parameters caused by VEGF concentrations within the range investigated. The maximum response value in $\Delta I/I_0$ for VEGF is below 3% and of comparable magnitude to the responses gathered in the blank assay therefore demonstrating the selectivity of the biosensor for HER2 detection. This demonstrates that the biorecognition elements retain the selectivity in their binding whilst also showing that the blocking steps used in gate functionalisation where effective in reducing non-specific binding, in this case from VEGF protein.

7.2 THC sensing using OBPs and Lipoic acid-based SAM

Tetrahydrocannabinol (THC) is the primary psychoactive compound found in marijuana plants. As the legalisation of medical and recreational use of marijuana expands in North America and across the globe the demand for novel sensing methods is increasing. Biosensors that allow the label-free and selective detection of THC are therefore promising platforms for further development. OBPs have been demonstrated as biorecognition elements for the selective detection of a range of drugs of abuse using a QCM biosensor that was functionalised using a lipoic acid to covalently attach the OBPs to the gate electrode. Therefore, using the methods discussed in section 4.5.2, OBPs raised for the selective detection of THC were used to functionalise gold gate electrodes for use in an EGOFET biosensor to investigate the proof of principle for the detection of THC. The experimental protocol used for the sensing measurements was performed in the same manner as that investigated with the BioSAM devices discussed in section 7.1 with a few variations which are explained below.

THC is a member of the cannabinoid family, a group of naturally occurring compounds that are found in the marijuana plant. Other cannabinoids which are closely chemically related to THC include cannabidiol (CBD) and cannabinol (CBN) and their chemical structures are shown in Figure 75. CBD is the major non-psychoactive component of marijuana and CBN in the primary product of THC degradation so the selective detection of THC relative to these compounds is highly desirable. Therefore, the biosensor response to these compounds was also investigated to determine the selectivity of the OBP-based EGOFET biosensor.

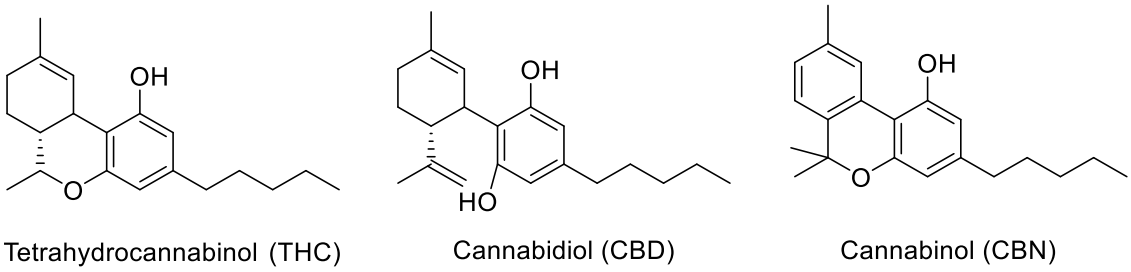

Figure 75 The chemical structures of the cannabinoids of interest THC, CBD and CBN.

Prior to testing the EGOFET devices were incubated for 18 hours in DI water in order to minimise current drift. The I_{DS} was further stabilised by repeating the measurement of the transfer curve until three successive curves perfectly overlap. The transfer characteristics for the devices in this section were recorded by measuring the I_{DS} as a function of V_G ranging from 0.2 to -0.4V at a constant V_D of -0.4V. All the subsequent data discussed in this section were recorded on devices that were cycled until the traces overlap and the transistors operational stability was reached for each measurement. In contrast to the procedure described in section 7.1 the analyte measurements were recorded using the analyte solution as the gating medium after incubation of the functionalised gate in the analyte filled device well for 5 mins. This is because the binding constants of the OBPs used as the biorecognition element are significantly lower than in antibodies therefore making the formation of the R-L complex a reversible process. As a result, in order to allow biosensor detection, the analyte solution must remain in contact with the gate electrode in order to prevent dissociation of the analyte when the gate is placed in a more dilute solution. This is in alignment with the methods reported for other OBP-based EGOFET biosensors.[79] Between each sequential analyte measurement the gate electrode and well were thoroughly rinsed in order to minimise any non-specific interactions at the device interfaces.

The device response was measured with 0.1 µM concentration of THC and the relative current response $\Delta I/I_0$ is shown Figure 76. Following measurement of the device in response to THC the gate electrode and well were thoroughly rinsed. The device performance was then measured in DI water to investigate the recovery to the response of the baseline value (I_0) to probe the reversible

nature of the response. The QCM-biosensor demonstrated the reversible behaviour of analyte binding with the OBPs used in the device, it was therefore expected to return to the initial value, this behaviour was also shown for the OBP-based EGOFET biosensor developed by Mulla et al.[79] However, the recovery of response was not achieved in DI water and this was attributed to the low solubility of THC in water, which may promote non-specific adsorption of the analyte to the device surface which was not fully removed by rinsing. Therefore, the use of isopropanol (IPA) and Tween 20 (a non-ionic surfactant) were investigated as solubilising agents for THC to aid the expected device response recovery.

Solutions of 0.0035% w/v Tween-20 in DI water and 2% solution of isopropanol (IPA) in DI water were investigated. The CMC level of Tween 20 is approx. 0.0074 %w/v. and the concentration adopted was half of the CMC level in order to ensure micelles should not be formed. Each solvent system was used for all measurements (I_0, I and recovery) in that group, the THC was also dissolved into the sample solvent and the results are shown in Figure 76. The data show that the devices tested were more reversible after exposure to THC when isopropanol was used in the sample solvent. Hence further experiments that were carried out were performed using solutions of 2% IPA in DI water as the sample solvent.

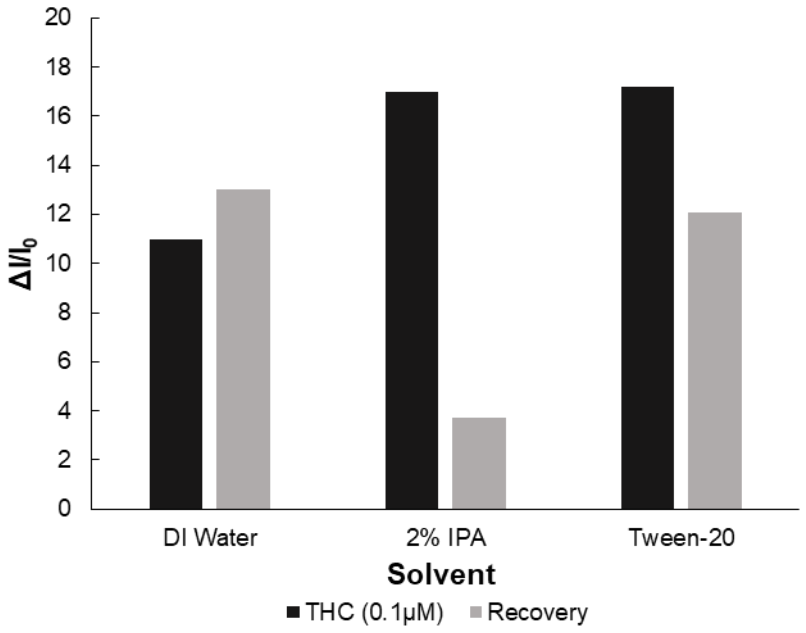

Figure 76 The effect of solvent and solubilising agent on EGOFET OBP-lipoic acid SAM device response measured as $\Delta I/I_0$ from 0.1 µM concentration of THC. The recovery to the baseline I_0 value is investigated to the reversible nature of the response. The solvent used are DI water, 2% solution of isopropanol (IPA) in DI water and 0.0035% w/v Tween-20 detergent in water. Each solvent system was used for all measurements (I_0, I and recovery) in that group.

The cannabinoid sensing assays were performed by measuring the transfer characteristics of the EGOFET device after incubation of the device including the functionalised gate electrode in 2% IPA in DI water solutions spiked with analyte concentrations covering the range 1 x 10^{-14} M (10 fM) to 1 x 10^{-7} M (100 nM). Figure 77 shows the typical sensing transfer characteristics of an EGOFET device after incubation of the one functionalised gate electrode in sequentially higher concentrations of analyte. Prior to the initial analyte concentration, the functionalised gate was incubated in the sample solvent with no analyte (blank) in order to verify the stability of the baseline value before further testing which was only continued when $\Delta I/I_0$< 5%. The sensor response to no analyte is shown in Figure 77 by the black curves and are used as the initial baseline value (I_0) from which the relative response is calculated. Figure 77a shows that the incubation of the gate electrode in THC results in a significant decrease in I_{DS} relative to the baseline and the reduction in in I_{DS} becomes larger with progressively higher concentrations of analyte. In contrast, a significantly smaller variation in device I_{DS} is measured in response to the same range of concentrations of CBD and CBN (Figure 77b and c).

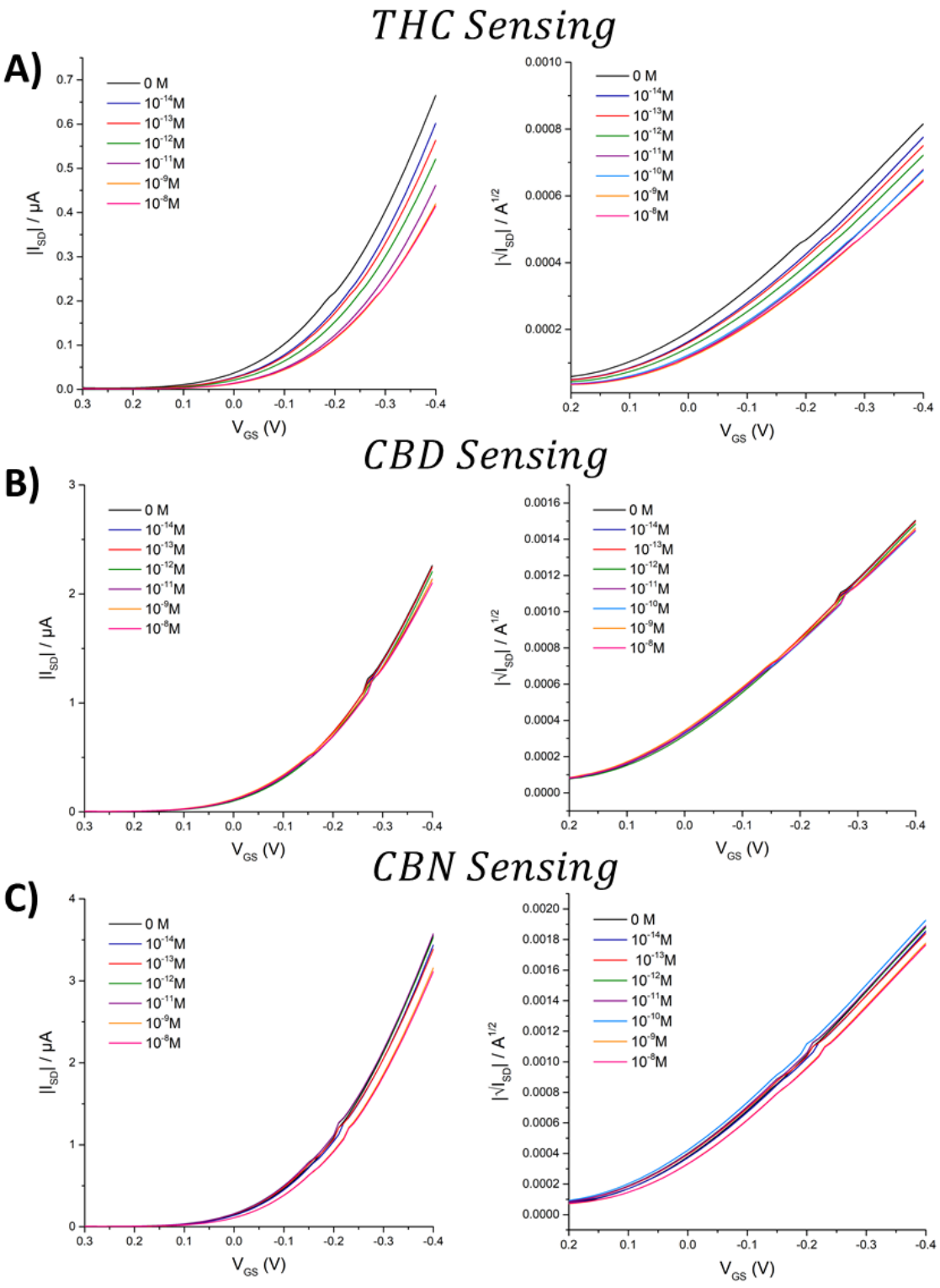

Figure 77 EGOFET biosensor with OBP-lipoic acid SAM sensing transfer characteristics (I_{DS} vs. V_G at V_D=-0.4V). Displayed are the measurements collected for the calibration curve for one of the device each in response to increasing concentrations of analyte covering the range 1 x 10^{-14} M to 1 x 10^{-8} M for: (a) THC; and the negative controls (b) CBD and (c) CBD. The measurements are displayed with I_{DS} in the linear scale on the left and as $\sqrt{I_{DS}}$ on the right which is used to extract V_T and µ*C.

The extraction of the characteristic parameters of the device at each point in the calibration assay allows the evaluation of the device response in changing I_{DS}, V_T and μ*C caused by sensing the analyte. The changes in I_{DS} monitored here is the current value when V_G is maximised at -0.4V. The normalised response for each parameter were calculated to give the calibration curves in Figure 78, and this enables the establishment of the relationship between the biosensor response and the known concentrations of the three cannabinoids.

A control assay was also performed by measuring the device response to a 2% IPA in DI water solution containing no analyte (blank sample) by the same gate incubation procedure as used for the analyte sensing. The procedure was repeated in the same manner as the blank assay measured in section 7.1 and the average value for three replicates at each point are shown in green in Figure 78. The reproducibly low variation in the characteristic parameters is further evidence of a stable EGOFET biosensor which displays little drift. The observed baseline values and calculated noise level reported for the BioSAM devices in section 7.1 (**Figure 74**) are comparable to the measurements taken in 2% IPA in DI water in Figure 78. This demonstrated that the presence of IPA in the gating medium has a negligible impact on the background noise and biosensor stability.

The $\Delta I/I_0$ response (Figure 78a) is used as the main parameter to analyse the sensor response to the different concentrations of analyte. The relative variation of the device current clearly shows the significant decrease in current in response to increasing concentrations of THC, with the response varying from 5% at the lowest concentration until saturation of the device response at 34%.

The evaluation of the underlying cause of the $\Delta I/I_0$ sensing response can be investigated by the extraction of the device response for V_T and μ*C as a function of concentration (Figure 78b and c) allows due to the relationship described in Equation 26. The assumption is again made that μ remains constant throughout the assay and as the analyte binding takes place at the gate electrode and does not impact the channel. Therefore, the changes in the measured μ*C are solely as a result of variation in capacitance (C_i) which is dominated by C_{Bio} contribution as it is the smallest in the series.

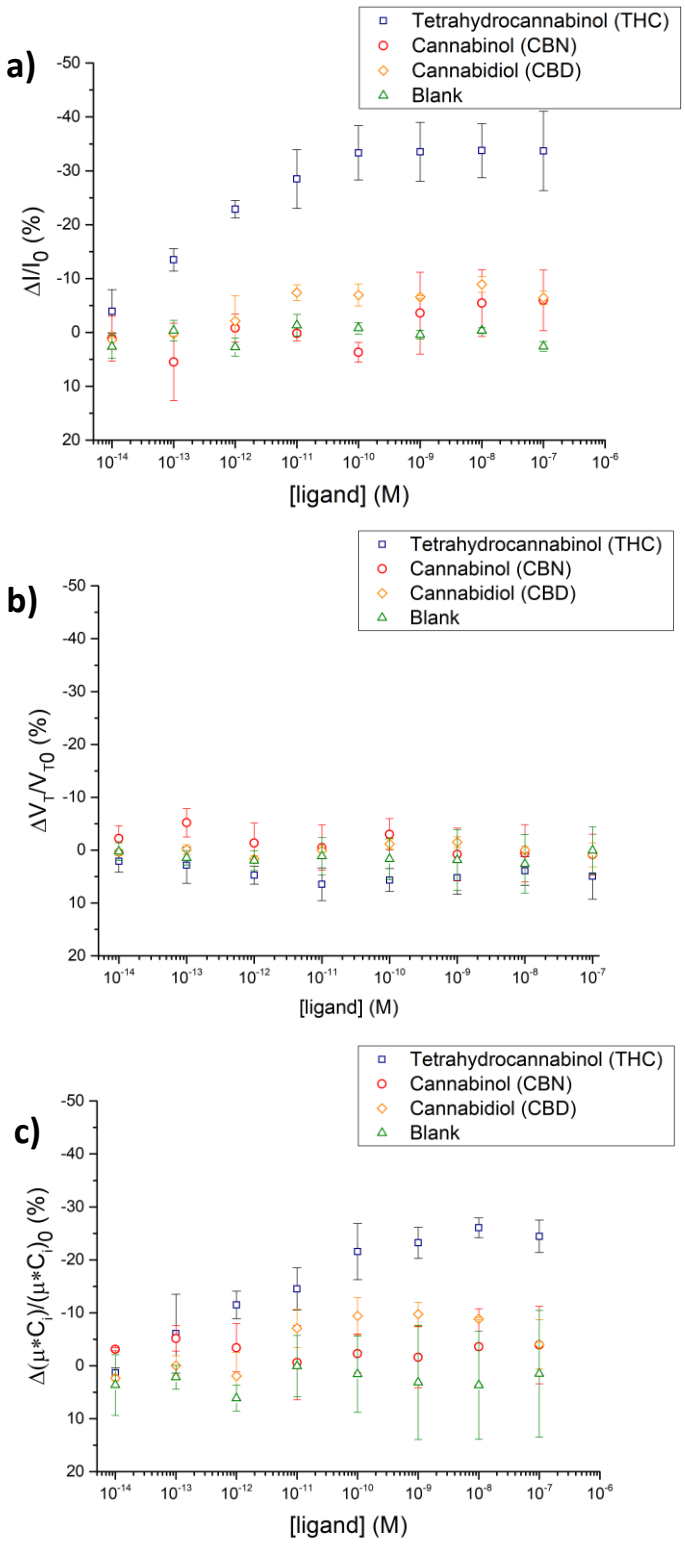

Figure 78 EGOFET biosensor with OBP-Lipoic acid SAM calibration curves of device response vs ligand concentration covering the range 1 x 10^{-14} M to 1 x 10^{-7} M. Top) The relative change of the I_{DS} current ($\Delta I/I_0$); Middle) the relative change of the V_T current ($\Delta V_T/V_{T_0}$); Bottom) the relative change of the μ*C ($\Delta \mu C/\mu C_0$). The blue squares are the responses for THC as the ligand. The red circles are the responses to CBN used as a negative control. CBD is investigated as a second control analyte shown by orange diamonds. The green triangles are the responses to a blank assay performed under the same conditions with PBS solutions but no analyte.

Inspection of Figure 78b and Figure 78c shows that both V_T and µ*C have some degree of concentration dependent response, however the magnitude of the response in the two parameters indicates their relative contribution to modulating $\Delta I/I_0$. At 100 nM of THC where the $\Delta I/I_0$ sensing response is fully saturated, $\Delta V_T/V_{T_0} \cong 5\%$, while $(\Delta \mu C/\mu C_0) \cong 25\%$ as can be seen in Figure 78b,c respectively. Therefore, the EGOFET sensing response in $\Delta I/I_0$ is mostly affected by the changes in the capacitance in the OBP layer (C_{Bio}) caused by the formation of R-L complex, which is in agreement with the findings of the capacitance modulated EGOFET discussed in section 1.4.1.2 that also utilised an OBP biorecognition element for small molecule detection. The observed low V_T response in the biosensor can be explained by the small electrostatic charge carried by the neutral ligands that are being detected.

To further analyse the performance a trend line was fitted for the THC responses (blue) using the Hill-Langmuir equation (Figure 79). The onset of response saturation begins above 1 pM concentrations of THC, which is the upper limit of linearity, at concentrations above 1 nM the sensor response is fully saturated.

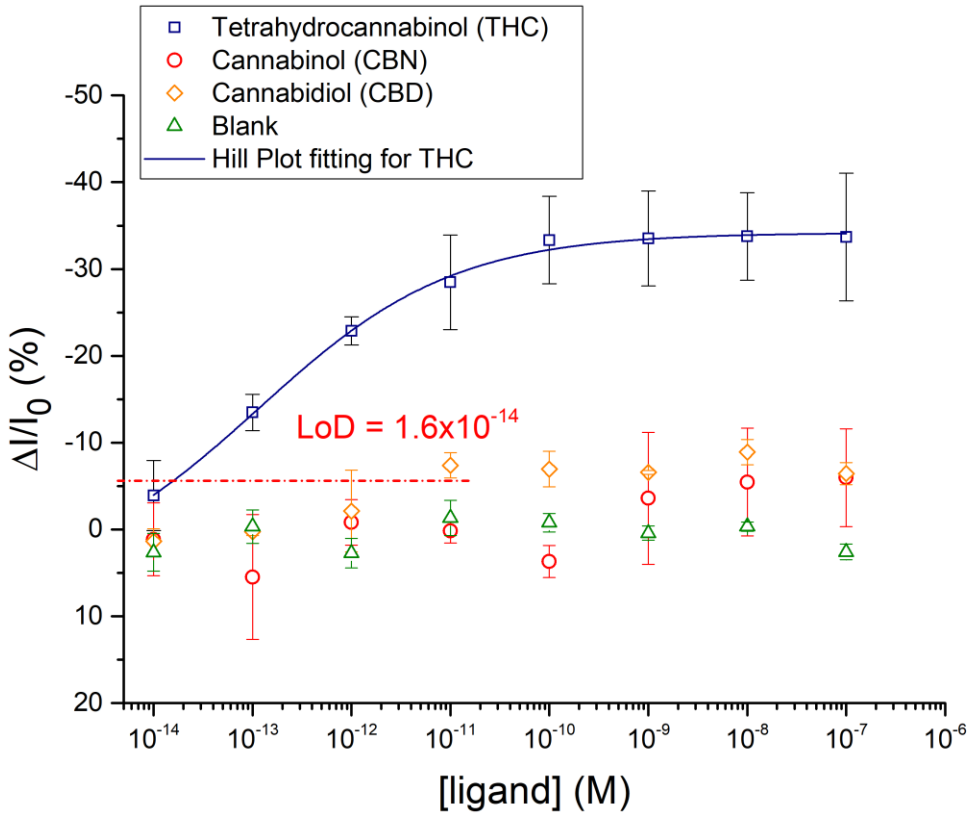

Figure 79 EGOFET biosensor with OBP-Lipoic acid SAM calibration curve of device response $\Delta I/I_0$ vs ligand concentration covering the range 1 x 10^{-14} M to 1 x 10^{-7} M. A trend line has been fitted for the THC responses (blue) using the Hill equation. From this the THC LoD is calculated as 1.6 x 10^{-14} M from the concentration equating to a signal response of -5.6%.

The LoD was calculated as the level of concentration that produces a response equal to the average noise level plus three times the standard deviation of the noise. The values gathered for the blank response assay (shown in green in Figure 79) where used to calculate the system noise by taking an average over all the individual blank response values for $\Delta I/I_0$. The mean relative current variation in the negative control blank assay was 0.5% (noise level) with a standard deviation of ±2.1%. Therefore, the computed LoD in the assay corresponds to the analyte concentration at a $\Delta I/I_0$ signal response of -5.6%, for THC results this gives an LoD of approximately 1.6×10^{-14} M by extrapolation of the fitted hill plot for the data set.

The negative control experiments were performed for the biosensor by measuring the dose response relationship for CBD and CBN across the same concentration range that was investigated for THC. The extracted normalised responses over the concentration range can be inspected in Figure 78 and Figure 79 to evaluate the selectivity of the sensor for THC.

The $\Delta I/I_0$ calibration curve for CBD shows that a weak concentration dependant response is visible although at a much lower response level compared to THC. This behaviour is as expected from relative the affinity constants calculated by fluorescent binding assay and shown in Table 10. The maximum response value for $\Delta I/I_0$ from the control analytes was measured -9% from 10 nM of CBD, significantly lower than the corresponding response at -34% from 10 nM of THC. Furthermore, the $\Delta I/I_0$ device response to THC is distinguishable from the controls down to a few fM, showing that the differential detection of THC can be achieved throughout the concentration range investigated demonstrating the selectivity of the sensor towards THC detection.

7.3 Summary

EGOFETs fabricated with gold gate electrodes functionalised with a BioSAM containing monoclonal HER2 antibodies was demonstrated to allow the proof of principle for the detection of HER2 ECD, a biomarker associated with breast cancer, using an EGOFET biosensor. The $\Delta I/I_0$ signal response gave a LoD for the HER2 ECD of approximately 1×10^{-18}M. The selectivity of the device was demonstrated through the negligible device response to VEGF protein over the same range of concentration investigated for HER2 ECD. In addition to improvements in sensing performance the detection of the HER2 ECD from blood serum would be a desirable step in the further development of the biosensor. For comparison the BioSAM-based EGOFET sensor has recently demonstrated analyte detection in a complex matrix demonstrated by the detection of CRP in saliva.[110]

Proof of principle for the detection of THC has been achieved for an EGOFET biosensor using a gate electrode functionalised using a Lipoic acid SAM attached to OBPs. The $\Delta I/I_0$ signal response gave a

LoD for THC of approximately $1.6x10^{-14}$ M. In addition, to the selective response of the sensor for THC was demonstrated by investigation of the calibration of the related cannabinoids CBN and CBD which were used as controls. Additionally, inspection of the relative variation in V_T and $\mu*C$ in response to THC concentrations showed that the device was mainly operating as a capacitance modulated biosensor.

Future work should focus on improving the reproducibility of the sensing response for both biosensors. This could be achieved through the use of a flatter more homogenous gold gate electrode which would improve the quality of the underlying SAM and may also increase the overall sensing response. Additionally, the integration of the device into a flow cell would be of merit to improve fluid handling. The development of a multi-plex analyte detection system using an array of appropriately developed OBPs could allow the detection of multiple analytes simultaneously.

8 Flow cell-based EGOFET devices

The evaporation of the electrolyte solution can be addressed by performing the electrical measurements in a water vapour saturated environment.[97] Alternatively, a larger volume of electrolyte solution is confined directly above the channel area of the devices within a PDMS reservoir, reducing the impact of evaporation (as used in chapter 7).[42,123,254] A more enticing prospect for developing a biosensor system is the integration of the device into a flow cell that enables easy fluid handling. Furthermore, flow cells remove the prospect of evaporation through confinement of the solution within a closed system. This has been successfully illustrated for OFET-based sensors.[74,86,258] For example, S. Algarni et al successfully demonstrated the use of a flow cell integrated PBTTT-based EGOFET sensor for the detection of water borne amines.[86] Therefore, to address these issues a flow cell integrated EGOFET-based sensors for the detection of biomarkers was developed in this project and developed in this chapter.

Ideally, a POC device allows the input of unprocessed samples from a patient and outputs useful information with minimal user-interaction. The integration of emerging technologies in biosensing with a simple electrical readout is essential to meet the requirements of POC testing platforms. Integration of EGOFETs into microfluidic channels (or flow cells) would be a first step towards integration of sensing devices with more advanced on-chip sample processing techniques.

Microfabrication technology can be utilised as a strategy to miniaturize and automate biomarker assays by providing platforms with the benefits of high sample throughput and very small sample consumption. Conventional sample preparation requires manual centrifuging, pipetting, mixing and filtering. Whereas on-chip processing techniques can deliver a greater level of automation in filtration, microfluidic sorting and concentrating essential to enable the conversion of raw samples into a sample compatible with the biosensor.[259]

In such a device the prepared fluid interacts with the functionalised interface of the POC device that is specific to the target analyte and the resulting induced signal can be processed into a readable output. The inherent transduction of the sensing event into a measurable electrical signal is particularly desirable for simplifying the detection and assay process and reducing the required device components. The combination of these advantages directly translates into a miniaturised, low-cost simplified analytical system needed for POC applications.

Solid phase immunoassays such as sandwich immunoassays, ELISA and the assay developed in chapter 5, typically benefit from superior sensitivity, specificity and kinetics relative to solution-

based assays. However, solid phase assays also suffer from large volume of reagent consumption, long incubation times due to high volume-to-surface area ratios.

The improved surface-to-volume ratio of microfluidic devices can improve mass transport permitting reduced assay times and improved sensitivity. They also enable multiple processing steps to be conducted within one device in contrast to conventional analytical techniques.[259260] Therefore microfluidic devices are particularly attractive for integration into heterogeneous solid phase immunoassays due to improving analytical performance, reduced sample and reagent consumption and cost.

The simplified fluid handling and reduced incubation times of microfluidic devices was demonstrated in a fluorescence-based immunoassay that utilised EDC/NHS coupling of an antibody to a Au-SAM.[216] The enhanced mass transport in the microfluidic device allowed covalent attachment of the antibodies in 25 mins and subsequent sample incubation and detection could also be completed in as little as 25 mins. This is a significant improvement over the hours or days typically required in conventional ELISA-based assays.

Therefore the integration of the EGOFET devices within a flow cell was investigated to enable easy fluid handling and eliminated problems with water evaporation that hampered the utility of droplet-based devices. Different OSCs were compared for use in the biosensor device by the analysis of the electrical performance for both pristine OSC and bilayer devices, with the aim of demonstrating comparable device operation to the droplet-based devices.

The impact of the developed functionalisation procedure on bilayer device performance was also investigated by monitoring the change in device operation at various stages of the functionalisation procedure. Furthermore, to allow valid sensing experiments the performance of the device against appropriate control conditions was investigated and a control baseline experiment was performed to replicate measuring several analyte concentrations during a biosensing assay experiment.

8.1 Design of flow cell and measuring platform

The design of the flow cell to be utilised in this project is outlined in Figure 80. It consists of an EGOFET device fabricated on a glass substrate, coupled with a flow cell using double-sided adhesive tape and an acrylic top cover fitted with gold plated pins. The gold-plated pins are used as gate electrodes and their position is fixed by the CNC milled acrylic top cover; this eliminates any possible positioning variation. Holes are placed through the acrylic top cover and tape to allow access to the source and drain contact pads. The bottom surface of the pin serves as the gate electrode surface, which is fitted flush with the acrylic top cover and mounted onto the substrate with the double-

sided adhesive tape. The components are combined to give a flow cell as depicted in Figure 80, creating a chamber volume of 14.5 µl and a gate electrode height of 280 µm, controlled through the thickness of the adhesive tape (Figure 119). The solutions were delivered by stainless-steel tubes into the flow cell chamber to allow *in-situ* functionalisation and introduction of an electrolyte solution. This solute was confined by the strong seal provided by the double-sided adhesive tape. Additionally, the flow cell allows for efficient cleaning procedures, removing evaporation issues and easy interfacing with a micro-pump station and characterisation platform. The flow cell can be easily adapted to accept the delivery of fluid by peek tubing by the machine cutting of an appropriately sized hole.

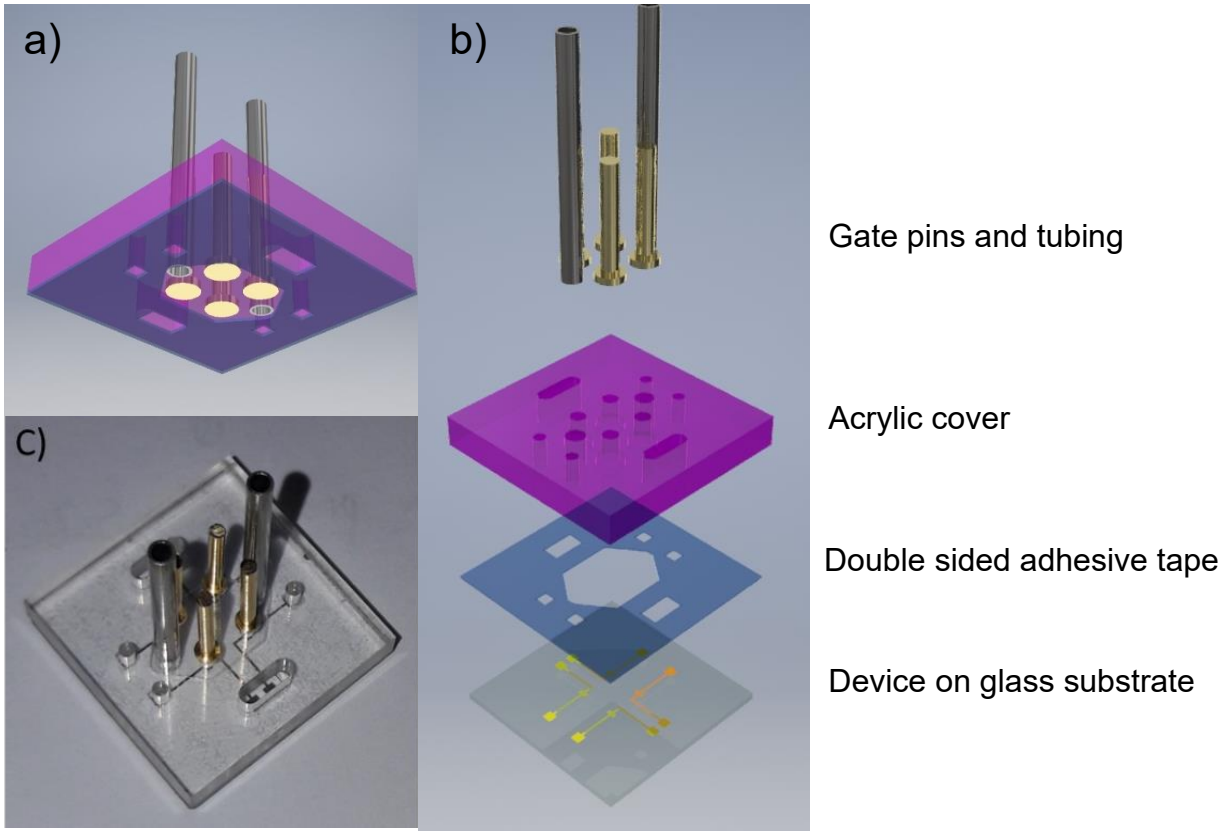

Figure 80 Flow cell design V1. Clockwise A) 3D rendered image showing acrylic top cover (pink), laser cut tape (blue) and gold plated gate electrode pins. B) Exploded CAD image of the flow cell components in isometric view. C) Picture showing constructed flow cell. Gold plated pins are used as gate electrodes and their position fixed within the CNC milled acrylic top cover. Holes are placed through the acrylic and tape to allow access to the source and drain contact pads. The bottom surface of the pin serves as the gate electrode surface, which is fitted flush with the acrylic top cover and mounted onto the substrate with the double sided adhesive to give a controlled gate height of 280 µm. The double sided tape has a laser cut design to produce a sealed flow cell of 51.8 mm^2 in area and controlled chamber volume of 14.5 µl. The flow cell is accessed by inlet and outlet holes to which stainless steel tubing is inserted for connection to a syringe or micro-pump station.

However, in this design frequent leaking of fluids and trapped air bubbles were observed in the flow cell as demonstrated in Figure 82, most likely due to the large chamber width (7.2 mm). In millimetric dimensions, macro-fluidic behaviour is observed, and this results in greater resistance

and turbulent flow; in order for a device to be defined as “microfluidic” at least one of its defining dimensions must be in the tens of micrometre length scale.[261] At this sub-millimetre channel dimension viscous forces, responsible for resistance of the liquid body to deformation, dominate inertia and predictable laminar flow is observed.[261]

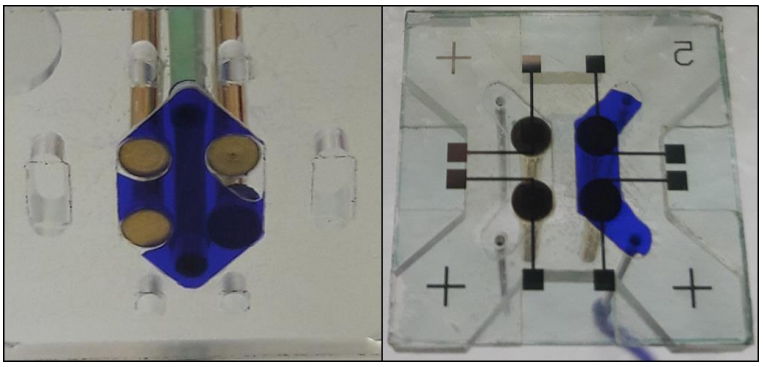

Figure 81 Images comparing liquid filling different designs of microfluidic flow cell with the water stained blue for visualisation purposes. Left: Original single chamber design as depicted in Figure 80, showing example of bubble formation. Right: Flow cell design V2 with two separate chambers as depicted in Figure 82, showing a typically filled chamber.

As a result, a two-chamber design was developed as depicted in Figure 82, with a reduced chamber width of 2.5 mm and a chamber volume of 7 µl. Whilst the device cannot be defined as “microfluidic” due to the dimensions used, Figure 81 demonstrates improved fluid flow and reduced incorporation of air bubbles. Furthermore, the two-chamber design allows for both simultaneous and independent, fluid delivery and device characterisation for 2 sets of 2 devices.

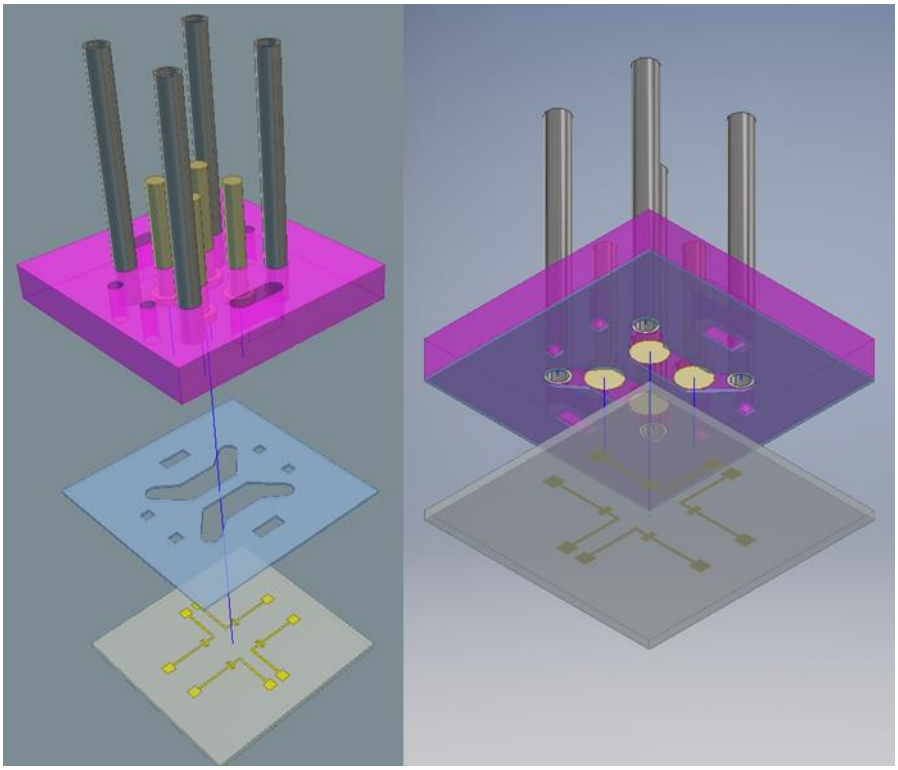

Figure 82 Flow cell design V2. The modified flow cell design features a two chamber design to improve fluid flow and reduce bubble formation. Each chamber has a width of 2.5 mm and a volume of 7 µl.

In parallel to the flow cell, a characterisation platform, as shown in Figure 83, was also developed to allow a more user friendly, time efficient and controlled setup for performing the electrical characterisation, removing the need for a microprobe station. The platform is composed of two blocks of PTFE that house spring loaded micro-pins for contacting the source and drain contact pads and socket connections for the gate electrodes that allowed contact with the devices electrodes and PCB and cabling allowed it to be interfaced with a Agilent semiconductor analyser for device analysis.

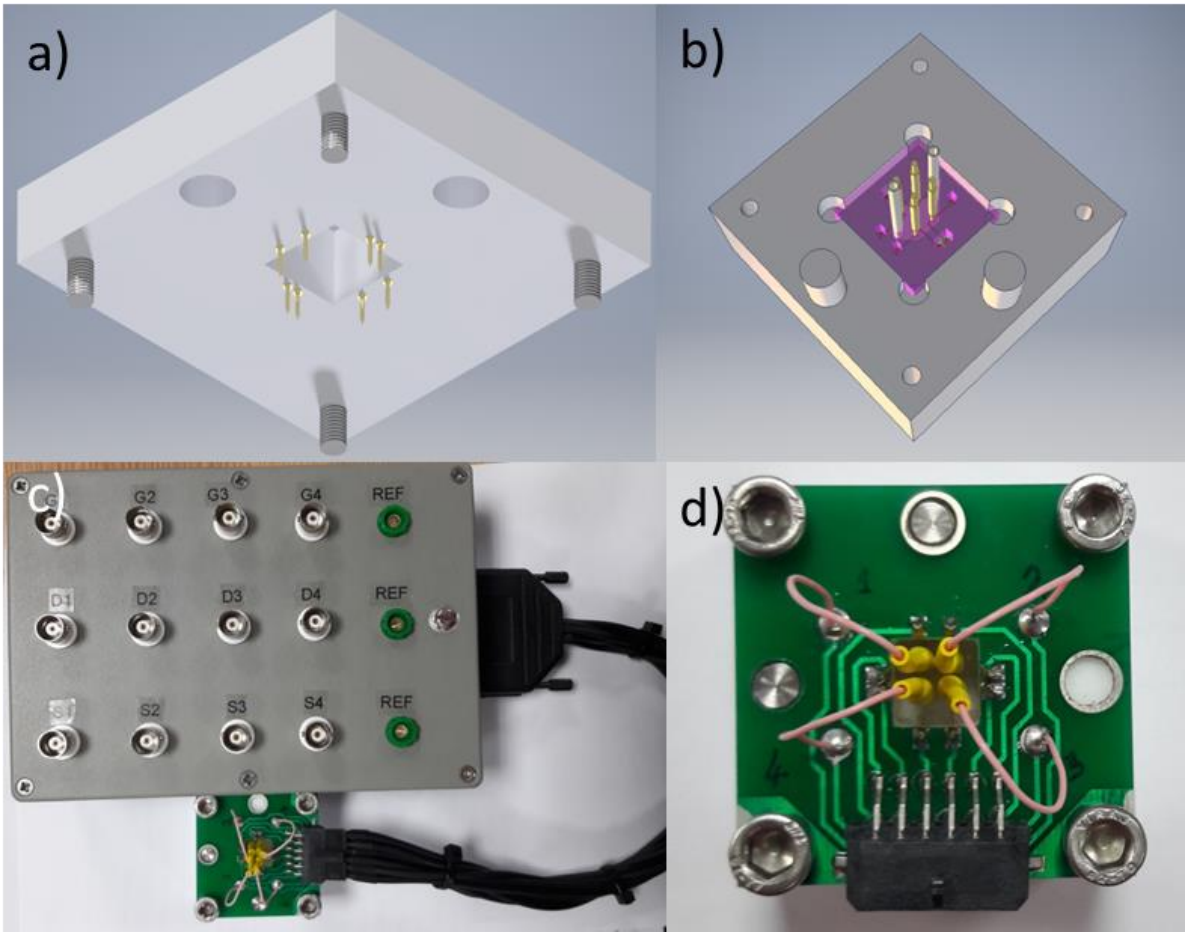

Figure 83 Design for characterisation platform. a) 3D rendered image of top plate housing spring loaded micro-pins that are positioned to contact the S/D contact pads. b) 3D rendered image of bottom plate with flow cell fitted with gate electrodes and inlet/outlet tubing. c) Picture of characterisation platform and interface box for connection to Agilent. d) Top down picture of characterisation platform including and gate electrode receptacles. Wiring from the connections on the characterisation platform is neatly minimised by the mounted printed circuit board (PCB), that is connected to a coaxial cable by a 12 pin Molex connector. The coaxial cabling provides screening from external interference when connecting the connecting the platform with a cable interfacing box which allows for simple cable connection to the Agilent for device characterisation.

8.2 PBTTT-based devices

8.2.1 PBTTT-based devices with shadow mask design

The droplet and flow cell-based testing platforms were compared by analysing PBTTT devices operated with water as the device electrolyte, as shown in Figure 84. The flow cell resulted in improved reliability of the device performance with increased stability and a more predictable decline in I_{on} over time. Additionally, the devices showed reduced hysteresis with improved reproducibility of the forward sweep, as shown in Figure 85, resulting in lower standard deviation in the characteristic parameters displayed in Table 15. When directly comparing absolute values a relative increase in both the I_{on} and I_{off} currents and slight decrease in V_T in the flow cell devices was observed.

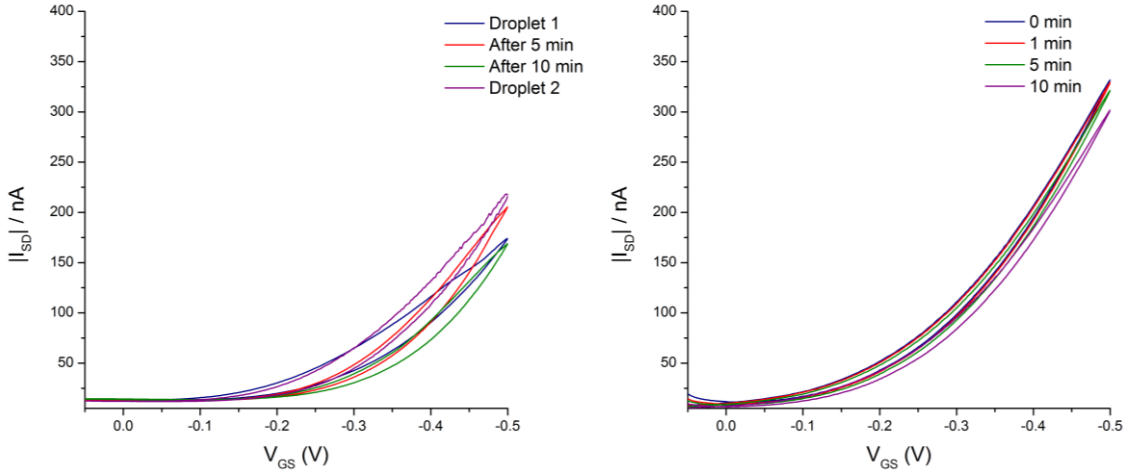

Figure 84 Transfer hysteresis of single layer device with DI water comparing the reproducibility of the characterisation platforms over a short period of time. Left – As analysed using the 3 point probe station and a 4µl droplet of DI water as the gating electrolyte. The device was analysed at regular timed intervals and after 10 mins the initial droplet was removed and replaced with a second droplet; Right – As analysed with the characterisation platform using a flow cell device. Source and drain electrode where patterned using a shadow mask (W = 1 mm, L = 60 µm). V_{DS} = -0.5V was used for device operation.

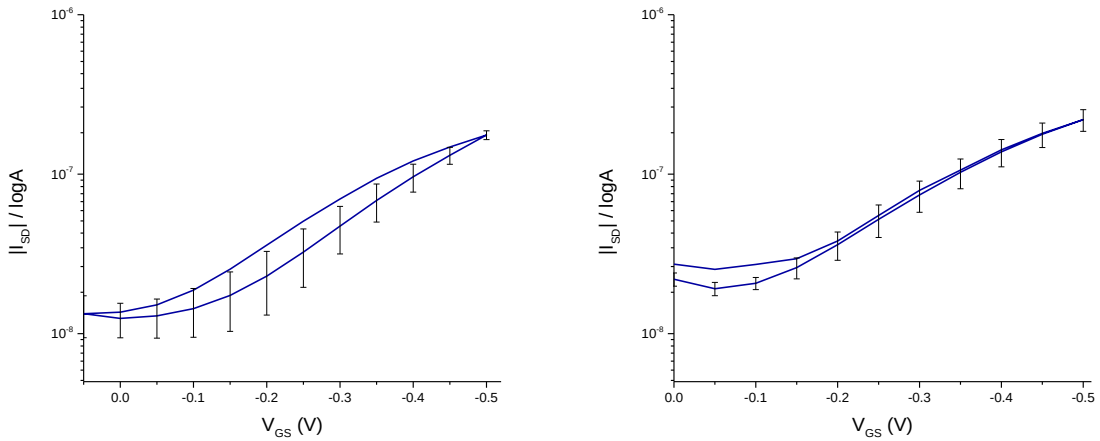

Figure 85 Comparing performance of PBTTT devices analysed by water droplet (left) and in a flow cell (right). Displayed are the averaged transfer hysteresis and standard deviation of 4 devices on the same substrate. Droplet-based devices were analysed using the 3 point probe station, W gate electrode and a 4µl droplet as the gating electrolyte. The flow cell devices were analysed with the characterisation platform. Source and drain electrode where patterned using a shadow mask (W = 1 mm, L = 60 µm). V_{DS} = -0.5V was used for device operation.

Table 14. Characteristic parameters extracted from the transfer hysteresis of a single layer device analysed using the 3 point probe station and a 4µl droplet of DI water as the gating electrolyte. The device was analysed at regular timed intervals and after 10 mins the initial droplet was removed and replaced with a second droplet. Transfer characteristics of the devices are shown in Figure 84.

	V_T (V)	μ*C (µF/Vs)	$I_{On/Off}$	I_{on} (nA)	I_{off} (nA)
Droplet 1	-0.1	0.25	13.8	174	13
After 5 mins	-0.16	0.37	16	206	13
After 10 mins	-0.15	0.28	12.3	169	14
Droplet 2	-0.13	0.35	18.5	218	12

Table 15. Averaged characteristic parameters extracted from the transfer hysteresis of single layer devices. The devices are analysed using the flow cell and characterisation platform with DI water as the gating electrolyte. The devices are tested over 10 sequential analyses over a 10 minute period. Displayed are the averaged values of the 4 devices on the substrate. Transfer characteristics of the devices are shown in Figure 84.

Cycle number	V_T (V)	Error (+/-)	μ*C (µF/Vs)	Error (+/-)	$I_{On/Off}$	Error (+/-)	I_{on} (nA)	Error (+/-)	I_{off} (nA)	Error (+/-)
1	-0.03	0.02	0.24	0.03	19	2	363	46	19	2
5	-0.04	0.02	0.23	0.03	18	4	338	53	20	2
10	-0.04	0.02	0.22	0.03	18	4	330	50	18	2

Integration into the flow cell system did not have significant impact of the device performance although a relative increase in I_{SD} and I_G was observed with the flow cell set up (Figure 86). This could be attributed to a combination of the larger gate electrode, increasing the overall capacitance;[105] or an increase in the area of source and drain pattern exposed to electrolyte within the flow cell

relative to a 4 µl droplet; or a change in the gate electrode metal from tungsten to gold as shown in chapter 4.[43]

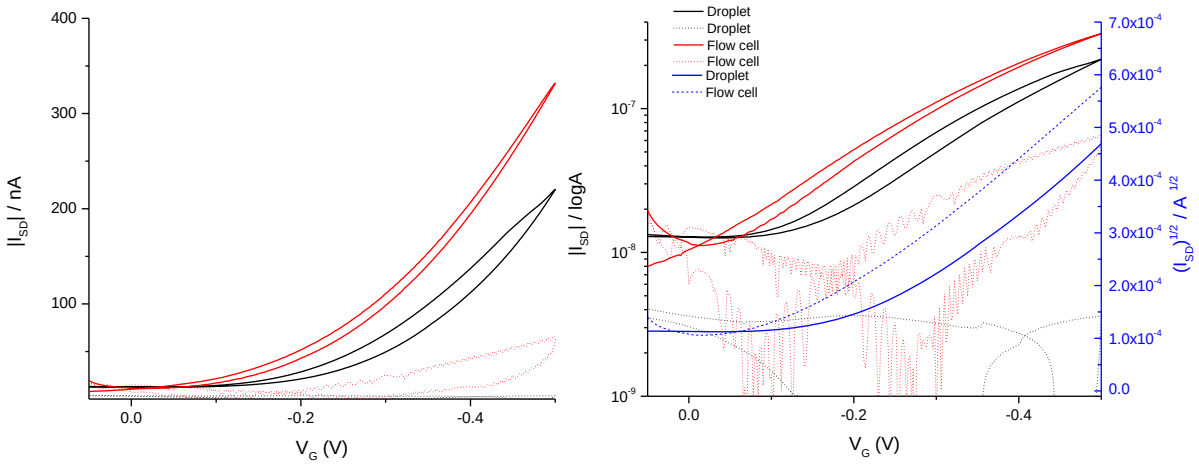

Figure 86 Comparing performance of PBTTT devices analysed by water droplet (black) and in a flow cell (red I_{SD} (solid lines) and I_G (dotted lines) are displayed on a linear scale (left graph) and plotted in a semi-log scale (right graph). Droplet devices are analysed using the 3 point probe station, W gate electrode and a 4µl droplet as the gating electrolyte. The flow cell devices were analysed with the characterisation platform. Source and drain electrode where patterned using a shadow mask (W = 1 mm, L = 60 µm). V_{DS} = -0.5V was used for device operation.

The stability of the PBTTT device operation in the flow cell was monitored by recording several successive transfer curves repeated over a 10 minute period, as shown in Figure 88 and Figure 89. Over this period the devices electrical parameters remain relatively stable with a gradual decrease in μ clearly observed. In addition the device performance changed after incubation in water for 24 hours as shown in Figure 87. The devices are still operable but I_{SD} has significantly reduced to a comparable level to that of I_G and thus clearly undesired for ideal device behaviour.

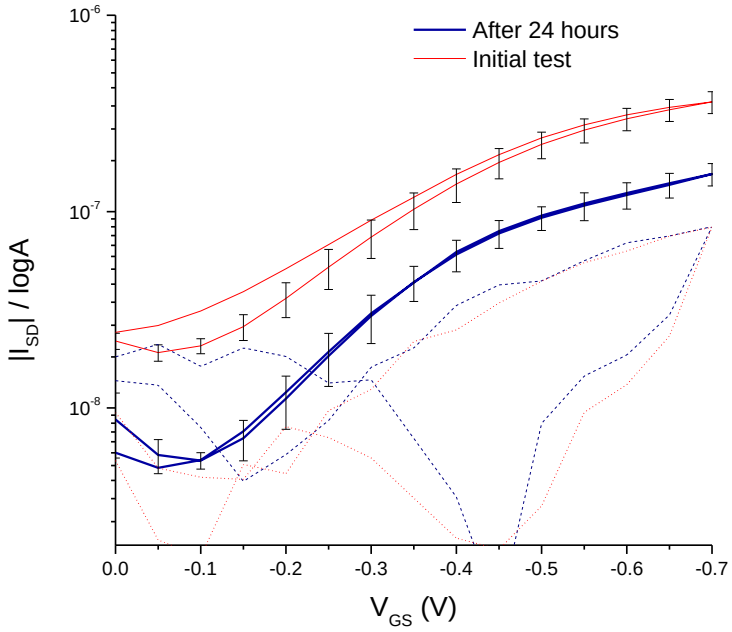

Figure 87 Change in transfer characteristic of PBTTT EGOFET device in a flow cell over 24 hours. The devices where tested initially in the flow cell (red) and after 24 hours incubation in water (blue). Source and drain electrode where patterned using a shadow mask (W = 1 mm, L = 60 µm). I_{SD} (solid lines) and I_G (dotted lines) are plotted in a semi-log scale. Plotted are the averaged transfer forwards sweep of transfer curve and standard deviation of 4 devices on the same substrate. V_{DS} = -0.5V was used for device operation.

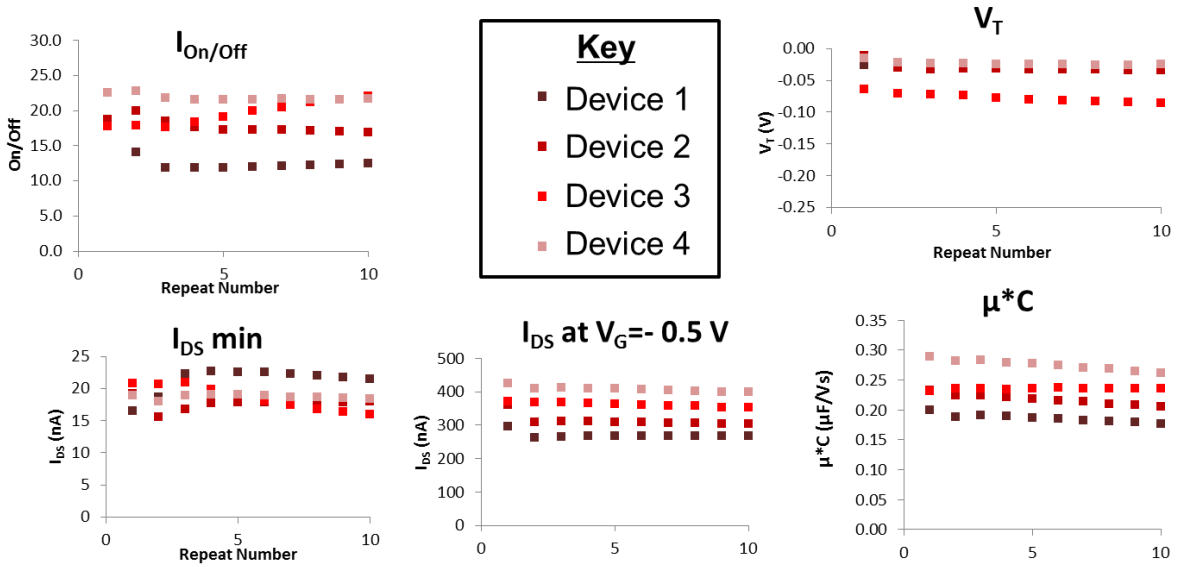

Figure 88 Variation in characteristic parameters extracted from the transfer hysteresis for a single layer device in DI water over 10 repeated cycles in a 10 minute period, analysed in characterisation platform using a flow cell device. Displayed are values for each of the four devices on the same substrate.

Bilayer devices were fabricated by depositing PMMA films on to the PBTTT layer by spin coating. The bilayer devices proved to have comparable performance and reproducible transfer hysteresis over multiple repeat analyses to those displayed in the single layer devices (Figure 89). As a result device characteristic parameters extracted also retained similar levels of performance and variation when

comparing Table 14 and Table 15. Additionally the robustness of the fabrication procedure was verified as the inter-substrate variation across three separate substrates was comparable to that observed for intra-substrate variation (Table 17). The device performance variation was comparable if not better than that observed by Mulla et al which showed standard deviation of around +/- 50 %, as shown in Table 18.[97] Further comparison of flow cell performance to Mulla et al devices highlighted V_T of similar values between 0 to -0.1V for all devices. The significant decrease in $I_{On/Off}$ or µ*C observed upon bilayer deposition was not observed in our devices. Although the $I_{On/Off}$ are at least an order of magnitude below those quoted in literature, they do scale to similar levels once accounting for the enhanced geometry factor that their devices benefit from as a result of photo-lithographically defined interdigitated source and drain electrodes. Of particular note are the µ*C literature values which are at least an order of magnitude lower than those calculated for our devices. The literature values are comparable to those obtained from devices that have been exposed to electrolyte for a prolonged duration of time, Table 18.

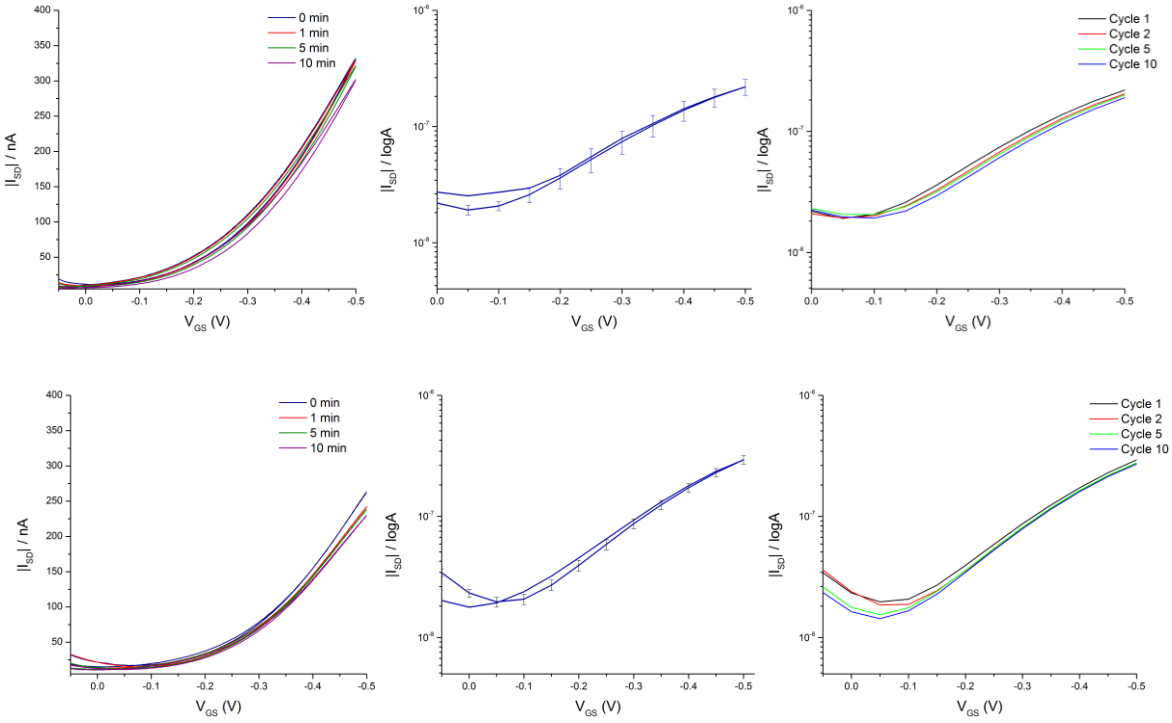

Figure 89 Transfer characteristic performance of single layer (top) and bilayer type devices (bottom), analysed in characterisation platform using a flow cell device. Left - Performance of a single device over 10 mins. Centre - Averaged transfer hysteresis and standard deviation of 4 devices on the same substrate on cycle 1. Right- Averaged transfer hysteresis during 10 repeat cycle tests. The source and drain electrode where patterned using a shadow mask. (W = 1 mm, L = 60 µm). V_{DS} = -0.5V was used for device operation.

Table 16 Averaged characteristic parameters extracted from the transfer hysteresis of bilayer layer devices. The devices are analysed using the flow cell and characterisation platform with DI water as the gating electrolyte. The devices are tested over 10 sequential analyses over a 10 minute period. Displayed are the averaged values of the 4 devices on the substrate. Transfer characteristic of the devices are shown in Figure 89.

Cycle number	V_T (V)	Error (+/-)	μ^*C (µF/Vs)	Error (+/-)	$I_{On/Off}$	Error (+/-)	I_{on} (nA)	Error (+/-)	I_{DS} min (nA)	Error (+/-)
1	-0.07	0.01	0.38	0.02	15	0	294	23	19	2
2	-0.07	0.01	0.37	0.04	16	2	277	33	18	2
5	-0.07	0.01	0.37	0.04	18	1	278	35	15	2
10	-0.08	0.01	0.36	0.03	19	1	272	36	14	2

Table 17. Averaged characteristic parameters extracted from the transfer hysteresis of bilayer devices on 3 different substrates analysed using the flow cell and characterisation platform.

V_T (V)	Error (+/-)	μ^*C (µF/Vs)	Error (+/-)	$I_{On/Off}$	Error (+/-)	I_{on} (nA)	Error (+/-)
-0.04	0.05	0.32	0.08	13	3	274	35

Table 18 Characteristic parameters quoted by Mulla *et al* for EGOFET Biosensors at various stages of fabrication.[97] The μ^*C parameter is back calculated from the assumed gate- channel capacitance per unit area of 3 µF cm^{-2} as is used in the paper.

	V_T (V)	Error (+/-)	Mobility (cm^2 V^{-1} s^{-1})	Error (+/-)	μ^*C (µF/Vs)	Error (+/-)	$I_{on/off}$	Error (+/-)
Bare PBTTT	-0.02	0.05	0.02	0.01	0.06	0.03	1000	-
PBTTT/PAA	-0.06	0.02	0.002	0.001	0.006	0.003	100	-
PBTTT/PAA/BPLs	0.04	0.02	0.001	0.001	0.003	0.003	1000	-

The ability of the devices to withstand a prolonged period of exposure to aqueous solutions is essential in order to allow sufficient time for the functionalisation steps required to covalently attach the antibodies to the PMMA layer. As a result device stability was also investigated over a longer period of time, as shown in Figure 90 and Figure 91. The device performance was again stable over a short period of time (0-10 mins) as previously shown by the cycled hysteresis analysis (Figure 89). The existing functionalisation protocol typically requires 2 hours of electrolyte exposure; over this period of time more significant performance degradation was observed for both single layer (Figure 90) and bilayer devices (Figure 91) and the extracted device characteristic parameters as a function of time are described in Figure 92. The encapsulating layer provided no additional benefit in device stability. A trend of gradual decline of the parameters can be observed for all devices. The decrease

in I_{DS} max and I_{DS} min is offset to give the overall effect of a similar $I_{On/Off}$. The trend for degradation is slightly more pronounced when exposed to PBS.

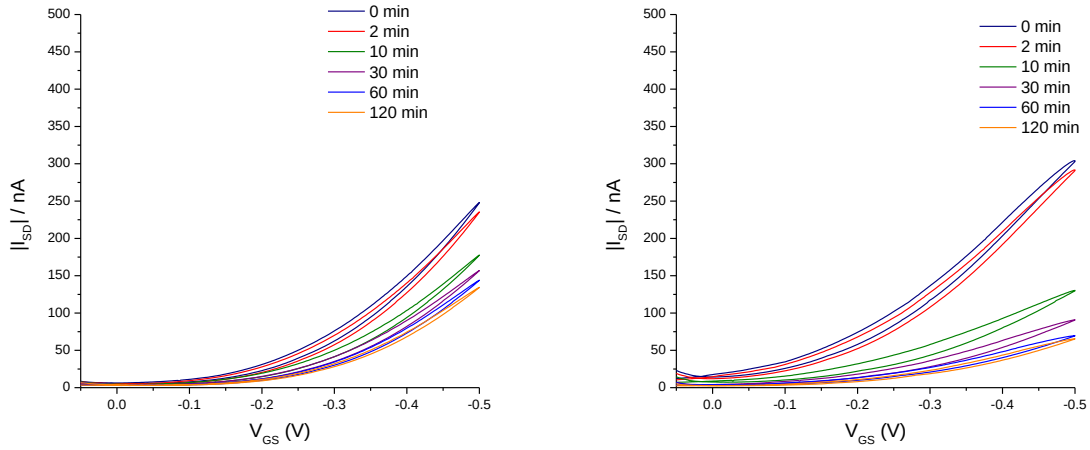

Figure 90 Transfer hysteresis of PBTTT device tested in a flow cell in DI water (left) and PBS (right) over 2 hours, analysed in the characterisation platform using a flow cell device. The source and drain electrode where patterned using a shadow mask. (W = 1 mm, L = 60 µm). V_{DS} = -0.5V was used for device operation.

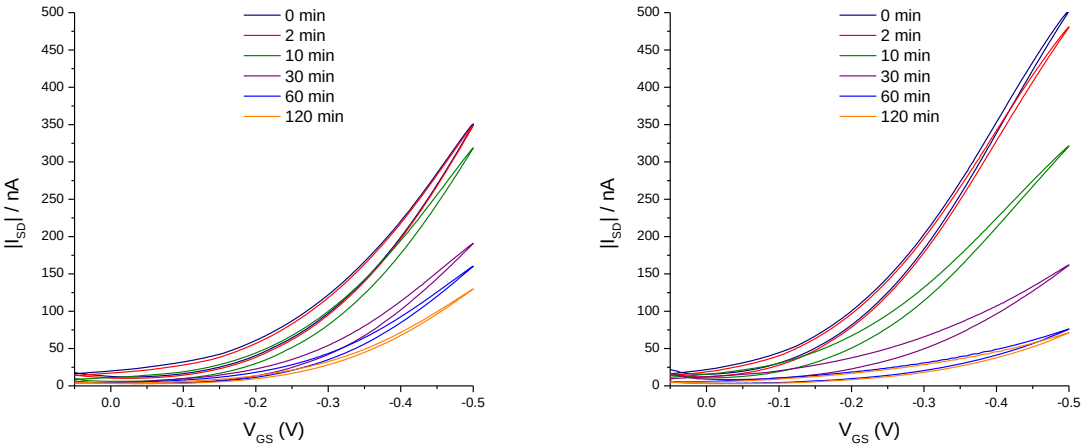

Figure 91 Transfer hysteresis of PBTTT/PMMA COOH layer device in DI water (left) and PBS (right) over 2 hours, analysed in the characterisation platform using a flow cell device. The source and drain electrode where patterned using a shadow mask. (W = 1 mm, L = 60 µm). V_{DS} = -0.5V was used for device operation.

The highly hydrophobic nature of the OSCs used should impede ion penetration, as highlighted by the high measured contact angles (Table 3). However, the degradation of device performance observed over time could be attributed to the absorption of electrolyte ions into the OSC thin film over time (such as hydroxyl groups). These ions would contribute to the formation of trap states in the OSC thin film.[262] Additionally, the deposition of a more hydrophilic layer on top of the OSC, (e.g. PMMA COOH) will more readily absorb water than the highly hydrophobic OSC. Charge trapped holes occupying localised trap states are no longer mobile, contributing to the reduced field effect mobility of the device and the resulting I_{SD}.[51,263]

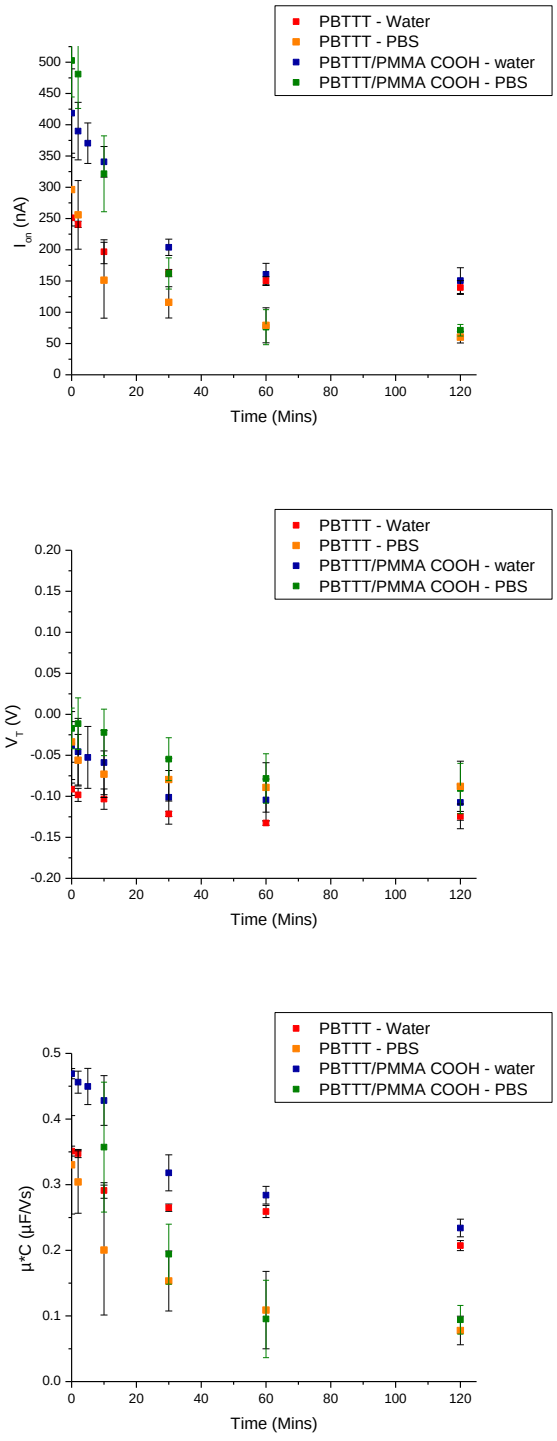

Figure 92 Variation in characteristic parameters extracted from the transfer hysteresis from the various PBTTT-based devices described in Figure 90-Figure 91 over 2 hours, analysed in the characterisation platform using a flow cell device. The mean average of the four devices on the same substrate and their standard deviation is displayed in each chart. Red - Single Layer devices in DI water. Orange - Single layer devices in PBS. Blue - Bilayer devices in DI water. Green - Bilayer devices in PBS. The Source and drain electrode where patterned using a shadow mask. (W = 1 mm, L = 60 μm). V_{DS} = -0.5V was used for device operation.

The 'On current' was also monitored over time, this was performed by holding the V_{DS} at -0.5V and V_{DS} at -0.4V (Figure 93). The device shows a rapid response with a large negative current produced signifying the establishment of an EDL and conductive channel in the OSC channel, however a stable system and a peak drain current is reached after approx. 30 seconds; and this drain current gradually lowers over an extended period. The gate leakage, however, significantly decreases after the initial 1 second of operation. A similar PBTTT flow cell device was analysed by Algarni *et al*, and these authors reported that a gradual lowering of current was shown to settle after 1 hour of continuous flow and operation.[86] Here, the drift in current is assigned to the gradual washing of water soluble dopants from the PBTTT thin film. The presence of unintentional dopants in the OSC layer contributes to a small current (the transistor off-current) but these dopants can aid in the formation of Schottky junctions at the contacts which can significantly improve carrier injection.[264] The subsequent loss would then result in reduced injection and reduced currents. This behaviour would explain the gradual decrease in I_{DS} max, I_{DS} min and mobility over time in the transfer hysteresis, with the mobility gradually decreasing to levels observed in literature. However, the previously described degradation of device performance shown in Figure 90 and Figure 91 over a comparable duration would suggest that stable device performance would not be achieved under constant bias stress with the existing set up.

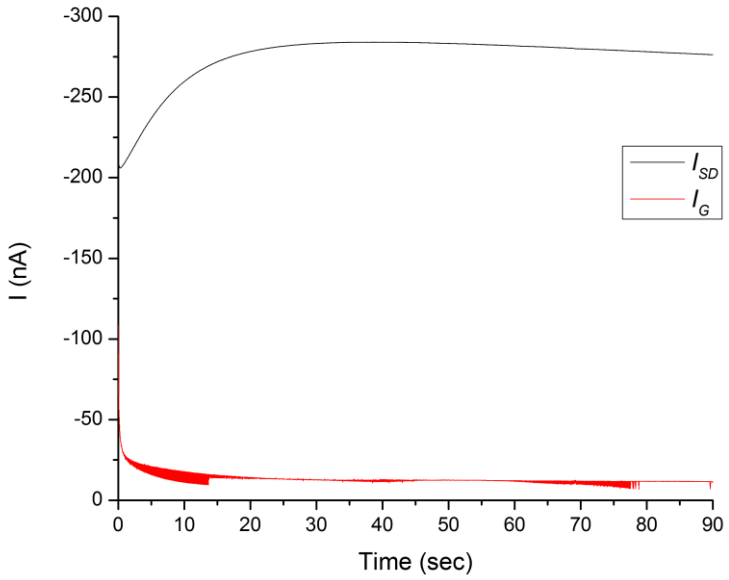

Figure 93. 'On current' monitored over time; this was performed by holding the V_{DS} at -0.5V and V_{GS} at -0.4V, using a flow cell device in DI water, analysed in the characterisation platform.

A prevailing issue for integration of the shadow mask defined source and drain electrode designs is the low I_{SD} current levels achieved due to the small geometry factor. The subsequent degradation of

the performance on the time-scale required for the developed functionalisation therefore hampers the utility of the set-up for biosensing. Of particular concern is the relatively high levels of I_G relative to I_{DS}, a factor that worsens over time and is not desirable for ideal EGOFET behaviour. The gate leakage relation to the surface area of source drain exposed has previously been reported where minimising the exposed area by encapsulate the source and drain electrodes can be used to limit the leakage.[42] Alternatively, interdigitated electrodes can be used to enhance the relative I_{DS} within the existing set-up.

8.2.2 PBTTT-based devices with IDE design

The integration of the interdigitated electrodes into the PBTTT/PMMA COOH-based flow cell resulted in an increase in I_{DS} relative to that observed in the shadow mask defined designs, with I_{DS} in the order of µA current observed for the interdigitated electrode devices. Good overall device performance and p-type OSC behaviour is typified by the well-shaped linear and saturation regimes for the I_{DS}–V_{DS} curves and low hysteresis. In addition, good modulation of I_{DS} with V_G in the transfer curves is displayed in Figure 94. The extracted characteristic parameters (V_T = -0.2V +/- 0.05 ; μ^*C = 0.08 µF/Vs +/- 0.05) are comparable to those acquired for the PBTTT/PMMA COOH devices previously analysed with Au gate electrode with water droplets (see section 6.3).

As desired, the relative levels of I_G (<0.2 µA) vs I_{DS} (7 µA) were significantly reduced even under the highest maximum applied potential difference at the gate (V_G = -1V). The use of IDE results in a more ideal transfer characteristic in particular a reduction in the relative level of hysteresis between the forward and backward sweeps. An improvement in the relative ratio of I_{SD} to I_G gave improved device performance. Interestingly, the gate leakage (I_G) remains within the same order of magnitude despite the large increase in I_{SD}. In addition to signifying that the increased current is due to good charge transport within the active material and not a corresponding increase in electrochemical reactions, it also suggests that the cause for I_G leakage is likely linked to the area of exposed source and drain contacts that remains relatively constant between both device designs.

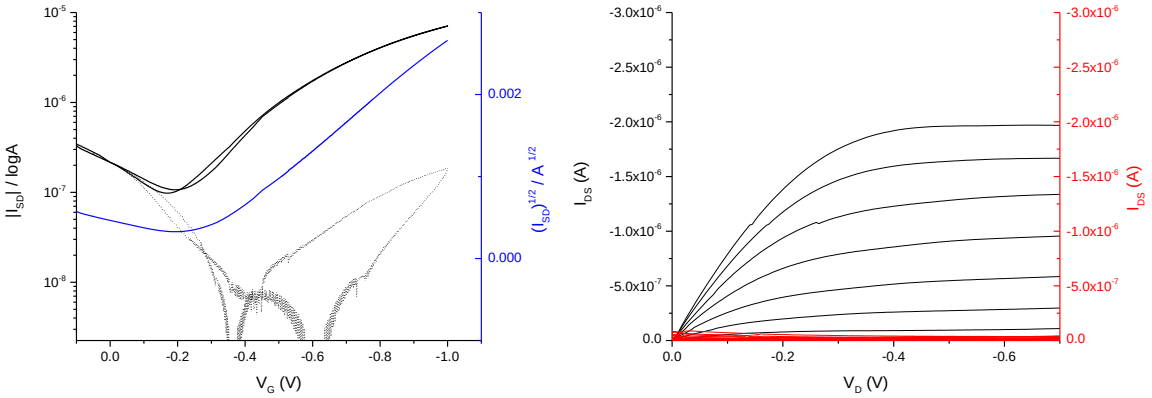

Figure 94 PBTTT / PMMA COOH IDE design in flow cell with water. Left) Transfer characteristic, V_{DS} = -0.7V was used for device operation.; Right) Output characteristic. The Source and drain electrode where patterned by photolithography with a IDE design. (W = 16.9 mm, L = 60 µm).

The performance of the PBTTT / PMMA COOH IDE devices operated in a PBS filled flow cell whilst under bias stress of repeated transfer hysteresis cycles over 2 hours was also investigated, as shown in Figure 96 and Figure 95. A similar degradation in device performance to that observed for the shadow mask designed devices operated in PBS (Figure 91), with a gradual decrease in I_{on} over the course of the 2 hour investigation, after an initial increase during the first 2 minutes of operation. The benefit of performing bias stress testing through cycled transfer curves was compared with operation under constant voltage. The former gives the opportunity to extract the device characteristic parameters from the transfer cycles to provide greater insight into the change in device performance, the extracted values are displayed in Figure 96. The trend of reduced I_{on} is more clearly observed in Figure 96, where an initial current of around 2 µA reduces to around 250 nA after around 70 mins of operation and the subsequent reduction in current is much less pronounced. Interestingly the gate leakage remains at a constant level of around 30-40 nA throughout the experiment. Despite the significant reduction in operational current, the relative ratio of I_G to I_{on} remains acceptable throughout the duration of the experiment from initial level of 2% to 15% after 2 hours. The variation in V_T is significantly less pronounced than I_{DS}, with a gradual change between -0.4 V and -0.5 V seen between 20 and 120 mins.

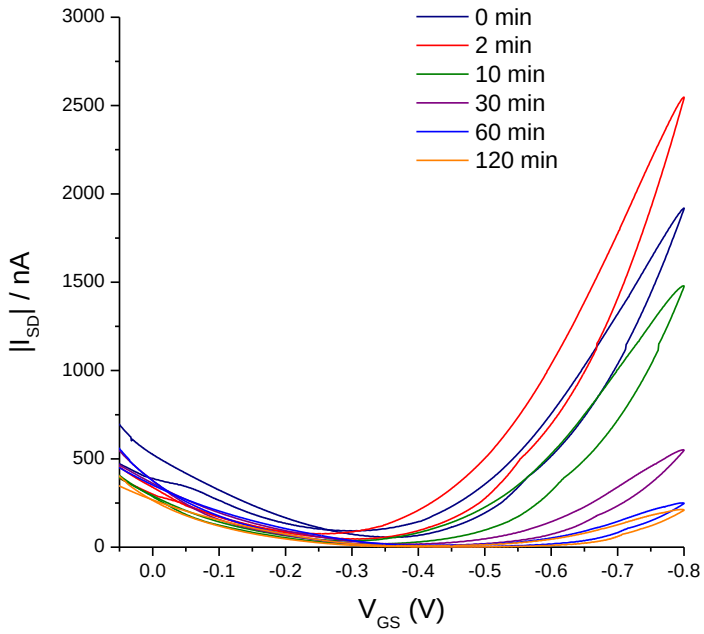

Figure 95 Transfer hysteresis of PBTTT / PMMA COOH IDE design device in PBS over 2 hours operated under constant bias stress of repeated transfer hysteresis cycles. The device was analysed in the characterisation platform using a flow cell device and the extracted parameters are displayed in Figure 96.

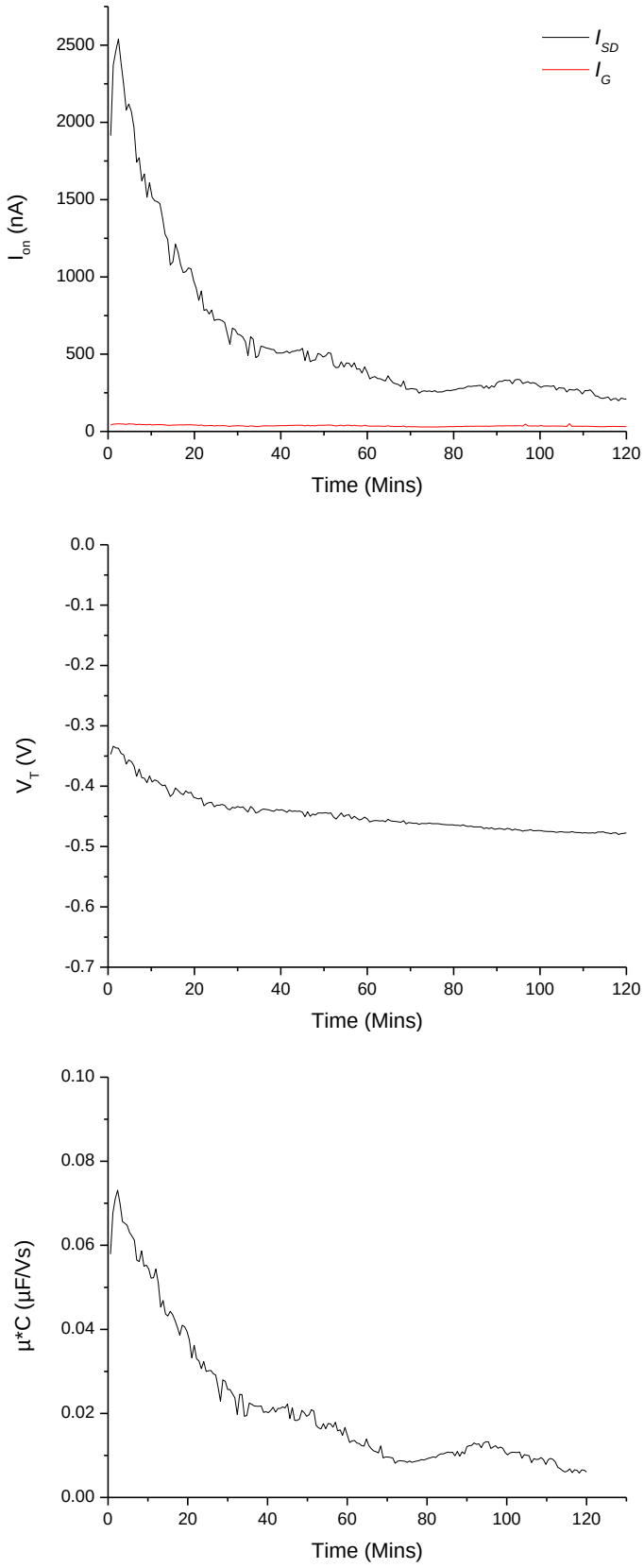

Figure 96 Variation in characteristic parameters extracted from the transfer hysteresis PBTTT / PMMA COOH IDE design device in PBS over 2 hours operated under bias stress of repeated transfer hysteresis cycles as described in Figure 95 over 2 hours. The devices were analysed in the characterisation platform using a flow cell device. Top; I_{SD} (black) and I_G (red) at maximum V_G extracted from transfer hysteresis cycles; Middle V_T extracted from transfer hysteresis cycles; Bottom μ^*C extracted from transfer hysteresis cycles.

The relative stability in device performance after 1 hour of device operation may suggest a suitable window for sensing experiments, although at the compromise of significant reduction in operational current which may impact on the sensors sensitivity. Additionally further reduction in device performance is probable and the drift in performance would have to be accounted for in any measurements for device response. However DPPTTT-based EGOFET devices have demonstrated exceptionally stable performance in aqueous environments and present an opportunity to improve the operational stability of the devices within flow cell system relative to PBTTT.[123]

8.3 DPPTTT-based devices

8.3.1 DPPTTT -based devices with shadow mask design

The exceptional stability of DPPTTT-based EGOFET devices under aqueous-gated operation has been shown in both water and saline solutions.[105,123] The fabricated devices benefit from the engineered properties of the OSC films such as the high ionisation potential, crystallinity, strong π- π stacking and side chain interdigitation in the polymer films. This results in stable device operation and is highlighted by the comparable electrical performance achieved during 6 days of submersion in saline solution.[123] Additionally, AFM images and Raman and FTIR spectral analysis of the OSC layer showed that device operation in water and saline environments had minimal impact on the films properties signifying negligible chemical modification of the polymer.[123]

Following the successful operation of DPPTTT-based droplet devices, the performance of the OSC in the flow cell was explored. Initially devices using the shadow mask defined source and drain electrodes were investigated and the transfer and output curves of the flow cell-based devices in water are shown in Figure 97, where good device operation is observed.

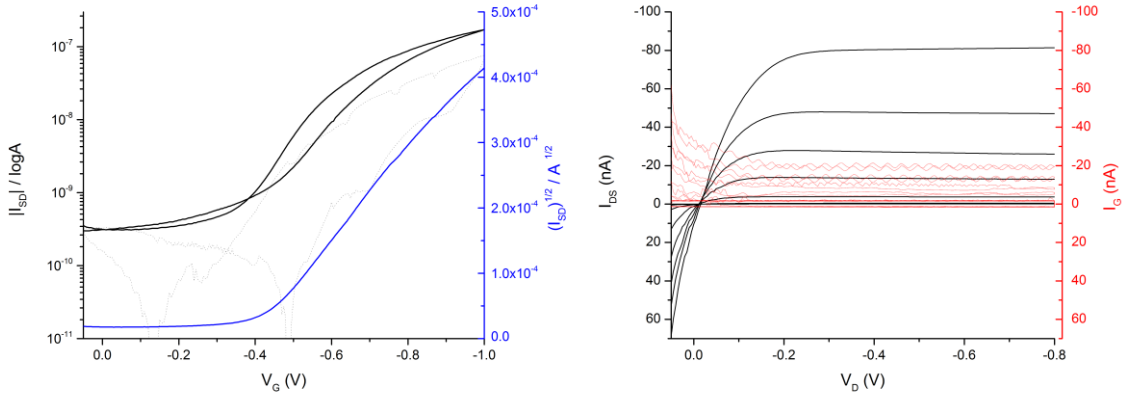

Figure 97 Typical performance of a single layer DPPTTT device with the shadow mask design (W = 1 mm, L = 60 µm) operated in flow cell with water as electrolyte. Left) Transfer characteristic, V_{DS} = -0.8V was used for device operation; Right) Output characteristic. The transfer characteristic was measured with V_{DS} = -0.8V.

Integration of the devices into the flow cell system did not significantly impact the device performance, although a significant increase in I_G was observed within the flow cell set up (Figure 98) and the relatively large ratio of I_G to I_{DS} is not desirable for ideal EGOFET behaviour. A similar increase in gate leakage was observed in PBTTT-based flow cell devices (Figure 86), which was attributed to the combination of a larger gate electrode;[105] and an increase in the area of source and drain pattern exposed to electrolyte within the flow cell relative to a 4 µl droplet.

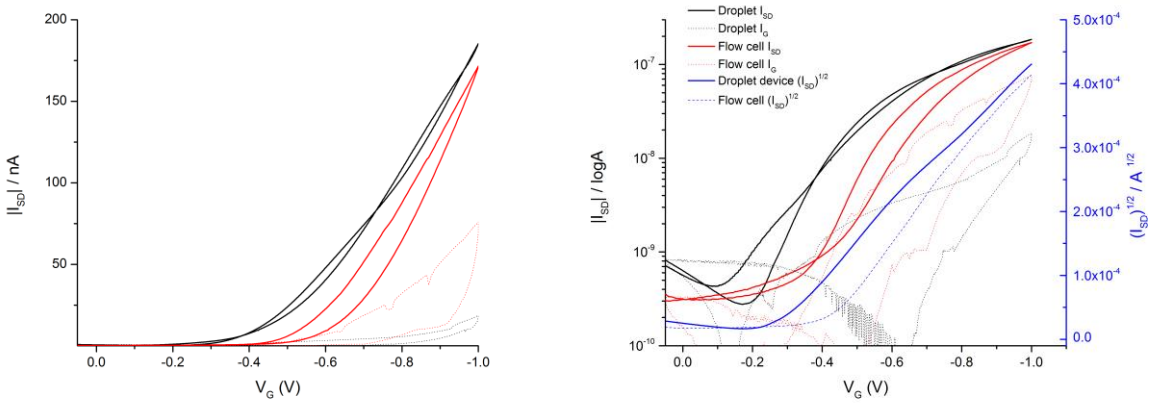

Figure 98 Comparing the electrical performance of typical DPPTTT devices analysed by water droplet (black) and in a flow cell (red). I_{SD} (solid lines) and I_G (dotted lines) are displayed on a linear scale (left graph) and plotted in a semi-log scale (right graph). Droplet devices are analysed using the 3 point probe station, Au gate electrode and a 4µl droplet as the gating electrolyte. The flow cell devices were analysed with the characterisation platform and V_{DS} = -0.8V was used for device operation. The Source and drain electrode where patterned using a shadow mask (W = 1 mm, L = 60 µm).

DPPTTT based bilayer devices utilising PMMA COOH co-polymer where fabricated following the previously validated procedure described in section 3.1 and section 6.2. Their electrical performance when integrated into the flow cell is shown in Figure 99. The output and transfer curves of the DPPTTT bilayer devices show good electrical performance for operation in both water and PBS.

The operation of devices in PBS solution generally results in a more negative V_T relative to water-gated devices, as shown in Figure 99. The observed threshold shift is common across our devices and is widely observed in EGOFET devices based on various OSCs, including DPPTTT.[42,64,84,123] The observed negative shift can be explained by the increased electrostatic screening of the charges or dipoles at the OSC interface caused by the increased ionic strength solution in the diffusion layer.[64]

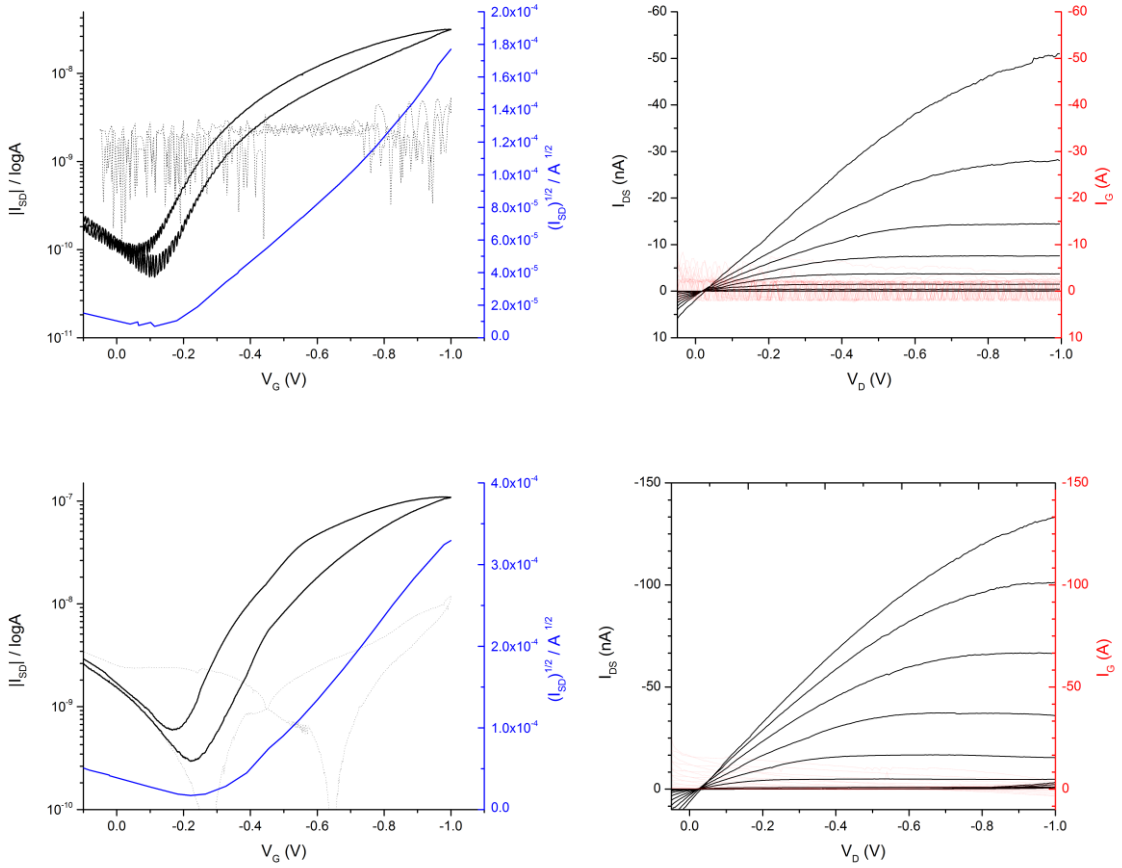

Figure 99 Typical transfer characteristic (left) and output characteristic (right) of DPPTTT/ PMMA COOH devices with the shadow mask design (W = 1 mm, L = 60 µm) operated in a flow cell with water (top) and PBS (bottom) as the electrolyte. The transfer characteristic was measured with V_{DS} = -0.8V.

A significant reduction in gate leakage is observed in the DPPTTT/ PMMA COOH devices, relative to the pristine OSC devices. This can be attributed to the encapsulating effect of the deposited PMMA-based films. However a prevailing issue for integration of the shadow mask defined source and drain electrode designs into the flow cell remains the low I_{SD} current due to the small geometry factor. Therefore, the use of interdigitated electrodes was investigated for DPPTTT-based devices as a route to enhance the relative I_{SD} within the existing flow cell set-up.

8.3.2 DPPTTT -based devices with IDE design

In order to maximise the possible I_{SD} current, IDE devices were investigated for use within the flow cell. The flow cell integrated DPPTTT based devices demonstrated good overall performance when operated in both water and PBS as shown by the typical transfer and output curves shown in Figure 100. Whilst low hysteresis of the device characteristics and good modulation with V_G of the transfer curves is present throughout; less well defined saturation regimes at high V_G is observed in the I_{DS}–V_{DS} curves when operated in PBS compared to water. The characteristic parameters (V_T = - 0.16 V +/-

0.07; $\mu*C$ = 0.03 µF/Vs +/- 0.01) are comparable to those acquired to the DPPTTT devices previously analysed with Au gate electrode with water droplets (see section 6.4).

The expected increase in I_{SD} relative to the shadow mask designed devices operated in flow cells is clearly observed, with I_{on}= 6 µA +/- 1 vs I_{on}<200 nA currents achieved due to the increased geometry factor. However a comparable I_{on} to those observed with Au gated water droplet devices (I_{on}~17 µA as shown in Figure 100) was not achieved. This may be due to the improved quality of gate material achieved from freshly cleaned pure gold wire used to analyse the droplet based devices. The gate leakage (I_G) remained within the same order of magnitude upon flow cell integration, despite the large relative increase in I_{SD}, leading to an improvement in the relative ratio of I_{SD} to I_G, suggesting good charge transport within the active material and not a corresponding increase in electrochemical reactions.

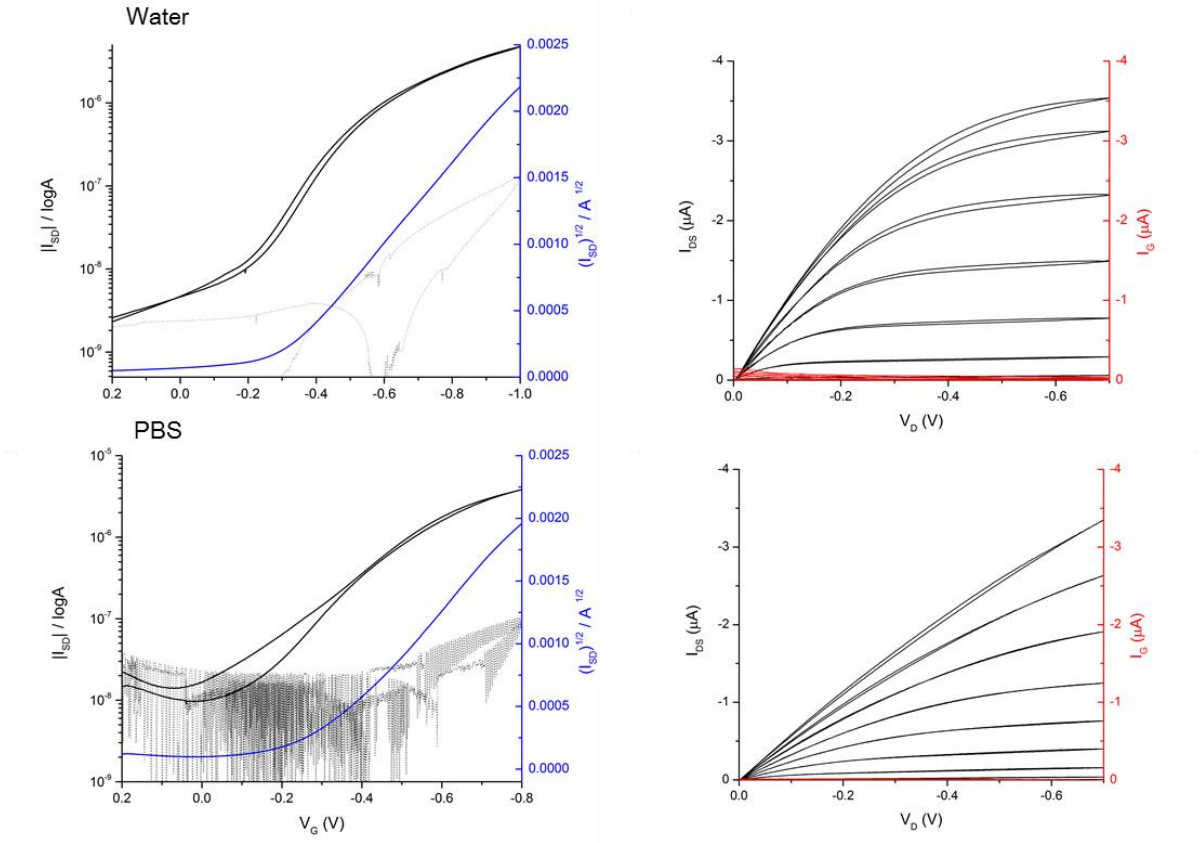

Figure 100 Typical transfer characteristic (left) and output characteristic (right) of DPPTTT devices with the IDE design operated in a flow cell with water (top) and PBS (bottom) as the electrolyte. The Source and drain electrode where patterned by photolithography with an IDE design (W = 16.9 mm, L = 20 µm). The transfer characteristic was measured with V_{DS} = -0.7V.

The reproducibility of the fabricated devices is further demonstrated by the low variation in the averaged transfer curves across four devices when operated in water, as displayed in Figure 103.

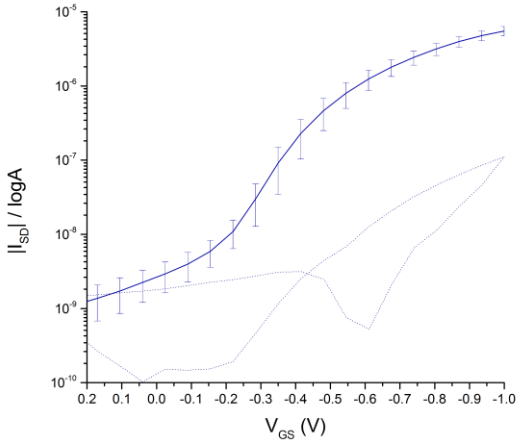

Figure 101 Averaged transfer characteristics of DPPTTT devices with IDE operated in a flow cell with water as the electrolyte. I_{SD} (solid lines) and I_G (dotted lines) are plotted in a semi-log scale. Plotted are the averaged forwards sweeps of the transfer curves and standard deviations of the 4 devices on the same substrate. The source and drain electrode where patterned by photolithography with an IDE design (W = 16.9 mm, L = 20 µm). The transfer characteristic was measured with V_{DS} = -0.7V.

The integration of the interdigitated electrodes into the DPPTTT/PMMA COOH-based flow cell again resulted in the desired increase in I_{on} relative to that observed in the shadow mask defined designs, with I_{DS} in the order of µA currents clearly observed in Figure 102. Good overall device performance is again achieved for the devices with a low variation in electrical performance typified by the averaged transfer curves displayed in Figure 101. The use of an IDE results in a more ideal transfer characteristic in particular a reduction in the relative level of hysteresis between the forward and backward sweep. This is attributed to the improved relative ratio of I_{SD} to I_G, as I_G remains below 50 nA at the highest applied gate potential. As previously observed the deposition of the PMMA COOH layer resulted in a slight reduction in I_{on} (I_{on} = 1-2 µA) relative to the pristine DPPTTT flow cell-based devices (I_{on} = 5-6 µA), however overall performance was deemed to be within an acceptable regime for further investigation as a biosensing platform.

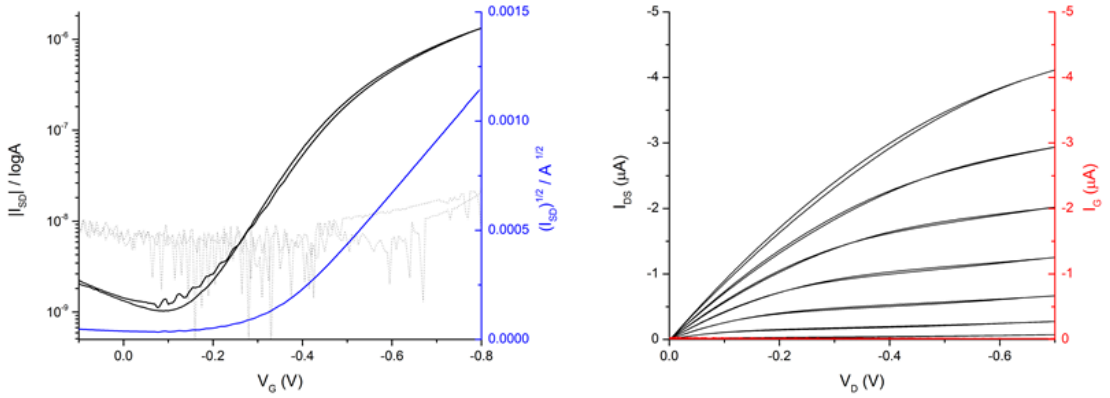

Figure 102 Typical transfer characteristic (left) and output characteristic (right) of a DPPTTT/ PMMA COOH device with the IDE design operated in a flow cell with PBS as the electrolyte. The source and drain electrode where patterned by photolithography with an IDE design (W = 16.9 mm, L = 20 µm). The transfer characteristic was measured with V_{DS} = -0.7V.

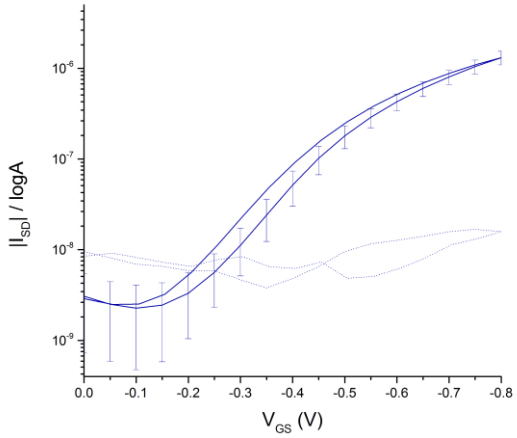

Figure 103 Averaged transfer characteristics of DPPTTT/ PMMA COOH devices with IDE operated in a flow cell with PBS as the electrolyte. I_{SD} (solid lines) and I_G (dotted lines) are plotted in a semi-log scale. Plotted are the averaged forwards sweeps of the transfer curves and standard deviations of the 4 devices on the same substrate. The source and drain electrode where patterned by photolithography with an IDE design (W = 16.9 mm, L = 20 µm). The transfer characteristic was measured with V_{DS} = -0.7V.

8.3.3 Functionalisation of DPPTTT/PMMA COOH devices

Following successful integration of DPPTTT/PMMA COOH devices into the flow cell system, the impact of the functionalisation procedure on device performance was investigated by monitoring the change in device operation at various stages of the functionalisation procedure as shown in Figure 104 and Figure 105. The functionalisation procedure developed during chapter 5 was followed and the devices analysed in the flow cell with PBS as the electrolyte. Figure 104 compares I_{DS}-V_{DS} output characteristics and transfer curves of the devices before functionalisation, following immobilisation of the antibodies and after blocking with BSA. Comparable performance was displayed throughout the procedure, although a slight increase in I_{SD} is observed after functionalisation procedure. In addition a slight increase in hysteresis between the forward and

backward sweeps is observed during the procedure. These observations can be linked to the prolonged exposure to PBS (2 hours), allowing time for the penetration of mobile ions from the PBS solution into the hydrophilic PMMA COOH coating, or the modification of interface capacitance caused by deposited antibodies and BSA during the functionalisation process.[93,97] The comparable and reproducible device behaviour throughout the procedure is highlighted by the averaged transfer curves shown in Figure 105.

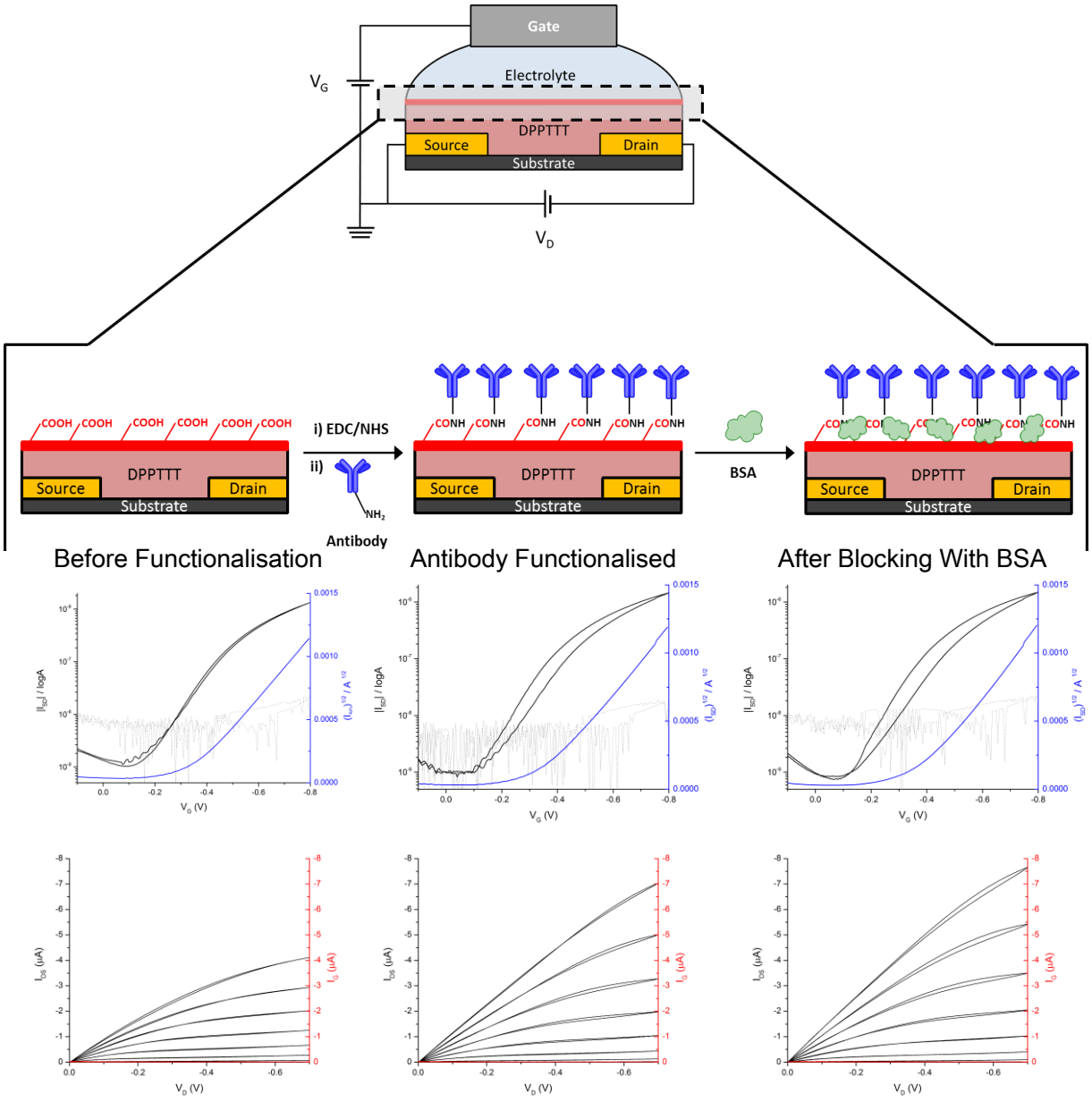

Figure 104 Monitoring the typical device performance during the functionalisation procedure for DPPTTT/ PMMA COOH devices. A schematic representation of the tested EGOFET devices is shown for before functionalisation (left), following immobilisation of the antibodies by EDC/NHS (middle) and after blocking with BSA (right). The transfer (top) and output characteristics (bottom) of typical devices are shown. The devices were fabricated with the IDE design and operated in a flow cell with PBS as the electrolyte. The source and drain electrode where patterned by photolithography with an IDE design (W = 16.9 mm, L = 20 µm). The transfer characteristic was measured with V_{DS} = -0.7V.

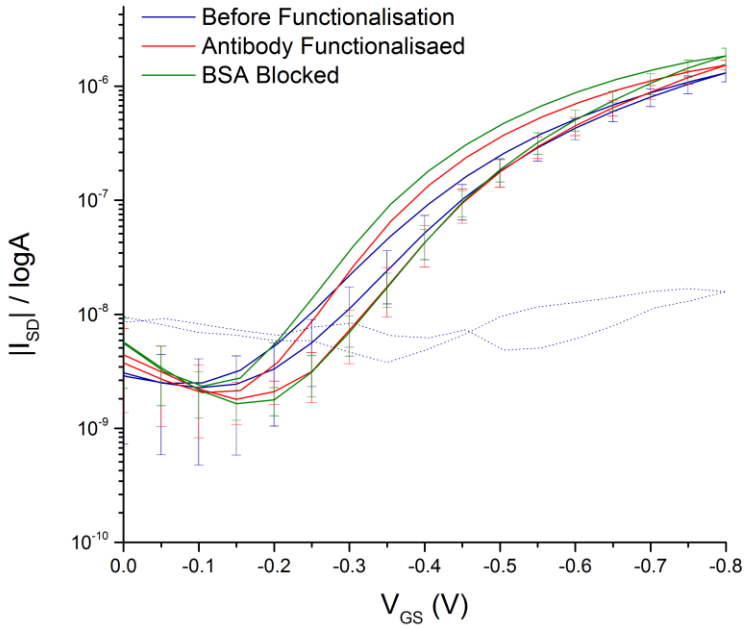

Figure 105 Averaged transfer characteristics of DPPTTT/ PMMA COOH devices during the functionalisation procedure. Plotted are the averaged transfer curves and standard deviations of 4 devices on the same substrate before functionalisation, following immobilisation of the antibodies and after blocking with BSA. The devices were fabricated with the IDE design and operated in a flow cell with PBS as the electrolyte. I_{SD} (solid lines) and I_G before functionalisation (dotted lines) are plotted in a semi-log scale. The source and drain electrode where patterned by photolithography with an IDE design (W = 16.9 mm, L = 20 µm). The transfer characteristic was measured with V_{DS} = -0.7V.

The trend is further investigated through the averaged extracted parameters from the transfer curves collected in Table 19. During the procedure the parameters are relatively unchanged, in particular V_T is consistently around -0.3V, a trend which is also observed by Mulla *et al* during the phospholipid bilayer immobilisation onto UV crosslinked PAA in a PBTTT-based EGOFET.[97] In this work the devices remain operable in similar manner with comparable performance before and after functionalisation, without the decrease in current and mobility observed by Mulla *et al*.[97] This demonstrates the greater environmental stability of DPPTTT when compared to PBTTT and the PMMA-COOH deposition process, that avoided the harmful exposure of the device to UV crosslinking procedure required to make water stable PAA films. A slight increase in both I_{on} and $\mu*C$ is observed during the procedure, however it is unclear whether the relative increase is caused by the chemical modification of the PMMA COOH/electrolyte interface during the functionalisation process or a result of bias stress effects which are discussed in section 8.3.4.

Table 19 Averaged characteristic parameters extracted from the transfer curves of DPPTTT/ PMMA COOH devices during the functionalisation procedure. The devices were fabricated with the IDE design and operated in a flow cell with PBS as the electrolyte. The average is taken over 4 different devices.

	Before Functionalisation		Antibody Functionalised		After Blocking With BSA	
	Mean	Error (+/-)	Mean	Error (+/-)	Mean	Error (+/-)
V_T (V)	-0.31	0.02	-0.33	0.03	-0.33	0.01
µ*C (µF/Vs)	0.011	0.001	0.014	0.002	0.015	0.003
$I_{on/off}$	1000	400	1400	300	1600	300
I_{on} (nA)	1300	200	1500	200	1800	300
I_{off} (nA)	2	2	1	0	1	0
I_G max (nA)	20	1	26	10	37	19

8.3.4 Calibration curve and baseline stability assays

The validation of a biosensing assay and biosensor performance is essential in order to assess the capability for reliable analyte detection. The detection of an analyte is measured through variation in the biosensor electrical parameters and the response should be assessed to ascertain the devices selectivity (specificity), calibration range, linearity, accuracy, reproducibility, limit of detection (LOD) and quantification (LOQ) of the device for HER2 detection.[29]

The relationship between sensor response and concentration of analyte is investigated through calibration curve experiments. The EGOFET biosensing response is commonly performed by measuring relative change to the initial device response before the analyte is applied (blank) and all subsequent concentrations within the calibration curve are then performed on the same device.[29,88] Typically a calibration curve that relies on extracted data from transfer curves to measure sensing response necessitates switching the device on and off during the various assay steps, such as washing and analyte incubation.[79,93,97,105] This is partly due to the majority of previous EGOFET sensors relying on a droplet configuration, and this does not allow continuous device operation during the procedure as the gating electrolyte is removed during the various assays stages. In this work a calibration curve was constructed by measuring the performance of functionalised devices after incubation in sequentially higher concentrations of HER2 ECD in PBS across a concentration range from 0.1 to 1000 ng/ml. The flow cell was used to handle all the liquids used in the assay by the method described in section 4.6. The transfer curve measurements taken for one of the four devices analysed across the full range of concentrations investigated is shown in Figure 106.

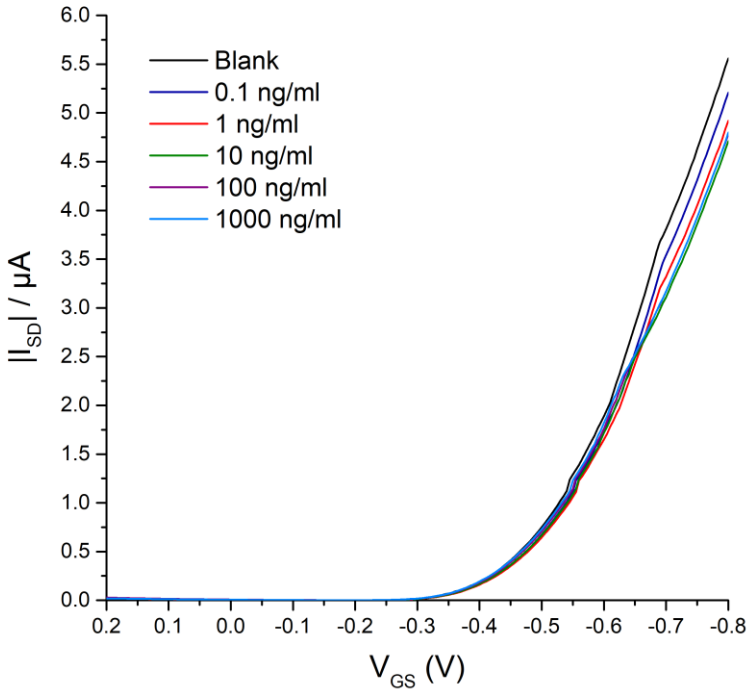

Figure 106 Transfer characteristics of functionalised DPPTTT/ PMMA COOH devices in the flow cell across the range of concentrations investigated in the calibration curve. Plotted are the measurements recorded using PBS as the gating medium following incubation at each concentration level. The measurements displayed here correspond to the extracted parameters for D3 in Figure 107. The source and drain electrode where patterned by photolithography with an IDE design (W = 16.9 mm, L = 20 µm). The transfer characteristic was measured with V_{DS} = -0.7V.

The device response to the analyte was calculated by calculating the change relative to the signal measured in the absence of analyte (the background or blank response). However, it is often of greater merit to analyse the normalised response as this should account for any device to device variation that may frustrate meaningful analysis of the variation of absolute values and therefore improving the reproducibility of the response. The normalised response variation in the devices characteristic parameters is therefore calculated for each of the concentration points investigated and is shown in Figure 107.

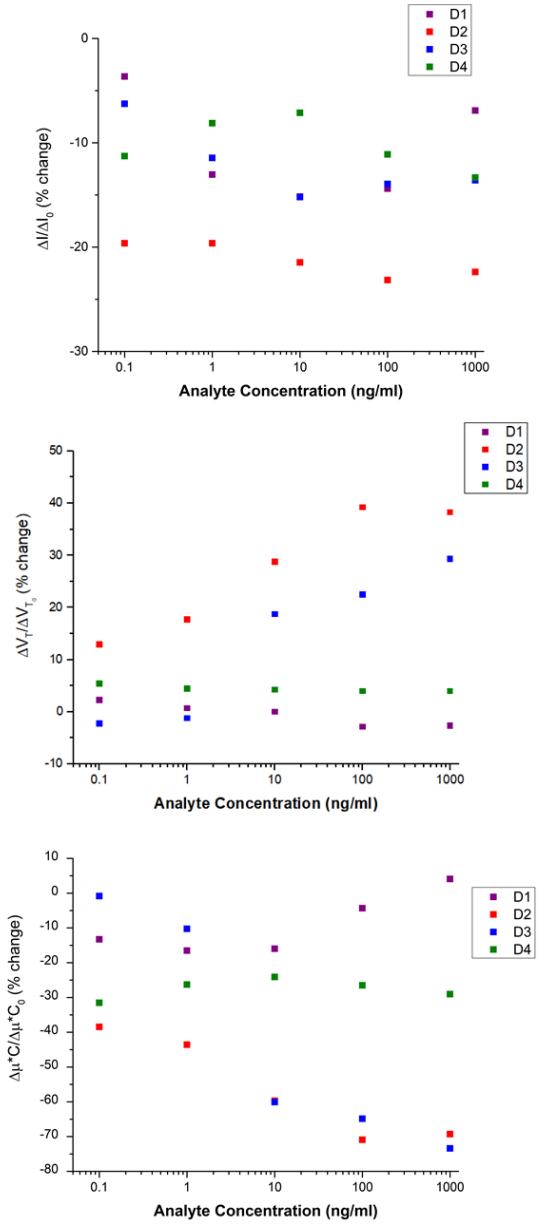

Figure 107 Calibration curves for the antibody functionalised flow cell devices for the detection of HER2 ECD in PBS. The normalised response calculated from the extracted I_{DS}, V_T and μ*C is shown across the 0.1 to 1000 ng/ml concentration range which was investigated.

Despite the normalisation of the response values a significant variation in response for all the parameters is seen across the devices that were analysed. A general trend towards a negative response in current ($\Delta I/I_0$) with increasing analyte concentration is visible but the lack of reproducibility in any of the responses limits the value of results. Therefore, it cannot be confirmed if the observed device response is a result of HER2 detection.

In the development of a biosensor it is essential to confirm that any given signal, in this case device response, is caused by the interaction with only the target analyte. Therefore, the sensor should be capable of distinguishing interference from any other factor that may cause a variation in

performance such as interfering substances (*i.e.* a non-specific analyte), impurities, bias stress or degradation of the device performance.

Therefore, in order to investigate the lack of reproducibility that has frustrated analyte detection in the calibration curve, the evaluation of device response from calibration curve of blank solutions was investigated as a control experiment for sensor calibration. To provide a meaningful control experiment the background measurements should be performed under identical operating and assay conditions to the planned calibration curve. An appropriate baseline experiment closely matching the planned calibration curve procedure was performed using PBS solution as the 'blank sample', the results of which are shown in Figure 89.

Hence, a control baseline experiment was performed by testing the devices in groups of 20 cycled transfer curve measurements in order to collect a stable and reproducible device performance from each stage of the experiment. In order to replicate measuring several analyte concentrations within the assay seven sequential groups of measurements were taken with 20 mins incubation period and 2 mins rinsing of the flow cell in between each test group. The I_{on}, V_T and μ^*C were extracted from the transfer curves of each of the four devices tested during the assay, the average values taken from the last five transfer curves of each of the seven sequentially tested groups are displayed in Figure 89.

Figure 89 demonstrates a drift in the extracted parameters taken from the measurements across the seven tested groups during the assay, with a considerable increase in I_{on} observed and a more gradual positive shift in V_T and decrease in μ^*C. The exceptional stability of DPPTTT EGOFET devices has previously been demonstrated for operation in both water and saline solutions,[123] therefore the variation in performance is more linked to the bias stress conditions as opposed to a general degradation in OSC caused by environmental instability. Bias stress is caused by the continuous or alternating application of voltage signal to the electrodes during the repeated transfer curve measurements over a prolonged period of time, and the resulting device degradation is manifested by the shift in V_T and decrease in μ^*C.[265] The observed drift in performance of the DPPTTT-based devices is significantly less pronounced than the clearly defined degradation observed in the PBTTTT devices operated under bias stress as described in section 8.2.2.

The induced shift in the parameters remained in the devices after the break in transfer curve measurement and becomes more pronounced during the assay, suggesting that the device does not relax back to the original state during this 25 mins period. Typically bias stress induced degradation

is caused by trapping of charge carriers into localised states in the OSC interface, where a V_T shift to towards the direction of the applied maximum gate voltage of the transfer curve.[265]

However, the observed shift in V_T is in the opposite direction of the bias stress towards a more positive value, this could be explained by the prolonged exposure to PBS solution allowing more ion penetration into the hydrophilic film. The penetration of ions could then contribute to a larger concentration of mobile charge carriers at the interface, resulting in an effective increase in the dielectric constant contributing towards a positive V_T shift.

A stable or at least predictable and reproducible baseline is desired for accurate measurement of the relative variation in device performance caused by analyte detection, and a poorly defined baseline will negatively impact on the LOD i.e. the lowest response that can be defined from the baseline measurement. In addition, the poorly defined baseline is indicative of the variation in device performance and background noise which hampered the previously measured calibration curves for HER2 response. Therefore, it is necessary to minimise the observed drift in the device performance, to allow effective analyte detection.

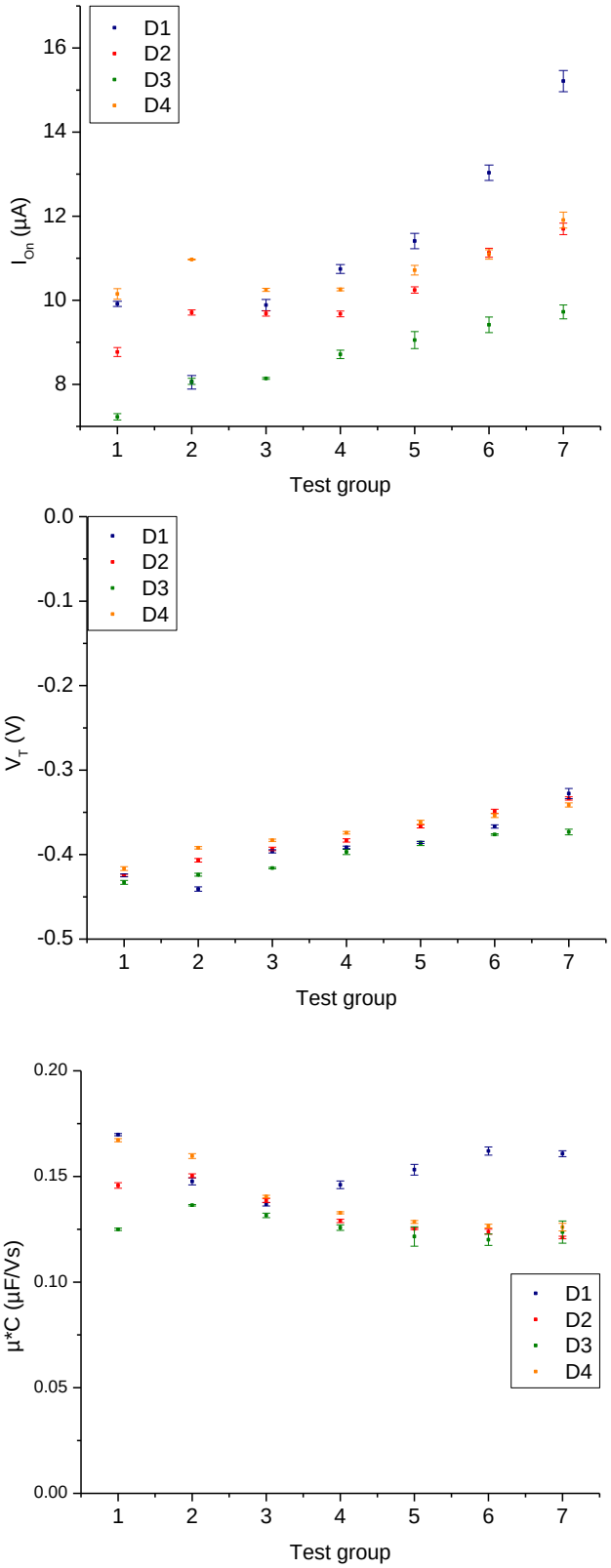

Figure 108 Device transfer characteristic parameter variation during baseline assay experiment in PBS. Tests were conducted in groups of 20 cycled transfer curve measurements with 20 mins incubation period and 2 mins rinsing of the flow cell in between each test group. Displayed is the average of the last 5 transfer curves of each of the 7 sequentially tested groups. The source and drain electrode where patterned by photolithography with an IDE design (W = 16.9 mm, L = 20 µm). The transfer characteristic was measured with V_{DS} = -0.7V and V_{GS} swept in both directions from + 0.2.V to -0.8V.

8.3.5 Stabilising bias stress drift

In order to stabilise the apparent drift in device performance of the DPPTTT-based devise when under bias stress, the impact of the deposited PMMA layer on device performance re-evaluated. In this process we investigated the impact of the PMMA layer thickness and annealing temperature on device operational stability.

A PMMA solution 30 mg/ml in n-butyl acetate was spin coated at 4000 rpm for 2 mins onto the DPPTTT layer and annealed at 80 °C for 1 hour to yield a PMMA thickness of 110 nm. In addition devices fabricated following the previous method of spincoating from 10 mg/ml solutions, were prepared and annealed at 80 °C and 110 °C to yield PMMA thicknesses of around 20 nm measured by Dektak as described in section 3.1.

In order to investigate the impact on device performance the transfer characteristics of the devices operated in PBS in a flow cell where collected and are compared in Figure 109. As previously established the deposition of the PMMA layer onto the DPPTTT resulted in a significant decrease in I_{on}, however the effects are significantly more pronounced with a very thick PMMA layer where I_{on} <200 nA are typically achieved. The low current observed can be attributed to a significant reduction in μ*C as V_T remained at a similar level. A similar observation had been noted by Magliulo *et al,* where thicker layers of pdEthAA deposited on top of their OSC resulted in a significant reduction in current.[100] Due to the significant reduction in performance observed, devices fabricated with thick PMMA layers were not pursued any further.

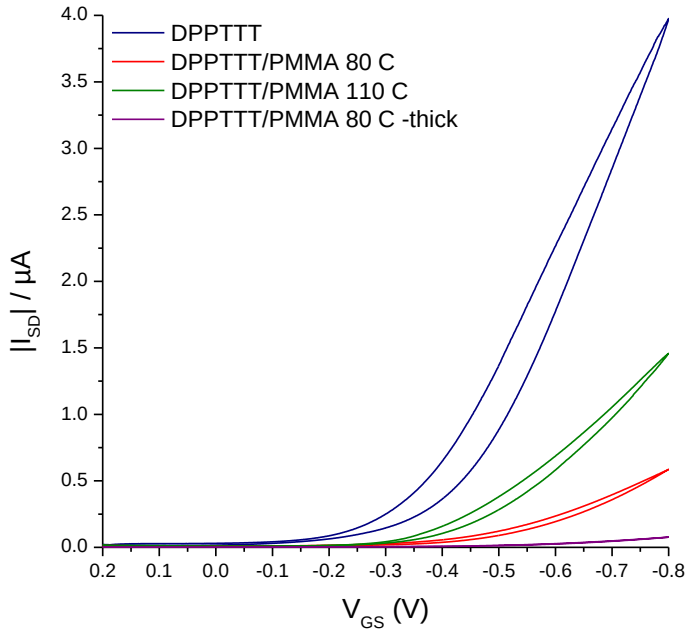

Figure 109 Typical transfer characteristic of DPPTTT-based devices with the IDE design operated in a flow cell with PBS as the electrolyte. Compared are devices fabricated with pristine DPPTTT, DPPTTT/PMMA devices annealed at 80 °C and 110 °C for 1 hour to give PMMA thickness of 20 nm and DPPTTT/PMMA device fabricated to give a PMMA thickness of 110 nm and annealed at 80 °C. The source and drain electrode where patterned by photolithography with an IDE design (W = 16.9 mm, L = 20 µm).

In contrast, the DPPTTT-PMMA devices fabricated with PMMA thicknesses in the order of 20 nm, yielded improved device performance to thicker PMMA layers. Although, the observed I_{on} is still reduced relative to the pristine DPPTTT devices (4 µA) it remains within a suitable regime (I_{on} ~ 1-2 µA) for further investigation, with scope for sufficient current modulation and interfacial sensitivity required for biosensing. It is possible that device performance of more comparable nature to pristine DPPTTT-based devices could be achieved by the deposition of thinner PMMA layers. However, due to the difficulty in reproducibly depositing films <20 nm, we have not investigated this further, although with further refinement of the spin coating procedure it may be possible.

DPPTTT EGOFET devices have previously shown good operational stability in ON-OFF testing with minimal variations in on and off currents over 3 h and 270 cycles, with the device reaching a stable operation status after around 15 mins operation in saline solution.[123] Therefore, the impact of bias stress on the device performance was investigated through cycled transfer characteristics measurements on the DPPTTT devices and DPPTTT-PMMA devices annealed at 80 °C and 110 °C. The bias stress induced change in device performance is clearly shown by the transfer curves for a both representative individual devices (Figure 110) and the averaged transfer curves across four devices, as shown in Figure 111.

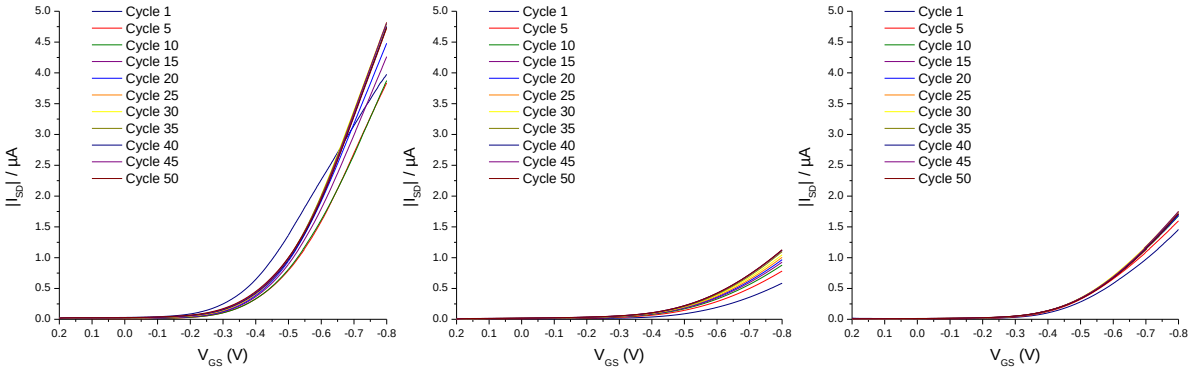

Figure 110 Typical transfer curves of DPPTTT-based devices during bias stress measurements of 50 repeated cycles. Compared is a single device fabricated with pristine DPPTTT (left) and DPPTTT/PMMA devices annealed at 80 °C (middle) and 110 °C (right) fabricated with the IDE design and operated in a flow cell with PBS as the electrolyte. The source and drain electrode where patterned by photolithography with an IDE design (W = 16.9 mm, L = 20 µm). The transfer characteristic was measured with V_{DS} = -0.7V.

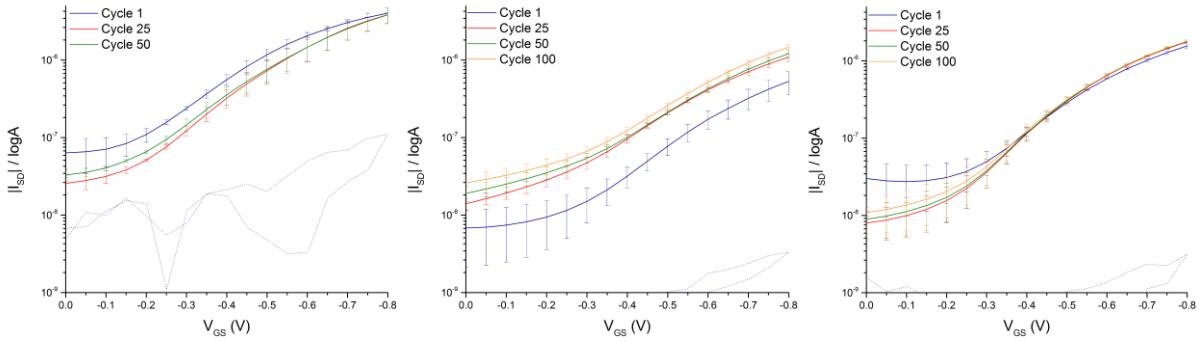

Figure 111 Bias stress averaged transfer curves over repeated cycles. Compared are devices with pristine DPPTTT (left) and DPPTTT/PMMA devices annealed at 80 °C (middle) and 110 °C (right) fabricated with the IDE design and operated in a flow cell with PBS as the electrolyte. I_{SD} (solid lines) and I_G (dotted lines) are plotted in a semi-log scale. Plotted are the averaged forwards sweeps of the transfer curves and standard deviations of the 4 devices on the same substrate. The source and drain electrode where patterned by photolithography with an IDE design (W = 16.9 mm, L = 20 µm). The transfer characteristic was measured with V_{DS} = -0.7V.

All the fabricated devices demonstrated some bias stress induced variation from the initial performance in cycle 1, however the variation is most pronounced in the first 25 cycles of the investigation after which a more stable operation status was achieved. This is generally in agreement with the 15 mins of bias stress operation previously observed in DPPTTT devices operated in saline solution.[123] Additionally, the relative variation in performance across the four devices is significantly less pronounced in the PMMA-based devices, as shown by the smaller error bars. The impact of bias stress on the device performance is further investigated through the extracted parameters from the transfer curves, as shown in Figure 119, where the variation in pristine DPPTTT devices is more easily identified.

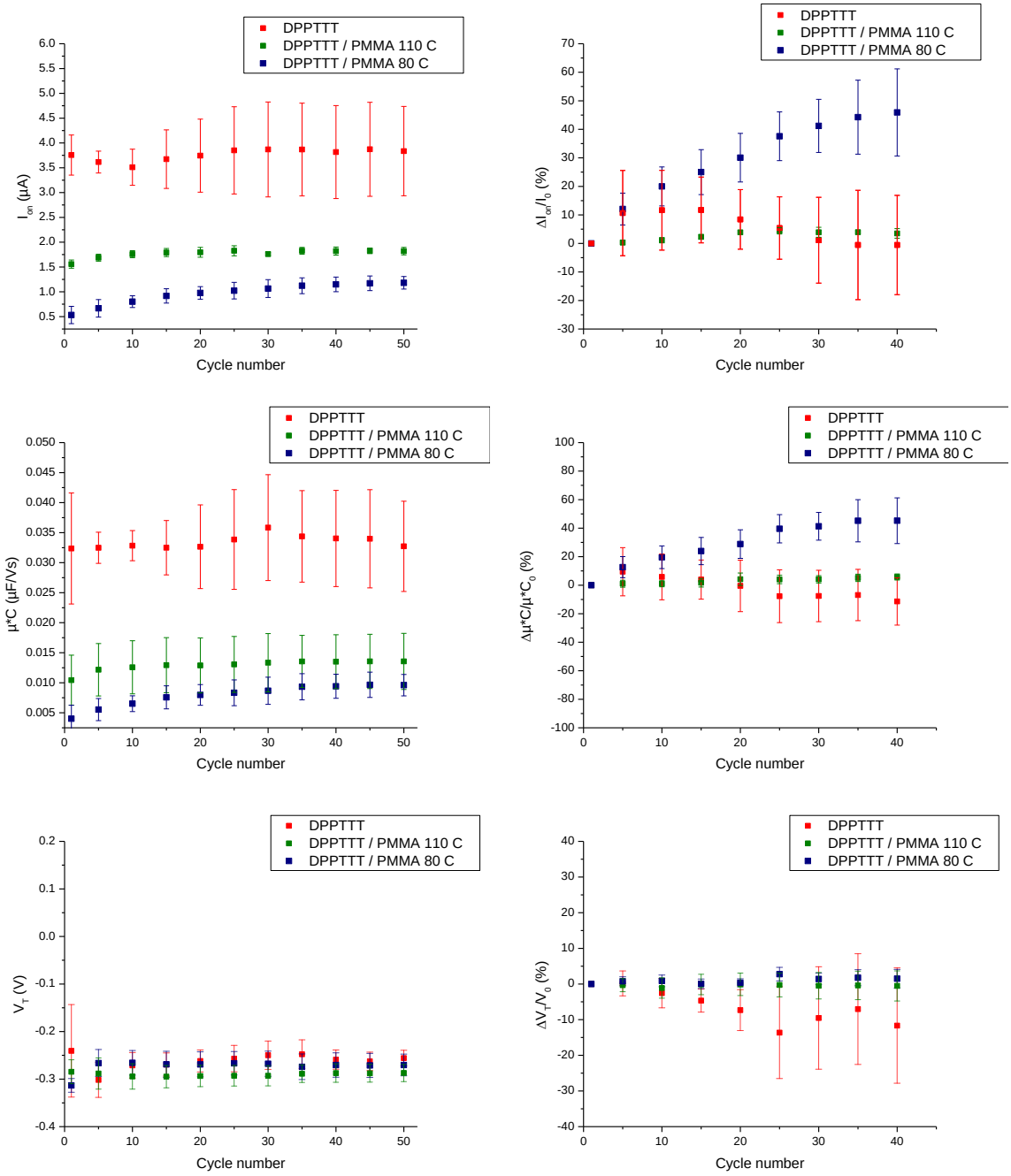

Figure 112 The device transfer characteristic parameter variation of DPPTTT-based devices under bias stress. Displayed are the absolute parameters values (left) and relative change as a percentage (right) for I_{on}, μ^*C and V_T. The percentage change is calculated relative to the 10th cycle. The averages and standard deviations are taken across 4 devices. Compared are devices with pristine DPPTTT (red) and DPPTTT/PMMA devices annealed at 80 °C (green) and 110 °C (blue) fabricated with the IDE design and operated in a flow cell with PBS as the electrolyte. The source and drain electrode where patterned by photolithography with an IDE design (W = 16.9 mm, L = 20 µm). The transfer characteristic was measured with V_{DS} = -0.7V and V_{GS} swept in both directions from + 0.2.V to -0.8V.

Normalising the relative change in the extracted values for the characteristic parameters allows for an easier interpretation of the drift caused by the bias stress operation. In addition, it is analogous to

the method used to measure the device response upon analyte interaction. In the absence of analyte (*i.e.* baseline measurement) no change in device parameters is desired, although a consistent and reproducible drift in baseline could be corrected for. The right column of graphs in Figure 112 displays the relative change after the first 10 measurements, where more stable operation status is achieved.

The initial V_T for all the fabricated devices is comparable (V_T= -0.25 to -0.35 V), however the deposition of PMMA layer results in a slightly more negative V_T as was previously observed in Table 14. V_T is a parameter frequently probed to investigate device stability and bias stress induced degradation in OFETs.[265] Typically a shift in V_T towards the direction of the applied gate bias, therefore for a p-type OSC a more negative shift, would be expected upon gate bias stress, usually due the formation of trapped charge carriers.[265] The trapping of mobile charge carriers in localised trap states can occur at the OSC, dielectric or the active interface and charges can be trapped in stress generated or pre-existing trap sites that originate in the fabrication process or are inherent to the materials. Trapped charge carriers typically no longer contribute towards the induced current, meaning the application of a higher gate field is required to achieve equivalent number of mobile charge carriers.[265] The normalised variation for V_T shows no significant change observed and remains relatively stable throughout the bias stress investigation, especially for PMMA-based devices which remain almost unchanged and only a slight change of at most ± 5% is observed and slightly larger variation for pristine DPPTTT based devices.

An overall reduction in the absolute values of I_{on} and μ^*C is observed in the PMMA-based devices relative to pristine DPPTTT, this can be attributed to the reduced capacitance of the deposition PMMA dielectric/OSC relative to the high capacitance of the EDL/OSC interface. Drift in mobility and the linked drift in I_{on} is more commonly observed in solid state OFETs, where solid dielectric materials are used, and is caused by the retention of some of the interfacial charges established during V_{GS} sweeps.[265] Given the extremely high capacitance of the EDL, the OSC/PBS electrolyte interface is comparable to a high *k* dielectric system, even a small amount of trapped charges would result in an inflation of μ^*C and could explain the high levels of drift observed in the pristine DPPTTT devices. The application of a low *k* dielectric such as PMMA and PS is commonly used to reduce the drift by lowering the number of charges held at the interface allowing quicker recovery times. Therefore, a reduction in drift may be expected in the PMMA-based devices.

However, a relative increase in hydrophilicity of the deposited PMMA films relative to the highly hydrophobic DPPTTT was evidenced by water contact angle measurements in section 3.1. The increased hydrophilicity makes the PMMA layer more prone to water and salt ion absorption from

the PBS electrolyte solution, which may be a contributing factor the observed drift in the PMMA based devices. Additionally, the increased capacitive effect of the absorbed water into the dielectric film and the accumulation of mobile salt ions into the film may also contribute to the increasing mobility and currents observed in the PMMA-based devices annealed at 80 °C.

Annealing the PMMA-based devices at 110 °C resulted in a significantly reduced drift in both I_{on} and $\mu*C$ as the variation in these parameters remained at around 0% change. In addition the relative variation in behaviour across the four devices is significantly more reproducible under the bias stress conditions compared to the other devices, as highlighted by the small standard deviations displayed. PMMA based polymers typically have a glass transition temperature (T_g) in the order of 100-105°C,[266,267] and annealing above the T_g of the insulator polymer has proven effective for improving performance in OSC-blended films.[235] The induced molecular motions in the polymer act as a plasticiser at the OSC/PMMA-dielectric interface which can facilitate rearrangement and the formation of more ordered microstructures at the interface allowing improved charge transport behaviour and device operation.[235] This is shown by the increased I_{DS} and $\mu*C$ of the devices annealed at 110 °C. Annealing above the T_g also allows for better packing of the deposited film by reducing the free volume making it less permeable to water and ion penetration.[268] The reduced free volume also makes the dielectric polymer less polarisable, where annealing at the T_g of PMMA has been demonstrated to reduce the dielectric constant.[269] These factors may contribute towards the reduced drift observed in the devices annealed at a higher temperature, where annealing at even higher temperature could also be investigated to further optimise the process.

As shown above, the PMMA-based devices annealed at 110°C have demonstrated reduced drift under bias stress conditions and are now well suited for further investigation. Re-investigation of the baseline assay experiments (in section 8.3.4) with the improved stability of these devices may provide the stable baseline required for effective biosensing.

9 Conclusions and future work

9.1 Conclusions

In this work the functionalisation of an EGOFET biosensors at both the OSC and gate interface where investigated. In order to functionalise the OSC interface dielectric copolymers, derived from PMMA containing pendant carboxylic acid side chains groups were synthesised for use in bilayer type devices by spin-coating onto OSC films. The labile carboxylic acid groups introduced to the surface of the device allowed for the immobilisation of HER2 antibodies by *in-situ* covalent attachment by EDC/NHS coupling. The functionalisation procedure was confirmed by fluorescent binding assay, AFM and water contact angle measurements. The AFM measurements and fluorescence binding assay indicate a high surface coverage of HER2 antibody deposited onto PMMA COOH films which retain their bioavailability in good agreement with that reported by others using similar polymer coatings for covalent immobilisation.

The EGOFET devices initially produced by shadow mask evaporation typically displayed a relatively low I_{on} due to the low geometry factor of the design used during source and drain metal deposition. Device operation was improved by using photolithography defined interdigitated source and drain electrodes. The improved geometry factor resulted in I_{SD} of μA to be achieved, with reduced hysteresis and an improved ratio of I_{SD} to I_G gave improved device performance.

The choice of gate electrode material was shown to be an effective tool for V_T tuning. The use of a Au gate electrode shifted the device operation into a more suitable regime and allowed effective DPPTTT/PMMA COOH operation with a low threshold and operating voltage.

In addition, the use of an Au gate electrode was utilised to investigate the functionalisation of the gate electrode by the covalent attachment of the biorecognition element to the carboxylic acid groups of SAMs chemisorbed onto gold wire gate electrodes, two different SAM systems where investigated. In order to allow this, a device set-up was constructed to reliably hold the gate electrodes inside a measurement well that confines the gating medium used in the EGOFET over the channel.

Gold gate electrodes functionalised with a BioSAM containing monoclonal HER2 antibodies was demonstrated proof of principle for the detection of HER2 ECD using an EGOFET biosensor. The $\Delta I/I_0$ signal response gave a LoD for the HER2 ECD of approximately $1x10^{-18}$M. Biosensor selectivity was demonstrated through negligible device response to VEGF protein over the same range of concentration investigated for HER2 ECD.

The versatility of SAM based gate functionalisation was demonstrated by the proof of principle for the detection of THC with an EGOFET biosensor using a gate electrode functionalised using a Lipoic acid SAM attached to OBPs. The $\Delta I/I_0$ signal response gave a LoD for THC of approximately 1.6×10^{-14} M. In addition, the sensor displayed a selective response to THC over the negative control cannabinoids CBN and CBD. Additionally, inspection of the relative variation in V_T and μ^*C in response to THC concentrations showed that the device was mainly operating as a capacitance modulated biosensor.

The integration of the EGOFET devices within a flow cell demonstrated comparable device operation, enabled easy fluid handling and eliminated problems with water evaporation that hampered the utility of droplet-based devices. In parallel, a bespoke characterisation platform was also developed to allow a user-friendly time efficient and controlled set-up for performing the electrical characterisation, removing the need for a microprobe station.

The use of PBTTT and DPPTTT as the active layer in the biosensor device was investigated by the analysis of both pristine semiconductor and bilayer devices. The PBTTT-based devices suffered from significant degradation in device performance upon prolonged exposure to aqueous solutions; this limited its utility for developing a stable biosensor. However, the superior environmental stability of the DPPTTT-based devices was highlighted by stable device performance after prolonged exposure to PBS solutions and under bias stress conditions.

The impact of the developed functionalisation procedure on DPPTTT/PMMA COOH device performance was investigated by monitoring the change in device operation at various stages of the functionalisation procedure. Comparable performance was displayed throughout the procedure demonstrating greater environmental stability of DPPTTT. This is an improvement over the bilayer PBTTT-based device developed by Mulla and co-workers where a decrease in current and mobility was observed.[97] Additionally it highlights the benefit of the PMMA-COOH spin-coating deposition process, that avoided the harmful exposure of the device to UV crosslinking procedure required to make water stable PAA films.

A calibration curve was attempted for the functionalised flow cell use in the detection of HER2 ECD however the large variation in sensing response frustrated a meaningful analysis. A control baseline experiment was performed to replicate measuring several analyte concentrations during a biosensing assay experiment in order to investigate the noise in the calibration curve. However, bias stress induced drift in electrical performance was observed in DPPTTT/PMMA COOH devices, probably due to ion penetration from the PBS solution into the hydrophilic film. In order to create a

platform of optimal biosensing capability it is important to minimise any variation in device performance that is not associated with the analyte interaction, such as device stability and reproducibility. Increasing the final annealing temperature in device fabrication to above the Tg of PMMA resulted in the desired improved performance and reduced drift. The resulting platform is now better positioned for improved sensing performance and further development as a biosensor.

9.2 Future work

The ultimate objective is for a design with multiple microfluidic chambers each housing separately functionalised EGOFET devices. This would make it an ideal platform capable of multiplexed analysis of separate biomarkers in parallel and miniaturisation of a complex assay for use in POC setting.

A comparison of the two approaches investigated in this thesis for the functionalisation of an EGOFET biosensor demonstrates that functionalisation of the gate electrode provides the easiest route to developing biosensor devices for the novel detection of analytes. The lack of stability in the bilayer type devices significantly hindered the devices application in sensing experiments. Following the improved stability to bias stress of the PMMA-based devices annealed at 110°C re-investigation of the baseline assay experiments with these devices may provide the stable baseline required for effective biosensing.

Future work on the gate functionalised biosensors should focus on improving the reproducibility of the sensing response and could be achieved through the use of a flatter more homogenous gold gate electrode which would improve the quality of the underlying SAM and may also increase the overall sensing response. Additionally, the integration of the device into a flow cell would be of merit to improve fluid handling. The development of a multi-plex analyte detection system using an array of appropriately developed OBPs is a feasible option that would allow the detection of multiple analytes simultaneously.

In addition to improvements in sensing performance the detection of the HER2 ECD from blood serum would be a desirable step in the further development of the biosensor. Operation in blood serum will also provide a comprehensive test of specificity, as well as the impact of salt concentration on device operation. For comparison, the BioSAM-based EGOFET sensor has recently demonstrated analyte detection in a complex matrix demonstrated by the detection of CRP in saliva.

10Appendix

10.1 Tables

Table 20 Calculated initiator half-life times for Vazo 67 using Equation 31.The reaction length is taken to be approximately three times half-life duration.

Reaction Temperature °C	$t_{1/2}$ (mins)	Aprox. Reaction Duration (hours)
65	873	43.6
80	100	5.0
85	51	2.5

$$\log(t_{1/2}) = 7492\left(\frac{1}{T}\right) - 19.215$$

Equation 31 Initiator half-life ($t_{1/2}$) for Vazo™ 67 in 1,3,5-trimethylbenzene.[270]

Table 21 Variation in reaction solvent and duration on polymerisation reaction

Name	Solvent	Reaction Conc (mmol/ ml)	Reaction temperature (◦C)	Reaction duration (hrs)	Mn (kDa)	Mw (kDa)	Đ (Mw/ Mn)	Loading of COOH from NMR (%)	Yield (%)
A	THF	1.50	65	4.0	34.6	68.1	2.0	10.0	16.5
B	THF	1.50	65	48.0	11.6	35.6	3.1	10.2	81.0
C	Toluene	1.50	85	3.0	16.5	38.0	2.3	13.1	53.5

Table 22 Variation in reaction concentration on polymerisation reaction in toluene

Name	Reaction Conc (mmol/ml)	Initiator concentration (mol. %)	Reaction duration (hrs)	Mn (kDa)	Mw (kDa)	Đ (Mw/Mn)	Loading of COOH from NMR (%)	Yield (%)
A	**2.72**	0.43	4.5	23.0	47.3	2.1	10.3	73.4
B	**1.50**	0.43	3.0	16.5	38.0	2.3	13.1	53.5
C	**0.68**	0.43	3.0	10.7	21.7	2.0	13.7	43.8

Table 23 Variation in initiator concentration and reaction length on polymerisation reaction in toluene

Name	Reaction Conc (mmol/ml)	Initiator concentration	Reaction duration (hrs)	Mn (kDa)	Mw (kDa)	Đ (Mw/Mn)	Loading of COOH from NMR (%)	Yield (%)
A	**0.68**	0.43	2.0	10.4	19.2	1.8	14.5	31.8
B	**0.68**	0.43	3.0	10.7	21.7	2.0	13.7	43.8
C	**0.68**	0.43	4.5	12.2	24.0	2.0	12.5	46.8
D	**0.68**	0.2	3.0	15.6	30.4	2.0	14.4	36.3
E	**0.68**	0.2	4.5	12.3	26.0	2.1	14.4	32.9

Table 24 Variation in initiator concentration on polymerisation reaction in dioxane

Name	Reaction Conc (mmol/ml)	Initiator concentration (mol. %)	Reaction duration (hrs)	Mn (kDa)	Mw (kDa)	Đ (Mw/Mn)	Loading of COOH from NMR (%)	Yield (%)
A	0.68	0.43	3	18.3	39.7	2.2	9.1	61.4
B	0.70	0.1	3	46.1	80.4	1.7	9.6	39.7
C	0.62	0.05	3	50.2	118.8	2.4	9.1	23.3

Table 25 Repeatability of polymerisation reaction in dioxane

Name	Reaction Conc (mmol/ml)	Initiator concentration (mol. %)	Reaction duration (hrs)	Mn (kDa)	Mw (kDa)	Đ (Mw/Mn)	Loading of COOH from NMR (%)	Yield (%)
A	0.70	0.1	3	47.6	85.6	1.8	9.5	34.9
B	0.70	0.1	3	47.4	82.6	1.7	9.6	34.2
C	0.70	0.1	3	46.1	80.4	1.7	9.6	39.7

Table 26 Control of loading of COOH containing monomer in polymerisation reaction in dioxane

Name	Theoretical Loading of COOH monomer (%)	Reaction Conc. (mmol/ml)	Initiator concentration (mol. %)	Reaction duration (hrs)	Mn (kDa)	Mw (kDa)	Đ (Mw/Mn)	Loading of COOH by NMR (%)	Yield (%)
A	10	0.70	0.1	3	46.1	80.4	1.7	9.6	39.7
B	5	0.70	0.1	3	49.4	87.0	1.8	4.6	34.2
C	2	0.70	0.1	3	50.3	92.8	1.8	2.2	51.5

10.2 Figures

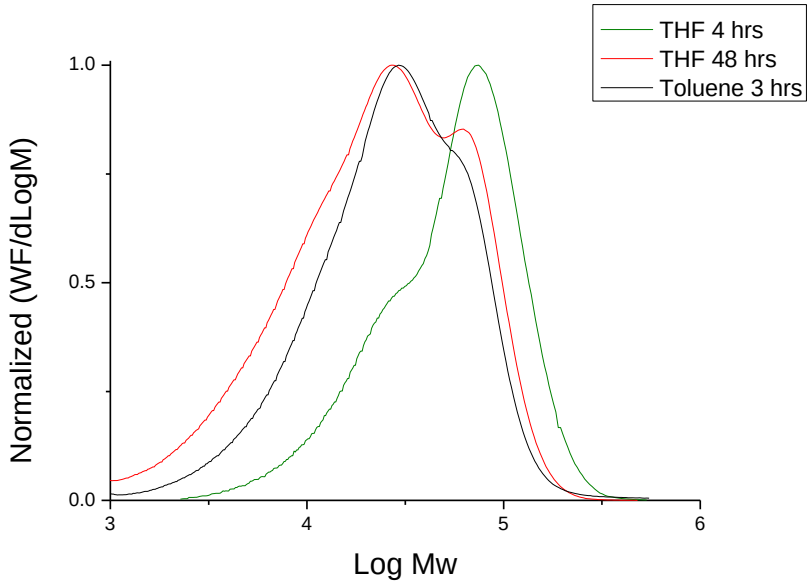

Figure 113 GPC showing variation in reaction solvent and duration on Mw distribution

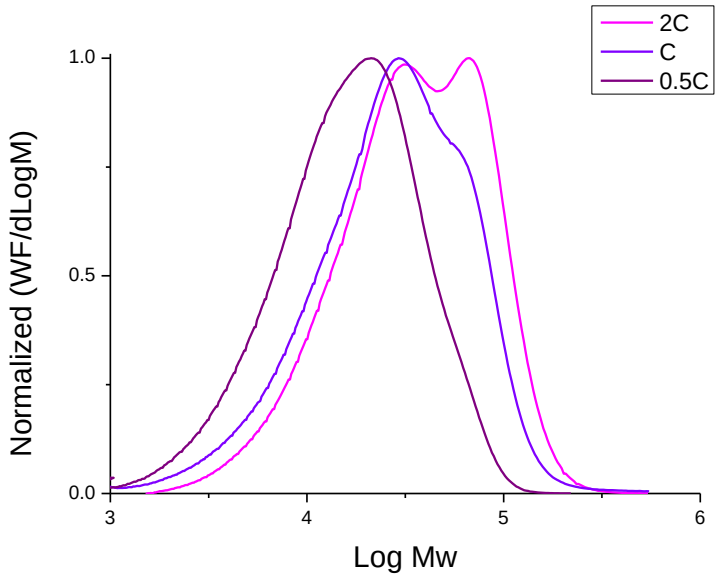

Figure 114 GPC showing effect in reaction concentration on Mw distribution from polymerisation reaction in toluene

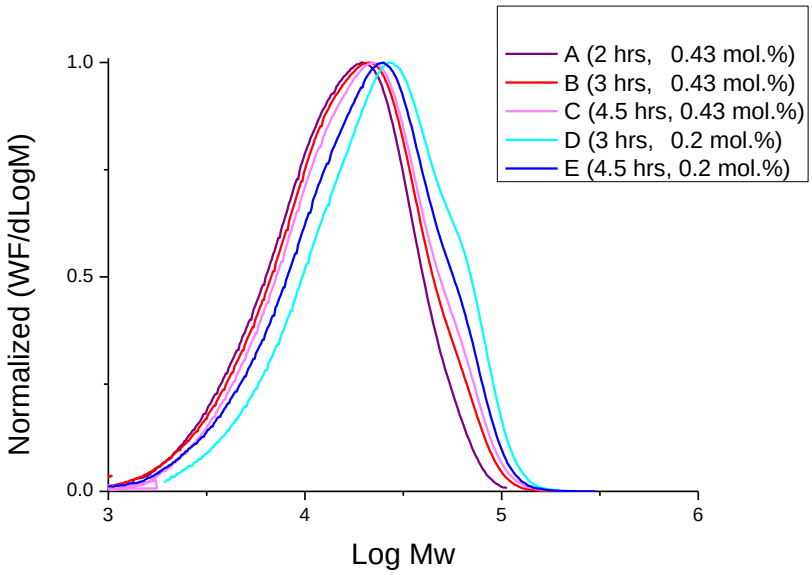

Figure 115 GPC showing effect of initiator concentration and reaction duration on Mw distribution from polymerisation reaction in toluene

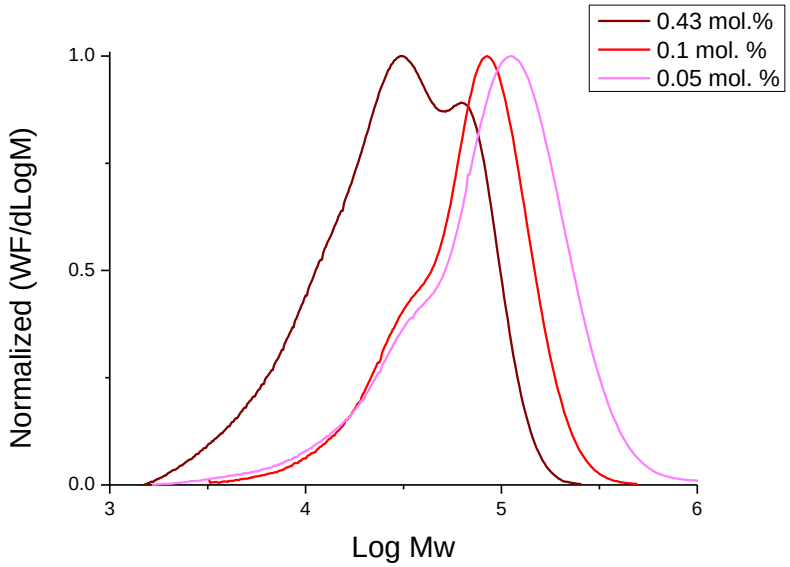

Figure 116 GPC showing effect of initiator concentration on Mw distribution from polymerisation reaction in dioxane

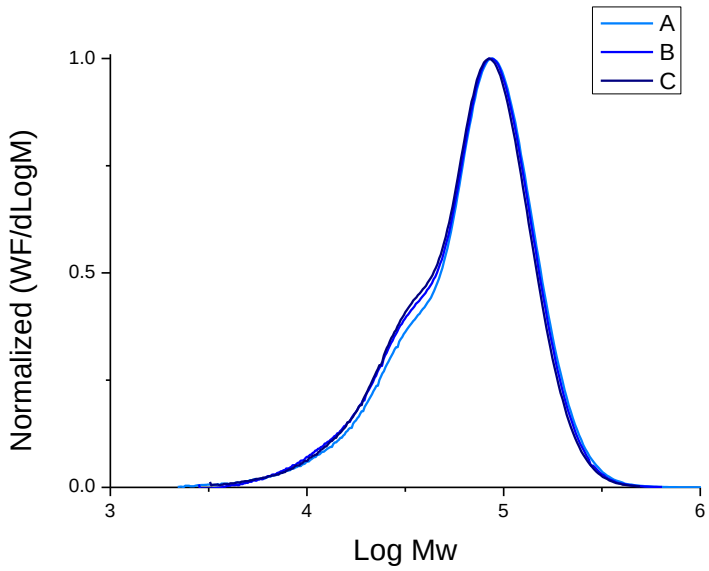

Figure 117 GPC showing repeatability of Mw distribution from polymerisation reaction in dioxane

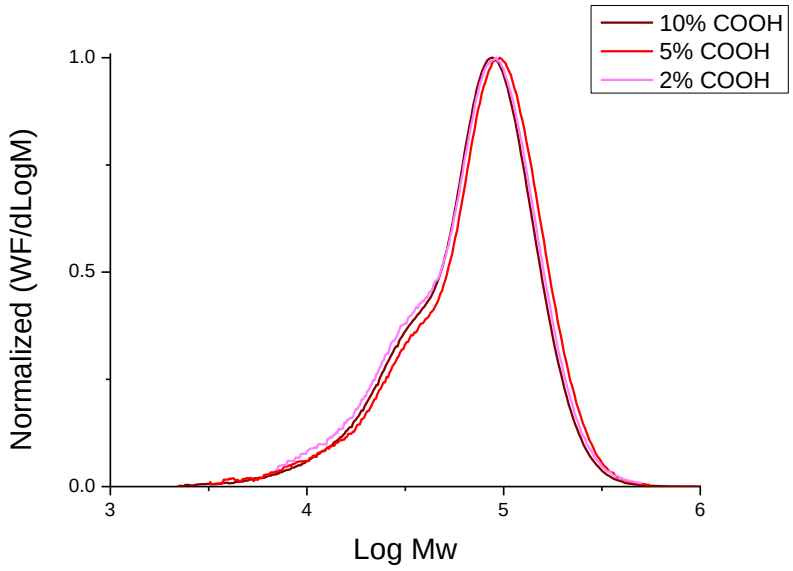

Figure 118 GPC showing Mw distribution from polymerisation reaction in dioxane with different loadings of COOH containing monomer

Figure 119. Cross section image of 3M™ Double Coated Membrane Switch Spacer (3M 7961MP). Features 0.05 mm adhesive layers, 0.18 mm PET carrier and 0.11 mm Polycoated Kraft Paper (Liner). This gives an applied thickness of ~280 µm.

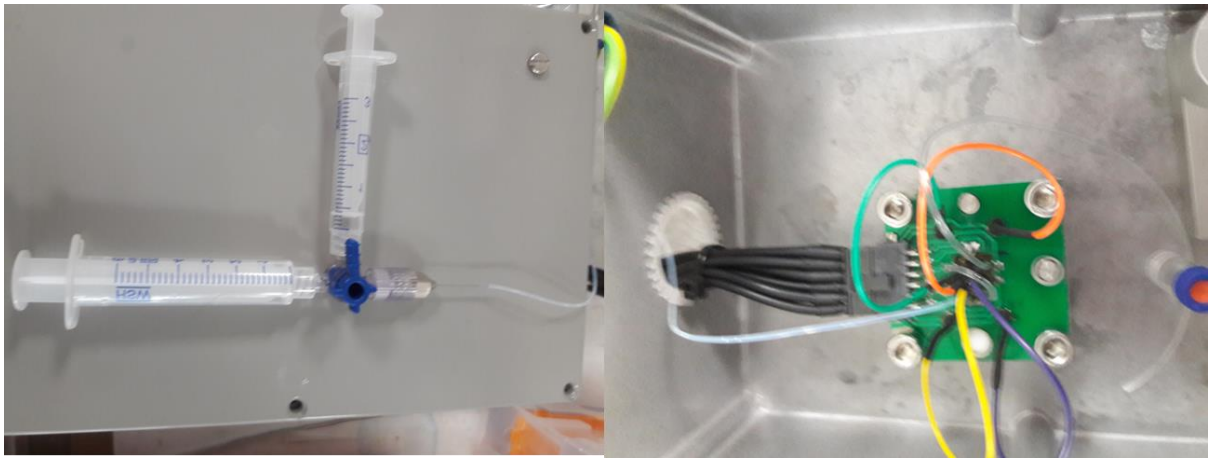

Figure 120 The set up used for flow cell measurements. A three-way stopcock tap is connected to two syringes containing the prepared fluids needed for the experiment. The syringes are mounted on to separate syringe pumps allowing the flow rate to be controlled. Only one syringe pump is used at a time. The fluid is introduced into the cell through by PTFE tubing connected to the stainless-steel inlet tube. The system dead volume (including the three-way stopcock and tubing) was ~150 µl.

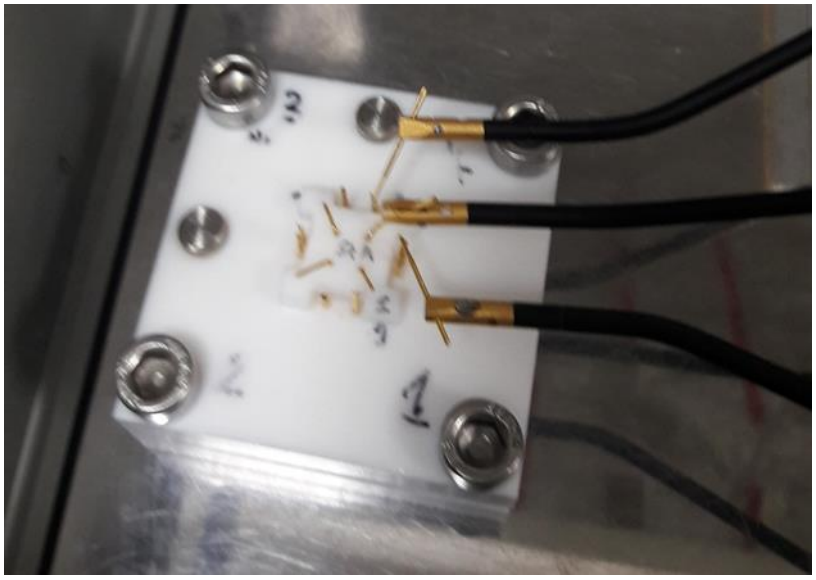

Figure 121 Assembled measurement system inside a probe station and the contacts are connected to the electrical measurement system.

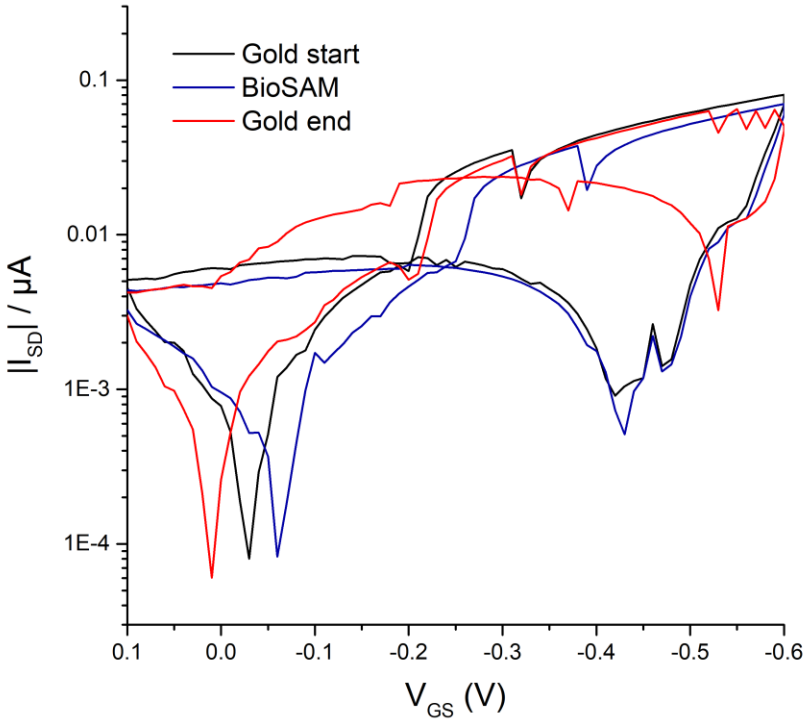

Figure 122 Gate leakage measured for the transfer I-V curves in Figure 72 (I_{DS} vs. V_G at V_D=-0.4V) displaying the change in the device performance before and after the completion of the HER2 calibration curve for one device. The black (before) and red (after) curves show the measurement recorded with a bare Au gate, and the blue curve was recorded using the functionalised Biosam gate before the calibration curve measurements are taken.

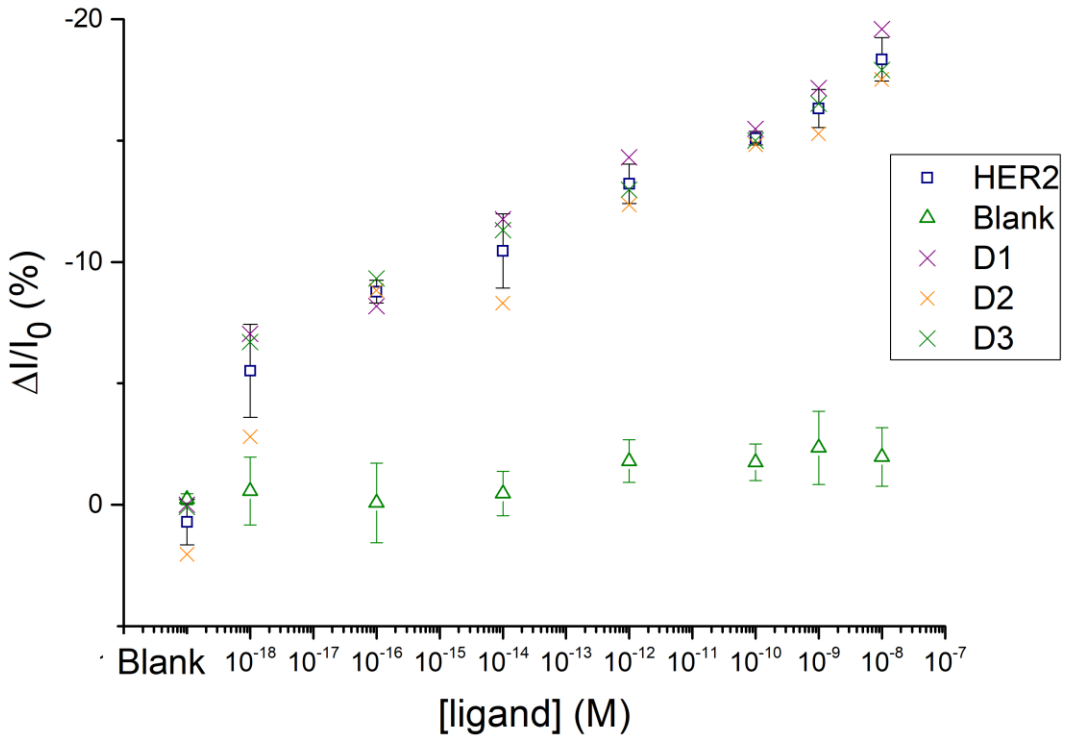

Figure 123 EGOFET HER2 antibody BioSAM calibration curves of device current ($\Delta I/I_0$) response vs ligand concentration covering the range 1 x 10^{-18} M to 1 x 10^{-8} M. The blue squares are the average responses for HER2 ECD as the ligand. The crosses represent the individual device responses. The green triangles are the responses to a blank assay performed under the same conditions with PBS solutions but no analyte.

10.3 Achievements

List of achievements below in the following categories including conference presentations, posters, and attendance:

G. Sunley Saez, M. Turner, M. Webb; (2017) *Integrated Electrolyte Gated OFET and microfluidics for developing a biosensor platform* [Presentation]; Sensors 2017 - Smart Chemical and Biological Sensing Technologies, 16 June. London: Royal Society of Chemistry.

G. Sunley Saez, M. Turner, M. Webb; (2015) *Developing a low cost point of care biosensor for breast cancer prognosis* [Presentation]; Annual Manchester Breast Centre PhD Students and PostDocs Symposium, 10 July. Manchester: The University of Manchester.

G. Sunley Saez; (2015) *Developing a low cost point of care biosensor for breast cancer prognosis* [Poster]; Institute of Human Development PGR Showcase, 16 June. Manchester: The University of Manchester.

ProtoFab Course: Thin Film Fabrication and Patterning [Delegate]; 23 – 24 March 2018. Sedgefield: Centre for Process Innovation.

Innovations in Large-Area Electronics (innoLAE) 2016 [Delegate]; 1-2 February 2016. Cambridge, UK: University of Cambridge.

11 References

1 M. Mascini and S. Tombelli, *Biomarkers*, 2008, **13**, 637–57.

2 A. D. McNaught and A. Wilkinson, *IUPAC Compendium of Chemical Terminology (The 'Gold Book')*, 2014.

3 M. Zarei, *TrAC - Trends Anal. Chem.*, 2017, **91**, 26–41.

4 C. D. Chin, T. Laksanasopin, Y. K. Cheung, D. Steinmiller, V. Linder, H. Parsa, J. Wang, H. Moore, R. Rouse, G. Umviligihozo, E. Karita, L. Mwambarangwe, S. L. Braunstein, J. van de Wijgert, R. Sahabo, J. E. Justman, W. El-Sadr and S. K. Sia, *Nat. Med.*, 2011, **17**, 1015–1019.

5 S. K. Sia and L. J. Kricka, *Lab Chip*, 2008, **8**, 1982.

6 A. Romeo, T. S. Leung and S. Sánchez, *Lab Chip*, 2016, **16**, 1957–1961.

7 C. D. Chin, V. Linder and S. K. Sia, *Lab Chip*, 2012, **12**, 2118.

8 J. F. Rusling, C. V. Kumar, J. S. Gutkind and V. Patel, *Analyst*, 2010, **135**, 2496.

9 K. K. Jain, *The Handbook of Biomarkers*, Springer New York, New York, NY, 2017.

10 N. Michael Green, in *Methods in Enzymology*, Academic Press, 1990, vol. 184, pp. 51–67.

11 S. K. Vashist, D. Zheng, K. Al-Rubeaan, J. H. T. Luong and F. S. Sheu, *Anal. Chim. Acta*, 2011, 703, 124–136.

12 D. J. Macaya, M. Nikolou, S. Takamatsu, J. T. Mabeck, R. M. Owens and G. G. Malliaras, *Sensors Actuators, B Chem.*, 2007, **123**, 374–378.

13 A. Koulman, G. A. Lane, S. J. Harrison and D. A. Volmer, *Anal. Bioanal. Chem.*, 2009, **394**, 663–670.

14 M. Mamas, W. B. Dunn, L. Neyses and R. Goodacre, *Arch. Toxicol.*, 2011, **85**, 5–17.

15 C. Bartic, A. Campitelli and S. Borghs, *Appl. Phys. Lett.*, 2003, **82**, 475.

16 X. Luo and J. J. Davis, *Chem. Soc. Rev.*, 2013, **42**, 5944–62.

17 A. Poghossian and M. J. Schöning, *Electroanalysis*, 2014, **26**, 1197–1213.

18 Y. Le Basle, P. Chennell, N. Tokhadze, A. Astier and V. Sautou, *J. Pharm. Sci.*, 2020, **109**, 169–190.

19 D. B. Bush and T. A. Knotts, *J. Chem. Phys.*, 2015, **143**, 61101.

20 A. A. Ansari, N. S. Hattikudur, S. R. Joshi and M. A. Medeira, *J. Immunol. Methods*, 1985, **84**, 117–124.

21 A. J. Heeger, *Chem. Soc. Rev.*, 2010, **39**, 2354–2371.

22 S. Allard, M. Forster, B. Souharce, H. Thiem and U. Scherf, *Angew. Chem. Int. Ed. Engl.*, 2008, **47**, 4070–98.

23 A. Pron, P. Gawrys, M. Zagorska, D. Djurado and R. Demadrille, *Chem. Soc. Rev.*, 2010, **39**, 2577–632.

24 P. Weimer, *Proc. IRE*, 1962, **50**, 1462–1469.

25 A. Tsumura, H. Koezuka and T. Ando, *Appl. Phys. Lett.*, 1986, **49**, 1210–1212.

26 C. L. Chochos and S. a. Choulis, *Prog. Polym. Sci.*, 2011, **36**, 1326–1414.

27 S.-C. Lo and P. L. Burn, *Chem. Rev.*, 2007, **107**, 1097–1116.

28 L. Kergoat, B. Piro, M. Berggren, G. Horowitz and M.-C. Pham, *Anal. Bioanal. Chem.*, 2012, **402**, 1813–26.

29 L. Torsi, M. Magliulo, K. Manoli and G. Palazzo, *Chem. Soc. Rev.*, 2013, **42**, 8612–28.

30 L. Torsi, A. Tafuri, N. Cioffi, M. C. Gallazzi, A. Sassella, L. Sabbatini and P. G. Zambonin, in *Sensors and Actuators, B: Chemical*, 2003, vol. 93, pp. 257–262.

31 C. K. Chiang, C. R. Fincher, Y. W. Park, A. J. Heeger, H. Shirakawa, E. J. Louis, S. C. Gau and A. G. MacDiarmid, *Phys. Rev. Lett.*, 1977, **39**, 1098–1101.
32 L. Leonat, G. Sbârcea and I. V. Brañzoi, *UPB Sci. Bull. Ser. B Chem. Mater. Sci.*, 2013, **75**, 111–118.
33 O. Ostroverkhova, D. G. Cooke, F. A. Hegmann, J. E. Anthony, V. Podzorov, M. E. Gershenson, O. D. Jurchescu and T. T. M. Palstra, *Appl. Phys. Lett.*, 2006, **88**, 162101.
34 M. Klues and G. Witte, *CrystEngComm*, 2018, **20**, 63–74.
35 D. Venkateshvaran, M. Nikolka, A. Sadhanala, V. Lemaur, M. Zelazny, M. Kepa, M. Hurhangee, A. J. Kronemeijer, V. Pecunia, I. Nasrallah, I. Romanov, K. Broch, I. McCulloch, D. Emin, Y. Olivier, J. Cornil, D. Beljonne and H. Sirringhaus, *Nature*, 2014, **515**, 384–388.
36 H. R. Tseng, H. Phan, C. Luo, M. Wang, L. A. Perez, S. N. Patel, L. Ying, E. J. Kramer, T. Q. Nguyen, G. C. Bazan and A. J. Heeger, *Adv. Mater.*, 2014, **26**, 2993–2998.
37 G. Kim, S. J. Kang, G. K. Dutta, Y. K. Han, T. J. Shin, Y. Y. Noh and C. Yang, *J. Am. Chem. Soc.*, 2014, **136**, 9477–9483.
38 C. B. Nielsen, M. Turbiez and I. McCulloch, *Adv. Mater.*, 2013, 25, 1859–1880.
39 H. Sirringhaus, *Adv. Mater.*, 2014, **26**, 1319–1335.
40 E. Danesh, D. J. Tate, S. Faraji, K. C. Persaud, L. A. Majewski, S. G. Yeates, M. L. Turner and C. Engineering, *Print. Fabr. 2016*, 2016, 162–164.
41 I. Kymissis, *Organic Field Effect Transistors*, Springer US, Boston, MA, 2009.
42 K. Schmoltner, J. Kofler, A. Klug and E. J. W. List-Kratochvil, in *Proceedings of SPIE - The International Society for Optical Engineering*, eds. Z. Bao, I. McCulloch, R. Shinar and I. Kymissis, 2013, vol. 8831, p. 88311N.
43 L. Kergoat, L. Herlogsson, D. Braga, B. Piro, M.-C. C. Pham, X. Crispin, M. Berggren and G. Horowitz, *Adv. Mater.*, 2010, **22**, 2565–9.
44 D. Elkington, N. Cooling, W. Belcher, P. Dastoor and X. Zhou, *Electronics*, 2014, **3**, 234–254.
45 A. Loi, I. Manunza and A. Bonfiglio, *Appl. Phys. Lett.*, 2005, **86**, 1–3.
46 K. Schmoltner, J. Kofler, A. Klug and E. J. W. List-Kratochvil, *Adv. Mater.*, 2013, **25**, 6895–6899.
47 X. Strakosas, M. Bongo and R. M. Owens, *J. Appl. Polym. Sci.*, 2015, **132**, 1–14.
48 F. A. Larik, M. Faisal, A. Saeed, Q. Abbas, M. A. Kazi, N. Abbas, A. A. Thebo, D. M. Khan and P. A. Channar, *Thiophene-based molecular and polymeric semiconductors for organic field effect transistors and organic thin film transistors*, Springer US, 2018, vol. 29.
49 C. R. Newman, C. D. Frisbie, D. A. da Silva Filho, J.-L. Brédas, P. C. Ewbank and K. R. Mann, *Chem. Mater.*, 2004, **16**, 4436–4451.
50 A. F. Paterson, S. Singh, K. J. Fallon, T. Hodsden, Y. Han, B. C. Schroeder, H. Bronstein, M. Heeney, I. McCulloch and T. D. Anthopoulos, *Adv. Mater.*, 2018, **30**, 1801079.
51 I. McCulloch, M. Heeney, C. Bailey, K. Genevicius, I. Macdonald, M. Shkunov, D. Sparrowe, S. Tierney, R. Wagner, W. Zhang, M. L. Chabinyc, R. J. Kline, M. D. McGehee and M. F. Toney, *Nat. Mater.*, 2006, **5**, 328–333.
52 Z. Chen, M. J. Lee, R. Shahid Ashraf, Y. Gu, S. Albert-Seifried, M. Meedom Nielsen, B. Schroeder, T. D. Anthopoulos, M. Heeney, I. McCulloch and H. Sirringhaus, *Adv. Mater.*, 2012, **24**, 647–652.
53 J. Li, Y. Zhao, H. S. Tan, Y. Guo, C.-A. Di, G. Yu, Y. Liu, M. Lin, S. H. Lim, Y. Zhou, H. Su and B. S. Ong, *Sci. Rep.*, 2012, **2**, 1–9.
54 Y. Li, S. P. Singh and P. Sonar, *Adv. Mater.*, 2010, **22**, 4862–4866.
55 X. Zhang, H. Bronstein, A. J. Kronemeijer, J. Smith, Y. Kim, R. J. Kline, L. J. Richter, T. D.

Anthopoulos, H. Sirringhaus, K. Song, M. Heeney, W. Zhang, I. McCulloch and D. M. Delongchamp, *Nat. Commun.*, 2013, **4**, 1–9.
56 R. a. Street, *Adv. Mater.*, 2009, **21**, 2007–2022.
57 A. Dodabalapur, H. E. Katz, L. Torsi and R. C. Haddon, *Science*, 1995, **269**, 1560–1562.
58 Y. Aleeva and B. Pignataro, *J. Mater. Chem. C*, 2014, 2, 6436–6453.
59 M. Waldrip, H. Haneef, A. Wadsworth, I. McCulloch and O. D. Jurchescu, *Flex. Print. Electron.*, **5,** 014015.
60 G. Horowitz, *J. Mater. Res.*, 2004, 19, 1946–1962.
61 S. D. Brotherton, *Introduction to Thin Film Transistors*, Springer International Publishing, Heidelberg, 2013.
62 M. Singh, M. Y. Mulla, M. V. Santacroce, M. Magliulo, C. Di Franco, K. Manoli, D. Altamura, C. Giannini, N. Cioffi, G. Palazzo, G. Scamarcio and L. Torsi, *J. Phys. D. Appl. Phys.*, 2016, **49**, 275101.
63 T. Cramer, a. Campana, F. Leonardi, S. Casalini, a. Kyndiah, M. Murgia and F. Biscarini, *J. Mater. Chem. B*, 2013, **1**, 3728.
64 F. Buth, D. Kumar, M. Stutzmann and J. A. Garrido, *Appl. Phys. Lett.*, 2011, **98**, 153302.
65 A. Laiho, L. Herlogsson, R. Forchheimer, X. Crispin and M. Berggren, *Proc. Natl. Acad. Sci. U. S. A.*, 2011, **108**, 15069–15073.
66 R. Porrazzo, S. Bellani, A. Luzio, E. Lanzarini, M. Caironi and M. R. Antognazza, *Org. Electron.*, 2014, **15**, 2126–2134.
67 G. S. Ryu, J. S. Kim, S. H. Jeong and C. K. Song, *Org. Electron. physics, Mater. Appl.*, 2013, **14**, 1218–1224.
68 Y. Nakajima, *JSID*, 2011, **19**, 94–99.
69 K. S. Johnson, J. A. Needoba, S. C. Riser and W. J. Showers, *Chem. Rev.*, 2007, 107, 623–640.
70 D. C. Wedge, A. Das, R. Dost, J. Kettle, M.-B. Madec, J. J. Morrison, M. Grell, D. B. Kell, T. H. Richardson and S. Yeates, *Sensors Actuators B Chem.*, 2009, **143**, 365–372.
71 R. M. Owens and G. G. Malliaras, *MRS Bull.*, 2012, **35**, 86–89.
72 M. Berggren and A. Richter-Dahlfors, *Adv. Mater.*, 2007, **19**, 3201–3213.
73 C. Bartic and G. Borghs, *Anal. Bioanal. Chem.*, 2005, **384**, 354–365.
74 H. U. Khan, M. E. Roberts, O. Johnson, R. Förch, W. Knoll and Z. Bao, *Adv. Mater.*, 2010, **22**, 4452–4456.
75 M. Magliulo, A. Mallardi, M. Y. Mulla, S. Cotrone, B. R. Pistillo, P. Favia, I. Vikholm-Lundin, G. Palazzo and L. Torsi, *Adv. Mater.*, 2013, **25**, 2090–2094.
76 S. Cotrone, M. Ambrico, H. Toss, M. D. Angione, M. Magliulo, A. Mallardi, M. Berggren, G. Palazzo, G. Horowitz, T. Ligonzo and L. Torsi, *Org. Electron.*, 2012, **13**, 638–644.
77 M. L. Hammock, A. N. Sokolov, R. M. Stoltenberg, B. D. Naab and Z. Bao, *ACS Nano*, 2012, **6**, 3100–3108.
78 T. Minamiki, T. Minami, R. Kurita, O. Niwa, S. Wakida, K. Fukuda, D. Kumaki and S. Tokito, *Materials (Basel).*, 2014, **7**, 6843–6852.
79 M. Y. Mulla, E. Tuccori, M. Magliulo, G. Lattanzi, G. Palazzo, K. Persaud and L. Torsi, *Nat. Commun.*, 2015, **6**, 6010.
80 F. Yan, S. M. Mok, J. Yu, H. L. W. Chan and M. Yang, *Biosens. Bioelectron.*, 2009, **24**, 1241–5.
81 T. Someya, A. Dodabalapur, A. Gelperin, H. E. Katz and Z. Bao, *Langmuir*, 2002, **18**, 5299–5302.
82 F. Maddalena, M. J. Kuiper, B. Poolman, F. Brouwer, J. C. Hummelen, D. M. de Leeuw, B. De

Boer and P. W. M. Blom, *J. Appl. Phys.*, 2010, **108**, 124501.
83 S. H. Kim, K. Hong, W. Xie, K. H. Lee, S. Zhang, T. P. Lodge and C. D. Frisbie, *Adv. Mater.*, 2013, 25, 1822–1846.
84 L. Kergoat, B. Piro, M. Berggren, M.-C. C. Pham, A. Yassar and G. Horowitz, *Org. Electron.*, 2012, **13**, 1–6.
85 F. Buth, A. Donner, M. Sachsenhauser, M. Stutzmann and J. a Garrido, *Adv. Mater.*, 2012, **24**, 4511–7.
86 S. A. Algarni, T. M. Althagafi, A. Al Naim and M. Grell, *Talanta*, 2016, **153**, 107–110.
87 P. Jonkheijm, D. Weinrich, H. Schröder, C. M. Niemeyer and H. Waldmann, *Angew. Chemie Int. Ed.*, 2008, **47**, 9618–9647.
88 D. Wang, V. Noël and B. Piro, *Electronics*, 2016, **5**, 9.
89 C. Nicosia and J. Huskens, *Mater. Horiz.*, 2014, **1**, 32–45.
90 K. Manoli, M. Magliulo, M. Y. Mulla, M. Singh, L. Sabbatini, G. Palazzo and L. Torsi, *Angew. Chemie - Int. Ed.*, 2015, **54**, 12562–12576.
91 M. L. Hammock, O. Knopfmacher, B. D. Naab, J. B.-H. Tok and Z. Bao, *ACS Nano*, 2013, **7**, 3970–3980.
92 E. Macchia, K. Manoli, B. Holzer, C. Di Franco, M. Ghittorelli, F. Torricelli, D. Alberga, G. F. Mangiatordi, G. Palazzo, G. Scamarcio and L. Torsi, *Nat. Commun.*, 2018, **9**, 3223.
93 P. Seshadri, K. Manoli, N. Schneiderhan-Marra, U. Anthes, P. Wierzchowiec, K. Bonrad, C. Di Franco and L. Torsi, *Biosens. Bioelectron.*, 2018, **104**, 113–119.
94 M. Magliulo, D. De Tullio, I. Vikholm-Lundin, W. M. Albers, T. Munter, K. Manoli, G. Palazzo and L. Torsi, *Anal. Bioanal. Chem.*, 2016, **408**, 3943–3952.
95 W. Huang, K. Besar, R. Lecover, P. Dulloor, J. Sinha, J. F. Martínez Hardigree, C. Pick, J. Swavola, A. D. Everett, J. Frechette, M. Bevan and H. E. Katz, *Chem. Sci.*, 2014, **5**, 416.
96 S. J. Kuhn, S. K. Finch, D. E. Hallahan and T. D. Giorgio, *J. Magn. Magn. Mater.*, 2007, **311**, 68–72.
97 M. Y. Mulla, P. Seshadri, L. Torsi, K. Manoli, A. Mallardi, N. Ditaranto, M. V. Santacroce, C. Di Franco, G. Scamarcio, M. Magliulo, C. Di Franco, G. Scamarcio, M. Magliulo, C. Di Franco, G. Scamarcio and M. Magliulo, *J. Mater. Chem. B*, 2015, **3**, 5049–5057.
98 C. Suspène, B. Piro, S. Reisberg, M.-C. C. Pham, H. Toss, M. Berggren, A. Yassar and G. Horowitz, *J. Mater. Chem. B*, 2013, **1**, 2090.
99 J. Huang, J. Miragliotta, A. Becknell and H. E. Katz, *J. Am. Chem. Soc.*, 2007, **129**, 9366–9376.
100 M. Magliulo, B. R. Pistillo, M. Y. Mulla, S. Cotrone, N. Ditaranto, N. Cioffi, P. Favia and L. Torsi, *Plasma Process. Polym.*, 2013, **10**, 102–109.
101 K. Manoli, G. Palazzo, E. Macchia, A. Tiwari, C. Di Franco, G. Scamarcio, P. Favia, A. Mallardi and L. Torsi, in *Organic Sensors and Bioelectronics X*, eds. R. Shinar, I. Kymissis and L. Torsi, SPIE, 2017, p. 17.
102 M. Medina-Sánchez, C. Martínez-Domingo, E. Ramon and A. Merkoçi, *Adv. Funct. Mater.*, 2014, **24**, 6291–6302.
103 J. Song, J. Dailey, H. Li, H.-J. Jang, L. Russell, P. Zhang, P. C. Searson, J. T.-H. Wang, A. D. Everett and H. E. Katz, *Adv. Funct. Mater.*, 2018, **28**, 1802605.
104 B. Piro, D. Wang, D. Benaoudia, A. Tibaldi, G. Anquetin, V. Noël, S. Reisberg, G. Mattana and B. Jackson, *Biosens. Bioelectron.*, 2017, **92**, 215–220.
105 T. T. K. N. Nguyen, T. T. K. N. Nguyen, G. Anquetin, S. Reisberg, V. Noël, G. Mattana, J. Touzeau, F. Barbault, M. C. Pham and B. Piro, *Biosens. Bioelectron.*, 2018, **113**, 32–38.

106 T. Cramer, A. Kyndiah, M. Murgia, F. Leonardi, S. Casalini and F. Biscarini, *Appl. Phys. Lett.*, 2012, **100**, 143302.
107 L. Kergoat, N. Battaglini, L. Miozzo, B. Piro, M.-C. Pham, A. Yassar and G. Horowitz, *Org. Electron.*, 2011, **12**, 1253–1257.
108 K. Manoli, M. M. Patrikoussakis, M. Magliulo, L. M. Dumitru, M. Y. Mulla, L. Sabbatini and L. Torsi, *Org. Electron.*, 2014, **15**, 2372–2380.
109 R. A. Picca, K. Manoli, E. Macchia, A. Tricase, C. Di Franco, G. Scamarcio, N. Cioffi and L. Torsi, *Front. Chem.*, 2019, **7**, 1–10.
110 E. Macchia, K. Manoli, B. Holzer, C. Di Franco, R. A. Picca, N. Cioffi, G. Scamarcio, G. Palazzo and L. Torsi, *Anal. Bioanal. Chem.*, 2019, **411**, 4899–4908.
111 E. Macchia, A. Tiwari, K. Manoli, B. Holzer, N. Ditaranto, R. A. Picca, N. Cioffi, C. Di Franco, G. Scamarcio, G. Palazzo and L. Torsi, *Chem. Mater.* 2019, **31**, 17, 6476–6483.
112 Y. Pei-Wen, H. Che-Wei, H. Yu-Jie, C. Min-Cheng, L. Hsin-Hao, L. Shey-Shi and L. Chih-Ting, *Biosens. Bioelectron.*, 2014, **61**, 112–8.
113 F. Shen, J. Wang, Z. Xu, Y. Wu, Q. Chen, X. Li, X. Jie, L. Li, M. Yao, X. Guo and T. Zhu, *Nano Lett.*, 2012, **12**, 3722–30.
114 T.-W. Lin, P.-J. Hsieh, C.-L. Lin, Y.-Y. Fang, J.-X. Yang, C.-C. Tsai, P.-L. Chiang, C.-Y. Pan and Y.-T. Chen, *Proc. Natl. Acad. Sci. U. S. A.*, 2010, **107**, 1047–52.
115 K. Maehashi, T. Katsura, K. Kerman, Y. Takamura, K. Matsumoto and E. Tamiya, *Anal. Chem.*, 2007, **79**, 782–787.
116 S. Liu and X. Guo, *NPG Asia Mater.*, 2012, **4**, e23.
117 X. Guo, *Adv. Mater.*, 2013, **25**, 3397–408.
118 M. B. Lerner, J. D'Souza, T. Pazina, J. Dailey, B. R. Goldsmith, M. K. Robinson and a T. C. Johnson, *ACS Nano*, 2012, **6**, 5143–9.
119 S. Myung, A. Solanki, C. Kim, J. Park, K. S. Kim and K.-B. Lee, *Adv. Mater.*, 2011, **23**, 2221–2225.
120 Y. Ohno, K. Maehashi and K. Matsumoto, *J. Am. Chem. Soc.*, 2010, **132**, 18012–18013.
121 A. C. Arias, F. Endicott and R. A. Street, *Adv. Mater.*, 2006, **18**, 2900–2904.
122 M. Di Lauro, M. Berto, M. Giordani, S. Benaglia, G. Schweicher, D. Vuillaume, C. A. Bortolotti, Y. H. Geerts and F. Biscarini, *Adv. Electron. Mater.*, 2017, **3**, 1700159.
123 Y. Zhang, G. Han, M. Qin, Y. Shen, X. Lu, Y. Yi and N. Zhao, *Chem. Mater.*, 2018, **30**, 5422–5428.
124 D. Karley, *J. Mol. Biomark. Diagn.*, 2011, **2**, 1–7.
125 A. Alkhateeb, L. Zubritsky, B. Kinsman, K. Leitzel, C. Campbell-Baird, S. M. Ali, J. Connor and A. Lipton, *J. Gastrointest. Cancer*, 2014, **45**, 161–7.
126 A. A. Alkhateeb, K. Leitzel, S. M. Ali, C. Campbell-Baird, M. Evans, E.-M. M. Fuchs, W. J. Köstler, A. Lipton and J. Connor, *PLoS One*, 2012, **7**, e51379.
127 G. J. Zhang, K. T. C. Chai, H. Z. H. Luo, J. M. Huang, I. G. K. Tay, A. E. J. Lim and M. Je, *Biosens. Bioelectron.*, 2012, **35**, 218–223.
128 A. Qureshi, J. H. Niazi, S. Kallempudi and Y. Gurbuz, *Biosens. Bioelectron.*, 2010, **25**, 2318–2323.
129 G. Zheng, F. Patolsky, Y. Cui, W. U. Wang and C. M. Lieber, *Nat. Biotechnol.*, 2005, **23**, 1294–1301.
130 A. F. Chrimes, K. Khoshmanesh, P. R. Stoddart, A. Mitchell and K. Kalantar-zadeh, *Chem. Soc. Rev.*, 2013, **42**, 5880–5906.

131 E. Stern, A. Vacic, N. K. Rajan, J. M. Criscione, J. Park, T. M. Fahmy and M. A. Reed, in *ICSICT-2010 - 2010 10th IEEE International Conference on Solid-State and Integrated Circuit Technology, Proceedings*, 2010, pp. 1392–1393.
132 A. H. Nguyen, J. Lee, H. Il Choi, H. Seok Kwak and S. Jun Sim, *Biosens. Bioelectron.*, 2015, **70**, 358–365.
133 P. Casal, X. Wen, S. Gupta, T. Nicholson, Y. Wang, A. Theiss, B. Bhushan, L. Brillson, W. Lu and S. C. Lee, *Philos. Trans. A. Math. Phys. Eng. Sci.*, 2012, **370**, 2474–88.
134 A. R. Statz, R. J. Meagher, A. E. Barron and P. B. Messersmith, *J. Am. Chem. Soc.*, 2005, **127**, 7972–3.
135 S. Hideshima, R. Sato, S. Inoue, S. Kuroiwa and T. Osaka, *Sensors Actuators B Chem.*, 2012, **161**, 146–150.
136 M. Steinitz, *Anal. Biochem.*, 2000, **282**, 232–238.
137 H. Vaisocherová, W. Yang, Z. Zhang, Z. Cao, G. Cheng, M. Piliarik, J. Homola and S. Jiang, *Anal. Chem.*, 2008, **80**, 7894–7901.
138 H. Vaisocherová, V. Ševců, P. Adam, B. Špačková, K. Hegnerová, A. de los Santos Pereira, C. Rodriguez-Emmenegger, T. Riedel, M. Houska, E. Brynda and J. Homola, *Biosens. Bioelectron.*, 2014, **51**, 150–157.
139 V. Krivitsky, L. C. Hsiung, A. Lichtenstein, B. Brudnik, R. Kantaev, R. Elnathan, A. Pevzner, A. Khatchtourints and F. Patolsky, *Nano Lett.*, 2012, **12**, 4748–4756.
140 J. N. Israelachvili, *Intermolecular and Surface Forces*, 2011.
141 E. Stern, R. Wagner, F. J. Sigworth, R. Breaker, T. M. Fahmy and M. A. Reed, *Nano Lett.*, 2007, **7**, 3405–3409.
142 F. N. Ishikawa, H. K. Chang, M. Curreli, H. I. Liao, C. A. Olson, P. C. Chen, R. Zhang, R. W. Roberts, R. Sun, R. J. Cote, M. E. Thompson and C. Zhou, *ACS Nano*, 2009, **3**, 1219–1224.
143 O. Knopfmacher, M. L. Hammock, A. L. Appleton, G. Schwartz, J. Mei, T. Lei, J. Pei and Z. Bao, *Nat. Commun.*, 2014, **5**, 2954.
144 G. Palazzo, D. De Tullio, M. Magliulo, A. Mallardi, F. Intranuovo, M. Y. Mulla, P. Favia, I. Vikholm-Lundin and L. Torsi, *Adv. Mater.*, 2014, 911–916.
145 R. Elnathan, M. Kwiat, A. Pevzner, Y. Engel, L. Burstein, A. Khatchtourints, A. Lichtenstein, R. Kantaev and F. Patolsky, *Nano Lett.*, 2012, **12**, 5245–5254.
146 M. J. Schöning and A. Poghossian, *Analyst*, 2002, **127**, 1137–1151.
147 K. Murphy, P. Travers and M. Walport, *Janeway's Immunobiology*, 2008, vol. 7.
148 H. U. Khan, J. Jang, J. J. Kim and W. Knoll, *J. Am. Chem. Soc.*, 2011, **133**, 2170–2176.
149 C.-S. Chen, K.-N. Chang, Y.-H. Chen, C.-K. Lee, B. Y.-J. Lee and A. S.-Y. Lee, *Biosens. Bioelectron.*, 2011, **26**, 3072–6.
150 S. Lai, M. Barbaro and A. Bonfiglio, *Sensors Actuators, B Chem.*, 2016, **233**, 314–319.
151 S. Song, L. Wang, J. Li, C. Fan and J. Zhao, *TrAC Trends Anal. Chem.*, 2008, **27**, 108–117.
152 V. Knutson, *J. Biol. Chem.*, 1988, **263**, 14146–14151.
153 Z. Kuang, S. N. Kim, W. J. Crookes-Goodson, B. L. Farmer and R. R. Naik, *ACS Nano*, 2010, **4**, 452–458.
154 S. Cheng, K. Hotani, S. Hideshima, S. Kuroiwa, T. Nakanishi, M. Hashimoto, Y. Mori and T. Osaka, *Materials (Basel).*, 2014, **7**, 2490–2500.
155 S. Okamoto, Y. Ohno, K. Maehashi, K. Inoue and K. Matsumoto, *Jpn. J. Appl. Phys.*, 2012, **51**, 06FD08.
156 J. Huang, J. Sun and H. E. Katz, *Adv. Mater.*, 2008, **20**, 2567–2572.

157 T. M. Althagafi, S. A. Algarni and M. Grell, *Talanta*, 2016, **158**, 70–76.
158 J. Ferlay, I. Soerjomataram, R. Dikshit, S. Eser, C. Mathers, M. Rebelo, D. M. Parkin, D. Forman and F. Bray, *Int. J. Cancer*, 2015, **136**, E359–E386.
159 F. Bray, in *World cancer report*, 2014, pp. 54–68.
160 D. Hanahan and R. A. Weinberg, *Cell*, 2011, **144**, 646–674.
161 N. L. Henry and D. F. Hayes, *Mol. Oncol.*, 2012, 6, 140–146.
162 K. K. Jain, in *The Handbook of Biomarkers*, Springer New York, New York, NY, 2010, pp. 189–326.
163 S. Ozturk, A. W. Lambert, C. K. Wong, P. Papageorgis and S. Thiagalingam, in *Systems Biology of Cancer*, 2015, pp. 282–294.
164 S. J. Cheang MCU, Chia SK, Voduc D, Gao D, Leung S, *J Natl Cancer Int*, 2015, **10**, 736–750.
165 M. Smid, Y. Wang, Y. Zhang, A. M. Sieuwerts, J. Yu, J. G. M. Klijn, J. A. Foekens and J. W. M. Martens, *Cancer Res.*, 2008, **68**, 3108–3114.
166 X. Dai, T. Li, Z. Bai, Y. Yang, X. Liu, J. Zhan and B. Shi, *Am. J. Cancer Res.*, 2015, 5, 2929–2943.
167 Z. Kos and D. J. Dabbs, *Histopathology*, 2016, **68**, 70–85.
168 A. Goldhirsch, E. P. Winer, A. S. Coates, R. D. Gelber, M. Piccart-Gebhart *et al*, *Ann. Oncol.*, 2013, **24**, 2206–2223.
169 L. Pusztai, K. Broglio, F. Andre, W. Fraser Symmans, K. R. Hess and G. N. Hortobagyi, *J. Clin. Oncol.*, 2008, **26**, 4679–4683.
170 M. Dowsett, C. Allred, J. Knox, E. Quinn, J. Salter, C. Wale, J. Cuzick, J. Houghton, N. Williams, E. Mallon, H. Bishop, I. Ellis, D. Larsimont, H. Sasano, P. Carder, A. L. Cussac, F. Knox, V. Speirs, J. Forbes and A. Buzdar, *J. Clin. Oncol.*, 2008, **26**, 1059–1065.
171 M. Y. C. Polley, S. C. Y. Leung, L. M. McShane, D. Gao, J. C. Hugh, M. G. Mastropasqua, G. Viale, L. A. Zabaglo, F. Penault-Llorca, J. M. S. Bartlett, A. M. Gown, W. F. Symmans, T. Piper, E. Mehl, R. A. Enos, D. F. Hayes, M. Dowsett and T. O. Nielsen, *J. Natl. Cancer Inst.*, 2013, **105**, 1897–1906.
172 M. Mengel, R. Von Wasielewski, B. Wiese, T. Rüdiger, H. K. Müller-Hermelink and H. Kreipe, *J. Pathol.*, 2002, **198**, 292–299.
173 M. A. Aleskandarany, E. A. Rakha, R. D. MacMillan, D. G. Powe, I. O. Ellis and A. R. Green, *Breast Cancer Res. Treat.*, 2011, **127**, 591–599.
174 A. Perrier, J. Gligorov, G. Lefèvre and M. Boissan, *Lab. Investig.*, 2018, **98**, 696–707.
175 H.-S. Cho, K. Mason, K. X. Ramyar, A. M. Stanley, S. B. Gabelli, D. W. Denney and D. J. Leahy, *Nature*, 2003, **421**, 756–760.
176 R. Molina, J. Jo, X. Filella, J. Bruix, A. Castells, M. Hague and A. M. Ballesta, *Tumor Biol.*, 1997, **18**, 188–196.
177 D. J. . Slamon, B. Keyland-Jones and S. Shak, *N. Engl. J. Med.*, 2001, **344**, 783–792.
178 J. Bayani, C. Q. Yao, M. A. Quintayo, F. Yan, S. Haider, A. D'Costa, C. L. Brookes, C. J. H. van de Velde, A. Hasenburg, D. G. Kieback, C. Markopoulos, L. Dirix, C. Seynaeve, D. Rea, P. C. Boutros and J. M. S. Bartlett, *npj Breast Cancer*, 2017, **3**, 3.
179 D. T. Tsoi, M. Inoue, C. M. Kelly, S. Verma and K. I. Pritchard, *Oncologist*, 2010, **15**, 457–465.
180 M. J. Duffy, E. W. McDermott and J. Crown, *Tumor Biol.*, 2018, **40**, 1–11.
181 Liu, M.C.Liu, Minetta C.Cummings, Steven R. Absalan, Farnaz Curtis, Christina *et al*.
Annals of Oncology, Volume 31, Issue 6, 745 - 759.
182 D. Di Gioia, M. Dresse, D. Mayr, D. Nagel, V. Heinemann, S. Kahlert and P. Stieber, *Clin. Chim. Acta*, 2014, **430**, 86–91.

183 J. H. Ha, M. K. Seong, E. K. Kim, J. K. Lee, H. Seol, J. Y. Lee, J. Byeon, Y. J. Sohn, J. S. Koh, I. C. Park, W. C. Noh and H. A. Kim, *J. Breast Cancer*, 2014, **17**, 33–39.
184 A. C. Pedersen, P. D. Sørensen, E. H. Jacobsen, J. S. Madsen and I. Brandslund, *Clin. Chem. Lab. Med.*, 2013, **51**, 1511–1519.
185 J. Cuzick, M. Dowsett, S. Pineda, C. Wale, J. Salter, E. Quinn, L. Zabaglo, E. Mallon, A. R. Green, I. O. Ellis, A. Howell, A. U. Buzdar and J. F. Forbes, *J. Clin. Oncol.*, 2011, **29**, 4273–4278.
186 L. Mauriac, A. Keshaviah, M. Debled, H. Mouridsen, J. F. Forbes, B. Thürlimann, R. Paridaens, A. Monnier, I. Láng, A. Wardley, J. M. Nogaret, R. D. Gelber, M. Castiglione-Gertsch, K. N. Price, A. S. Coates, I. Smith, G. Viale, M. Rabaglio, N. Zabaznyi and A. Goldhirsch, *Ann. Oncol.*, 2007, **18**, 859–867.
187 V. Sieben, C. S. Debes Marun, P. Pilarski, G. V. Kaigala, L. M. Pilarski and C. J. Backhouse, *IET Nanobiotechnology*, 2007, **1**, 27.
188 T. Iman, S. Amani and A. Mona, *J. Cancer Ther.*, 2013, **4**, 41–48.
189 J. L. Fox, P. H. Hsu, M. S. Legator, L. E. Morrison and S. A. Seelig, *Clin. Chem.*, 1995, 41, 1554–1559.
190 D. W. Piston and G.-J. Kremers, *Trends Biochem. Sci.*, 2007, **32**, 407–414.
191 S. a Soper, K. Brown, A. Ellington, B. Frazier, G. Garcia-Manero, V. Gau, S. I. Gutman, D. F. Hayes, B. Korte, J. L. Landers, D. Larson, F. Ligler, A. Majumdar, M. Mascini, D. Nolte, Z. Rosenzweig, J. Wang and D. Wilson, *Biosens. Bioelectron.*, 2006, **21**, 1932–42.
192 E. Macchia, A. Tiwari, K. Manoli, B. Holzer, N. Ditaranto, R. A. Picca, N. Cioffi, C. Di Franco, G. Scamarcio, G. Palazzo and L. Torsi, *Chem. Mater.*, 2019, **31**, 6476–6483.
193 B. Holzer, K. Manoli, N. Ditaranto, E. Macchia, A. Tiwari, C. Di Franco, G. Scamarcio, G. Palazzo and L. Torsi, *Adv. Biosyst.*, 2017, **1**, 1700055.
194 F. Torricelli, E. Macchia, K. Manoli, C. Di Franco, Z. M. Kovacs-Vajna, G. Palazzo, G. Scamarcio and L. Torsi, *2019 IEEE 8th Int. Work. Adv. Sensors Interfaces*, 2019, 70–74.
195 K. Cali and K. C. Persaud, *Sci. Rep.*, 2020, **10**, 1–13.
196 A. F. Al Baroot and M. Grell, *Mater. Sci. Semicond. Process.*, 2019, **89**, 216–222.
197 R. Porrazzo, S. Bellani, a. Luzio, C. Bertarelli, G. Lanzani, M. Caironi and M. R. Antognazza, *APL Mater.*, 2015, **3**, 14905.
198 L. Kergoat, L. Herlogsson, B. Piro, M. C. Pham, G. Horowitz, X. Crispin and M. Berggren, *Proc. Natl. Acad. Sci. U. S. A.*, 2012, **109**, 8394–9.
199 I. Brodie, J. J. Muray and J. J. Murray, *The physics of micro/nano-fabrication*, Springer International Publishing, 1992, vol. 49.
200 M. L. Forcada and C. M. Mate, *J. Colloid Interface Sci.*, 1993, **160**, 218–225.
201 M. Kang, J. S. Yeo, W. T. Park, N. K. Kim, D. H. Lim, H. Hwang, K. J. Baeg, Y. Y. Noh and D. Y. Kim, *Adv. Funct. Mater.*, 2016, **26**, 8527–8536.
202 K. Manoli, L. M. Dumitru, M. Y. Mulla, M. Magliulo, C. Di Franco, M. V. Santacroce, G. Scamarcio and L. Torsi, *Sensors (Switzerland)*, 2014, **14**, 16869–16880.
203 B. Urasinska-Wojcik, M. Wrackmeyer, D. Das, J. Opoku, L. Majewski and M. L. Turner, *Unpublished*.
204 J.-Y. Le Brazidec, C. A. Gilson and M. F. Boehm, *J. Org. Chem.*, 2005, **70**, 8212–8215.
205 M. a Pilkington-miksa, M. J. Writer, S. Sarkar, Q. Meng, S. E. Barker, P. A. Shamlou, H. C. Hailes, S. L. Hart and A. B. Tabor, *Society*, 2007, **4**, 1800–1810.
206 M. S. Chisholm, *J. Chem. Educ.*, 2000, **77**, 841.
207 J. A. Cholmeley, *BMJ*, 1945, **2**, 585–585.

208 N. G. Semaltianos, *Microelectronics J.*, 2007, **38**, 754–761.
209 H. Wensink, F. Benito-Lopez, D. C. Hermes, W. Verboom, H. J. G. E. Gardeniers, D. N. Reinhoudt and A. van den Berg, *Lab Chip*, 2005, **5**, 280–284.
210 J. M. Goddard and J. H. Hotchkiss, *Prog. Polym. Sci.*, 2007, **32**, 698–725.
211 S. Hosseini, F. Ibrahim, I. Djordjevic and L. H. Koole, *Appl. Surf. Sci.*, 2014, **300**, 43–50.
212 S. Hosseini, P. Azari, M. Aeinehvand, H. Rothan, I. Djordjevic, S. Martinez-Chapa and M. Madou, *Appl. Sci.*, 2016, **6**, 336.
213 S. T. Sanjay, G. Fu, M. Dou, F. Xu, R. Liu, H. Qi and X. Li, *Analyst*, 2015, **140**, 7062–7081.
214 Y. Bai, C. G. Koh, M. Boreman, Y.-J. J. Juang, I.-C. C. Tang, L. J. Lee and S.-T. T. Yang, *Langmuir*, 2006, **22**, 9458–9467.
215 S. Hosseini, F. Ibrahim, H. a. Rothan, R. Yusof, C. Van Der Marel, I. Djordjevic and L. H. Koole, *Biochem. Eng. J.*, 2015, **99**, 183–192.
216 F. Darain, K. L. Gan and S. C. Tjin, *Biomed. Microdevices*, 2009, **11**, 653–661.
217 F. Darain, M. A. Wahab and S. C. Tjin, *Anal. Lett.*, 2012, **45**, 2569–2579.
218 S. Hosseini, P. Azari, E. Farahmand, S. N. Gan, H. a. Rothan, R. Yusof, L. H. Koole, I. Djordjevic and F. Ibrahim, *Biosens. Bioelectron.*, 2015, **69**, 257–264.
219 S. Hosseini, M. M. Aeinehvand, S. M. Uddin, A. Benzina, H. a Rothan, R. Yusof, L. H. Koole, M. J. Madou, I. Djordjevic and F. Ibrahim, *Sci. Rep.*, 2015, **5**, 16485.
220 S. Patris, P. De Pauw, M. Vandeput, J. Huet, P. Van Antwerpen, S. Muyldermans and J. M. Kauffmann, *Talanta*, 2014, **130**, 164–170.
221 J. G. Vilhena, a. C. Dumitru, E. T. Herruzo, J. I. Mendieta-Moreno, R. Garcia, P. a. Serena and R. Pérez, *Nanoscale*, 2016, **8**, 13463–13475.
222 D. J. Shaw, in *Introduction to Colloid and Surface Chemistry*, Elsevier, 1992, pp. 151–173.
223 I. Vikholm-Lundin and W. M. Albers, *Biosens. Bioelectron.*, 2006, **21**, 1141–1148.
224 S. Hosseini, F. Ibrahim, I. Djordjevic, H. a. Rothan, R. Yusof, C. van der Marel and L. H. Koole, *Appl. Surf. Sci.*, 2014, **317**, 630–638.
225 S. Hosseini, F. Ibrahim, I. Djordjevic and L. H. Koole, *Analyst*, 2014, **139**, 2933–43.
226 L. Brown, T. Koerner, J. H. Horton and R. D. Oleschuk, *Lab Chip*, 2006, **6**, 66–73.
227 S. Casalini, F. Leonardi, T. Cramer and F. Biscarini, *Org. Electron.*, 2013, **14**, 156–163.
228 S. Casalini, A. C. Dumitru, F. Leonardi, C. A. Bortolotti, E. T. Herruzo, A. Campana, R. F. De Oliveira, T. Cramer, R. Garcia and F. Biscarini, *ACS Nano*, 2015, **9**, 5051–5062.
229 P. Pelosi, J. Zhu and W. Knoll, *Sensors (Switzerland)*, 2018, 18.
230 J. C. Thomas, D. P. Goronzy, K. Dragomiretskiy, D. Zosso, J. Gilles, S. J. Osher, A. L. Bertozzi and P. S. Weiss, *ACS Nano*, 2016, **10**, 5446–5451.
231 Z. A. Lamport, H. F. Haneef, S. Anand, M. Waldrip and O. D. Jurchescu, *J. Appl. Phys.*, 2018, **124**, 71101.
232 W. Osikowicz, M. P. de Jong, S. Braun, C. Tengstedt, M. Fahlman and W. R. Salaneck, *Appl. Phys. Lett.*, 2006, **88**, 193504.
233 A. Härtl, B. Baur, M. Stutzmann and J. A. Garrido, *Langmuir*, 2008, **24**, 9898–9906.
234 E. Macchia, P. Romele, K. Manoli, M. Ghittorelli, M. Magliulo, Z. M. Kovács-Vajna, F. Torricelli and L. Torsi, *Flex. Print. Electron.*, 2018, **3**, 34002.
235 B. Kang, F. Ge, L. Qiu and K. Cho, *Adv. Electron. Mater.*, 2017, **3**, 1600240.
236 X. Wang, W. H. Lee, G. Zhang, X. Wang, B. Kang, H. Lu, L. Qiu and K. Cho, *J. Mater. Chem. C*, 2013, **1**, 3989.

237 G. Lu, J. Blakesley, S. Himmelberger, P. Pingel, J. Frisch, I. Lieberwirth, I. Salzmann, M. Oehzelt, R. Di Pietro, A. Salleo, N. Koch and D. Neher, *Nat. Commun.*, 2013, **4**, 1588.
238 Y. Lei, P. Deng, J. Li, M. Lin, F. Zhu, T.-W. Ng, C.-S. Lee and B. S. Ong, *Sci. Rep.*, 2016, **6**, 24476.
239 J. Liu, D. Haynes, C. Balliet, R. Zhang, T. Kowalewski and R. D. McCullough, *Adv. Funct. Mater.*, 2012, **22**, 1024–1032.
240 Y. Lin, Q. Wei, G. Qian, L. Yao and J. J. Watkins, *Macromolecules*, 2012, **45**, 8665–8673.
241 S. Fabiano, S. Braun, M. Fahlman, X. Crispin and M. Berggren, *Adv. Funct. Mater.*, 2014, **24**, 695–700.
242 S. Rentenberger, A. Vollmer, E. Zojer, R. Schennach and N. Koch, *J. Appl. Phys.*, 2006, **100**, 53701.
243 David R. Lide, *J. Am. Chem. Soc.*, 2007, **129**, 724–724.
244 A. Wan, J. Hwang, F. Amy and A. Kahn, *Org. Electron. physics, Mater. Appl.*, 2005, **6**, 47–54.
245 G. Kelsey, *J. Electrochem. Soc.*, 1977, **124**, 814–819.
246 M. Anik and K. Osseo-Asare, *J. Electrochem. Soc.*, 2002, **149**, B224.
247 R. S. Lillard, *J. Electrochem. Soc.*, 1998, **145**, 2718.
248 T. Heumann and N. Stolica, *Electrochim. Acta*, 1971, **16**, 643–651.
249 K. Schmoltner, A. Klug, J. Kofler and E. J. W. List, in *Proceedings of SPIE*, eds. R. Shinar and I. Kymissis, International Society for Optics and Photonics, 2012, vol. 8479, p. 84790J.
250 A. Klug, A. Meingast, G. Wurzinger, A. Blümel, K. Schmoltner, U. Scherf and E. J. W. List, eds. R. Shinar and I. Kymissis, 2011, p. 811809.
251 L. Herlogsson, Y. Y. Noh, N. Zhao, X. Crispin, H. Sirringhaus and M. Berggren, *Adv. Mater.*, 2008, **20**, 4708–4713.
252 D. Braga, M. Ha, W. Xie and C. D. Frisbie, *Appl. Phys. Lett.*, 2010, **97**, 193311.
253 R. Porrazzo, A. Luzio, S. Bellani, G. E. Bonacchini, Y.-Y. Y. Noh, Y.-H. H. Kim, G. Lanzani, M. R. Antognazza and M. Caironi, *ACS Omega*, 2017, **2**, 1–10.
254 M. Berto, C. Diacci, R. D'Agata, M. Pinti, E. Bianchini, M. Di Lauro, S. Casalini, A. Cossarizza, M. Berggren, D. Simon, G. Spoto, F. Biscarini and C. A. Bortolotti, *Adv. Biosyst.*, 2018, **2**, 1700072.
255 A. Ravalli, D. Voccia, I. Palchetti and G. Marrazza, *Biosensors*, 2016, **6**, 39.
256 A. Ravalli, C. G. da Rocha, H. Yamanaka and G. Marrazza, *Bioelectrochemistry*, 2015, **106**, 268–275.
257 A. Qureshi, Y. Gurbuz and J. H. Niazi, *Sensors Actuators B Chem.*, 2015, **220**, 1145–1151.
258 W. Huang, A. K. Diallo, J. L. Dailey, K. Besar and H. E. Katz, *J. Mater. Chem. C*, 2015, **3**, 6445–6470.
259 B. Reddy, E. Salm and R. Bashir, *Annu. Rev. Biomed. Eng.*, 2016, **18**, 329–355.
260 H. Becker and L. E. Locascio, *Talanta*, 2002, 56, 267–287.
261 J. Novotný and F. Foret, *J. Sep. Sci.*, 2017, **40**, 383–394.
262 H. Jiang, Z. Huang, G. Xue, H. Chen and H. Li, *J. Mater. Chem. C*, 2018, **6**, 12001–12005.
263 A. F. Al Naim and M. Grell, *J. Appl. Phys.*, 2012, **112**, 114502.
264 R. Schroeder, L. a. Majewski and M. Grell, *Appl. Phys. Lett.*, 2004, **84**, 1004–1006.
265 H. Sirringhaus, *Adv. Mater.*, 2009, **21**, 3859–3873.
266 I. S. Tsagkalias, T. K. Manios and D. S. Achilias, *Polymers (Basel).*, 2017, **9**, 432.
267 C. Duval-Terrié and L. Lebrun, *J. Chem. Educ.*, 2006, **83**, 443.
268 L. Malekmotiei, G. Z. Voyiadjis, A. Samadi-Dooki, F. Lu and J. Zhou, *J. Polym. Sci. Part B Polym. Phys.*, 2017, **55**, 1286–1297.
269 J. H. Park, D. K. Hwang, J. Lee, S. Im and E. Kim, *Thin Solid Films*, 2007, **515**, 4041–4044.

270 Chemours, *Vazo™ Grade Sel.*, https://www.chemours.com/Vazo/en_US/products/grade.